Università degli Studi di Bologna
Facoltà di Scienze Matematiche, Fisiche e Naturali
Dipartimento di Astronomia dell'Universitá di Bologna
Settore Scientifico Disciplinare FIS/05

Probing the innermost regions around supermassive black holes through X–ray spectral variability

PhD Thesis of:
Gabriele Ponti

Supervisor
Prof. Giorgio G.C. Palumbo

Coordinator
Prof. Lauro Moscardini

Co–Supervisors
Dr. Massimo Cappi
Prof.ssa Laura Maraschi

Scuola di dottorato in Scienze Matematiche, Fisiche e Astronomiche
Dottorato di Ricerca in Astronomia - XIX ciclo
PhD Thesis in Astronomy
Bologna, Marzo 2007

Contents

Chapter 1

Introduction

In the center of many galaxies, as well as in our own, there exists a massive dark object pulling at nearby stars and gas clouds with its gravity (Genzel et al. 1997). The mass of these invisible bodies can be estimated through the measurements of the orbital speed of the gas clouds and it turned out to be in the range between about millions and billions of solar masses (Kormendy & Richstone 1995; Kormendy & Gebhardt 2001). The compact surroundings of these dark objects are generally quiet, but in about 10–20% of galaxies they have a luminosity ranging from about 10^{41} up to 10^{47} erg s^{-1}. These are called "active galaxies" (AGN).

Already in the 1940s the AGNs were known (Seyfert 1943; Schmidt 1963) and the astronomers had the problem to explain how the incredibly high luminosity could be produced in a volume significantly smaller than a cubic parsec. Soon after this, Zel'dovich & Novikov (1964) and Salpeter (1964) suggested what is still the current paradigm for the AGN phenomenon: AGN consist of a "central engine" made by a hot accretion disc surrounding a supermassive black hole (BH). Since then this model and the BH hypothesis have been supported by increasing observational evidence.

Because of its angular momentum, the matter does not fall directly into the hole, but instead orbits around the black hole first to form an accretion disc. The material in the accretion disc moves faster as it approaches the central black hole and due to friction produced in the accretion disc (Balbus & Hawley 1991) it is heated to very high temperatures and emits light. The energy produced by the matter falling into the BH could be so high as a significant fraction (even much more than ten per cent) of its energy rest mass. In fact, this is one of the most efficient processes known to produce energy, it is so strong that it can explain how such a high luminosity of AGNs can come from a so compact region.

The standard model of accretion (Shakura & Sunyaev 1973) predicts that the bulk of the gravitational energy is released in the few last stable orbits of the accretion disc. In fact the emission of AGNs being extremely variable, it demonstrates that most of the emitted light originates very close to the black hole. For example in the case of MCG-6-30-15 it is possible to observe variations as short as a few hundred seconds during which the source doubles its flux. Thus, the causality argument imposes an upper limit to the X-ray source dimensions of about 20-40 r_g.

The primary X-ray source is, most probably, located above the accretion disc in a fully

ionized plasma, the so called "corona". In the corona the electrons have very high temperatures (as observed by *OSSE* and *BeppoSAX*; Jourdain et al. 1992; Zdziarski et al. 1995; Matt 2000; Perola et al. 2002) and interact with soft photons from the accretion disc by Compton up-scattering (Haardt & Maraschi 1993; 1994, Haardt, Maraschi & Ghisellini 1997). The source being above the accretion disc, part of the X-ray radiation is reflected by the optically thick disc. This reflected component is particularly important because it carries information about the physical conditions of the accreting material. Thanks to the new generation of X-ray telescopes on board satellites (like XMM-Newton, Chandra and Suzaku) we now have sufficient sensitivity to observe the variability of the reflected component in detail. This enables us to study, for the first time, not only the kinematics but also the dynamics and the temporal variations of the physical conditions of the accreting matter. In particular the study of these variations has the potential to probe the effects of extreme gravity as predicted by general relativity in its strong regime.

1.1 The main components of the X–ray spectrum

Figure 1.1 shows the typical X–ray spectrum of a Seyfert 1 galaxy and a schematic picture of the regions close to the BH that are thought to be responsible for the observed spectral features. In the framework of the standard model, these components can be identified as follows:

- The X–ray spectrum is dominated by a power law (red dashed line in Figure 1.1) component with a cut off at high energy. It is widely believed that this component is generated through Compton up scattering of soft photons emitted by the accretion disc. These photons interact with the relativistic electrons of an optically thin medium above the accretion disc, generally called "corona". At each interaction the soft photons are energized by the coronal electrons. The high energy cut off is then produced when they reach the energy of the electrons.

- Part of the emission that is produced by the corona is directed towards the disc where it generates a reflection component. This secondary emission is composed by a reflection continuum peaking between 20 and 40 keV plus fluorescence lines. The blue dotted line in Figure 1.1 shows the expected reflection continuum and Fe K line from a neutral accretion disc. As shown by Fabian et al. (2000) the reflection is shaped by the material motions in the accretion disc and by the presence of the central BH, thereby providing important physical information.

- In a significant fraction of type 1 AGNs the nuclear radiation passes through a partially ionized plasma, the so called "warm absorber" (Reynolds 1997; Fabian 1999; George et al. 2000; Piconcelli et al. 2005). This plasma absorbs the nuclear radiation imprinting the main narrow absorption features in the soft X–ray band (see Fig. 1.1).

- In most sources, when the power law component is extrapolated at low energy, an excess of emission is observed below 1 keV, called "soft excess". In the standard interpretation the soft excess (see the violet long dashed line in Fig. 1.1) is thought to be thermal

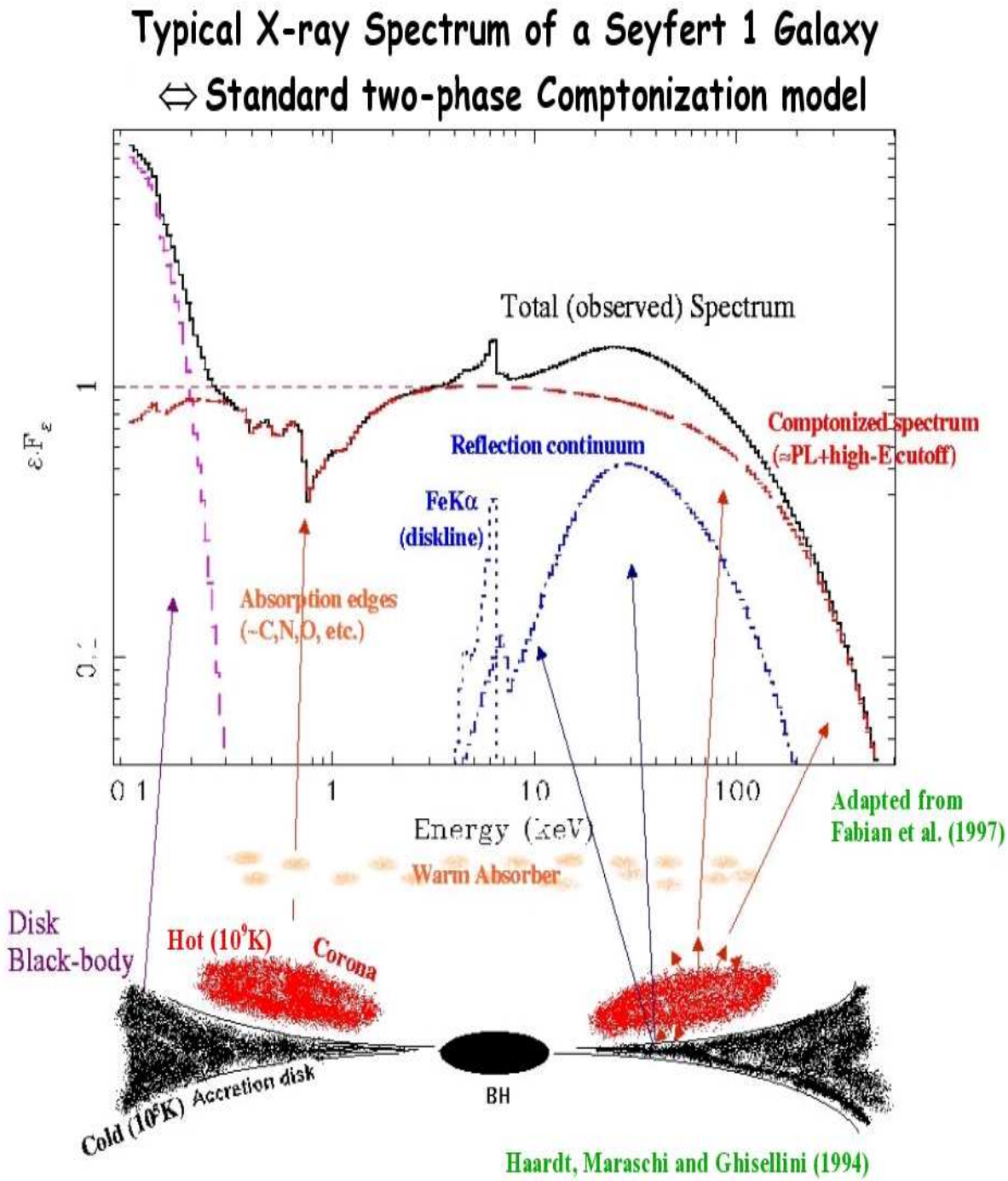

Figure 1.1: Typical X–ray spectrum of Seyfert 1 galaxies and a schematic picture of the region close to the BH indicating the different physical components responsible for the observed spectral features. (Courtesy of M. Cappi).

in origin and has been identified as the high energy tail of the multitemperature black body emission of the accretion disc. This picture has recently come under debate.

The main topics of this dissertation will be the investigation of the origin of the soft excess as well as the study of the reflection coming from the innermost parts of the accretion disc. In order to pursue these topics the spectral variability of a sample of bright type 1 AGNs will be investigated.

1.1.1 The X–ray continuum emission: Thermal Comptonization

The broadband X–ray spectrum (2-300 keV) of Seyfert 1 galaxies is, in first approximation, generally well fitted by a cutoff power–law continuum with superimposed secondary components. The standard accretion disc model predicts, for AGNs, that the highest energy emission from the disc is in the optical–far UV band (Shakura & Sunyaev 1973). Thus it cannot reproduce this hard X–ray power law component. Successful models for the X-rays should also satisfy two main observational constraints. The size of the X–ray production region must be small due to the fast variability, with time scales shorter than hours (e.g. McHardy 1989; McHaardy et al. 2004; Vaughan et al. 2005). The observed power law spectrum in the medium X–ray range (2–20 keV) should have a small dispersion in the values of photon index, whose average for Seyfert galaxies is $\Gamma\sim1.9\pm0.15$ (Nandra et al. 1997; Pounds et al. 1990; Piconcelli et al. 2005).

Two main classes of models can explain the power law shape of the X–ray spectrum. The first is based on the production of very high energy primaries and strong reprocessing via electromagnetic cascades leading to the formation of a pair cascade (e.g. Zdziarski et al. 1990). The second involves multiple Compton scattering (Comptonization) of soft photons on a thermal population of hot electrons (e.g., Walter & Courvoisier 1992; Haardt & Maraschi 1993; 1994 Haard, Maraschi & Ghisellini 1997).

Thanks to the OSSE and *BeppoSAX* observations of a break or an exponential cutoff in the high–energy spectrum of the brightest Seyfert galaxies (Jourdain et al. 1992; Maisack et al. 1993; Zdziarski et al. 1995; Matt 2000; Perola et al. 2002), thermal or quasi–thermal Comptonization models are favored (Haardt & Maraschi 1993; 1993; Haardt, Maraschi & Ghisellini 1997), although they do not completely rule out pure non-thermal pair models (Zdziarski et al. 1993).

The origin of the Comptonizing electrons is basically unknown. Maybe for its similarities with the Solar corona there is a general consensus in considering that the coronal heating mechanism is due to dissipation of accretion energy generated in magneto–rotational instabilities in the disc and transferred in the corona via reconnection of magnetic loops (Rosner & Vaiana 1978). The coronal electron temperature is constrained by a thermal balance where the heating rate is the total (direct plus reprocessed) luminosity and the cooling mechanism is Comptonization of soft photons (Haardt & Maraschi 1993; 1994).

Nevertheless, in its simplest version, such a model with a cold disk covered by a uniform hot corona is not in agreement with the observations. In fact in this scenario the number of Comptonized photons is strongly tied to the soft seed photons, while many observations indicate a soft luminosity several times larger than the hard luminosity. For this reason it is

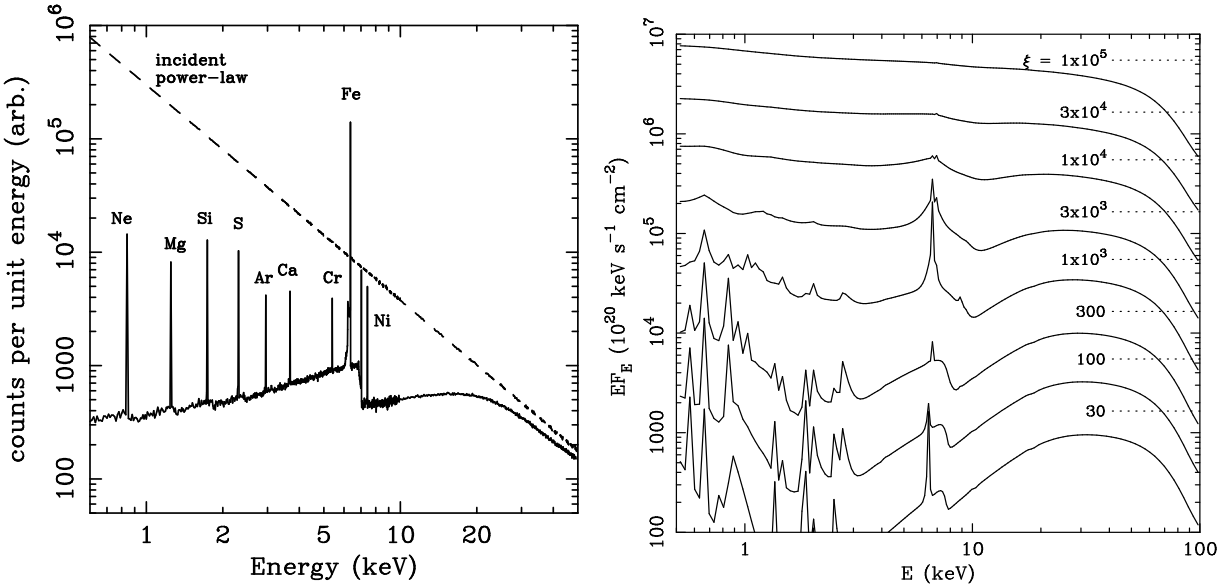

Figure 1.2: *Left panel* shows the X–ray reflection from a neutral, constant density illuminated slab. The dashed line shows the incident continuum and the solid line shows the reflected spectrum (integrated over all angles). Most of the radiation below 20 keV is absorbed by the metals and re-radiated at lower energies. The Figure was taken from Fabian et al. (2000) and was based on calculations by Reynolds (1996). *Right panel* shows reflection spectra from ionized constant density slabs with ionization parameter ξ. When ionized reflection is considered, a strong contribution due to soft X–ray lines (such as e.g. Oxygen, Carbon, Nitrogen, Neon, Iron L and others) appears below about 1–2 keV. The dotted lines on the right-hand side of the plot show the incident Γ=2 power laws, and the solid lines are angle-averaged reflection spectra. The disc becomes more ionized toward the top of the Figure, which greatly affects the strength and the shape of the spectral features. Figure taken from Ross et al. (1999).

believed that only a fraction of the seed photons emerging from the accretion disc interacts with the corona, in a geometry called "patchy corona" or lamppost corona (Haard, Maraschi & Ghisellini 1994; Haardt 1997).

1.1.2 The reflection

The optically thick material of the disc is irradiated by the primary X–ray emitting source. The hard X–ray photons penetrate the slab of material and are subjects to many interactions like Compton scattering by free or bound electrons, photoelectric absorption and either fluorescent line emission, or Auger de–excitation. Each photon undergoes either destruction through Auger de–excitation, or is scattered out of the slab, or reprocessed into a fluorescent line photon which escapes from the slab.

The left panel of Figure 1.2 shows the expected X–ray reflection from an illuminated slab. The dashed line shows the incident spectrum while the solid line shows the reflected component (Reynolds 1996; Fabian et al. 2000). When the disc ionization is low, as shown if the left

panel of Fig. 1.2, low energy photons (E≤10 keV) are mainly photoelectrically absorbed by the ions because of the energy dependence of photoelectric absorption, while photons with higher energies incident on the disc are generally back-scattered via Compton scattering. At energies above few tens of keV, Compton recoil reduces this back-scattered emission, thus the reflection component from the optically thick disc (George & Fabian 1991) results in a broad hump peaking at ∼30–40 keV, due to the combination between Compton scattering at high energies and absorption at low energies. This feature has been observed in most Seyfert galaxies, first with *Ginga* (Pounds et al 1990; Nandra & Pounds 1994), then with *BeppoSAX* (Perola et al. 2002) and now with *Suzaku* (Reeves et al. 2006).

In the framework of thermal Comptonization disc–corona models, this reflection component would be the mechanism coupling (acting as an energy exchange) the disc emission with the coronal one. In fact, if the emission of the corona increases, the disc would reprocess a fraction of the Comptonized radiation that would then cross the corona acting as seed photons cooling the corona. This feedback effect keeps a quasi–constant spectral shape and can explain the relatively small dispersion in the distribution of spectral indices of Seyfert 1 galaxies (Nandra & Pounds 1994).

In addition to the continuum, the reflection component contains also a series of emission lines (see left panel of Figure 1.2). The Fe Kα is the strongest of these lines because of its higher fluorescent yield and abundance. This emission feature is produced through fluorescence and for a neutral slab of material it is emitted at ∼6.4 keV with a threshold absorption energy of ∼7.1 keV. This feature is almost ubiquitous in the spectra of AGNs.

The high luminosity of the corona can photoionize the surface layers of the disc (Ross & Fabian 1993; Ross, Fabian & Young 1999; Ross & Fabian 2005). The right panel of Figure 1.2 shows the expected reflection continuum and the associated lines for different values of the ionization parameter $\xi = 4\pi\frac{L}{R^2 n}$, where L is the X–ray luminosity received and n is the electron number density of the disc. When a moderately ionized disc is considered, strong emission lines appear at low energy. These lines are mainly due to Oxygen, Carbon, Nitrogen, Neon, Iron L-shell transitions and others less abundant elements. On the other hand when the disc is highly ionized ($\xi \geq 5000$ erg cm s^{-1}) all the elements (even iron) are completely ionized and the reflection spectrum mimics the incident power-law and the slab is an almost perfect mirror.

1.1.3 The soft excess

As already discussed in §1.1.1, the 2–10 keV spectrum of type 1 AGNs shows, at first order, a power law continuum. When this continuum is extrapolated at lower energies an excess of emission is generally observed below ∼2 keV. The origin of this component is not clear. In the standard interpretation, it is thought to be the high energy tail of the thermal emission of the accretion disc. Nevertheless, standard models of accretion discs (Shakura & Sunyaev 1973) predict that, even if the object is accreting at the Eddington limit, the maximum temperature of the accretion disc is of ∼20 eV for a 10^8 M$_\odot$ black hole. The observed temperatures of this component appear to be too high compared to this predicted value (Gierlinski & Done 2004; Piconcelli et al. 2005; Crummy et al. 2006). An alternative explanation for the soft excess is that it is produced by a second Comptonization region with temperature cooler than the

corona. This second Comptonization may arise in a transition region between the disc and the corona (a sort of warm skin at the disc surface, Magdziarz et al. 1998; Janiuk, Czerny & Madejski 2001).

In order to test these hypothesis, Gierlinski and Done (2004) have studied a sample of PG quasars. They fit the 0.3–10 keV spectra with a double Comptonization model, one reproducing the high energy continuum and one for the soft excess. Figure 1.3 show their best fit results. Panel a, b and c of Fig. 1.3 show the best fit temperature of the soft excess as a function of its strenght, the central black hole mass and the expected maximum temperature (accretion at the Eddington limit is assumed). For all objects under investigation, the observed soft excess temperatures are too high to be the high energy tail of the thermal emission of the accretion disc. Moreover, standard accretion disc models predict a relation between the disc temperature, T_{disc}, the source luminosity, L, and the central black hole mass, M: $T_{disc} \propto (\frac{L}{L_{Edd}})^{\frac{1}{4}} M^{-\frac{1}{4}}$. On the contrary, the best fit temperatures are distributed in a very narrow range of values between 0.1 and 0.2 keV (see also the histogram in the panel d of Fig. 1.3). This constancy (within a factor of 2) is not in agreement with the expected variations in disc temperature (of a factor of 20) due to the different black hole masses and luminosities of the objects considered. The constancy of the observed temperature of the soft excess does not agree with the double Comptonization either. Panel e and f of Fig. 1.3 show the spectral index of the hard power law as a function of the fraction between the luminosity and the Eddington luminosity and the temperature of the soft component. From these Figures, it is clear that the hot Comptonized component is variable and these variations imply variations in the soft excess temperature that are not observed.

As a result, and as suggested by Gierlinski & Done (2004), the constancy of the observed temperature seems to indicate that the soft excess increase is related to atomic transitions. In the soft X–ray energy band there are strong opacity jumps related to many different emission/absorption features due to elements like Oxygen, Carbon, Iron etc. Thus the nature of the soft excess seems to be related to an important and strong absorption or reflection component.

1.1.4 The warm absorber

In a large fraction, probably as high as 50 % (Piconcelli et al. 2005) of type 1 AGNs, the nuclear radiation is transmitted through a gas, photoionizing it, and generating a partially ionized plasma, the so called "warm absorber". Even though ionized absorbing gas was already observed in many Seyfert 1s (Reynolds 1997; Fabian 1999) and some quasars (George et al. 2000) with previous X–ray telescopes, only observations performed with grating spectrometers on board *XMM-Newton* and *Chandra* have provided the adequate tool to precisely constrain the physical nature of these features. The effect of the warm absorber is better seen in the soft X–ray spectrum where many narrow absorption lines and a few emission lines from H–like and He–like ions of the most abundant metals, like Oxygen, Nitrogen, Carbon, Neon and the complex of Iron L lines, are present.

This warm absorbing gas is generally characterized by a large range of ionization parameters going from $\log(\xi) = 0$ to 3. The total column densities are observed to be in the range between 10^{21-22} cm^{-2} and they are typically outflowing with velocities of a few hundreds km

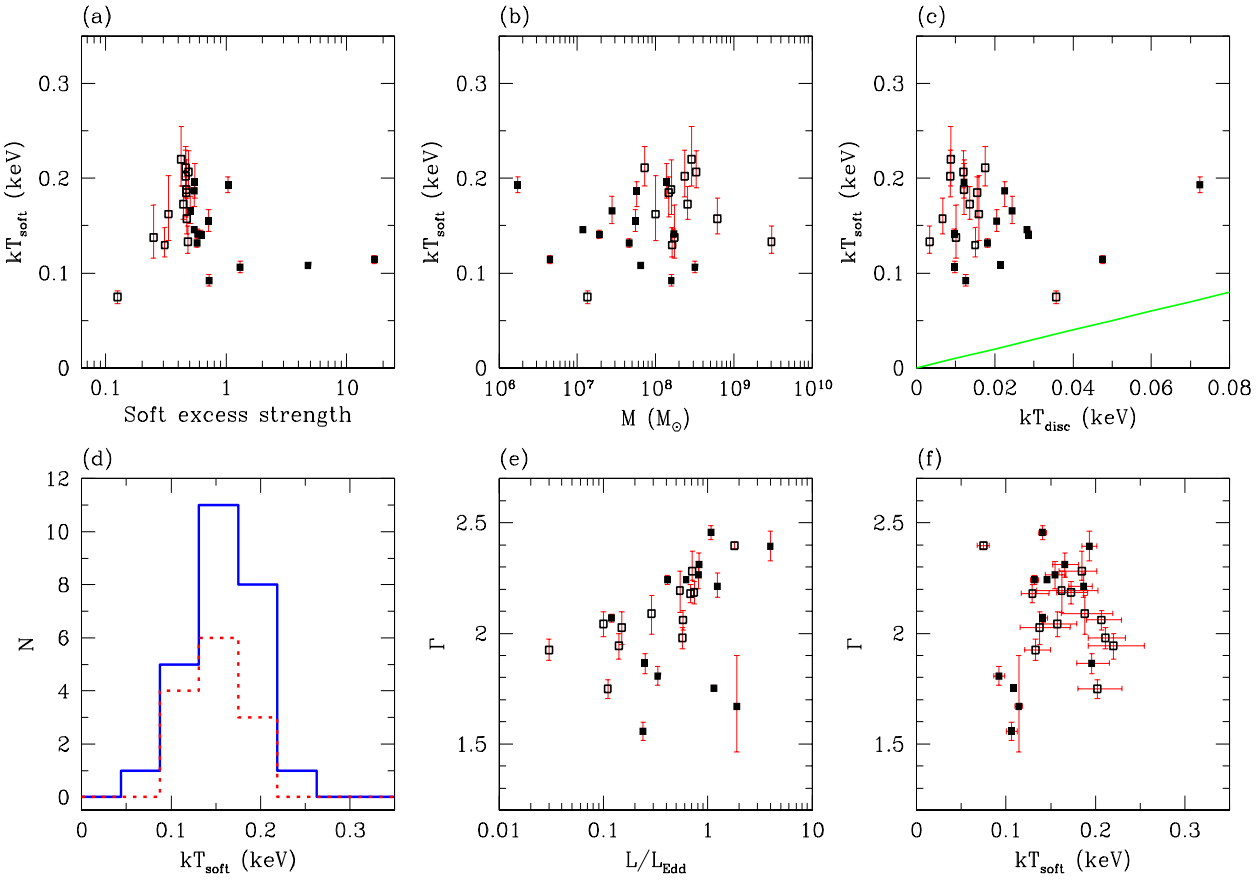

Figure 1.3: Spectral fitting results from the model of two Comptonizing regions applied to 26 radio quiet PG quasars. *Panel a* shows the temperature of the cool component which produces the soft excess, T_{soft}, versus strength of the soft excess. *Panel b* shows the distribution of T_{soft} versus black hole mass. *Panel c* shows the comparison of the estimated accretion disc temperature, $T_{disc} \propto (L/L_{Edd})^{1/4} M^{-1/4}$ and observed T_{soft}. The line represents T_{disc}=T_{soft}. *Panel d* shows the histogram of T_{soft}. *Panel e* shows the photon spectral index Γ of the hot component versus fraction of the Eddington luminosity. *Panel f* shows the spectral index of the hot Comptonization, Γ, versus T_{soft}. Figure taken from Gierlinski & Done 2004.

s^{-1}. The features imprinted by the warm absorber are always narrow and, in the few cases where the turbulent velocities are measurable, they results to be of the order of a few hundreds km s^{-1}. The location of the warm absorber as well as their mass outflow rate are still highly debated (Otani et al. 1996; Krongold et al 2007). The outflow may be so massive to influence the surrondings of the AGN or even the host galaxy.

1.2 Open questions:

The work that will be presented in this dissertation is aimed at addressing two main open questions in this field:

1.2.1 Is the reflection component in AGNs broadened by the relativistic effects?

The iron Kα line, produced in the reflection component, is intrinsically rather narrow, thus its broadening could be used to study the geometry and the dynamics of the accretion disc. In fact, if the line is actually reflected by the accretion disc, it must be shaped by Doppler shifts and may be affected by gravitational redshift. Figure 1.4 shows the modifications introduced by each single effect in a schematic way.

The first broad iron line ever observed is the one in the *ASCA* observation of MCG-6-30-15 (Tanaka et al. 1995). After this discovery, in many other sources a broad Fe line has been detected, with the *ASCA* satellite, showing that the presence of these broad lines is a common property of Seyfert galaxies (Nandra et al. 1997).

The new generation high sensitivity (*XMM-Newton*) and high resolution (*Chandra*) X-ray satellites have shown clear evidence of an almost ubiquitous narrow component of the Fe Kα line, produced by distant material (Yaqoob & Padmanabhan 2004; Pounds et al. 2003; Pounds et al. 2004). Despite confirming the presence of a curvature red-ward of the Fe K line. Some authors (i.e. Boller et al. 2003; Pounds et al. 2003; Pounds et al. 2004; Tanaka et al. 2004) have cast doubts on the interpretation in terms of a broad line because the analysis of the mean spectrum showed that the red wing of the line could be reproduced by complex absorption models partially covering the nuclear source (Pounds et al. 2003; Pounds et al. 2004; Turner et al. 2005).

These two models (broad line and complex partial covering absorber) are hardly distinguishable from the mean spectrum, even in the best available data. Nevertheless different spectral variations are expected from the two models. We thus attempt, in this dissertation to distinguish between the two scenarios through time resolved spectral analysis.

Having a clear demonstration of the existence of broad lines is important because these may allow to directly measure the geometry and the flow patterns of the material falling into the black hole. In particular reverberation studies of the line have the potential to map the innermost regions around black holes (Iwasawa et al. 1999; Ponti et al. 2004; Iwasawa et al. 2004; Tombesi et al. 2007). Moreover, it may provide a tool to test the general relativity in its strong field domain and it gives the possibility to measure the spin of black holes (Brenneman & Reynolds 2006).

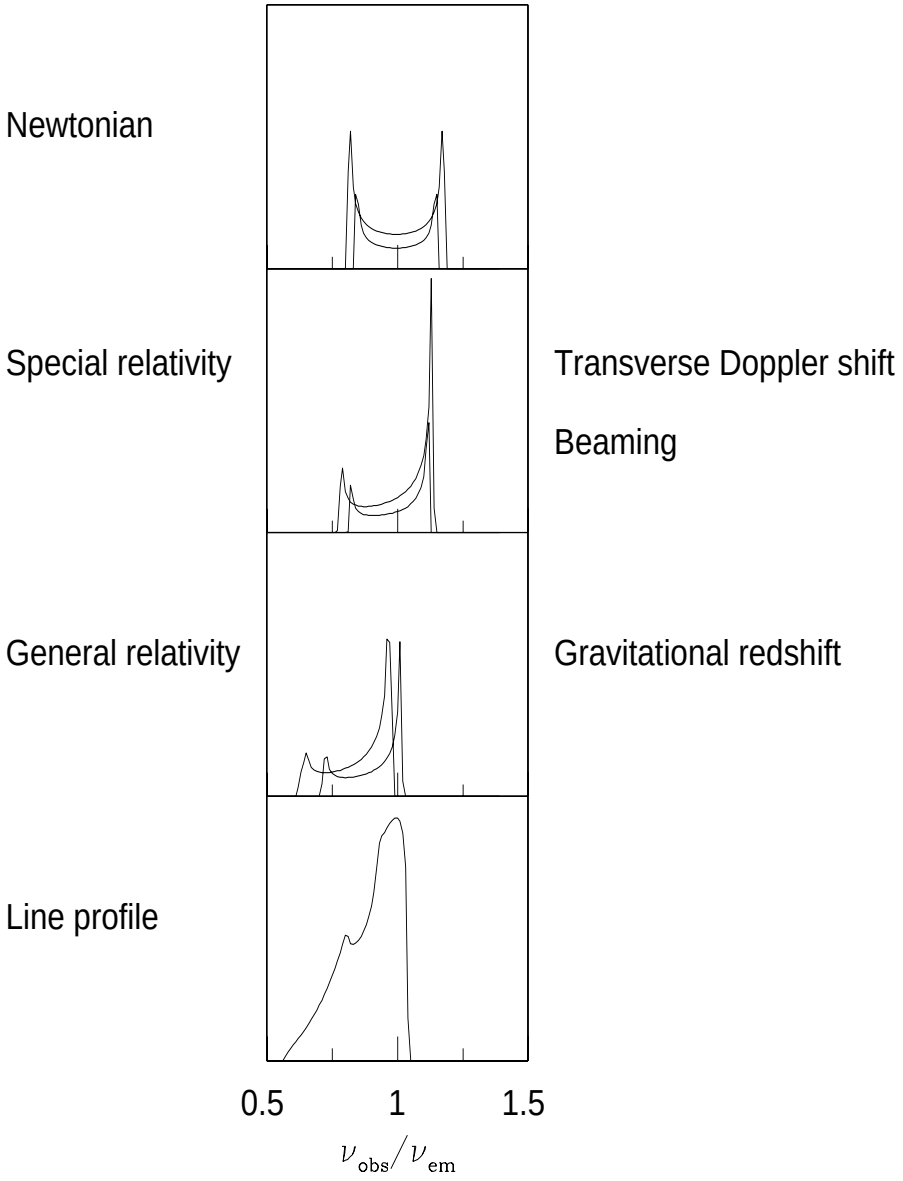

Figure 1.4: The shape of reflection lines from the accretion disc is sculpted by the interplay of Doppler and transverse Doppler shifts, relativistic beaming and gravitational redshift. The upper panel shows the symmetric double-peaked profiles from two narrow annuli on a non–relativistic disc. In the second panel the effects of transverse Doppler shifting and relativistic beaming have been included, and in the third panel gravitational redshift has been included. Once all these effects are taken into account (panel 4) and the emissivity is integrated over all the disc radii, the profile is broad, skewed and highly redshifted. Figure taken from Fabian et al. 2000.

1.2.2 What is the origin of the soft excess?

As already detailed in §1.1.3, the constancy and large value of the best fit temperature of the soft excess seem to disfavor the standard thermal interpretation for this component (Gierlinski & Done 2004; Piconcelli et al. 2005; Crummy et al. 2006). It has been proposed that its nature may possibly be linked to atomic processes like reflection or absorption. Thus, the best candidates appear to be either a warm absorbing gas along the line of sight or ionized reflection from the accretion disc. Nevertheless, in order to reproduce the observed soft excesses, these absorption (reflection) components have to be relativistically broadened, otherwise absorption (emission) lines from low-z elements would have been already detected in the high resolution spectra observed with the gratings aboard *XMM-Newton* and *Chandra*.

In the sources where a broad Fe K line is detected an extremely exciting possibility is that the same reflection component that reproduces the shape of the Fe K line could reproduce also the soft excess. In fact, if the reflection component is ionized, strong emission lines appear in the soft X–ray region (see right panel of Fig. 1.2). This complex of lines, if coming from the innermost part of the accretion disc, will be broadened and will generate a smooth continuum with a shape similar to the sof excess. In this case, only one spectral component (the disc ionized reflection) may reproduce both the soft excess and the broad Fe K line.

In this dissertation this possibility will be addressed, testing whether this scenario is consistent with not only the soft excess spectral shape, but also its variability.

1.3 X-ray variability studies

Neglecting the relativistic regime, it is possible to easily have an idea of which is the expected variability of the primary and the reflected component. In fact if the observed power law continuum drives the iron fluorescence of the reflection component then the line flux should respond to variations in the incident continuum on timescales comparable to the light-crossing, or hydrodynamical time scale of the inner accretion disc (Fabian et al 1989; Stella 1990; Matt & Perola 1992; Reynolds et al. 1999). This timescale ($\sim 100\ M_6$ s for reflection from within 10 $r_{\rm g}$ around a black hole of mass $10^6 M_6\ {\rm M}_\odot$) is short enough that a single, long observation with *XMM-Newton* and/or *Chandra* does actually span many light-crossing times.

From these rough and non relativistic considerations it would follow that the broad component of the reflection lines should be as variable as the continuum, if not more.

Nevertheless, when the bulk of the emission is released at radii lower than 15–20 r_g from the black hole (as the shape of the broad Fe K line in MCG-6-30-15 suggests), the relativistic effects are no more negligible.

The effects of the strong gravitational field on the line shape and variability have been explored by Martocchia, Matt & Karas (2000); Dabrowski & Lasenby (2001); Miniutti et al. (2003); Miniutti & Fabian (2004); Dovčiak et al. (2004); Suebsuwong et al. (2006). A fully relativistic study of the expected correlation between primary emission and reflection component variability has been studied by Miniutti et al. (2003), in the framework of the so called "light bending model".

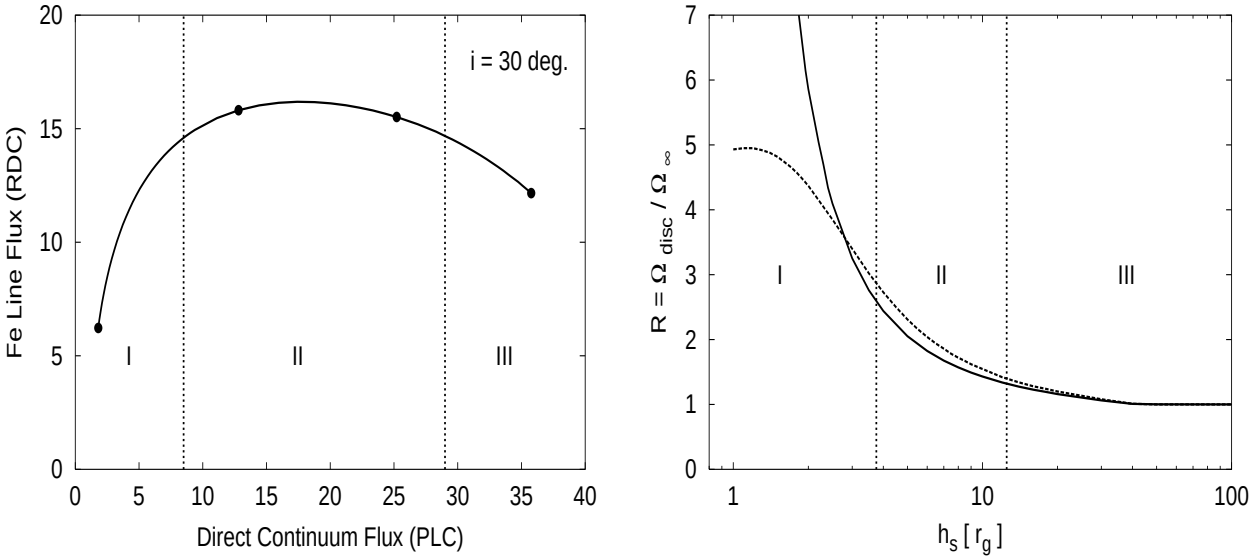

Figure 1.5: *Left panel*: The Fe line flux (representative of the whole ionized reflection component) as a function of the power law flux observed at infinity. The variability is only due to changes in the primary source height. Black dots represent heights of $h = 1$, 5, 10, 20 r_g. Three regimes can be identified. In regime II the disc reflection variation is within 10 per cent while the power law varies by about a factor 4. *Right panel*: The reflection fraction as a function of the source height (nearly the same if plotted versus the power law flux). We show the cases of a source on the disc axis (solid) and one at 2 r_g from the axis. Figure taken from Miniutti & Fabian (2004).

1.3.1 The light bending model

In the model a geometry in which a maximum Kerr BH is surrounded by the accretion disc extending down to the innermost stable circular orbit is assumed. The power law component is assumed to be emitted from a primary source above the accretion disc. Its location is defined by its radial distance from the BH axis and its height (h) above the accretion disc. The main parameter in the model is the height of the primary source above the accretion disc and the main requirement is for the source to be compact. The primary power law source could be physically realized by flares related to magnetic reconnection in the inner corona, emission from the base of a jet close to the BH, internal shocks in aborted jets, dissipation of the rotational BH energy via magnetic processes, etc. Any mechanism producing a compact power law emitting region above the innermost region of the accretion flow would be relevant for the model (e.g. Blandford & Znajek 1977; Markoff, Falcke & Fender 2001; Li 2003; Ghisellini, Haardt & Matt 2004).

A fraction of the radiation emitted by the primary source directly reaches the observer at infinity and constitutes the direct continuum which is observed as the power law component of the spectrum. The remaining radiation illuminates the accretion disc (or is lost into the black

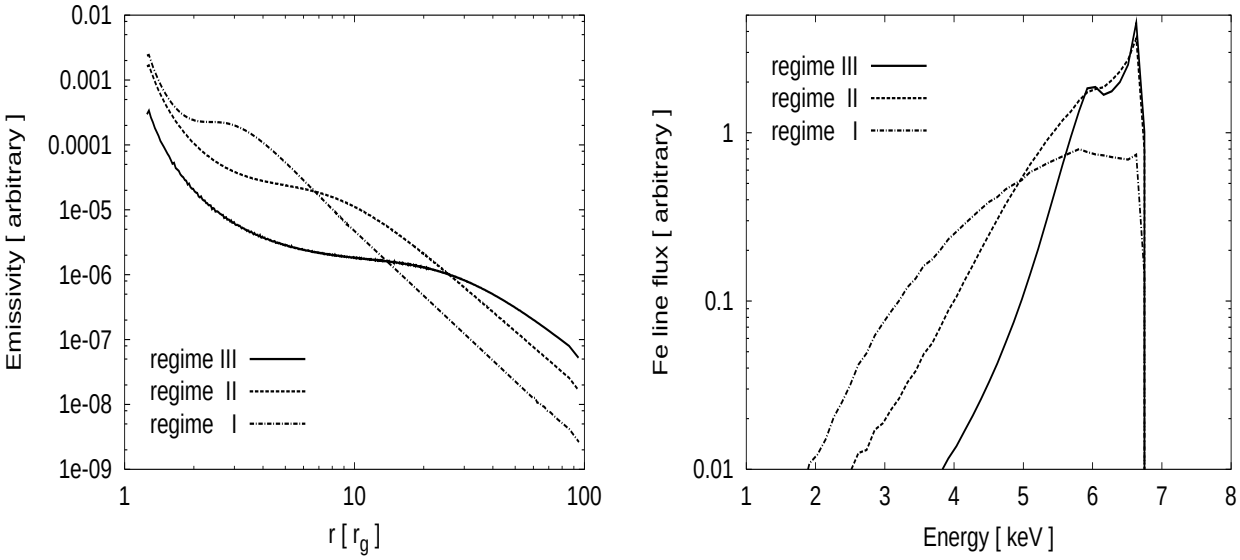

Figure 1.6: *Left panel*: Typical emissivity profiles computed in the light bending model for the three relevant regimes. The emissivity is steeper in the inner part of the disc and flattens outwards. *Right panel*: Typical line profiles in the three regimes. A log scale is used to enhance the line profile differences. Figure taken from Miniutti & Fabian (2004).

hole event horizon). The radiation that illuminates the disc is reprocessed into the ionized disc reflection component. For simplicity, it is assumed that the intrinsic luminosity of the primary source is constant. The basic idea is that the relevant parameter for the variability of both the power law and the illuminating continuum on the disc (which drives the reflection component variability) is the height of the primary source above the accretion disc and that the variability is driven by general relativistic effects the most important of which is gravitational light bending.

As an example, if the source height is small (of the order of few gravitational radii) and on the disc axis, a large fraction of the emitted photons is bent towards the disc by the strong gravitational field of the BH enhancing the illuminating continuum and strongly reducing the power law component at infinity, so that the spectrum is reflection–dominated. If the source height increases, gravitational light bending is reduced so that the observed power law component increases. Finally, if the height is very large so that light bending has little effect, the standard picture of reflection models with approximately half of the emitted photons being intercepted by the disc and the remaining half reaching the observer as the power law is recovered.

With this setup, the power law and Fe line flux (representative of the whole disc reflection component) has been computed as a function of the primary source height above the disc (Miniutti et al 2003; Miniutti & Fabian 2004; see also Suebsuwong et al. 2006). The results are presented in the left panel of Fig. 1.5 for the case of an accretion disc seen at an inclination

of 30° (the relevant case for type 1 AGNs). The black dots indicate different values for the source height ($h = 1, 5, 10, 20\ r_g$ from left to right). What the Figure shows is that, once general relativistic effects are properly accounted for, the broad Fe line (and disc reflection) is not expected to respond simply to the observed power law component variation anymore. Three regimes can be identified (I, II, and III in the Figure). A correlation is seen only in regime I, where the primary source height is between about 1 and 3–4 r_g. On the other hand, if the primary source has a height between about 4 r_g and 12 r_g (regime II) the broad Fe line (and disc reflection) variability is confined within 10 % only, while the PLC can vary by a factor ~ 4.

In the right panel of Fig. 1.5 the value of the reflection fraction predicted by the model as a function of the source height is shown. When the source height is large, the standard value $R = 1$ is recovered. However, as the height decreases, light bending comes into play increasing the number of photons bent towards the disc while simultaneously reducing the number of those able to escape from the gravitational attraction. Thus, the reflection fraction increases dramatically. Two cases are shown in the Figure, one for a source on the disc axis (solid), one for a ring–like configuration at 2 r_g from the black hole axis.

The left and the right panels of Fig. 1.6 show the, self-consistently computed, emissivity profile and the Fe K line profile. In regimes I and II, the emissivity profile can be described by a broken power law very steep in the innermost region of the disc and and flattening outwards. The line profile becomes broader lowering the height of the source above the accretion disc.

Chapter 2

On the measurement of the spectral variability of black hole accreting systems: The RMS tool

2.1 Introduction

The X-ray emission of Active Galactic Nuclei (AGN) and Galactic Black Hole Candidates (GBHC) comes from a region very close to the central power engine and therefore is important for understanding physical processes of energy generation around BHs. This region cannot be resolved by imaging instruments, only the variability of the emission allows us to speculate about it through, for example, reverberation mapping techniques. Thus, to study the source physics it is important to study both the spectrum and the variability of its emission.

A powerful method for variability study is the Power Spectral Density (PSD) analysis. This function shows the power of a deconvolution in Fourier series of the source light curve as a function of temporal frequencies. Accreting black hole sources, over the frequency range of a typical X-ray observation, are characterized by PSD well-represented by power-laws with slopes $\alpha = 1$–2 (Lawrence & Papadakis, 1993; Uttley, M^{c}Hardy & Papadakis, 2002; Markowitz et al. 2003; McHardy et al. 2004; Vaughan et al. 2005; Remillard & McClintock 2006). Such a spectrum, with a slope $\alpha \gtrsim 1$ is usually called 'red noise'. A lot of processes may be described as "red noise processes". An example is the random walk. In particular the displacement of a random walk point from its initial position is a red noise quantity.

The PSD of red noise processes shows increasing power at lower frequency (it has a $1/f^2$ slope). If we integrate this power from some finite frequency down to zero frequency, we get an infinite value, the power spectrum diverges. From this it follows that if we look over longer and longer timescales, the value of a random walk function wanders farther and farther away from its initial value. In the same way the observed flux of an accreting source should diverge on long timescales. This is clearly unphysical, thus a flattening at low frequency is expected. In fact, recent timing studies have found evidence that the steep power-law PSDs of AGNs and GBHCs show a flattening, or turnover, at low frequencies (Edelson & Nandra 1999; Uttley et al. 2002; Markowitz et al. 2003). Anyway, over the frequency domain of

interest for *XMM-Newton* observations, where the source emission is dominated by red noise process, it has no well-defined mean value over long times (for more details to red noise see Press 1978). Therefore the mean values of the red noise quantity have an intrinsic scatter due to the nature of the process itself.

The PDS analysis is, maybe, the best way to study the source variability. Nevertheless, it requires data with a lot of statistics and spanning a wide frequency range. The Root Mean Square variability (RMS), instead, could be calculated with lower statistics. This capability of the RMS function reflects in the possibility of having, in the case of good statistics data, a finer spectral resolution in the calculation of the source variability. Therefore, the RMS function should allows us to disentangle the different spectral components through their variability behavior.

The RMS is the Fourier pair, in the time domain, of the PSD (as states the Parseval's theorem $\langle S^2 \rangle = \int_{f_1}^{f_2} \mathcal{P}(f) df$, and it is defined as the square root of the source variance. Since the variance is a mean value, it is affected by the red noise scatter. That is, if it is calculated at different times, its values varies even if the underlying process is stationary[1]. Consequently, we have to take into consideration this scatter in the error treatment. As the Parseval's theorem shows, the RMS functions sum the amount of variability occurring in the time domain between the entire observation exposure and the time bin over which X_i is calculated. Varying the time bin and the observed exposure, we will measure different variability processes.

2.2 Basic RMS formulas

In literature there are a lot of different tools (variance, RMS, excess variance, fractional variability amplitude and RMS spectra) to measure the magnitude of a varying quantity. Since all these functions are based on the source variance calculation, they provide approximately the same information. The purpose of this chapter is to summarize the differences and the advantage/disadvantage of each tool (Edelson et al. 2002; Vaughan et al. 2003; Ponti et al. 2004) with particular attention to the treatment of the measurement errors and to simulate the expected spectral variability in simple conditions.

Variance (S^2)

The basic tool for the measure of the RMS variability of a light curve is the source variance defined as:

$$S^2 = \frac{\sum_{i=1}^{N} (X_i - \langle X \rangle)^2}{N - 1} \tag{2.1}$$

where, S^2 is the variance of the binned data comprising the light curve; X_i is the count rate during the i^{th} time bin; N is the number of time bins and $\langle X \rangle$ is the mean count rate.

[1] A stationary process is one for which the statistical properties (such as mean, variance, etc.) do not depend on time.

Root Mean Square Variability (RMS)

The RMS function is the square root of the variance:

$$RMS = \sqrt{S^2}. \tag{2.2}$$

Excess variance (σ^2_{XS})

The variance sum up not only the source contribution, but also the variation due to Poisson noise. In fact, even a constant quantity, as a result of being a measurement, would have a non zero variance because of the scatter due to the measurement noise. To avoid this problem and to have an absolute estimate of the source variability the fractional excess variance is usually used:

$$\sigma^2_{XS} = \frac{S^2 - \langle\sigma^2_{\rm err}\rangle}{\langle X\rangle^2}. \tag{2.3}$$

where $\langle\sigma^2_{\rm err}\rangle$ is the contribution of the measurement noise.

Fractional variability amplitude ($F_{\rm var}$)

The fractional variability amplitude is the square root of the excess variance:

$$F_{\rm var} = \sqrt{\frac{S^2 - \langle\sigma^2_{\rm err}\rangle}{\langle X\rangle^2}}. \tag{2.4}$$

The statistic $F_{\rm var}$ is often chosen in preference to σ^2_{XS}, although the two convey exactly the same information, because $F_{\rm var}$ is a linear statistics and can therefore give the RMS variability amplitude in percentage, i.e. fractional, terms.

Normalized Root Mean Square variability spectrum (RMS spectrum)

When the signal to noise of the source light curve is high, the Poissonian noise and the related estimate $\langle\sigma^2_{\rm err}\rangle$ become negligible. In this limit ($S^2 >> \langle\sigma^2_{\rm err}\rangle$), the fractional variability amplitude becomes equal to the normalized RMS:

$$rms = \sqrt{\frac{S^2}{\langle X\rangle^2}}. \tag{2.5}$$

The RMS function is interesting (although in this limit it is equal to F_{var}) because in this case it is possible to analytically derive the uncertainty related to measurement errors.

2.3 Error estimate associated to the RMS

As discussed above, the X–ray light curves of accreting black hole systems are dominated by a red noise process. Like all the other red noise quantities (for example the random walk) the

mean and the variance of the source count rate show random changes with time[2], even if the process is stationary. This intrinsic scatter is due to the stochastic nature of the variability and it is unrelated to the measurement uncertainties. For this reason they can be estimated separately.

The scatter introduced by the nature itself of red noise processes arises because any given light curve considered represents only a realization of the random process, and can exhibit different mean and variance from the "real" value, or from another segment. This noise is generally large and must be considered when comparing the variance of the same source at different times. It must also be considered when different sources are compared. It is possible to overcome this scatter if we compare two simultaneous light curves of the same source calculated at sligthly different energies. In this case the red noise scatter is still present, but it is safe to assume that it is the same in both light curves.

2.3.1 Comparing RMS spectra taken at different observing times or in different objects (estimate of red noise scatter)

The scatter due to red noise processes does not allow us to associate to a source an amount of variability (the "true intrinsic" source variability), because it changes with time even if the underlying process is not changing. As demonstrated by Vaughan, Edelson, Warwick & Uttley (2003), this effect does not depend on the number of data points used and is true even if the source emission process is stationary, or the measurement errors are null.

However, it is also possible that the underlying process responsible for the variability itself changes with time, in which case the variability is non-stationary. Such changes in the variability process could provide insight into the changing physical conditions in the nuclear regions. On the other hand the random changes expected for a red noise process yield no such physical insight. A method to measure the non-stationarity of the process, is to compare the scatter calculated by the data with the expected scatter from red noise processes. The expected scatter could be estimated if we assume that the process is governed by Gaussian statistic, $\sigma_{S^2} = (\frac{2}{N-1})S^4$ (Trumpler & Weaver 1962; Edelson et al. 2002). This approach cannot however be correct since the emission from accreting black holes is known not to be governed by uncorrelated Gaussian processes. A more robust approach was therefore followed by Vaughan et al. (2003) who calculated the expected scatter through Monte Carlo simulations (see Figure **??**) assuming a certain shape for the PSD. This could be measured or assumed on the basis of the observed relation with the black hole mass (Lawrence & Papadakis, 1993; Uttley, M^{c}Hardy & Papadakis, 2002; Vaughan, Fabian & Nandra 2003; Markowitz et al. 2003).

The results of the simulations are given in Table 2.1 of Vaughan et al. (2003) and are fitted by the formula:

$$S^2_{max} = aN^bS^2 \quad \text{and} \quad S^2_{min} = cN^dS^2. \tag{2.6}$$

where S^2_{max} and S^2_{min} are the variance upper and lower confidence interval respectively; N is the number of data points over which the variance is calculated and a, b, c and d are

[2]This is due to the fact that the variability power of red noise diverges as $f \to 0$.

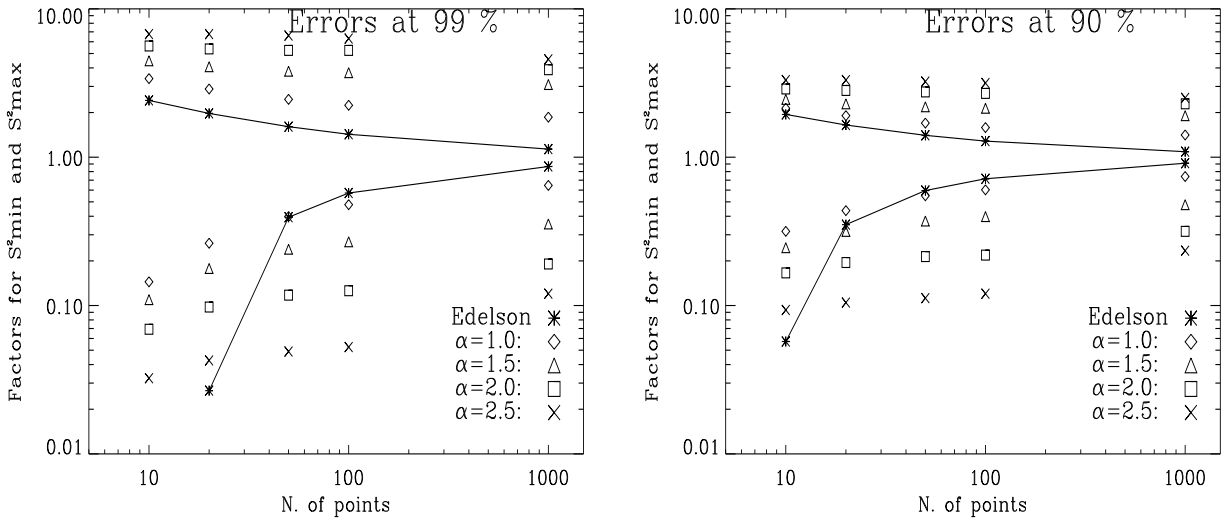

Figure 2.1: Multiplicative factors that give the upper/lower limits (at 99% and 90% of probability) of the source variance scatter through the formula: $S^2_{max/min} = S^2 * factor$. The different values shown were calculated through Monte Carlo simulations by Vaughan et al 2003 for different values of the PSD spectral index and were estimated by Edelson et al. 2002 assuming uncorrelated Gaussian processes.

the parameters of the fit (given in Table 2.1) in the case of 99 % and 90 % confidence limit respectively.

From the scatter on S^2 it is trivial to calculate the uncertainty on the other functions. Figure 2.1 shows the multiplicative factors ($S^2_{max} = S^2 * factor$ and $S^2_{min} = S^2 * factor$) of the upper/lower limit at 90%, 99% of the source variance scatter, estimated by Edelson et al. (2002; marked with asterisks) and calculated by Vaughan et al. (2003) for different values of the PSD spectral index (α = 1 - 2.5), as a function of N. The assumption that the source emission is governed by uncorrelated Gaussian processes (thick line and asterisks in Figure 2.1) leads us to a wrong, under-estimate of the source variance scatter. In particular, the errors calculated by Vaughan et al. (2003) are not symmetric and grow with α.

Figure 2.1 shows that the constant of proportionality depends on the power spectrum shape (Vaughan et al 2003). Moreover, power spectra of well studied AGNs are well described by broken power law shapes (Papadakis et al. 2002; Mc Hardy et al. 2004; Vaughan & Fabian 2003; Vaughan et al. 2003; Vaughan et al. 2005). Generally the frequency of the break (ν_{HFB}) occurs within the observed light curve ranges and the PSD is composed by two parts with different power law spectral shape. Thus, to estimate the red noise scatter, the combination of two multiplicative factors are generally needed (O'Neill et al. 2005). Moreover it is observed that the break frequency decreases with the black hole mass, as if by scaling the frequency

a99	b99	c99	d99	
4.23	-0.1256	0.0993	0.298	for $\alpha = 1.0$
5.21	-0.0761	0.0819	0.232	for $\alpha = 1.5$
6.95	-0.0777	0.0491	0.203	for $\alpha = 2.0$
8.83	-0.0878	0.0172	0.272	for $\alpha = 2.5$
a90	b90	c90	d90	
2.48	-0.08698	0.250	0.171	for $\alpha = 1.0$
2.72	-0.05211	0.203	0.133	for $\alpha = 1.5$
3.30	-0.05001	0.125	0.132	for $\alpha = 2.0$
3.99	-0.06178	0.055	0.197	for $\alpha = 2.5$

Table 2.1: Best fit values of the parameters of the equation 2.6, when the 99 % (upper panel) and 90 % (lower panel) symulated errors of the variance (see text and Vaughan et al. 2003) are interpolated. Two different best fit values are obtained because of the asymmetry of the simulated error and due to the different slopes of the PSD spectral index.

for the BH mass, a unique PSD shape could describe the variability properties of all accreting BHs (Mc Hardy et al. 2006). Thus, under this assumption it is possible to estimate the red noise scatter for all the AGN with know BH mass.

Finally, to have the total uncertainty this scatter has to be combined in quadrature with the measurement errors.

2.3.2 Comparing simultaneous RMS of the same source at different energies (uncertainties related with measurement errors only)

An X-ray light curve can be split into different energy bands. The light curves in each band will be strictly simultaneous and can be used to test whether the X-ray variability is a function of energy. The power of this kind of analysis is that the red noise scatter in the error estimate can be neglected because it is the same for the two simultaneous light curves. For this reason the uncertainty in this case is generally significantly smaller than in the previous case, allowing detailed study of the source spectral variability.

For this purpose, normalized and linear functions are preferred ($F_{\rm var}$ and RMS spectra) because they allow the comparison between light curves of different energy and statistic.

Fractional variability amplitude $F_{\rm var}$

To take into consideration the non-Gaussian statistic of red noise sources, Vaughan et al. (2003) used a Monte Carlo approach to develop a prescription of the effect of the measurement errors on estimates of $F_{\rm var}$. From these simulations it was found that the error on $F_{\rm var}$ decreases as the S/N in the light curve is increased according to the formula:

$$\sigma_{F_{\rm var}} = \sqrt{\left\{\sqrt{\frac{1}{2N}}\cdot\frac{\langle\sigma_{\rm err}^2\rangle}{\langle X\rangle^2 F_{\rm var}}\right\}^2 + \left\{\sqrt{\frac{\langle\sigma_{\rm err}^2\rangle}{N}}\cdot\frac{1}{\langle X\rangle}\right\}^2} \tag{2.7}$$

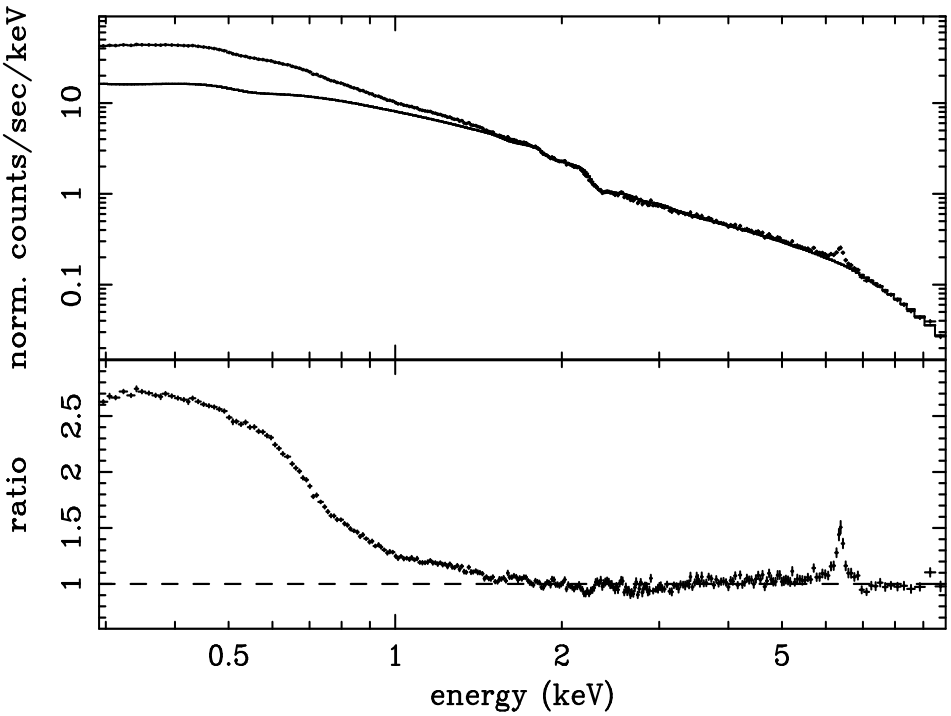

Figure 2.2: The mean spectrum of NGC 4051 during the rev. 263. The spectrum is fitted with a simple power law above 3 keV, excluding the Fe Kα region. At a first look the more evident spectral components are the strong soft excess, clearly present when the power law is extrapolated at low energy, and a narrow component of the Fe K line. The signature of a warm absorber is also imprinted between 0.5–2 keV as well as other spectral complexities at low and high energies (see § 5).

If the variability is not well detected, either because the S/N is low or the intrinsic amplitude is weak, then $S^2 \approx \overline{\sigma_{\rm err}^2}$, and it is the first term on the right hand side of equation 2.7 that dominates. If the variability is well detected, i.e. $S^2 \gg \overline{\sigma_{\rm err}^2}$, then it is the second term that dominates.

Differences in $F_{\rm var}$ significantly larger than the above uncertainty would indicate that the source variability amplitude is a function of energy. This would then mean that the PSD amplitude/shape is different in different energy bands. This tool is particularly useful because it has the potential to disentangle the multiple spectral components that vary independently.

Normalized RMS spectrum

In the limit of high signal to noise, i.e. more than $\sim$ 300 counts per bin for RMS values of $\sim$0.1 (see §2.4), the $F_{\rm var}$ function becomes indistinguishable from the RMS spectrum function (see Figure 2.3 and Ponti et al. 2004) because $S^2 \gg \langle\sigma_{\rm err}\rangle^2$. The RMS spectrum function has then the particularity to allow the analytical calculation of the associated error by the

standard propagation equation, yielding

$$\sigma_{rms} = \sqrt{\sum_{i=1}^{N}\left[\frac{\partial rms}{\partial X_i}\delta X_i\right]^2} \tag{2.8}$$

$$= \sqrt{\frac{\sum_{i=1}^{N}[(X_i - \langle X\rangle)\cdot\sigma_{err,i}]^2}{\sum_{i=1}^{N}(X_i - \langle X\rangle)^2}} \cdot \frac{1}{\langle X\rangle\cdot\sqrt{N-1}}$$

In the limit $S^2 \gg \langle\sigma_{\rm err}\rangle^2$, if $\sigma_{{\rm err},i} \sim \langle\sigma_{\rm err}\rangle$, this uncertainty is equivalent to the uncertainty proposed by Vaughan et al. 2003 through Monte Carlo simulations (see also Figure 2.3). In fact:

$$\lim_{\frac{\langle\sigma_{\rm err}^2\rangle}{S^2}\to 0} \sigma_{rms} = \tag{2.9}$$

$$\lim_{\frac{\langle\sigma_{\rm err}^2\rangle}{S^2}\to 0} \sqrt{\frac{\langle\sigma_{\rm err}^2\rangle\cdot\sum_{i=1}^{N}(X_i - \langle X\rangle)^2}{\sum_{i=1}^{N}(X_i - \langle X\rangle)^2}} \cdot \frac{1}{\langle X\rangle\cdot\sqrt{N-1}} =$$

$$\sqrt{\frac{\langle\sigma_{\rm err}^2\rangle}{N}}\cdot\frac{1}{\langle X\rangle} = \lim_{\frac{\langle\sigma_{\rm err}^2\rangle}{S^2}\to 0}\sigma_{F_{\rm var}}$$

The greatest advantage of this function is that, since the errors and the RMS data points are independent, one can estimate the significance of the variability structures by directly fitting the RMS spectrum.

2.3.3 Comparison in a real case: MCG-6-30-15

Figure 2.3 show the RMS spectra calculated with the equations used in Edelson et al. 2002 (Upper left panel), in Vaughan et al. 2003 (Upper right panel) and in Ponti et al. 2004 (Lower middle panel). The main difference in these functions is in their error estimates. Edelson et al. (2002) used a conservative approach in the calculation of the standard fractional variability function, leading to an overestimate of the measurement errors, while Vaughan et al. (2003) estimate the errors through Monte-Carlo simulations. The error associated to the normalized RMS is a good approximation of the Vaughan et al. (2003) results if Poisson noise is negligible. The advantage of the equation presented by Vaughan et al. (2003) is that it is always valid, also in the case of few counts/bin, but its disadvantage is that it cannot be formally used to be fitted to estimate the significance of its structures, since its errors are not independent. The advantage of the RMS equation presented in this work is that the errors are independent, so fine structures can be fitted and their significance quantified, the disadvantage is that it is applicable only with large enough statistics in order to ignore the Poisson noise.

2.4 RMS spectra simulations

In this section a few simulated RMS spectra (eq. 2.5 and 2.8) are presented. The goal of these simulations is to see which is the expected RMS shape when different model components vary

spectrally. This is then useful to compare the simulations with the real RMS spectra. For this reason the simulations are built using realistic parameters. In particular, as a basic spectral shape and integration time we take (except when differently specified) the mean spectrum and the total observation time (120 ks) of the *XMM-Newton* observation of NGC 4051 (rev. 263). We have chosen NGC 4051 because it is a bright and highly variable source and because it shows all the main spectral components typical of type 1 AGNs (see Figure 2.2). In particular it shows a strong soft excess below 1–2 keV, a warm absorber, a clear narrow plus broad components of the Fe Kα line and other spectral complexities at lower energies (see §5).

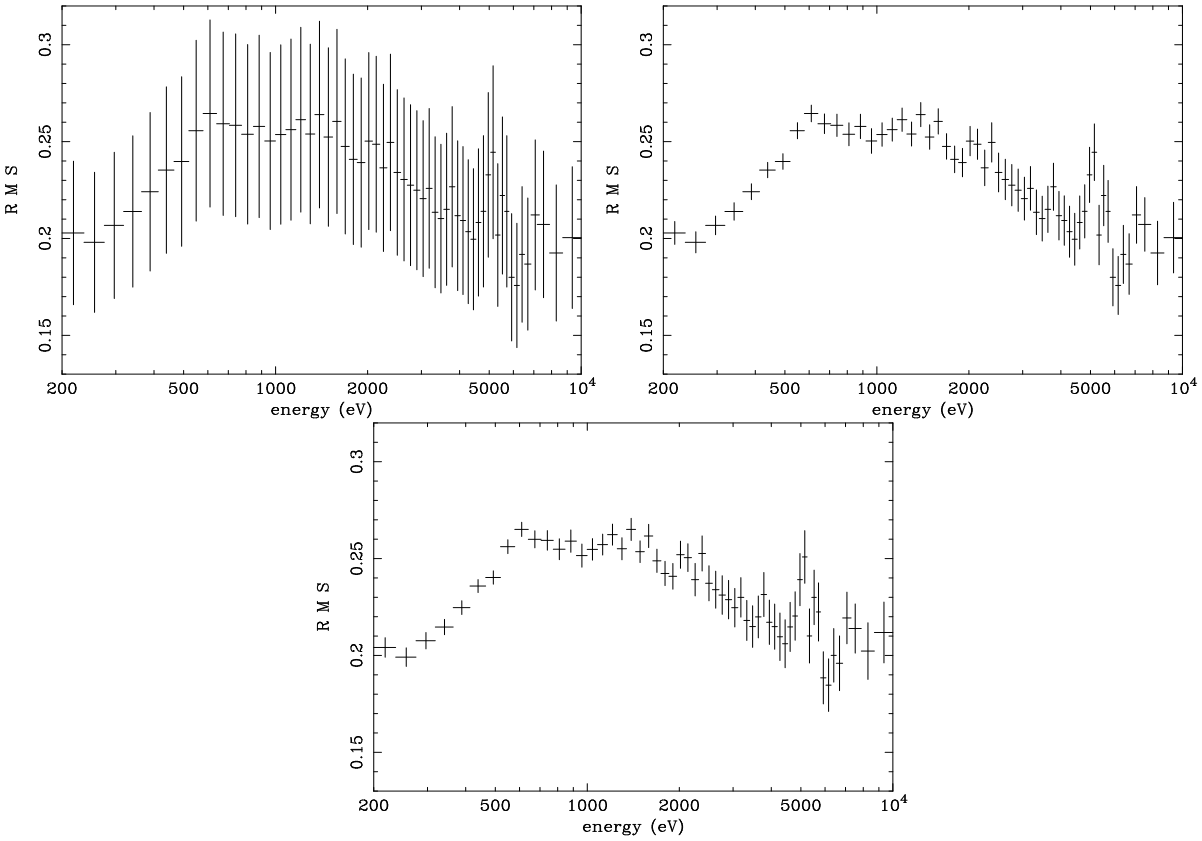

Figure 2.3: *Left, Right and Bottom panels* show the comparison between the RMS values and uncertainties using the equation used by Edelson et al. 2002 (assuming uncorrelated Gaussian processes), the F_{var} (eq. 2.4 and 2.7) and the RMS (eq. 2.5 and 2.9). The RMS spectra show the spectral variability of MCG-6-30-15 during the 2000 *XMM-Newton* observation. It is calculated with time bins of 6000 s and with energy bins grouped in order to have >350 counts per bin. Errors are 1σ.

The synthetic RMS spectra are calculated on the basis of a series of 20 equally long spectra obtained with the command fakeit in the software package Xspec. To simulate the spectra a model, convolved with the EPIC pn response matrix, is assumed. Then the sequence of 20 spectra is created varying linearly one or more of the model parameters. From this series of spectra we then extract a light curve for each selected energy band and then calculate the

RMS spectrum.

Poissonian noise

Before to go into the details of the spectral variability simulations, the actual effect of the Poissonian noise is considered. To have an order of magnitude estimate of this noise is important because the RMS function (eq. 2.5, 2.8), as detailed in § 2.2 and 2.3.2 measures not only the source variations (S^2), but also the Poissonian noise ($\langle\sigma_{\rm err}^2\rangle$).

In order to check the validity of all the tools that we implemented, we simulated the RMS spectra of a constant source (S^2=0), that is therefore a measurement of the amount of the Poissonian noise $\langle\sigma_{\rm err}^2\rangle$. It has been probed that the RMS value correctly follows the relation RMS$\simeq N^{-\frac{1}{2}}$. Moreover, each RMS spectra is very well consistent with a constant model. This indicates that the uncertainty associated to the RMS formula is accurate (the scatter due to different realizations of the Poissonian noise is of the order or lower than the RMS uncertainty).

We want to remind however that since the RMS function is applicable only if $\langle\sigma_{\rm err}^2\rangle << S^2$, this implies that for an almost constant source the RMS function could hardly be applicable and the $F_{\rm var}$ function should insted be used to obtain the proper errors.

2.4.1 Standard disc interpretation for the soft excess: BB + PL

In the standard interpretation of the Spectral Energy Distribution (SED) of AGNs, the Big Blue Bump is thought to be related with emission from an optically thick accretion disc (Elvis et al. 1994). The peak of the emission is expected in the optical-far UV region and the soft excess, observed in many AGNs, may be the high energy tail of the emission of the accretion disc.

For this reason the mean spectrum of NGC 4051 (see Fig. 2.2) has been fitted with a power law dominating at high energy and a black body component for the soft excess. NGC 4051 shows a rather typical soft excess with a ratio between the data and the low energy extrapolation of the power law of about 2–2.5 (see Fig. 2.2). Figure 2.4 shows the RMS spectra obtained if only the PL normalization is left free to vary from its minimum to its maximum value observed during the *XMM-Newton* observation.

The red stars show the spectral variability expected considering the best fit parameters of the mean spectrum ($T_{BB} = 103$ eV and $\Gamma = 1.97$). The RMS shows a constant value at high energy (where the contribution of the constant BB component is negligible) because the PL is varying with fixed spectral index. At lower energies the variability is decreasing where the contribution of the constant BB becomes more important. At energies below 500 eV the RMS shows a sort of plateau caused by the constant ratio between the flux of the PL and that of the BB component. Thus, if the soft excess is due to a constant BB component, the RMS at low energy should show a reduction of the variability proportional to the ratio between the data and the extrapolation of the PL component (see Fig. 2.2).

Nevertheless, standard models of the accretion disc emission (Shakura & Sunyaev 1973) predict that the maximum temperature of the optically thick material shall scale with the BH mass and be of the order of 20 eV for a black hole of 10^8 $M_\odot$ accreting at the Eddington rate.

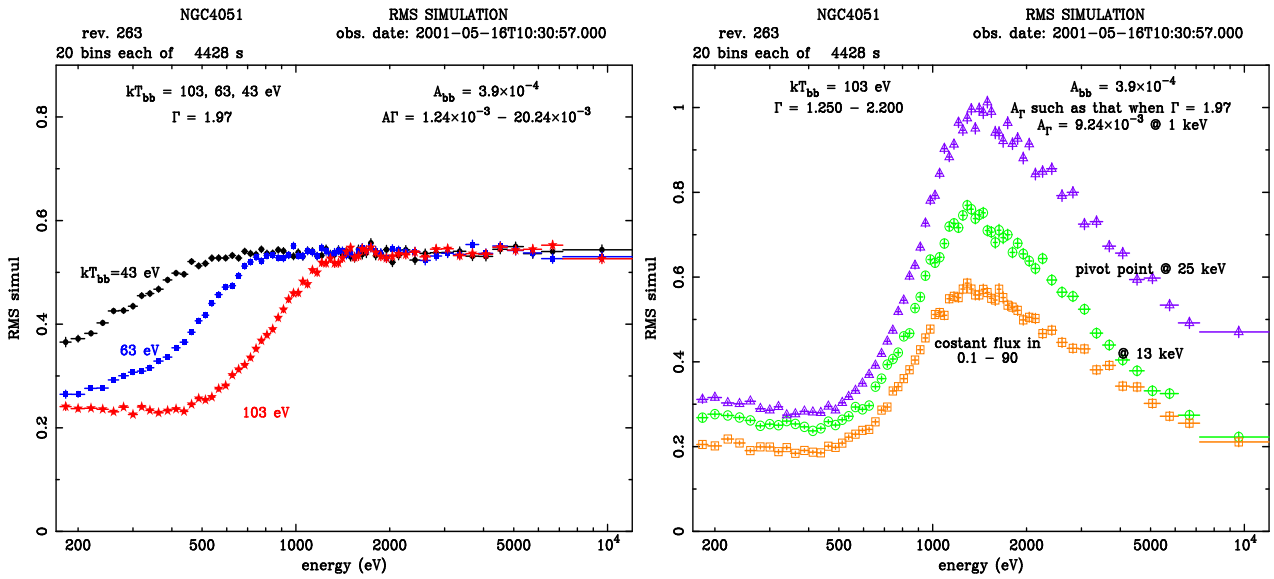

Figure 2.4: (*Left panel*) RMS spectra obtained by varying the normalization of a power law component between the lowest and highest value observed during the *XMM-Newton* observation of NGC 4051. At low energy the constant emission from a black body component is considered. The red stars show the expected RMS spectrum when the best fit black body temperature and luminosity are considered. The blue squares and the black dots show the RMS spectra when the BB temperature is 63 and 43 eV, respectively. (*Right panel*) Simulated RMS spectra assuming a spectral index variation of the power law between Γ 1.25-2.2 (as observed in during the *XMM-Newton* observation of NGC 4051). The low energy black body is constant and its parameters are fixed at the best fit values. The normalization of the power law is chosen so as to have the best fit value when the spectral index is equal to the best observed one. The green and violet open dots and triangles show the results of a variation with a pivot point at 13 and 25 keV, respectively. The orange open squares show the spectral index power law variations keeping fixed the flux in the 0.1-90 keV energy band.

Thus the cases of lower temperature BB have been simulated. The blue squares and the black dots in Figure 2.4 show the expected RMS if the BB temperature is 63 and 43 eV, respectively. In these simulations not only the PL parameters, but also the BB luminosity are kept fixed to their best fit values. These RMS spectra show that a decrease in the BB temperature shifts the drops in the RMS value at lower energies and that these should be "observable" for $T_{BB} \gtrsim$35–40 eV. A standard BB component with temperature of 20 eV should give no visible effect in the RMS spectrum in this energy band.

PL spectral index variations

The right panel of Figure 2.4 shows the RMS spectra obtained by varying the spectral index (Γ) of the PL from 1.25 to 2.2. The other parameters of the model are unchanged, with the BB temperature fixed at 103 eV. The green and violet open dots and triangles show the results

of a variation of the spectral index around a pivot point fixed at 13 and 25 keV, respectively, while the orange open squares show the same variations without pivot point, but keeping fixed the PL flux in the band 0.1–90 keV. In these simulations the PL normalizations are chosen in order to be identical to the mean spectrum and with the same spectral index.

All these RMS spectra show a peak of variability between 1 and 2 keV and a drop of variability at lower and higher energies. The high energy drop is monotonic, with a single slope, if the energy of the pivot point is fixed at a value higher than 10 keV. A more complex behavior is predicted if, instead of a pivot point, the total flux in a fixed band is conserved.

2.4.2 Partially ionized absorption

The soft X-ray spectra of many black hole accreting systems show the signature of a partially ionized absorption medium along the line of sight, the so called "warm absorber". In low resolution instruments, like the EPIC pn camera aboard *XMM-Newton*, the set of narrow absorption lines generated by the WA overlap each other and produce a features with a shape similar to edges.

The left panel of Figure 2.5 shows a series of RMS obtained by varying the optical depth τ, from 0.3 to 0.87, of absorption edges placed at different energies. The other spectral components of the assumed model (BB plus PL) are constant and they have all the parameters fixed to the best fit values of the mean spectrum. In order to increase their resolution to fine structures, the simulations in Figure 2.5 were calculated for a total observation time of 30 Ms. The black filled dots, red filled stars, blue filled squares, green open circles, orange open squares and violet open triangles show the RMS spectra produced by the variation of edges with threshold energies at 0.4, 0.6, 0.9, 1.5, 3 and 7 keV, respectively. Figure 2.5 shows that a variation in the optical depth of $\Delta\tau$=0.57, in 20 linear steps, generate a peak of RMS variability around 0.1 and 0.15. The different sharpness of the features depend on the energy resolution of the pn camera. The peak of variability is always located at higher energies with respect to the threshold energy. This effect is introduced by the spectral shape and the energy resolution of the instrument that, at each energy, mixes photons of nearby energies. As an example, at the edge threshold energy (where the peak of variability should be) there is an higher contribution of constant photons from lower energies than variable from higher ones. For this reason the peak of variability is shifted to slightly higher energies.

The right panel of Figure 2.5 shows the effects in the spectral variability of the presence of narrow emission lines with different Equivalent Widths (EW). The underlying model (BB plus PL) is the same of the present simulation (apart from the absorption edges that are not present anymore) as well as the integration time. The only variable components are the normalizations of the PL and BB. Also in this case the width of the features is generated by the instrumental energy resolution. Figure 2.5 shows that a narrow constant emission line at 0.4 keV generates a broad feature in the RMS spectrum with an important red tail at low energy. The red filled stars, blue filled squares and the black filled dots in the right panel of Fig. 2.5 show the effects of the presence of narrow constant lines with EW of 20, 100 and 200 eV above the continuum, respectively, with energies at 0.4, 0.9, 2, 4, and 6.4 keV. Figure 2.5 shows that a narrow constant line with an EW of 20, 100 and 200 eV lowers the variability of about 10–20, 40–50 and 50–60 %, respectively.

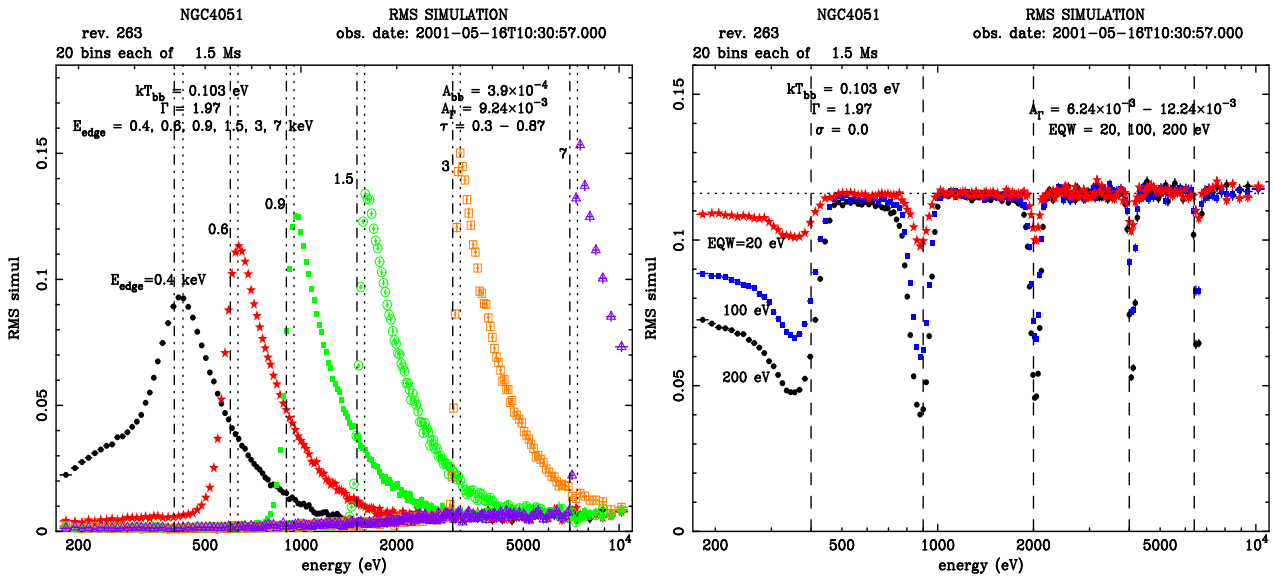

Figure 2.5: (*Left panel*) RMS simulations obtained by varying the optical depth (τ from 0.3 to 0.87) of a series of edges absorbing at 0.4, 0.6, 0.9, 1.5, 3 and 7 keV. The underlying constant model is composed by a black body component plus a power law. The parameters of these component are equal to the best fit parameters of the mean spectrum of NGC 4051. (*Right panel*) Synthetic RMS spectra result of a variation in normalization of the same underlying model (BB+pl), but instead of considering variable edges, narrow constant emission lines are taken into account. The EW of the lines correspond to 20, 100 and 200 eV and their energy is 0.4, 0.9, 2, 4 and 6.4 keV.

WA physical model

The geometric position of the WA in AGN is still debated. This ionized plasma may be located just above the accretion disc, well inside the BLR, or even in the NLR. Clearly observing the timescales of variability of the WA is a key information to measure its location. If the WA is far from the nuclear source (i.e. in the NLR) no variability should be seen during the *XMM-Newton* observations. Nevertheless, if the absorbing material is located inside the BLR and with an high density (so as to have a short enough recombination time), variability is expected. If we assume that the ionization parameter ξ (defined as $\xi = \frac{L}{nR^2}$, where L is the source luminosity, R the distance between the source and the absorbing material and n the density of the material) closely follows the variations of the luminosity, assuming that the position, the extension and the density of the WA are such that it immediately follows the variations of the continuum, it is possible to estimate the contribution to the spectral variability due to the WA.

Following Pounds et al. (2004) we considered a 2 components WA[3], the first with column

[3]The two components of the WA have been fitted with two Xstar tables (grid 18) that contain the Unresolved

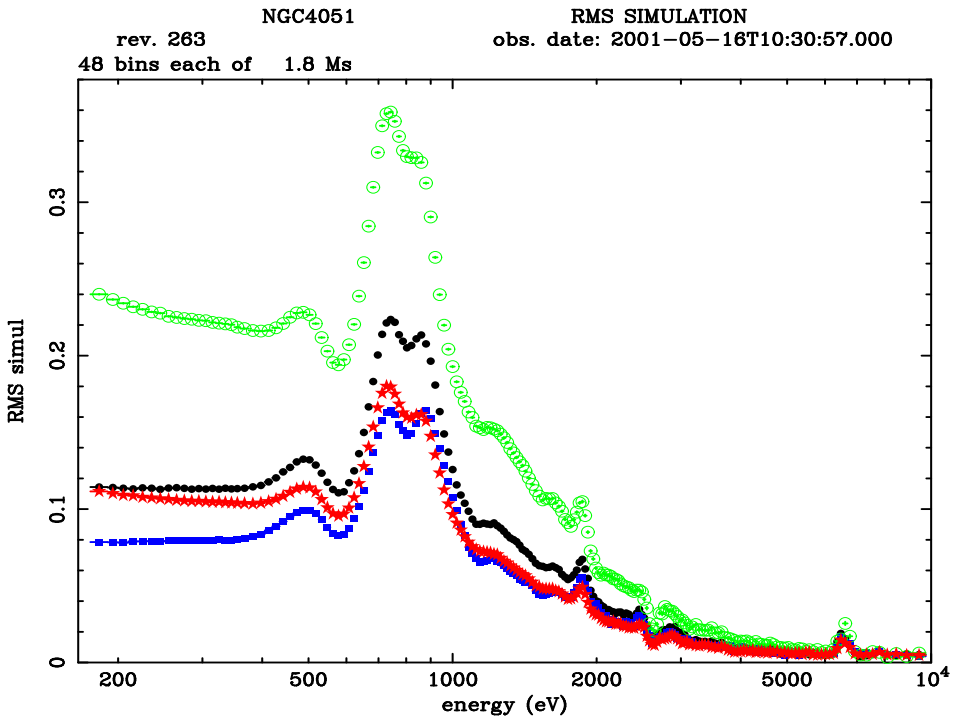

Figure 2.6: Contribution to the spectral variability introduced by the variation of the warm absorber. In the simulation a two component warm absorber model has been assumed (see text and Pounds et al. 2004). Moreover, to estimate the minimum and maximum ionization parameter the formula $\xi = \frac{L}{nR^2}$ has been assumed. The blue filled squares and the black filled dots show the variability expected if the ionization parameter is varying linearly or logarithmically within this range. The green open dots show the results if the ionization parameter is jumping between its minimum and maximum possible value (within the range). The red filled stars show the RMS expected if the assumed formula is valid in each moment. The underlying constant continuum is composed by the best fit standard model (BB + pl).

density $n_H = 6 \times 10^{21}$ cm^{-2} and ionization $log(\xi) = 2.7$ and the second with $n_H = 2 \times 10^{21}$ cm^{-2} and $log(\xi) = 1.4$. The other spectral components (BB plus PL) are fixed to the best fit of the mean spectra as before. All the spectral components are constant, only the ionizations of the two components of the WA are allowed to vary. The minimum and maximum values of the ionization parameter have been calculated by slicing the light curve of NGC 4051 (rev. 263) in 48 time intervals of ∼2 ks, then by measuring the source luminosity in each interval. The relation $\xi = \frac{L}{nR^2}$ has then been used to obtain from the maximum and minimum luminosity observed, the extreme values of the ionization parameter. For the calculation we assumed that the mean luminosity correspond to the ionization parameters found by Pounds et al. (2004).

Figure 2.6 shows the expected RMS obtained by varying only the ionization of the WA.

Transition Arrays.

As before, for the simulation, a long integration time has been considered[4]. The blue filled squares and the black filled dots in Fig. 2.6 show the expected variability if the ionization parameter is varying, within the allowed range, in a linear way in ξ or in $\log(\xi)$, respectively. The strongest peaks of variability occur at the energy of the O VII (∼0.74 keV) and O VIII (0.87 keV) edges. Other deviations are present at the energy of the C VI (∼0.49 keV) and of other elements (i.e. Ne, Mg, Si, Fe). At energies lower than 0.5 keV the variability is almost constant, while it is decreasing gradually at high energies. In order to measure the actual contribution to the total variability of the WA the knowledge of the unknown distribution in ξ is needed. Nevertheless, assuming that the relation $\xi = \frac{L}{nR^2}$ is valid at each moment, it is possible to estimate ξ (and thus its distribution) from the observed luminosity. The red filled stars in Fig. 2.6 show the RMS spectrum for this case. The variability introduced by the WA is of the order of 10 % at low energy with a peak around 15–20 % between 0.7 and 0.9 keV, then a decrease with energy. The green open circles in Fig. 2.6 show, instead, the RMS expected if the ionization parameter jumps continuously at the maximum and the minimum value of the allowed range. This RMS should give an upper limit to the variability introduced by the variation of ξ.

2.4.3 PL and ionized disc reflection

A possible explanation for the soft excess is that its nature is tied to ionized reflection from the accretion disc, with the primary X–ray source located close to the black hole. If the X-ray source is closer than about 10–20 gravitational radii (r_g), the effects of general relativity become important. In this condition, as shown by Miniutti & Fabian (2003), the ionized disc reflection component becomes almost constant, while the primary power law varies. Thus, during the low flux states, when the flux of the power law component is low, the spectrum should be dominated by the ionized disc reflection component.

Assuming that the ionized disc reflection is constant and that only the normalization of the power law varies, an RMS has been simulated (see Fig. 2.7). In order to constrain the spectrum of the constant ionized reflection we fitted the low flux spectrum of NGC 4051 with a model that is composed of a direct power law component and an ionized disc reflection component (from Ross & Fabian 2005) the spectrum of which is convolved with a `LAOR` kernel with fixed inner and outer disc radius (to 1.24 r_g and 100 r_g respectively), and fixed disc inclination (30°). The best fit value has an ionization parameter of the reflection $\xi \simeq 50$ and disc emissivity index of $\alpha \simeq 6$. The contribution from neutral distant reflection is also considered. We assume that the power law component has a spectral index fixed at $\Gamma = 2.4$ (Lamer et al. 2003) and that the reflection component is completely constant not only in normalization, but also in spectral shape (i.e. ionization and relativistic blurring parameters). We allowed the power law normalization to vary linearly in a range consistent with the lowest and the highest fluxes observed.

The red open circles and the blue filled squares in Figure 2.7 show the simulated RMS

[4]The simulated observation is about 700 times longer than the real NGC 4051 (rev. 253) *XMM-Newton* observation.

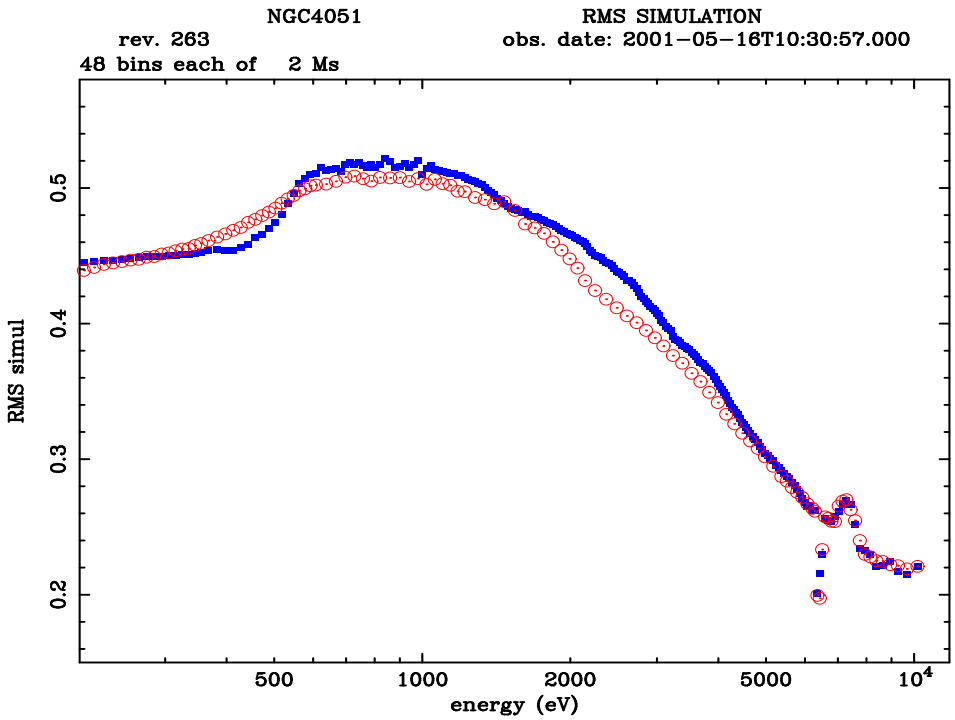

Figure 2.7: The observed RMS spectrum obtained during rev. 263 is compared with synthetic ones. The solid line (blue in the color version) is obtained varying in normalization (from the lowest to the highest value observed) a power law with Γ=2.4 and keeping a reflection component with ionization parameter ξ=5 and disc emissivity index α=4 completely constant. While the simulated RMS shown by the dotted line (green in color) is calculated in the same way as above, but with $\xi \simeq$50 and $\alpha \simeq$6. In both models the contribution from neutral distant reflection is considered.

spectrum and, for comparison, the simulated RMS with the reflection parameters of ξ=5 and α=4 (solid line, blue in the color version). These RMS have a shape proportional to the inverse of the contribution to the mean spectrum of the constant components (ionized disc reflection and reflection from distant material). In fact Fig. 2.7 shows that the RMS spectra have a peak of variability between about 0.5 to 2 keV, where the ionized reflection have their minima and lower variability at lower and higher energies.

Chapter 3

The sample

3.1 Definition of the sample

The main aim of this work is the study of the spectral variability of the Fe K line, as well as, the study of the nature of the soft excess, in order to better understand the physical processes at work in the innermost regions around black holes. A powerful way to perform these studies is through the time resolved spectral variability of AGN[1]. The key requirement to study spectral variability has been the number of photons collected. Thus, the highest sensitivity X-ray telescope is mandatory. For this reason it has been chosen to use the ESA Satellite *XMM-Newton* (see Appendix B for more details) and, in particular, the highest sensitivity camera, EPIC pn.

To define the sample we started from the *ROSAT* all sky survey (Voges et al. 1999). From the complete sample of bright and identified X-ray sources in the RASS (Schwope et al. 2000) we selected all the AGN except for BL Lac (which emission is dominated by the jet) and type 2 objects (which nuclear emission is obscured). We restricted the study to the sources with a low redshift z$\leq$0.1. The sample includes all the sources with a count rate in the PSPC instrument higher than 0.2 s^{-1}, which ensures a flux lower limit of 2.4×10^{-12} erg s^{-1} cm^{-2} in the 0.5 to 2.0 keV band. More than 200 sources have been obtained in this way. The total survey area comprises more than twenty thousands square degrees. Nevertheless this sample (Schwope et al. 2000) is limited only to sources with an absolute Galactic latitude higher than 30 degree. With this arbitrary choice many interesting sources are not considered. Thus I expanded the sample to lower Galactic latitudes, down to 15 degree but not lower in order to avoid sources with an high neutral absorption column density due to our own Galaxy. The sources obtained with this extension have been identified by correlating the sample with the SIMBAD and NED databases.

Of all these sources, I selected only the ones with an EPIC pn *XMM-Newton* observation longer than 30 ks present in the public archive up to July 2006 (except for the data for which I am PI or Co-I). This requirement is made in order to be able to calculate a RMS spectrum

[1] Although AGN are generally fainter than GBHCs, they are better targets for these studies because their collected number of photons per orbital time scale at a given radius is higher than for galactic black holes.

of good enough quality and to perform time resolved spectral variability for each source. Finally, the sample was composed of the 36 sources shown in Table 3.1. When more than one observation was available, the one with best statistics was considered.

The black hole masses have been obtained from the literature. I have used preferentially the reverberation–mapping mass estimate, from Peterson et al. (2004). If not available, I used the mass estimates determined from either stellar velocity dispersion (Gebhardt et al. 2000) or empirical relationships (Wandel et al. 1999). For ESO 198-G24, the only mass estimate available was obtained through the variability of the Fe K line (Porquet et al. 2004), while for CTS A08.12, HE 1143-1810 and MR2251-178 no proper measurement of the mass has been found. The masses are given in Table 3.1 together with the references.

The observed (absorbed) 0.2–10 keV luminosities have been obtained from the *XMM-Newton* observations. In the fitting process an absorbed power–law, with N_H constrained to be at least equal to the Galactic value[2] has been used. For luminosity calculations I used the redshifts obtained from NASA/IPAC Extragalactic Database, assuming H_0=75 km s^{-1} and q_0=0.5.

3.2 Light curves, spectra and RMS spectra

For each of these sources, the light curve, spectrum and RMS spectrum have been calculated. These are shown for each source in Figure 3.1 and discussed in details below.

3.2.1 Light curves

The light curves are calculated with a time binning of 500 s. Some periods of no data in the light curves are due to either telemetry holes or periods of high background, that have been excluded. The sources are ordered with increasing black hole mass.

The light curves of the less massive objects show a high degree of variability on all timescales probed. In particular, all AGNs of the sample with black hole masses lower than a few times 10^6 $M_\odot$ show a doubling time of the flux of less than a few thousands seconds. This is a strong constraint on the compactness of the nuclear X–ray source implying dimensions not larger than a few thousands light seconds ($\sim 3\times10^{10}$ cm). The more massive AGNs do not show such high degree of variability on such short time scales. Moreover, the light curves of the objects more massive than 10^8 $M_\odot$ are generally well represented by an almost constant curve with almost no variability. This different behavior suggests a variation of the observed variability properties with a clean relation with the black hole mass, as confirmed below.

3.2.2 Spectra

The spectra are fitted with a power law absorbed by Galactic neutral material in the 3–10 keV band and then extrapolated at low energy in order to check for the presence, shape and intensity of a soft excess. Figure 3.1 shows that a quite similar soft excess is present in all

[2]The N_H Galactic value have been obtained using the Xspec 'nH' tool.

Source Name (1)	M_{BH} (2)	$L_{0.2-10\ keV}$ (3)	Source Type (4)	pn time (5)	Refs. (6)
Fairall 9	8.41	43.84	Sy1	30	R,1,2
ESO 198-G24	8.60	44.06	Sy1	31	F,12
NGC7213	7.95	42.48	Sy1.5	42	S,9
PICTOR A	7.60	43.67	Sy1	52	S,10
MS2254.9-3712	7.04	43.31	Sy1	71	L,11
CTS A08.12		43.35	Sy1	46	
IC 4329A	7.00	43.59	Sy1	133	R,1,2
Ton S 180	7.09	44.41	NLS1/Sy1.2	30	L,3,4
HE 1143-1810		44.21	Sy1	31	
MR2251-178		44.43	Sy1	64	
HE 1029-1401	9.08	44.82	Sy1	46	L,6,7
NGC 985	8.05	43.78	Sy1	58	L,5
NGC 4593	6.73	43.15	Sy1	76	R,1,8
MKN 590	7.68	43.23	Sy1.2	107	R,1
NGC7469	7.09	43.56	Sy1.2	85	R,1,2
MKN 841	8.10	43.73	Sy1.5	46	L,6,2
I Zw 1	7.20	44.01	NLS1/Sy1	83	L,3,4
PG 1211+143	8.16	44.16	NLS1/Sy1	53	R,1
Mrk 335	7.15	43.80	NLS1/Sy1	32	R,1,2
NGC5548	7.83	43.65	Sy1.5	93	R,1,2
Mkn766	6.54	43.41	NLS1/Sy1.5	129	L,6,2
IRASF 12397+3333	6.66	43.76	NLS1/Sy1	78	L,5
Mkn478/PG1440+35	7.34	44.37	NLS1/Sy1	28	L,3,4
NGC4151	7.12	42.08	Sy1	57	R,1,2
NGC4051	6.28	41.91	NLS1/Sy1.5	117	R,1,2
MKN 110	7.40	44.26	NLS1/Sy1	47	R,1
Mkn 279	7.54	43.85	Sy1.5	30	R,1
IRAS 13224-3809	6.82	43.60	NLS1/Sy1	61	L,3
NGC3783	7.47	43.19	Sy1	136	R,1,2
MCG–6-30-15	6.19	42.87	Sy1.2	84	L,3,2
3C 390.3	8.45	44.66	Sy1/BLRG	52	R,1
1H 0707-495	6.31	43.46	NLS1	78	L,3
Mrk509	8.16	44.35	Sy1.2	85	R,1,2
Ark 120	8.18	44.24	Sy1	112	R,1,8
3C120	7.44	44.23	Sy1/BLRG	128	R,1
ARK 564	6.06	43.98	NLS1	99	L,3,4

Table 3.1: List of objects of the sample. (1) Object name. (2) Log of black hole mass in units of $M_\odot$. (3) Log of 0.2–10 keV observed (absorbed) luminosity in units of erg s^{-1}. (4) Source type as indicated by Schwope et al. (2000), SIMBAD and/or NED. (5) Total EPIC–pn observation time in ks. (6) Methods used to determine the black hole mass and references for the black hole mass. The methods are: R, reverberation mapping; S, stellar velocity dispersion; L, relationship between broad–line region radius and optical luminosity; F, variability of the Fe K line. References: 1, Peterson et al. (2004); 2, Nandra et al. (1997); 3, Bian & Zhao (2003); 4, Leighly (1999); 5, Grupe et al. (2004); 6, Woo & Urry (2002); 7, Reeves & Turner (2000); 8, Nandra & Pounds (1994); 9 Nelson & Whittle (1995); 10, Lewis Eracleous (2006); 11, Shields et al. (2003); 12, Porquet et al. (2004).

but five objects: NGC4151, Pictor A, 3C120, IC4329A and MR2251–178. NGC4151 is a highly absorbed source, with physical characteristics more similar to type 2 than unabsorbed objects; Pictor A, a radio loud AGN, has a spectrum possibly dominated by the emission of a jet and thus is well fitted by a single power law component (Grandi et al. 2001; Grandi et al. 2006); 3C120 is a radio loud AGN which shows an excess around 1 keV of still debated nature (Zdziarski & Grandi 2001; Kataoka et al. 2006); IC4329A and MR2251–178 are heavily absorbed by both a strong warm absorber component and by neutral material that may be due to a dust lane in the host galaxy.

It is clear from the spectra in Figure 3.1 that the shape of the soft excess is different from one source to the other. Generally, this component starts to emerge at 2 keV and gradually becomes stronger at lower energies. But the sources with a strong warm absorber component (like MCG-6-30-15, MKN 766, NGC 4051, NGC 3783 and NGC 5548) generally show a more structured soft excess. In particular, these show a fast rise of emission between 0.8 and 0.6 keV instead of a smooth increase starting from around 2 keV like in Mkn 590 or Mkn 335 which do not show sign of a warm absorber. These jumps in the soft excess shapes occur exactly where the opacity of the warm absorber abruptly changes due to the presence of the Oxygen features. For this reason one can not exclude that most of the differences observed in the soft excess shapes in Fig. 3.1 are introduced by the warm absorber.

The strenght of the soft excess is given by the low energy ratio between the data and the extrapolation of the high energy power law. Figure 3.1 shows that all the sources with a soft excess have a ratio between the data and the extrapolation of the power law going from about 1.5 to about 4. The only source with a ratio significantly higher than 4 is IRAS 13224–3809 that shows a value of about 10. The soft excess of this NLS1 galaxy is peculiar not only for its strenght, but also for its shape. In fact, this soft excess and the one of 1H0707-495 are the only two characterized by a steep and fast rise at about 1 keV, instead than between 0.6 and 0.8 keV. Moreover, once that the soft excess is modeled with a black body component, a broad absorption line at $\sim$1.2 keV is required (Leghly 1999; Boller et al. 2003). This feature, if real, would either require a non standard warm absorber model, or could be the result of a wrong parametrization of the underlying continuum. This source will be studied further in §6.

Finally, the spectra of Figure 3.1 show also an almost ubiquitous presence of a narrow component of the Fe K line. The presence of a broad red wing component of the Fe K line is, instead, clearly evident only in a few sources. Moreover, a strong and/or complex absorber may complicate the interpretation of the broad wing component (Boller et al. 2003; Pounds et al. 2003; Pounds et al. 2004; Tanaka et al. 2004). In order to distinguish between the two possible interpretations for the line which is the most plausible, spectral variability studies are useful.

3.2.3 RMS spectra

Figure 3.1 shows the RMS spectra for each source. They are all calculated with roughly the same time binning, of the order of a few thousands seconds. The time–energy binning has been chosen in order to have the maximum energy resolution and to have a negligible Poisson noise contribution compared to the measured spectral variability. For this reason the RMS spectra

of almost constant objects are heavily binned (see §2.4) providing little spectral variability information.

Figure 3.1 shows that some degree of variability is detected in all the sources and that the variability spectral shape is clearly complex. These RMS spectra confirm the trend observed by investigating the light curves, i.e. that there is lower variability for sources with larger black hole mass. In fact, 14 of the highest mass AGNs have a mean variability lower than 4 percent. The combination of this low degree of variability connected with short exposures and/or low statistics do not allow to have more information about the spectral variability. For this reason we do not consider these sources further in the study of the spectral variability. It is only possible to measure the total achromatic amount of variability for these objects and study further the possible correlation between black hole mass and amount of achromatic variability. This particular topic will be addressed in section §3.3.

For the remaining 22 sources strong and clear spectral variability is observed. The RMS spectra of these highly variable sources are reported in Figures 3.2, 3.3 and 3.4, after classifying them in three different categories, identified as follows:

- The first group of sources (Fig. 3.2) shows a lower variability value at low and high energies and a peak between a few hundred eV and 1, 2 keV. Imprinted on this gross shape are other features more characteristic of the different sources. The objects with the strongest soft excess, for example, like IRAS 13224–3809, 1H0707-495, NGC 4051 and MKN 841, generally show a plateau of variability between 0.2 and 0.5 keV. Instead, sources like MKN 766, NGC 4051, ARK 564 and MKN 335 show sharp features between 0.5 and 2 keV. Moreover, we observe that for many sources the amount of variability at high energy (at 10 keV) is at the same level than at $\sim$0.2 keV.

  The sources of this class generally have a high degree of variability, with values usually as high as a few tens percent. In this class fall the 7 objects of the sample with smaller black hole mass plus 3 sources with mass between 10^7 up to 10^8 $M_\odot$. This class is also characterized by having some of the strongest soft excesses.

  As seen in section 2.4 this RMS shape could be due to many different physical components. A pivoting power law with a less variable black body component or a power law varying in normalization and a less variable ionized disc reflection component (see Fig. 2.4 and 2.7; and §2.4.1 and §2.4.3). An important indication of this study is that, whatever the origin of the soft excess, the drop in variability at low energy indicates that there is an almost constant component in that energy band. Thus, the RMS spectra suggest that in these sources the soft excess is less variable than the power law continuum. In the standard interpretation (where the spectrum is composed by a power law plus a black body for the soft excess, see §1.1), the high energy drop may then be due to a power law continuum varying with a pivot point at energies higher than 10 keV as expected in thermal Comptonizations models (see Figure 2.4 and §2.4.1). Alternatively, in the strong disc ionized reflection interpretation (see §1.1.2), this high energy drop could be produced by the inter-combination of two different components. One flat and constant (the disc ionized reflection) and one steeper and variable only in normalization. The variability of the normalization of the steep power law would generate more variability at low energy than at high energy. In this scenario the steep power law would

interpolate the emission of the primary source, while the flat component would reproduce the shape of the ionized reflection component (see Figure 2.7 and §2.4.3). It should be noted that also a warm absorber component, if variable, would produce a similar RMS shape (see Fig 2.6 and §2.4.2). Furthermore, the sharp features observed between 0.5 and 1 keV in ARK 564, MKM 766, NGC 4051 and MKN 335 occur exactly where the warm absorber is expected to have its major effect, thus may be the signature of its presence (Fig 2.6). Clearly the warm absorber, if variable, gives a contribution to the RMS spectrum. Nevertheless, the modeling tested in this thesis (§2.4.2) indicate that the warm absorbing material, in order to reproduce alone the whole shape of the RMS should have a too high column density, that is excluded by the high resolution observation of these objects. The only way to overcome this "observational" problem would be to require that this absorbing component is relativistically blurred (see §1.2.2; Done & Gierlinski 2006; Gierlinski & Done 2006; Shurch et al. 2006; Sobolewska et al. 2006). The detailed study of this possibility is beyond the scope of this work.

In most of the RMS spectra, at the energy of the Fe K line, there is not enough statistics to perform a detailed spectral variability study. Nevertheless, for MCG-6-30-15 the broad component of the Fe K line is so strong that its variability clearly emerges above the underlying continuum (see §4.2). This is a strong (because model independent) evidence for the presence of a spectral component different from the continuum at those energies. The RMS spectra of the other three *XMM-Newton* pointings of this object have been studied (Ponti et al. 2005). Nevertheless, this red variable feature has been observed clearly only during this low flux observation (though a weak feature is observed also during rev. 302). This peculiar behavior is consistent with being be due to the light bending effect that inhibits the Fe K line variability during medium–high flux states (Miniutti et al. 2003; Miniutti & Fabian 2004). Also MKN 766 and MKN 335, although less significantly, show a higher degree of variability of a possible broad component of the Fe K line. MCG-6-30-15 as well as NGC 4051 show also a lower degree of variability of the narrow component of the Fe K line, consistent with the hypothesis that the narrow Fe component is being produced, at least in part, in a region distant from the nuclear source. The other RMS spectra have not enough signal to noise to study the details of the Fe K line variability.

- The second category of RMS spectra includes those which shape is either monotonically decreasing with energy or flat (see Figure 3.3). This spectral shape could be the result of a spectral pivoting of the power law at energies higher than 10 keV. The three RMS with flat shape (IC4329A, TonS180 and PG1440+356) could be considered a sub-sample of this group. A flat RMS could be produced by any spectral component or a combination of components varying in normalization only. In this case, the component producing the soft excess should follow the variations of the power law in order not to imprint any variability features at low energy. In fact, apart from NGC 4593, where a drop in variability is observed at low energies, no drop in variability is observed at the energies of the soft excess. Thus, for these sources, the soft excess should be variable as much as the nuclear power law, instead of being almost constant as observed in the previous class.

These sources (see Figure 3.3) show a slightly lower degree of variability with respect to the previous group, going from a few to twenty percent. This is in agreement with the observational fact that this class of objects is populated by higher mass AGNs with values going from about 5×10^6 to 10^8 $M_\odot$.

Many of these RMS provide also important information about the Fe K line variability: NGC 3783, NGC 4593, 3C120 and IC4329A show evidence of a less variable narrow component of the Fe K line, with a drop in variability at ∼6.4 keV (emitted frame). The RMS spectra of NGC 3783, IC4329A and NGC 4593 show a higher level of variability at energies redshifted as respect to the Fe K line, where in the spectrum is present an excess of emission that could be interpreted as the red wing of a broad Fe K line. In the case of NGC 3783 a particular detailed study of the variability of this broad redshifted component of the Fe K line has been performed (Tombesi et al. 2007). This study shows that the variability of the broad component of the Fe K line is correlated with the variations of the nuclear source occurring on time scales (∼25–30 ks) of the order of the orbital period at 10 r_g. The precise geometry and position of the primary X–ray source with respect to the accretion disc is not clear, but the variability timescales certainly implies a location at ∼10 r_g. The correlation between the primary and the reflected component is seen, probably, because the X–ray source is near (∼10 r_g) but sufficiently distant from the black hole and thus the light bending effect is not dominating (see §1.3.1). This evidence is in agreement with the absence of a drop in variability in the low energy band. In fact, if the origin of the soft excess is tied to an ionized disc reflection component and the X-ray source is sufficiently distant from the black hole, the soft excess as well as the broad component of the line should vary in a way correlated with the continuum generating no drop at low energy in the RMS spectrum. In this picture, the objects of the previous class should be dominated by X-ray sources located nearer to the black hole, where the light bending produces an almost constant reprocessed component.

At low energy in the higher quality RMS spectra, such as NGC 3783, wiggles are present (at about 0.7 keV) that most probably are generated by the strong warm absorber. Nevertheless, the warm absorber does not seem to generate the gross shape of the spectral variability. In fact the sources with a strong warm absorber, like NGC 3783 and IC4329A do not seem to show peculiar RMS spectra. Moreover the variations of the warm absorber should generate a peak of variability between 0.7 and 1 keV where its opacity is stronger (see Figure 2.6 and §2.4.2).

- The third group of objects is made of the 3 peculiar sources NGC 7469, PG 1211+143 and NGC 4151 (see Figure 3.4). In particular a degree of variability increasing with energy above 1–2 keV and a minimum of variability below, and in some case some structure below 0.5 keV is present. For PG 1211+143 and NGC 7469, the complex spectral shape, not easily reproduced by any model, could be the result of a highly variable power law component and a less variable soft excess. Their peculiar shape may need another component such as a strong warm or complex absorber to explain the drop in variability that is seen around 0.5 keV.

Finally, the most peculiar RMS shape is found for NGC4151. The X–ray spectrum of this source is absorbed by a high column density of neutral material of the order of $\sim 3 \times 10^{23}$ cm^{-2}, typical for a Compton thin type 2 object. Below 2 keV the nuclear emission is all absorbed and the X–ray spectrum is dominated by emission lines emitted from a photoionized plasma distant from the nuclear source. In fact the RMS spectrum indicates that this low energy component is substantially constant. Also the strong and narrow Fe K line component is observed to be constant, in agreement with its origin coming from distant material, possibly a molecular torus. The variability is detected only in the energy range where the nuclear emission is indeed observed directly. It should be stressed that this RMS spectral shape is likely typical of type 2 objects (like i.e. IRAS13197-1627; Miniutti et al. 2006).

3.3 Correlations between variability and black hole mass

As anticipated above, the light curves and RMS spectra shown in Figure 3.1 suggest that the total amount of variability depends on the mass of the central black hole in agreement with the anti correlation between the excess variance and mass as found by others (Lu & Yu 2001; Bian & Zhao 2003; Papadakis 2004; O'Neill et al. 2005; Nikolajuk et al. 2006). This correlation is tested here for the first time with the new *XMM-Newton* data.

In order to measure the total amount of variability I used the excess variance (see eq. 2.3). This function integrates all the source variations between the time resolution and the duration of the light curve. This means that different measurements of the excess variance are only strictly comparable if the duration and the time binning of the light curves are equal. For this reason, all the light curves were considered with the same time binning of 500 s. In order to have the best signal to noise, all the available energy band (from 0.2 to 10 keV) has been considered. This allowed to have always more than about 10^3 photons in each time bin. The variability was then integrated between 500 s and the shortest observation duration that is 30 ks. Following O'Neill et al. (2005), the observations longer than 30 ks were sub divided into several segments of about 30 ks. The excess variance was then calculated in each segment and then averaged between the segments of the same source. Taking the mean value of these multiple segments reduces the large scatter due to the stochastic nature of the process itself.

As detailed in §2.3, the excess variance uncertainty depends both on the measurement uncertainties and the stochastic nature of the variability. This latter component dominates over the measurement errors, when the variability is well detected. In section 2.3.1, following Vaughan et al. (2003), it has been shown that the scatter introduced by the red noise character of the process depends on the shape of the PSD, decreases with the number of segments over which it is calculated and is a factor of the measured excess variance (see Table 2.1 and Figure 2.1). For the uncertainty calculations, a spectral index of the power law describing the PSD equal to -2 has been assumed. Figure 2.1 and Table 2.1 show that a reasonable factor, for sources with such a spectral shape and with $\sim$40-50 time bins, is $\sim$0.71 (see also Table 1 in Vaughan et al. 2003). This value critically depends on the assumption of the PSD shape. The sources with lower mass (like NGC 4395, MCG-6-30-15, MKN 766, NGC 4051) have shown evidence for a break in the PSD with a shape flatter than -2 at low frequencies

(Edelson & Nandra 1999; Papadakis et al. 2002; Vaughan et al. 2003; McHardy et al. 2004; Vaughan et al. 2004; 2005), and with a break frequency within the frequency window used here. This should be taken into account in the calculation of the uncertainty. Nevertheless, PSD analysis of AGN have not revealed power law shapes steeper than -2. Moreover, the uncertainty associated to the excess variance is reduced when the PSD shape is flatter (see Figure 2.1). Thus, neglection of this effect generate only an overestimate of the real error. Thus, finally, I used the following equation (eq. 3.1) for the excess variance uncertainty.

$$\Delta\sigma^2_{XS} = \sqrt{(\frac{\sigma_{frac}\sigma^2_{XS}}{\sqrt{N_{seg}}})^2 + (\sigma_{Poisson})^2}, \tag{3.1}$$

where $\sigma_{Poisson}$ is the uncertainty related to the measurement errors (see eq. 2.7) and σ_{frac}=0.71.

Figure 3.3 shows the excess variance as a function of the black hole mass. A clear strong anti-correlation between these two quantities is present, confirming the indication inferred here by the light curves and RMS spectra, as well as the previous results obtained by Lu & Yu (2001), Bian & Zhao (2003), Papadakis (2004), O'Neill et al. (2005) Nikolajuk et al. (2006). The correlation coefficient results to be -0.66, thus the probability of being uncorrelated is lower than 0.5 percent.

The solid line in Figure 3.3 shows the best fit linear relationship between the black hole mass and the excess variance, with best fit relation: $\log(M_{BH})=\alpha\times\log(\sigma_{excess})$ with α=1.01±0.17.

Assuming, naively, no scatter in the relationship, a variability measurement may be translated in a determination of the black hole mass. For objects with a well determined variability, generally the sources with black hole masses between about 10^6 to few $\times10^7$ $M_\odot$, the black hole mass may be determined with an uncertainty of less than an order of magnitude. Larger errors are expected for the more massive objects, related to the higher uncertainty level in the excess variance determination.

The assumption of no scatter in the relationship shown in Figure 3.3 is clearly an oversimplification since outliers are present. The more evident is IRAS 13224–3809, which has an excess variance of -0.75 and a mass of $\log(M_{BH})$=6.82. However, the mass in this object has been inferred through the relation between the broad-line region radius and the optical luminosity and may be affected by large systematic errors. This source, in fact, belongs to a class of AGN, the NLS1s, showing no standard broad line regions. Other outliers are in the mass range between about $\log(M_{BH})$=7.4 and 8. For these objects the measurement of their variability is difficult because they generally have short exposure and flat light curves. For these reasons measurements with large uncertainties are associated to their variability. This is most evident in the case of NGC 7213 (the source with black hole mass $\sim10^8$ $M_\odot$ and $\log(\sigma_{excess}\sim$-5). Furthermore, two among the less variable objects (3C120 and Pictor A) could only appear as such because they have an important contribution from their jet that is thought to be variable on much longer timescales.

Neglecting these sources the shape of the linear relationship does not change significantly becoming α=0.95±0.13, while the reduced χ^2 goes from 6 to 3.6. This suggests that, although the two quantities are clearly correlated, significant scatter in the relationship is present.

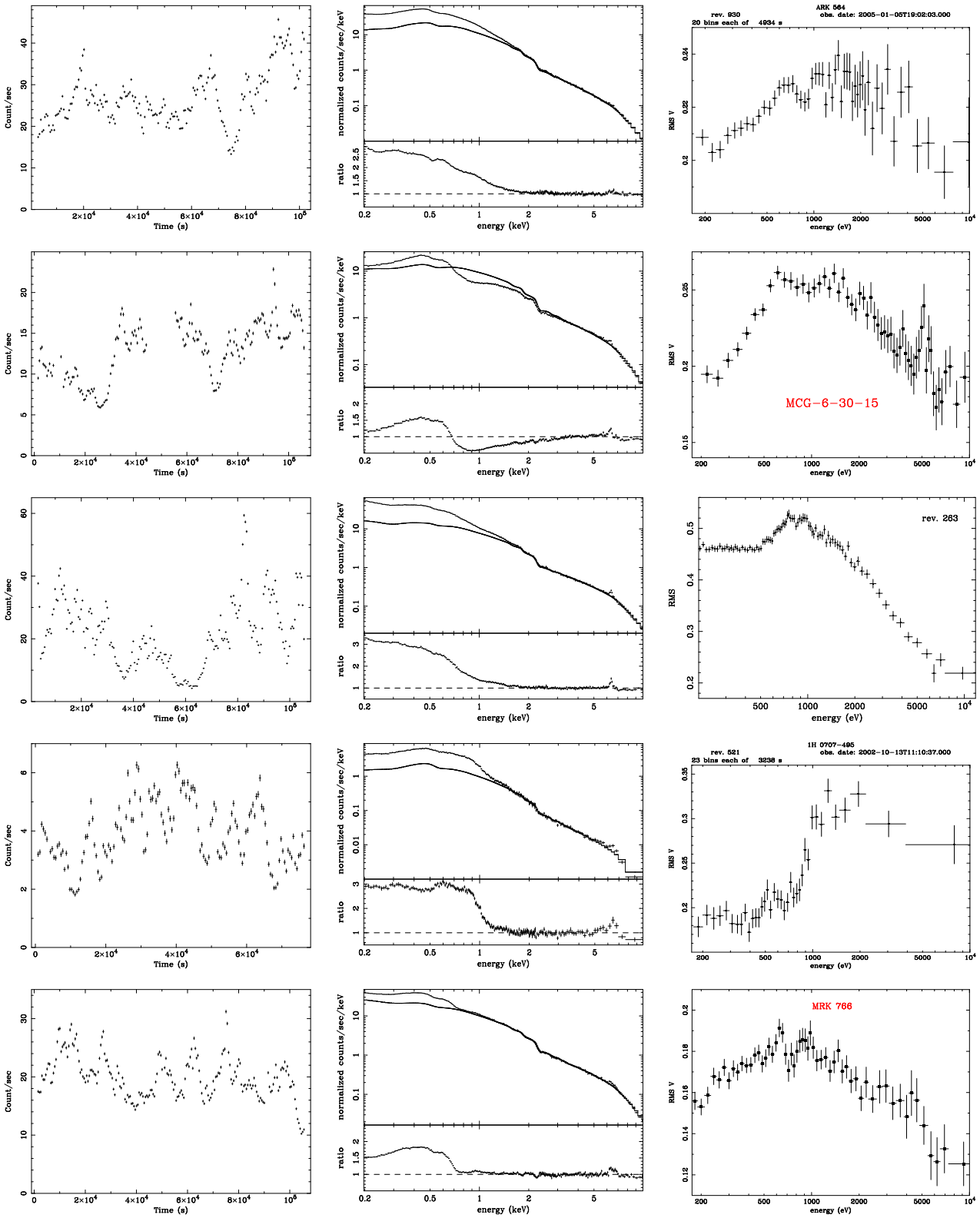

Figure 3.1: The Figure shows the light curve, the spectrum and the RMS spectrum, of the best statistics *XMM-Newton* observation, for each source. The light curves are calculated with a time binning of 500 s. The holes in the light curves are due to either telemetry holes or periods of high background. The sources are ordered by increasing black hole mass. See also the following Figures.

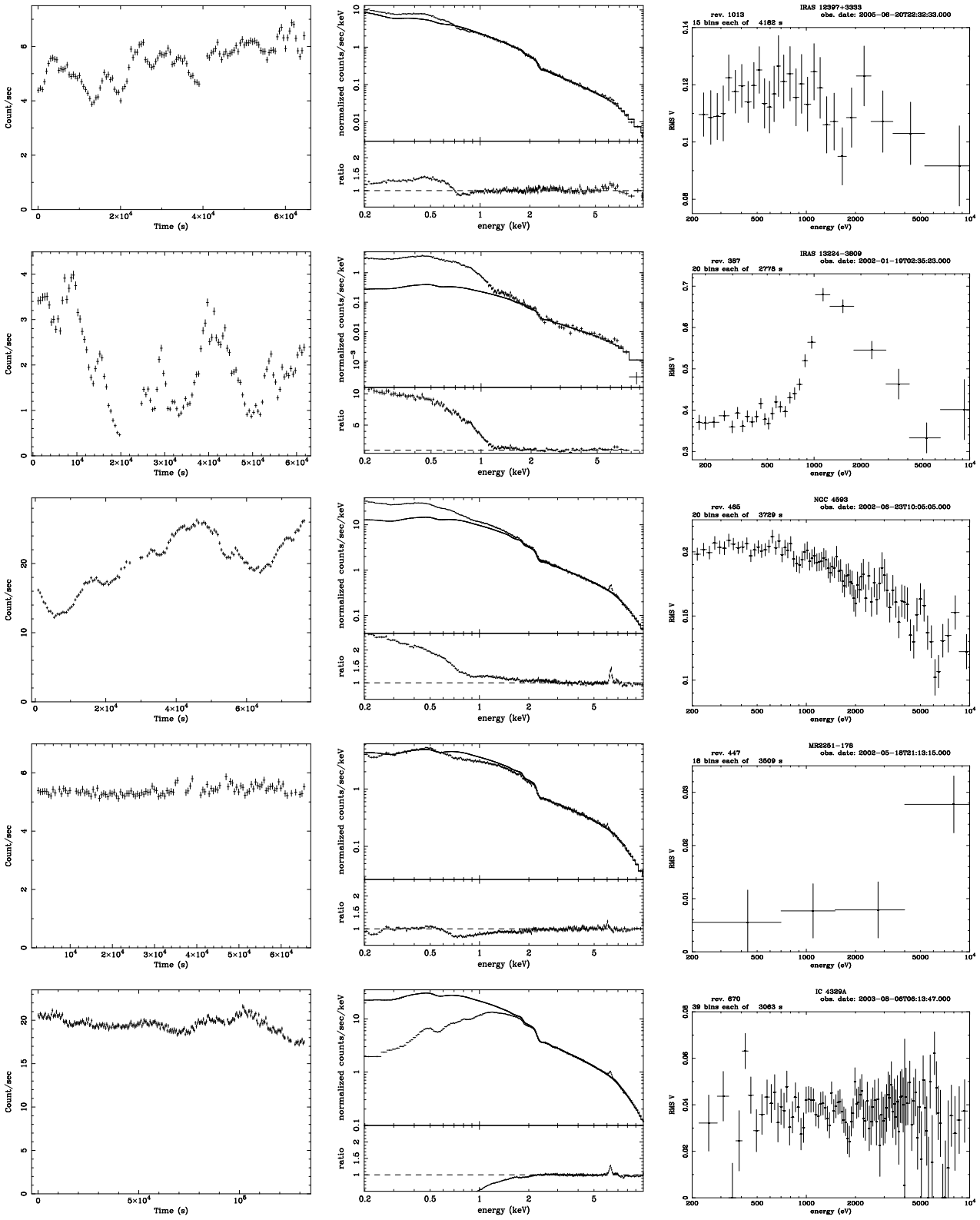
Count/sec
Time (s)
normalized counts/sec/keV
ratio
energy (keV)
IRAS 12397+3333
rev. 1013
obs. date: 2005-06-20T22:32:33.000
15 bins each of 4182 s
IRAS 13224-3809
rev. 387
obs. date: 2002-01-19T02:35:23.000
20 bins each of 2775 s
NGC 4593
rev. 465
obs. date: 2002-06-23T10:05:05.000
20 bins each of 3729 s
MR2251-178
rev. 447
obs. date: 2002-05-18T21:13:15.000
18 bins each of 3509 s
IC 4329A
rev. 670
obs. date: 2003-08-06T06:13:47.000
39 bins each of 3063 s
RMS V
energy (eV)

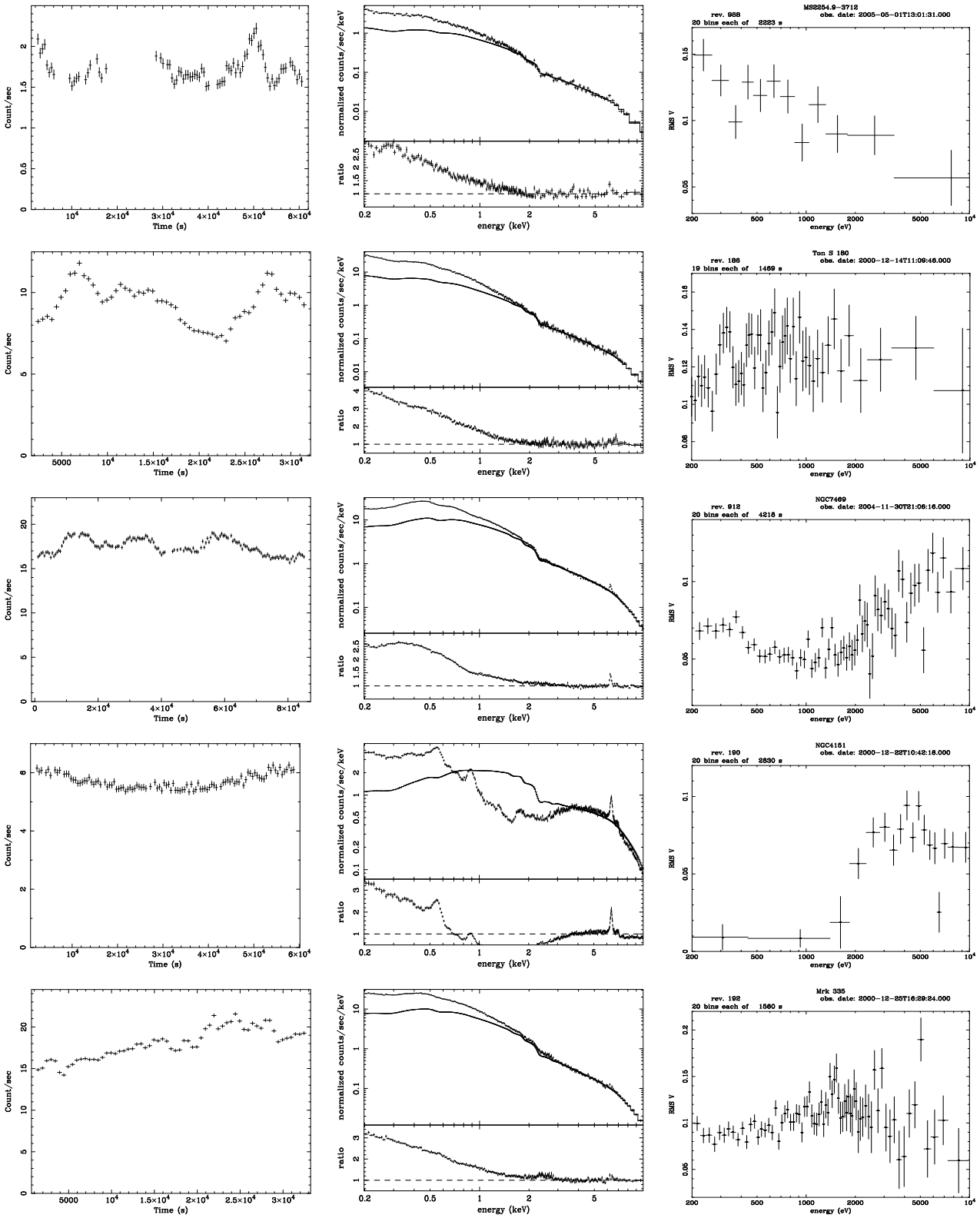
MS2254.9-3712
rev. 988
obs. date: 2005-05-01T13:01:31.000
20 bins each of 2223 s
Ton S 180
rev. 186
obs. date: 2000-12-14T11:09:46.000
19 bins each of 1469 s
NGC7469
rev. 912
obs. date: 2004-11-30T21:06:16.000
20 bins each of 4218 s
NGC4151
rev. 190
obs. date: 2000-12-22T10:42:16.000
20 bins each of 2830 s
Mrk 335
rev. 192
obs. date: 2000-12-25T16:29:24.000
20 bins each of 1560 s
Count/sec
Time (s)
normalized counts/sec/keV
ratio
energy (keV)
RMS V
energy (eV)

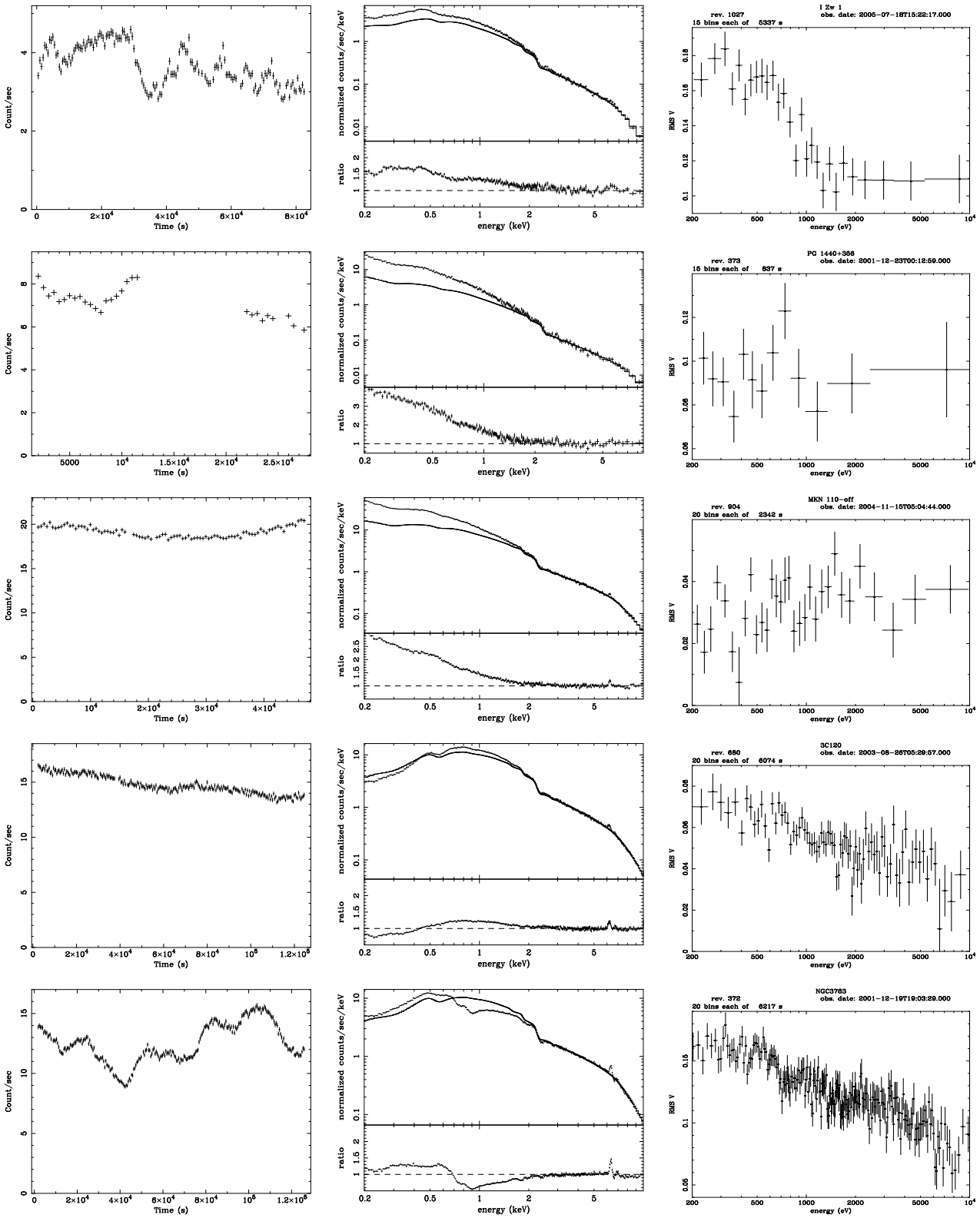
Count/sec
Time (s)
normalized counts/sec/keV
ratio
energy (keV)
I Zw 1
rev. 1027
15 bins each of 5337 s
obs. date: 2005-07-16T15:22:17.000
PG 1440+356
rev. 373
15 bins each of 837 s
obs. date: 2001-12-23T00:12:59.000
MKN 110-off
rev. 904
20 bins each of 2342 s
obs. date: 2004-11-15T05:04:44.000
3C120
rev. 680
20 bins each of 6074 s
obs. date: 2003-08-26T05:29:57.000
NGC3783
rev. 372
20 bins each of 6217 s
obs. date: 2001-12-19T19:03:29.000
RMS V
energy (eV)

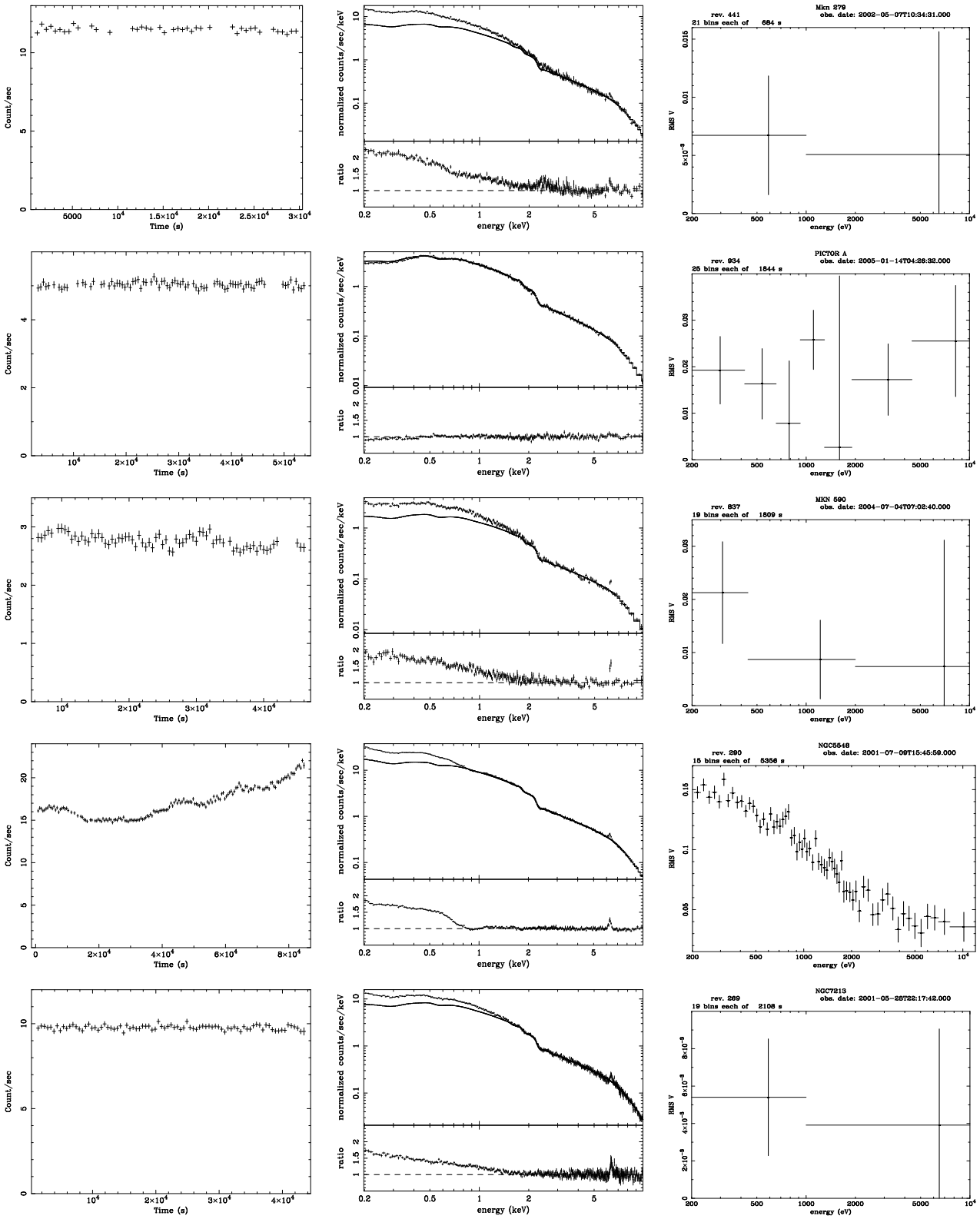
Count/sec
Time (s)
normalized counts/sec/keV
ratio
energy (keV)
Mkn 279
rev. 441
obs. date: 2002-05-07T10:34:31.000
21 bins each of 684 s
PICTOR A
rev. 934
obs. date: 2005-01-14T04:26:32.000
25 bins each of 1844 s
MKN 590
rev. 837
obs. date: 2004-07-04T07:02:40.000
19 bins each of 1809 s
NGC5548
rev. 290
obs. date: 2001-07-09T15:45:59.000
15 bins each of 5356 s
NGC7213
rev. 269
obs. date: 2001-05-28T22:17:42.000
19 bins each of 2108 s
RMS V
energy (eV)

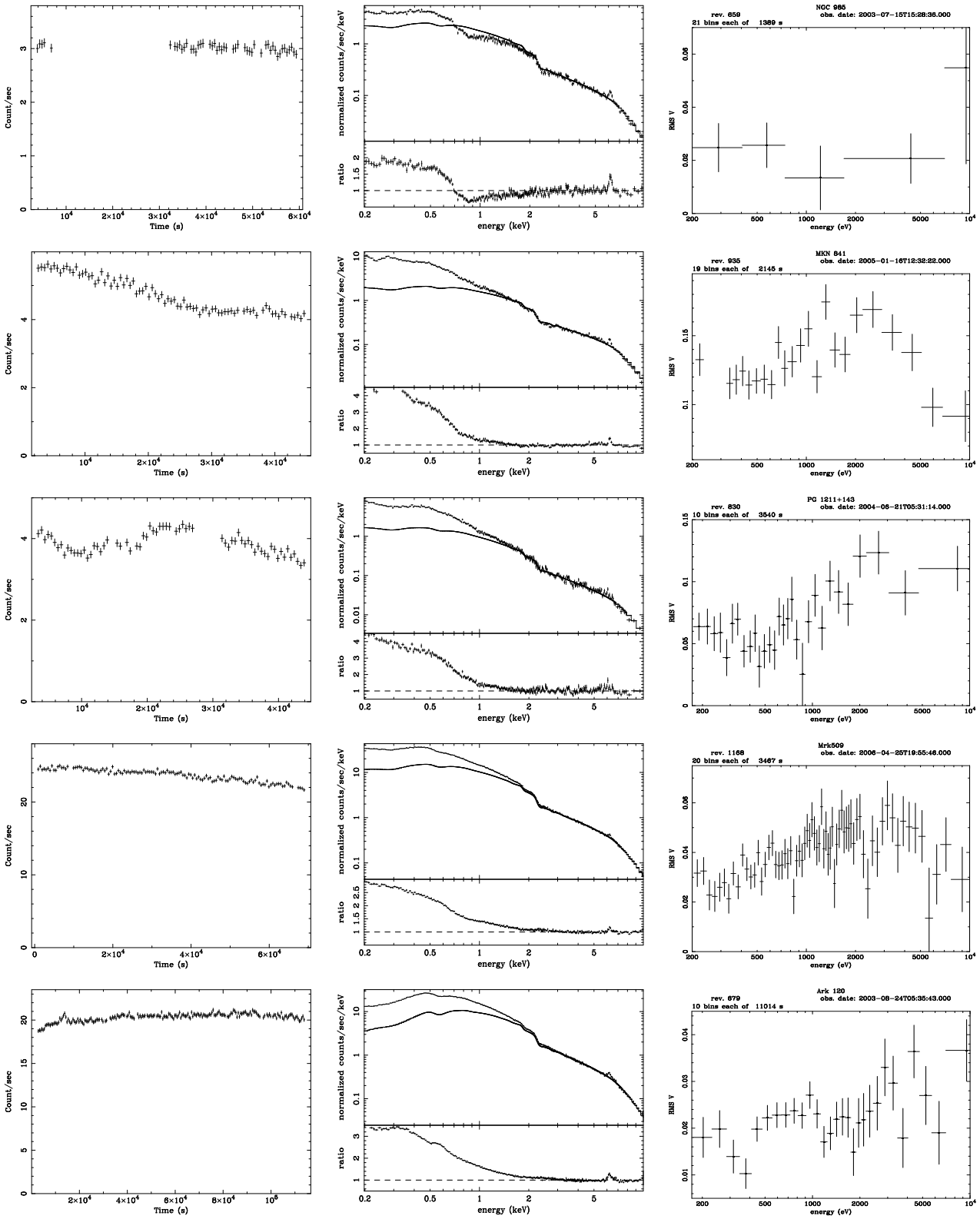
Count/sec
Time (s)
normalized counts/sec/keV
ratio
energy (keV)
NGC 985
rev. 859
obs. date: 2003-07-15T15:28:36.000
21 bins each of 1389 s
MKN 841
rev. 935
obs. date: 2005-01-16T12:32:22.000
19 bins each of 2145 s
PG 1211+143
rev. 830
obs. date: 2004-06-21T05:31:14.000
10 bins each of 3540 s
Mrk509
rev. 1168
obs. date: 2006-04-25T19:55:46.000
20 bins each of 3467 s
Ark 120
rev. 679
obs. date: 2003-08-24T05:35:43.000
10 bins each of 11014 s
RMS V
energy (eV)

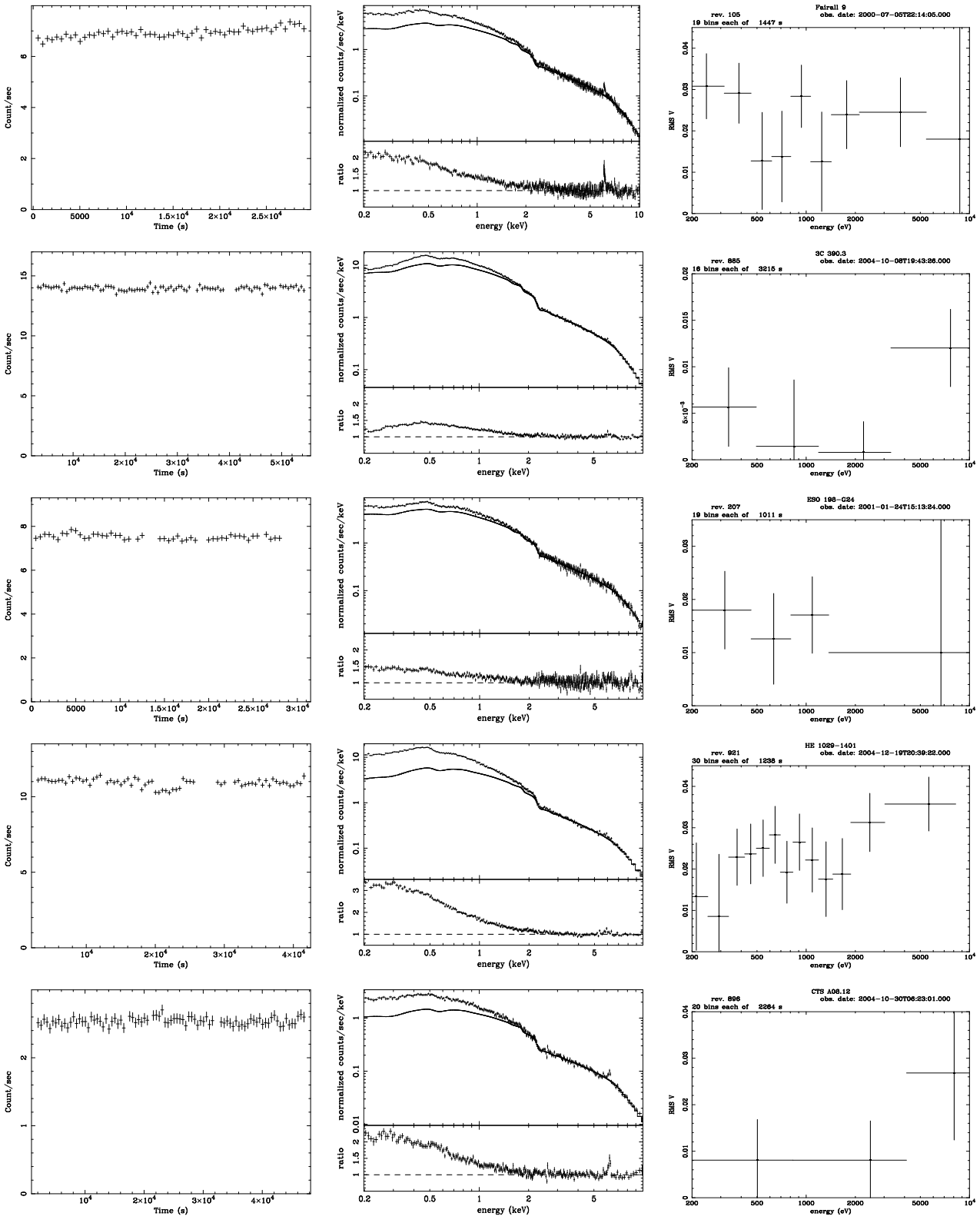
Count/sec
Time (s)
normalized counts/sec/keV
ratio
energy (keV)
RMS V
energy (eV)
Fairall 9
rev. 105
obs. date: 2000-07-05T22:14:05.000
19 bins each of 1447 s
3C 390.3
rev. 885
obs. date: 2004-10-08T19:43:26.000
16 bins each of 3215 s
ESO 198-G24
rev. 207
obs. date: 2001-01-24T15:13:24.000
19 bins each of 1011 s
HE 1029-1401
rev. 921
obs. date: 2004-12-19T20:39:22.000
30 bins each of 1238 s
CTS A08.12
rev. 896
obs. date: 2004-10-30T06:23:01.000
20 bins each of 2264 s

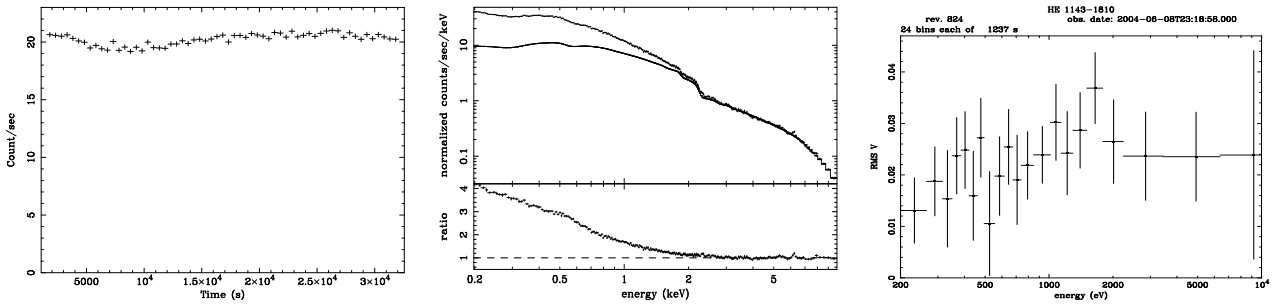
Count/sec
Time (s)
normalized counts/sec/keV
ratio
energy (keV)
HE 1143-1810
rev. 824
obs. date: 2004-06-08T23:18:58.000
24 bins each of 1237 s
RMS V
energy (eV)

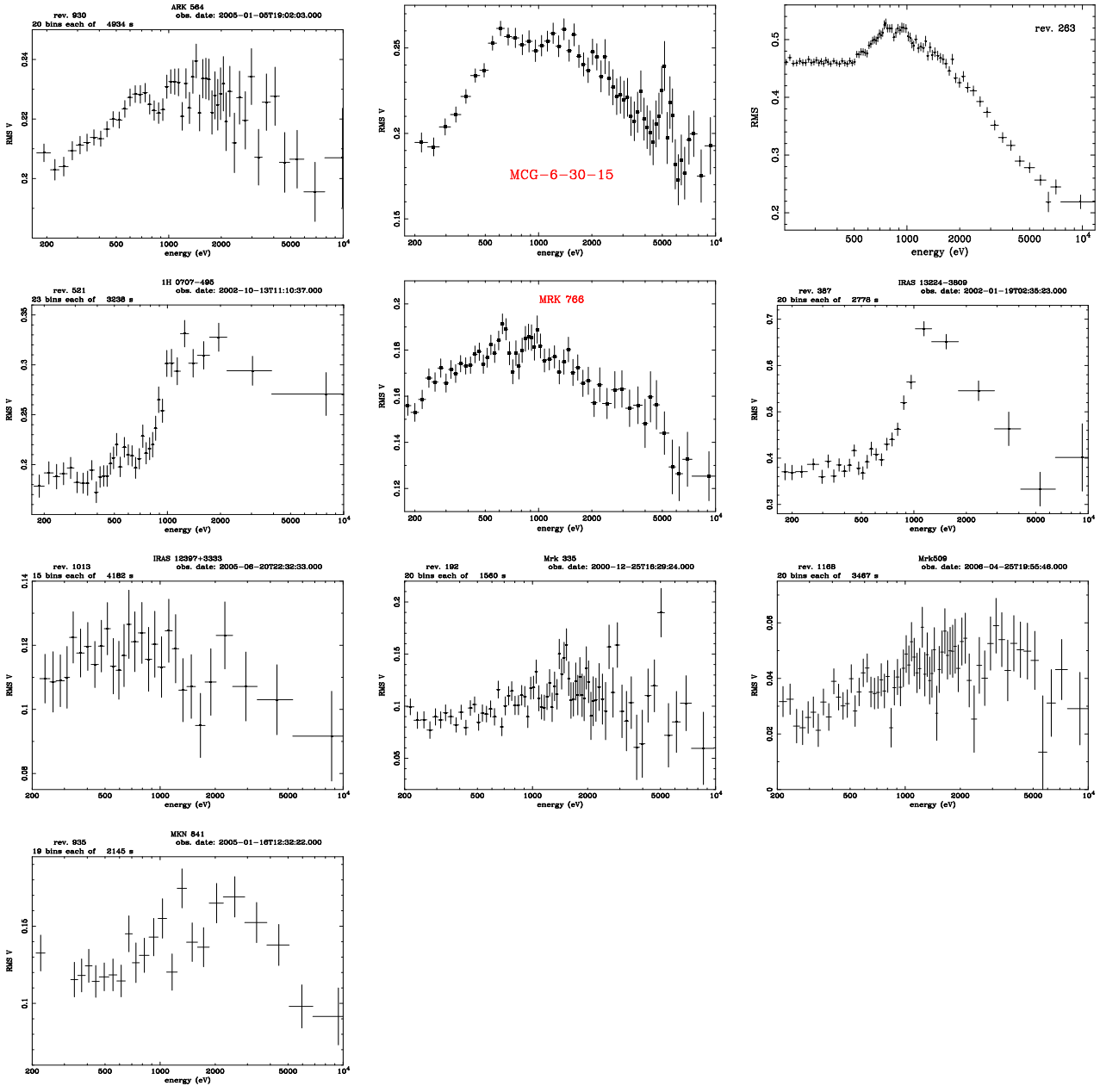

Figure 3.2: RMS spectra of the first group of objects. The broadband RMS shape is dominated by a peak of variability, between a few hundred eV and 1, 2 keV, and lower variability at high and low energy.

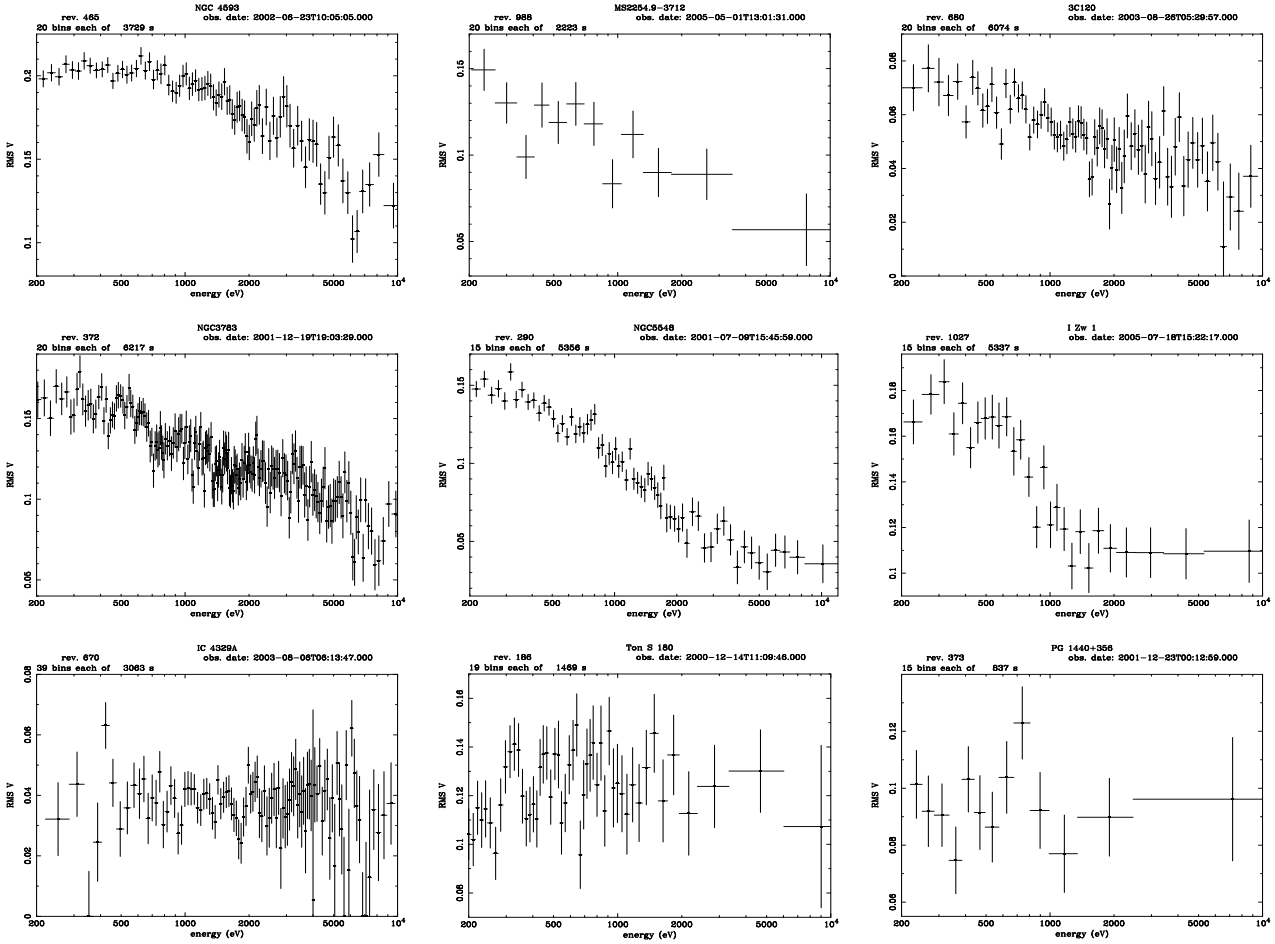

Figure 3.3: RMS spectra of the second class of sources. These objects are characterized by having a constant or monotonically decreasing level of variability with energy.

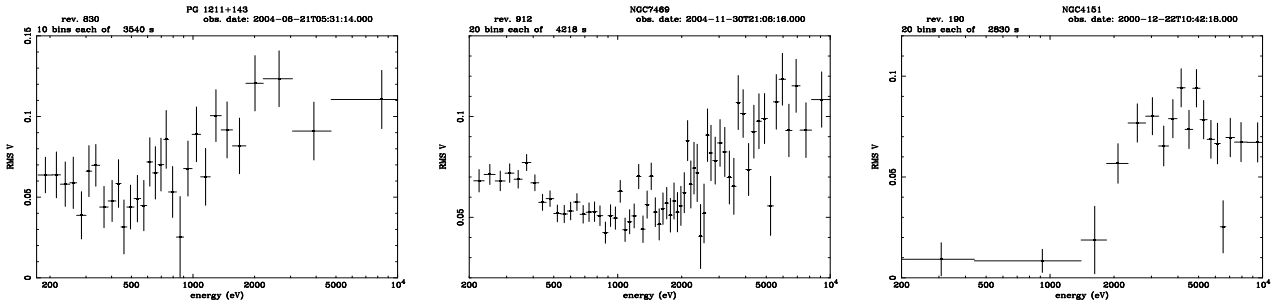

Figure 3.4: RMS spectra of the third group of objects. This category is made by 3 peculiar sources.

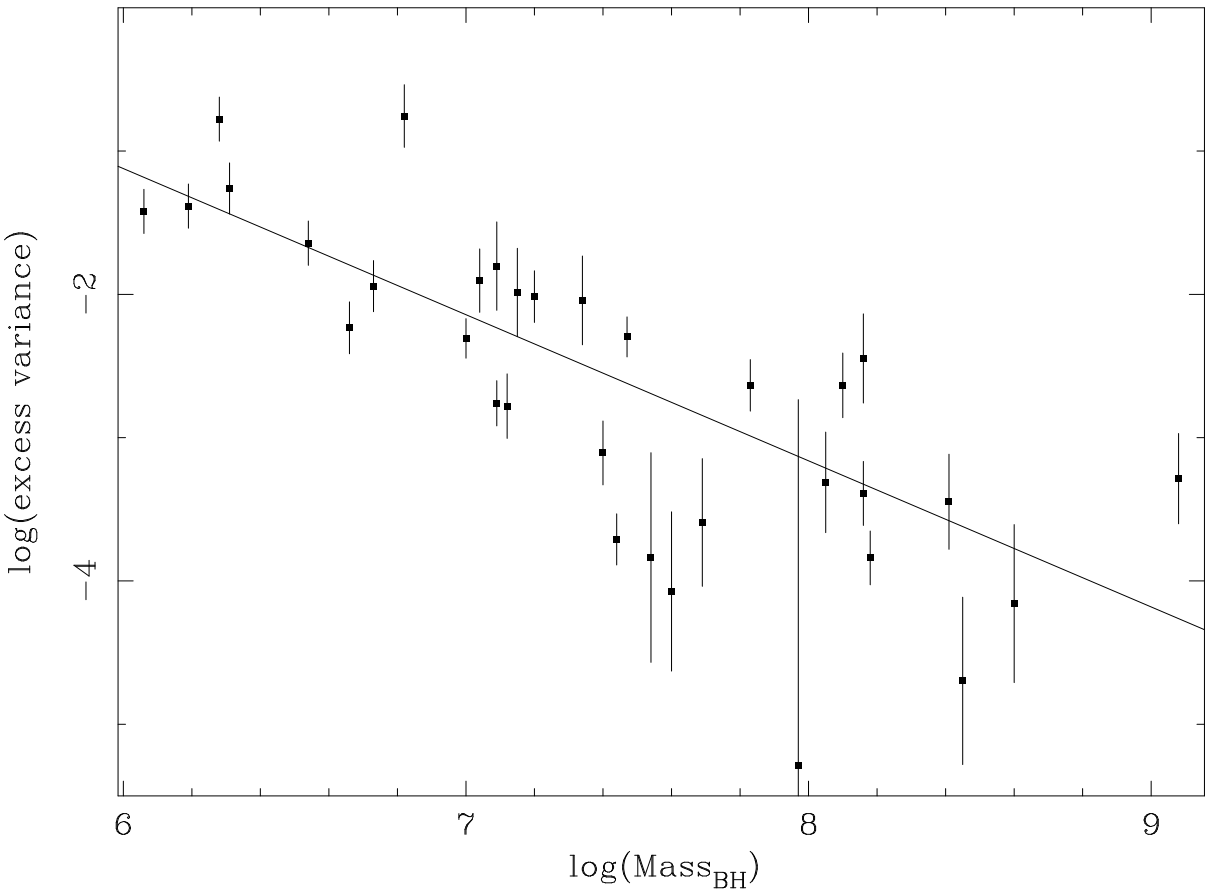

Figure 3.5: Log of the excess variance versus log of black hole mass. The line indicates the best fit linear relationship.

Chapter 4

Key study objects: i) MCG-6-30-15, the best candidate with a broad iron line

4.1 Introduction

MCG-6-30-15 (z=0.00775) is one of the brightest Seyfert 1 galaxies known in X-rays. It has remarkable flux and spectral variability properties, with doubling times as short as ∼1000 s. Its X–ray spectrum shows a broad emission feature stretching from below 4 keV to about 7 keV. This feature is skewed and peaks at about 6.4 keV. As shown first with *ASCA* data by Tanaka et al. (1995) its profile is consistent with that predicted from iron fluorescence from an accretion disc inclined at 30°. The broad Fe K line emitted by MCG-6-30-15 is extending down to a few gravitational radii from the BH and allows to infer the spin of the BH, $a_{MCG}=0.989^{+0.009}_{-0.002}$ (Brenneman & Reynolds 2006). After its discovery, with *ASCA*, the presence of a broad Fe K line in MCG-6-30-15 has been confirmed by all X–ray satellites. *XMM-Newton* observed this source twice, once in June 2000 for ∼100 ks (Wilms et al. 2001), and once in July 2001 for ∼300 ks (Fabian et al. 2002). During the first *Chandra* observation (Lee et al. 2002) the ∼6.4 keV peak of the line varied allowing to put a tight constrain (of less than 20%) on the flux contribution due to distant material. Thanks to the second longer *Chandra* observation (∼500 ks) it has been possible to probe that the 3–7 keV curvature generated by the broad line can not be produced by a standard warm absorber (Young et al. 2005) as it could be possible in other sources. Finally, the *BeppoSAX* data (Guainazzi et al. 1999), later confirmed by *Suzaku* (Miniutti et al. 2007), showed the presence of an important reflection hump between 20 and 40 keV. The amount of reflection required at the reflection hump is in agreement with the one expected according to the strength of the Fe K line and the soft excess.

The puzzling spectral variability

As shown by Reynolds et al. (1999) the reverberation mapping of the Fe K line potentially, could allow us to measure the geometry and physical conditions of the accreting matter close to the BH. For this reason, MCG-6-30-15 has been the subject of many spectral variability studies. The baseline picture predicts that if the observed power law component continuum drives the iron fluorescence, then the line flux should respond to variations in the incident continuum on timescales comparable to the light–crossing, or hydrodynamical time of the inner accretion disc (Fabian et al. 1989; Stella 1990; Matt & Perola 1992; Reynolds et al. 1999). This time scale, for MCG-6-30-15, is of the order of a few hundred seconds, much shorter than the common observation time. Thus, it is expected that the broad Fe K line shall closely follow variations of the X–ray source. Early works on *ASCA* data, in fact, showed that, during a strong flare event during a low flux state, the shape of the broad component of the line varied. In particular, the variations were consistent with what is expected if the line was produced from material close to the X–ray source and the BH (Iwasawa et al. 1999; Vaughan & Edelson 2001).

Nevertheless, during the long (∼300 ks) 2001 *XMM-Newton* observation, although the X–ray flux was highly variable, the broad Fe K line was found to be constant (Fabian et al. 2002; Fabian & Vaughan 2003). This peculiar behavior has been confirmed by many different analysis tools: difference spectra, flux–flux plots, time resolved spectral variability and RMS spectra. Moreover, all the spectral variability can be decomposed in a constant component (that contains the broad Fe K line) plus a steep power law varying in intensity only (Ballantyne et al. 2003; Vaughan & Fabian 2004). Remarkably, the constant component has a spectral shape that can be fitted by an ionized reflection coming from the innermost parts of the accretion disc. In this interpretation, the observed steepening of the 2–10 keV spectrum with flux is not due to a real variation, but it is due to the interplay of the steep power law component and the flatter ionized reflection component (Shih et al. 2002; Vaughan & Fabian 2004).

Instead, during the (∼100 ks) 2000 *XMM-Newton* low flux observation, the flux of the broad Fe K line as well as the flux of the ionized disc reflection were clearly correlated with the flux of the power law component (Reynolds et al 2004). Moreover, the shape of the broad Fe K line is broader and more extreme than during the 2001 observation.

A possible interpretation: the light bending model

It is possible to explain these complex spectral variability behaviors assuming that the X–ray source is located so close to the BH that relativistic effects, due to strong gravity, are important. In fact, when the strong gravity equations (i.e. the light bending effect) are accounted for, in the detailed calculations of the spectral/flux variations observed at infinity, the simple expected correlation between power law and reflection is broken (see §1.3.1; Martocchia et al. 2000; Miniutti et al. 2003; Miniutti & Fabian 2004; Suebsuwong et al. 2006). The simulations show that the main ingredient is the height of the primary source above the accretion disc. In

fact, as shown by Miniutti & Fabian (2004)[1], by varying the height of the primary source it is possible to identify different variability regimes. In particular, when the source is between about 1 and 3–4 r_g above the BH, a correlation between the power law flux and the reflection flux is predicted. When the source is higher, within the range from 4 to 12 r_g, the variations of the reflection flux are confined to the 10 % level, while the power law flux can vary by a factor of 4. Moreover, in consequence to the variations of the height of the primary source there is a variation in the shape of the Fe K line. In particular when the source is low the Fe line becomes more skewed and redshifted. Thus, in this "light bending model", the low flux observation would correspond to states during which the X–ray source is generally extremely low, located between 1 and 3–4 r_g. While the 2001 observation would be dominated by a source with a height generally between 4 and 12 r_g. It is interesting that, although this model is clearly an oversimplification, it may explain the main observed spectral variability properties of MCG-6-30-15.

The evidence for a broad Fe K line component in MCG-6-30-15 is now solid. In fact, different satellites probed the "broad line model" changing the energy resolution and the observational bandwidth. Nevertheless, although these evidences are strong and solid, they rely still on an assumption about the underlying continuum, meaning that they are somewhat model dependent. For this reason a study has been done with the aim to search model–independent evidences of the broad Fe K line, applying model–independent techniques such as RMS spectra and CCFs. The focus will be on the 2000 *XMM-Newton* observation only, because during the 2001 observation the reflection component is constant.

4.2 Analysis of the 2000 *XMM-Newton* observation

Figure 4.1 shows the 0.2-2 keV (upper panel), 2-10 keV (middle panel) light curves and their hardness ratio (lower panel). As already known, the source is highly variable with variations up to a factor of $\sim$4 during the observation time. The light curves show many shots/bursts, with a large prominent flare that occurred just before the end of the observation at $t \sim 9.2\times10^4$ s (see Figure 4.1, upper panel). Hereinafter we will refer to this event as the "Flare".

Figure 4.1 (lower panel) also clearly shows that this flux variability is associated to strong spectral changes, confirming previous findings on Seyfert galaxies that the spectrum becomes softer as the flux increases (e.g., Mushotzky et al. 1993; Lee et al. 2000; Shih et al. 2002).

4.2.1 RMS Spectrum

Figure 4.2 shows the normalized RMS spectrum. It clearly shows three different gross "patterns": a soft, smooth increase of the fractional variability from about 0.2 to 0.6 keV; a "plateau" of maximum variability between $\sim$0.6–2 keV; a gradual decrease of the variability at E $\gtrsim$2 keV (of the form $\propto E^{-0.16}$). Overall, the gross shape and normalization of this RMS spectrum is consistent with that observed one year later during the 2001 observation (Fabian

[1] See Figure 1.5 and 1.6.

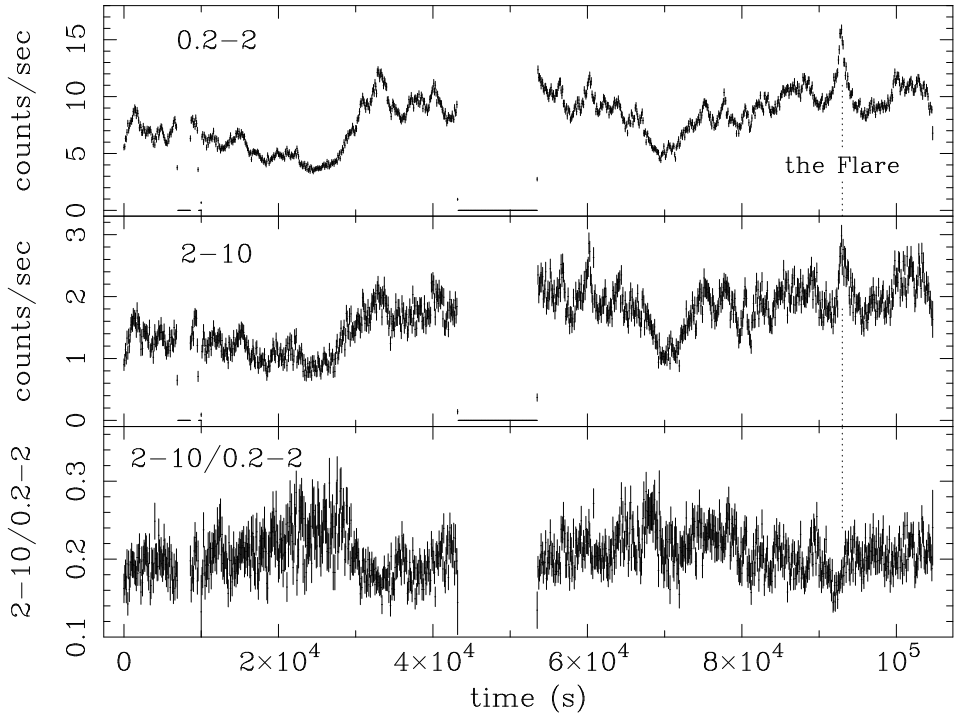

Figure 4.1: (*Upper panel*) Soft (0.2-2 keV) and (*middle panel*) hard (2-10 keV) EPIC pn light curves with 100 s time bins. (*Lower panel*) Hardness ratios ($\frac{2-10keV}{0.2-2keV}$) as a function of time. Note that count rates are not corrected for the "live time" (∼71%) for the pn small window operating mode (Strüder et al. 2001).

et al. 2002). Only, the normalization of the RMS spectrum is slightly less than the one from Fabian et al. (2002).

Most importantly, thanks to the finer sampling achieved at high energies, we detect for the first time some fine structures above 5 keV, i.e. close to the Fe K complex: a steep rise of variability in the ∼4.7-5.8 keV energy band followed by a drop at energies close to 6.4 keV, and a flattening at energies greater than ∼7 keV. To estimate the significance of the variability rise in the 4.7-5.8 keV energy band, we first fitted the 2-10 keV RMS spectrum with a power-law continuum. The fit then improved significantly ($\Delta\chi^2 \sim 15$, i.e. >99% confidence in an F-test) when adding to the model a Gaussian line at 5.3 keV, confirming that this excess is highly significant.

The drop in variability at ∼6.4 keV is consistent with a fraction of the FeKα line being produced in outer (less variable) parts of the accretion disk (see also Fabian et al. 2002; Lee et al. 2002). The variability excess located between 4.7 and 5.8 keV instead implies the presence of an intense, broad spectral component that varies more than the underlying continuum. This excess is most probably due to the broad, redshifted iron line component produced by fluorescence from an accretion disk around either a Schwarzschild or a Kerr black hole. If so, the emitting iron should have a bulk velocity of about 0.3-0.4 c. Another, maybe

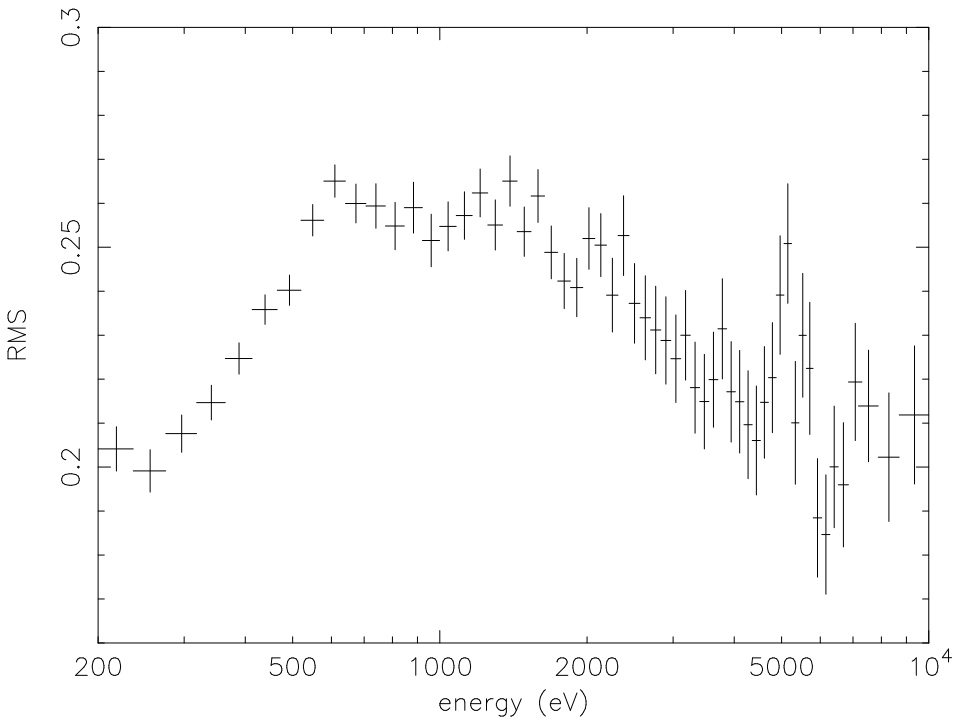

Figure 4.2: RMS spectrum calculated with time bins of 6000 s and with energy bins grouped in order to have >350 counts per bin. Our choice under-samples the detector energy resolution at low energies. Errors are 1σ.

more extreme, possibility could be that the excess of variability is associated to absorption, rather than emission, from almost fully ionized iron falling into the black hole (along our line of sight) at about ∼0.2-0.4 c (see e.g. Nandra et al. 1999, Ruszkowski & Fabian 2000, Longinotti et al. 2003; Dadina et al. 2005; for a review Cappi et al. 2006). Whatever its precise origin is, the excess of fractional variability detected here between ∼4.7 and 5.8 keV represents strong (because model-independent) evidence for the presence of relativistically moving matter (because redshifted) close to the black hole.

This excess of variability at the energy of the broad component of the Fe K line appears only in the RMS spectrum of this low flux observation. This is expected because, as observed by Fabian et al. (2002) and Vaughan & Fabian (2004) the reflection is almost constant during the 2001 observation. Moreover a variable Fe K line, during the low flux observation, is in qualitative agreement with the light bending model that predicts variability of the reflection component during the low flux periods. Nevertheless the light bending model predicts a correlation with similar amplitude of variations between the flux of the direct and the reflected components, while the excess in Fig. 4.2 indicates the presence of a component with a higher degree of variability than the continuum.

In the soft band, the sharp drop of variability at E $\lesssim$0.6 keV is likely due to the rise of a sharp soft-excess component clearly seen in the source-average spectrum (e.g. Fabian et al. 2002; Pounds & Reeves 2002). This feature, best fitted by a black-body component of average

temperature kT ∼100 eV, is consistent with either intrinsic or reprocessed thermal emission from the less variable optically thick accretion disk (see §2.4). In the hard band (E>2 keV), the drop of variability could be due to different interplaying phenomena. Phenomenologically, it could be explained as a single power-law spectrum that varies with a pivot point at E $\gtrsim$10 keV, as the analysis of the hardness ratio indicates (the spectral index softens as the flux increases). Physically, such behavior is consistent with what is expected if the coronal optical depth varies while the dissipated luminosity remains constant, and it is just what is expected for disk corona models as long as the spectral index $\Gamma_{[2-10]keV}$ is $\lesssim$2 (Haardt et al. 1997). Alternatively, in the framework of reprocessed emission models, the low energy and high energy drops of variability could be due to the almost constant contribution of the ionized disc reflection, as in the 2001 observation. In this case, the variability of the reflection would however need to be complex. In fact it should be higher than the variability of the continuum at the energy of the red wing of the Fe K line and lower elsewhere. Another contribution to the variability in this band could come from the warm absorber that has been observed to vary on timescales as low as 10^4 s (Otani et al. 1996), and could therefore produce an observable effect in the RMS spectrum.

4.2.2 Study of the Time Lags

To search for time lags, we used the cross correlation function (CCF; White & Peterson 1994) that we calculated using the *crosscor* package in FTOOLS v5.2 (this command implements the DCF, e.g. Edelson & Krolik 1988, in the "correl" routine of the "Numerical Recipes", Press et al. 1992).

The energy intervals for the CCF were chosen corresponding the RMS variability pattern. Light curves were, thus, extracted for the following energy bands: E_1 (0.2-0.6 keV), E_2 (0.6-2.2 keV), E_3 (2.2-2.6 keV), E_4 (2.6-4.5 keV), E_5 (4.5-6.8 keV), and E_6 (6.8-10 keV).

Due to the presence of an instrumental switch-off in the middle of the observation (see Fig. 4.1), the CCF study has been performed separately, before and after it. Moreover, we calculated the CCFs with and without the Flare period. E_2 was used as the energy band of reference for all CCFs because the light curve in this band had the highest statistics.

Figure 4.3 shows, as an example, the CCFs obtained during the 33 ks after the switch-off (which does not include the Flare period). The CCF peaks are fairly wide and show no significant time lag between the different energy bands, with an upper limit of about 200 s. The CCF appear also to be somewhat asymmetric, with a marginal excess of correlation moving from negative to positive time lags as the energy bands go from soft to hard (i.e. from top to bottom in Fig. 4.3). There is also an indication for a possible secondary peak in the hardest band corresponding to a time delay of ∼1.5-2 ks. Similar results have been found, extended to higher energies, by the analysis of the simultaneous XMM-Newton and RXTE data (J. Wilms, private communication). However, in our data the skewness parameter does not give any significant deviation from a symmetric profile. Better statistics are thus needed for any firmer conclusion on this point. CCF analysis of only the first part of the observation give the same inconclusive results.

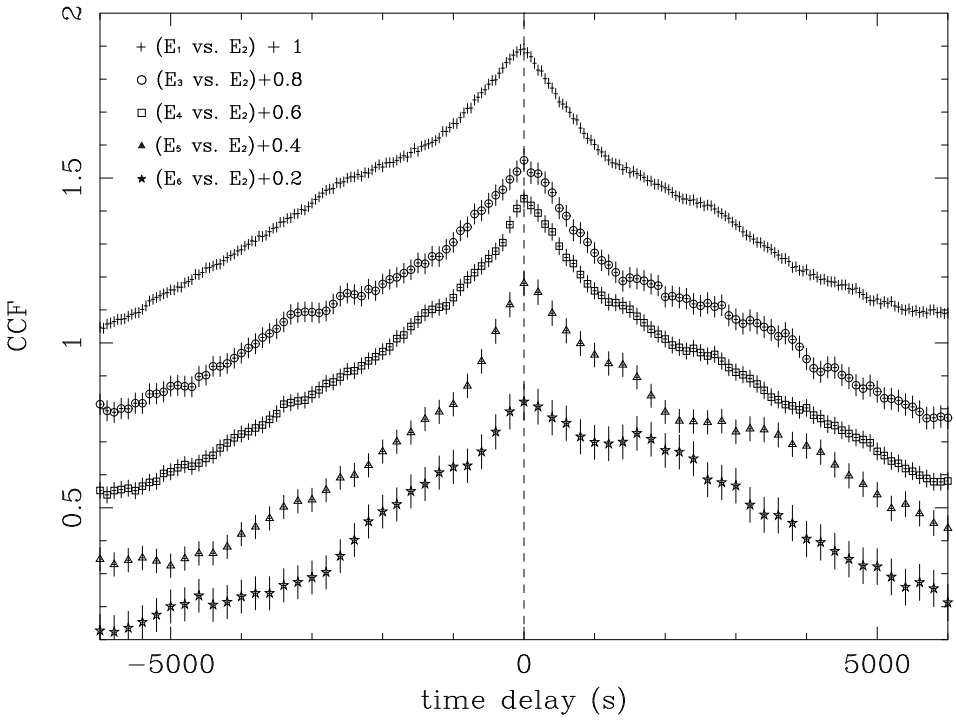

Figure 4.3: Rescaled CCFs calculated in different energy bands (E_1:0.2-0.6 keV, E_2:0.6-2.2 keV, E_3: 2.2-2.6 keV, E_4:2.6-4.5 keV, E_5:4.5-6.8 keV and E_6:6.8-10 keV) during the 33 ks following the instrumental switch-off. Values of CCFs have been increased by 1, 0.8, 0.6, 0.4 and 0.2 going from soft to hard (top to down) for clarity purposes.

4.3 Analysis of the Flare period

The present observation is characterized by the presence of a bright flare, an enlargement of which is shown in Fig. 4.4. In studying this event one hopes to isolate the physical mechanism(s) responsible for the variability in order to constrain emission models and, possibly, generalize these findings to other observation periods when the flares are more elusive and complex.

4.3.1 Spectral variability during the Flare

The light curve hardness ratios shown in Fig. 4.1 clearly demonstrate that MCG-6-30-15 exhibits spectral variations during the Flare. To quantify this effect, we first produced a set of ratios (commonly called "PHA ratios") between spectra acquired in 8 subsequent time intervals of 300 s during the Flare (see Figures 4.4 and 4.5) and the spectrum accumulated during the whole observation. Figure 4.5 shows the results of such an analysis. Before the Flare (panel A), the source shows a spectrum, which is close to the average one. At the beginning of the Flare, the source shows an increase of the soft counts (panel B, C and D) followed by a delayed response at higher energies (panel E and F). Finally, the source gradually

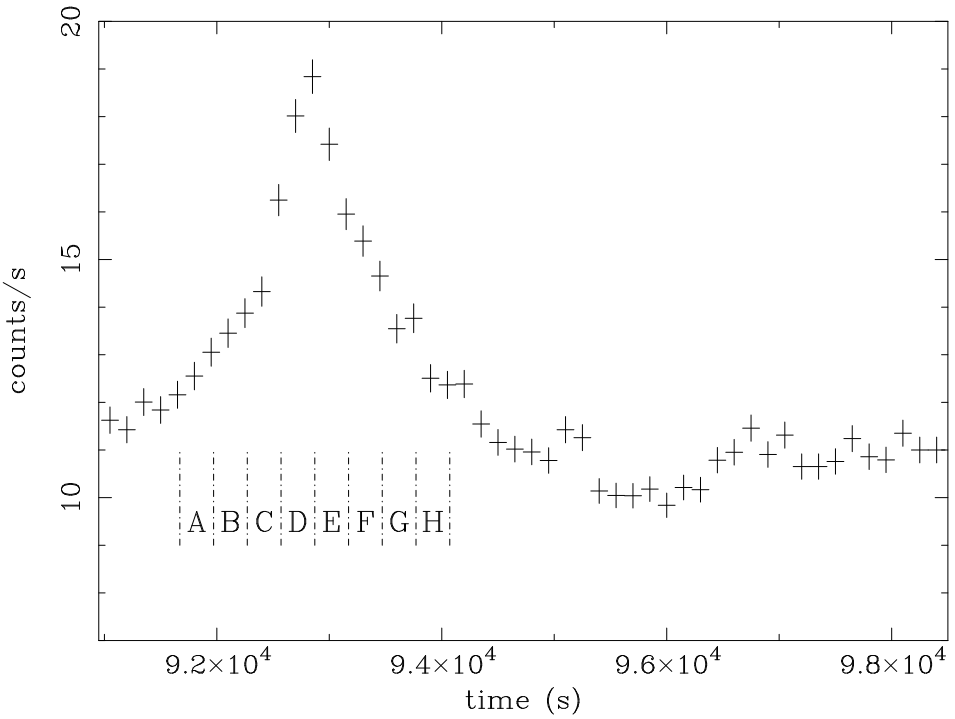

Figure 4.4: Enlargement of the Flare period (see also Fig. 4.1). The light curve is computed between 0.2-10 keV with time bins of 150 s. Periods during the Flare where PHA ratios have been calculated (see Sect. 4.1 and Fig. 4.5) are labeled from A to H, and are 300 s long.

returns to its initial spectral state (panel G and H). Overall, this result suggests the presence of a soft-to-hard time lag.

To quantify this effect in more details, we performed a CCF analysis limited to the Flare period using the same energy bands as defined in Sect. 4.2.2. As shown in Fig. 4.6 (left panel), we find that the harder light curves systematically lag the softer one by $\sim$ 80 s, 260 s, 310 s, 340 s, and 480 s, respectively. This soft-to-hard lag is even clearer from Fig. 4.6 (right panel) where the peak time lag is reported as a function of energy[2]. The time lag clearly increases with energy ($\tau_{\rm lag} \sim 0.071 \times E$; where E is in eV and the time lag is in s).

This result is consistent with the time lag ($\sim$ 200 s) that was found during the 2001 long ($\sim$300 ks) $XMM-Newton$ observation by Vaughan et al. (2003). In that case, however, the time lag was found only on timescales longer than $\sim 10^4$ s. This was interpreted as evidence for a drop of coherence on shorter timescales. The fact that we detect it only for a single Flare event (during which the source is likely to be dominated by a single active region, thus with maximum coherence), while we have a null result on the whole observation (Sect. 4.2.2)

[2]To calculate the errors associated to the time lag, we followed two different methods: CCF peaks were first "χ^2"-fitted with a Gaussian function and the errors were then estimated by assuming i) a $\Delta\chi^2 = 4$, and ii) $\frac{\sigma}{\sqrt{N}}$, where σ is the FWHM of the Gaussian and N is the number of time bins considered in the fit. Most conservative values obtained following either method were used and reported in Fig. 4.6.

confirms and strengthens this hypothesis.

Nevertheless, the nature of the physical mechanism producing this lag is still debated (Arévalo & Uttley 2006; Dasgupta & Rao 2006). In the framework of a hot corona model scenario, and assuming that the lag observed during the Flare is due to Comptonization, it is possible to estimate the density and dimensions of the active region producing the flare.

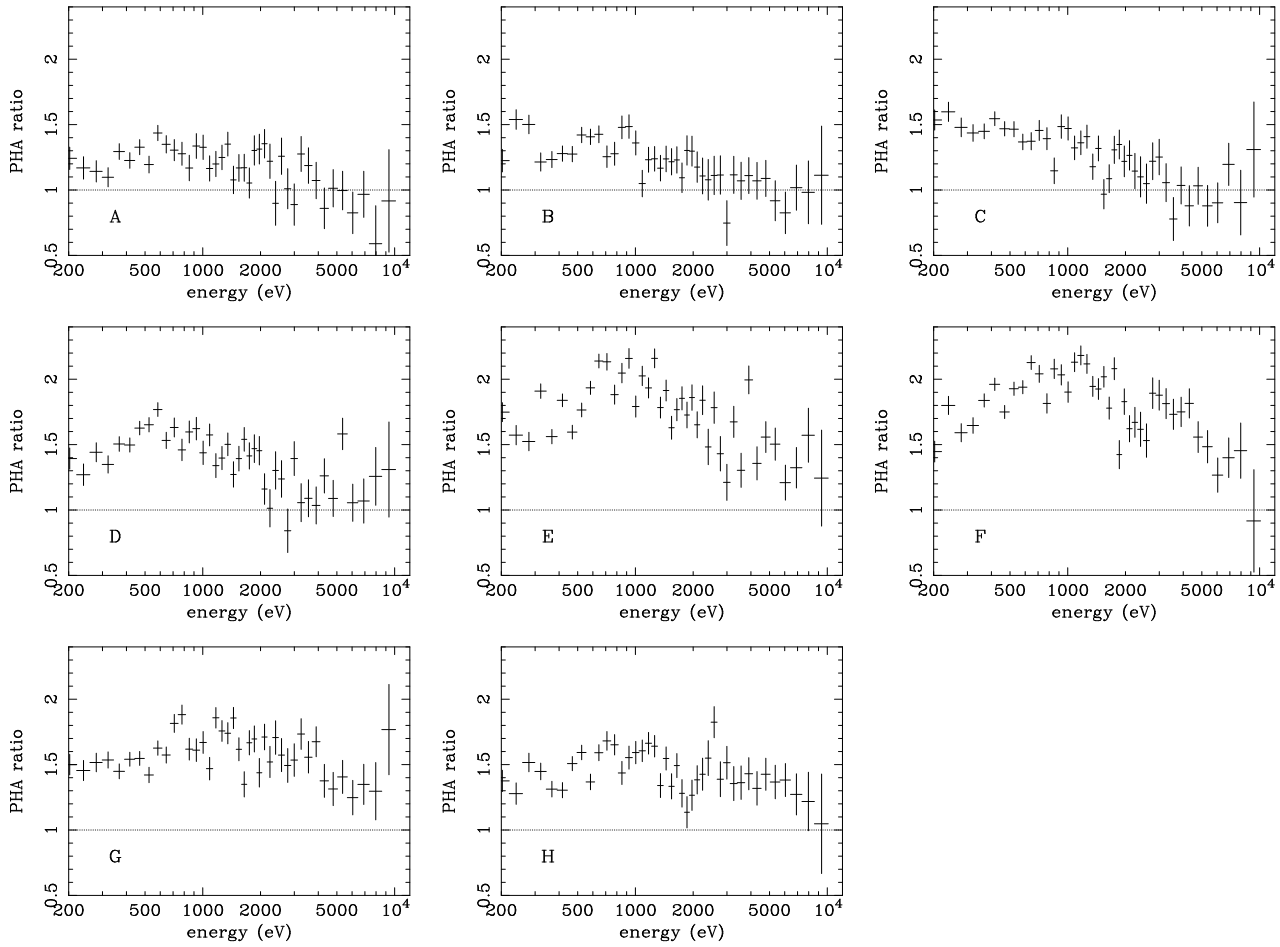

Figure 4.5: MCG-6-30-15 spectral variations during the Flare. PHA ratios are calculated by dividing spectra acquired in subsequent time intervals of 300 s (about 4500 counts, see Fig. 4.4) and the average spectrum of the entire observation. This figure illustrates the gradual softening, followed by a hardening and subsequent decrease of the spectrum during the Flare.

Thus, assuming that the electron temperature in the emission region, best constrained by the high-energy BeppoSAX data (Guainazzi et al. 1999; Fabian et al. 2002), is in the range of ∼100-300 keV, and seed soft photons emerging from the disk will need about 5-10 inter-

actions[3] ($N_{\rm int}$) to be up-scattered from ∼200 eV to 10 keV. Thus, the mean free path of 10 keV photons (λ_{10}) is linked to the Comptonization timescale ($t_{\rm Compt}$) through the equation: $\lambda_{10} = t_{\rm Compt} \times c = \frac{\tau_{\rm lag} \times c}{N_{\rm int}} \sim 2 - 4 \times 10^{12}$ cm, where $\tau_{\rm lag}$ is the time lag (∼600 s) between the 0.2 and 10 keV emission and c is the speed of light. Assuming a random walk motion and $N_{\rm int}$=10, this implies a displacement from their original production region of $\sim \sqrt{N_{\rm int}}\ \lambda_{10} \sim 6 \times 10^{12}$ cm. Therefore it is reasonable to assume that, when the bulk of 10 keV photons are produced, the Flare dimensions ($R_{\rm Flare}$) should be of the order of $\sim 6 \times 10^{12}$ cm. For values of the Thomson optical depth (τ) ranging between $\tau \sim 0.1 - 1$, a typical range for Seyfert galaxies including MCG-6-30-15 (e.g. Petrucci & Dadina 2004), this yields also a rough estimate of the Flare region electron density (ρ_{e^-}): $\rho_{e^-} = \frac{\tau}{\sigma_{\rm T} R_{\rm Flare}} \sim 2.5 - 25 \times 10^{10}$ cm^{-3}, where σ_T is the Thomson cross-section.

The dimensions of the Flare region ($R_{\rm Flare} \sim 6 \times 10^{12}$ cm) estimated above correspond to $\sim$ 40 gravitational radii ($r_{\rm g}$) assuming the mass of the black hole in MCG-6-30-15 to be $M_{\rm BH} \sim 10^6 M_{\odot}$ (e.g. Vaughan et al. 2003). This value is consistent with the limit implied by causality arguments for the factor 2 variation in ∼1000 s during the Flare (Fig. 4), which gives $R_{\rm Flare} \lesssim c \times t \simeq 3 \times 10^{13}$ cm $\simeq 200\ r_{\rm g}$.

It is important to remind that the obtained size of the flare would wash out the effects of strong gravity. Thus, in the light bending model interpretation either the physical mechanism producing the flare is not Comptonization or this flare demonstrates that during the life of the source some peculiar variability events occur.

4.3.2 Fe K reverberation in response to the Flare?

To study the Fe K line variations during the Flare period in a model-independent way, we extracted the source spectrum in three time intervals (1000 s long) before, during and after the Flare (we will refer to these time intervals as the PreFlare, Flare and PostFlare periods) and computed PHA ratios (see Fig. 4.5). The PHA ratios between the PostFlare/PreFlare periods highlights a strong line increase that took place during the PostFlare period. During the Flare, only a softening of the continuum is visible. To further investigate the variations, we performed a spectral analysis on a set of eight subsequent time intervals of ∼1000 s each around the Flare. We fitted these data using a simple power-law model (Γ ∼1.75-1.95) plus a Gaussian line at $\sim$ 6.4 keV. Figure 4.7 (Right Panel) clearly shows that only upper-limits on the EW (of ∼100-200 eV) were obtained for the FeK line before and during the Flare. On the other hand, the line recorded after the Flare (periods 5, 6 and 7 in Fig. 4.7) was remarkably strong (EW∼89±95, 680±200 eV and 280±150 eV) and broad (σ ∼0.39±0.20 and 0.19±0.12 keV, respectively). It should be noted that a similar effect was found for the absolute flux of the Fe K line, with $A_{\rm FeK} < 6.5 \times 10^{-5}$; $= 1.8^{+1}_{-0.3} \times 10^{-4}$; $< 1.6 \times 10^{-5}$ photons cm^{-2} s^{-2} at periods 5, 6 and 7 in Fig. 4.7 (right), respectively. More complex models for the line (e.g. a

[3]We estimated the number of interactions that a photon undergoes to be up-scattered from ∼200 eV to 10 keV by iterating the equation $h\nu'' \simeq \gamma_e^2 h\nu$ that links the average photon energy before ($h\nu$) and after ($h\nu''$) an inverse-Compton scattering event. In this equation, γ_e is the electron Lorentz factor given by the equation: $E_e = m_e c^2(\gamma_e - 1)$, and we assumed that the electron energy (E_e) is equal to the high-energy cut-off of the X-ray spectrum.

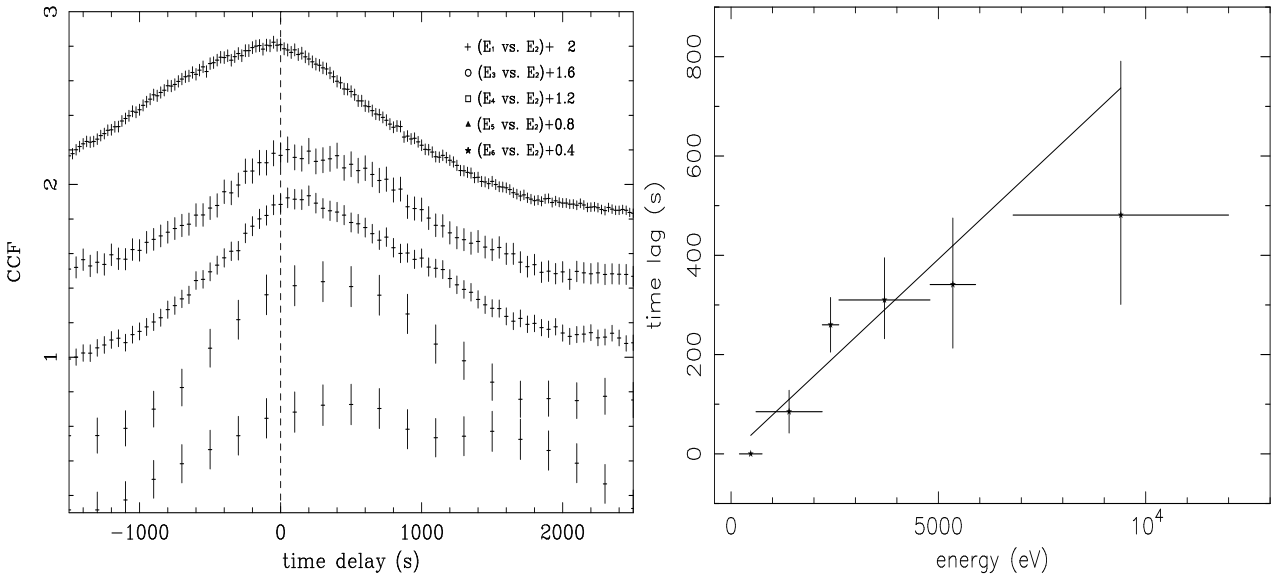

Figure 4.6: (*Left panel*) CCFs between light curves extracted during the Flare. Energy bands are as in Fig. 4.3, and values have been increased by 2, 1.6, 1.2, 0.8 and 0.4 going from soft/top to hard/bottom for clarity purposes. The dashed vertical line indicates a zero lag value. For each energy band, the differences between the peaks of CCF distributions and the dashed vertical line indicate the time lags. (*Right panel*) Time lag (in s) vs. energy (in eV) is shown. Peak time lag values and associated (68% confidence) errors have been estimated through a χ^2-fitting method (see footnote n. 1).

DISKLINE model; Fabian et al 1989) have not been applied given the low signal-to-noise ratio of these 1000 s spectra.

It is interesting to note that the spectral changes, detected here, are qualitatively similar to those found by ASCA in 1994 during another remarkably bright flare (Negoro et al. 1999; Negoro et al. 2000).

Assuming that the line is produced in the accretion disk and in response to the Flare, it is possible to estimate the distance between the Flare emission region and the disk. To perform this accurately, one should know when precisely the intensity of the line started to increase, the transfer function of the disk and the physical condition of the Flare region. These are all unknowns but, if ever significant, they would introduce delays. Thus the estimate given below shall be considered only as an upper limit.

Since the hard radiation ionizing the iron on the disk surface lags the Flare peak by about ∼600 s (§4.3.1 and Fig. 4.6) and since the line responded ∼3000 s after the flare peak, the upper limit on the distance between the Flare region and the disk ($\Delta l_{\rm F-d}$) is given by: $\Delta l_{\rm F-d} \lesssim \frac{3000-600}{2} \times c = 4 \times 10^{13}$cm $\sim 240\ r_{\rm g}$, also consistent with the marginal presence of a second peak in the CCFs at higher energies discussed in §4.2.2, Fig. 4.3. Also this estimation of the height of the flare suggests the peculiarity of this event, in fact most of the energy release should occur in a region much closer to the BH.

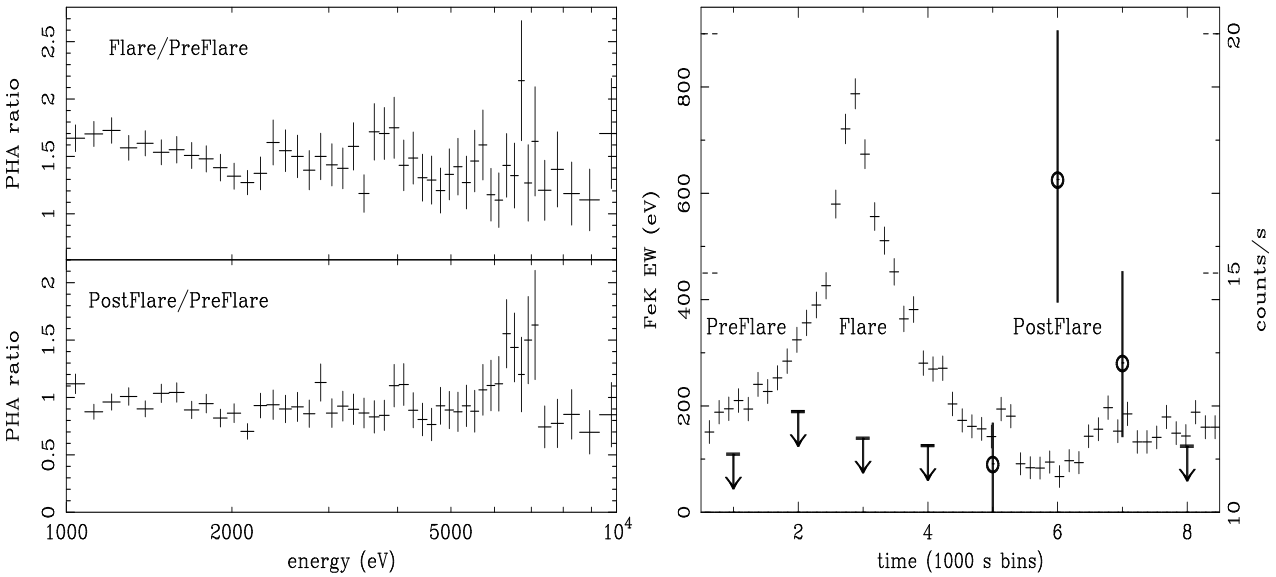

Figure 4.7: (*Left panel*) Flare/PreFlare and PostFlare/PreFlare PHA ratios. (*Right panel*) FeKα line equivalent width (in eV, left y axis) calculated in 1000 s spectra, over-plotted on light curve (right y axis) from Fig. 4.4. The errors are at 90% confidence level.

4.4 Discussion and summary

The model-independent timing analysis of a ∼95 ks long $XMM-Newton$ observation of MCG-6-30-15 presented in this work has shown that:

The fractional variability around the FeK line energy is "resolved" with unprecedented detail into two different components: a narrow component of lower variability at E ∼6.4 keV consistent with being produced by the outer parts of the accretion disk and a broad component in the 4.7-5.8 keV energy band, significantly more variable than the continuum itself (Ballantyne et al. 2003; 2005). Whether this second component is due to emission or absorption is unclear, but it is likely associated to a highly variable and redshifted iron line that probes the inner regions of the accretion disk.

The reduced variability of the source continuum at soft (E $\lesssim$600 eV) energies is consistent with the gradual onset of a soft thermal emission from the outer parts of the accretion disk and the reduced variability at higher (E $\gtrsim$2 keV) energies is possibly due to a power law having a pivot point at E $\gtrsim$10 keV. Anyway the presence of the relativistic disc line indicates the presence in the spectrum of a strong ionized reflection component. Thus, most probably, both the high and low energy drops are due to the gradually increasing contribution from a less variable reflection component. However, in this interpretation the variability of the reflected component would need to be complex since it should still have to explain the higher level of variability of the broad redshifted Fe K line component.

The relative lack of variability across the energy of the Fe K line and partly also the variability excess in its red wing could be reproduced in a multi-flare simulation (Goosmann et al. 2006). The model assumes that the X-ray variability is caused by many, short-living

flares being randomly distributed across the accretion disk. The RMS spectrum of MCG-6-30-15 is reproduced assuming a fast-spinning black hole and a dominant production of the X-rays very close to the last stable orbit. These findings are in agreement with previous results for this source.

During a remarkably strong Flare, a significant soft-to-hard time lag of ∼600 s is detected. Under the assumption that the delay is due to Comptonization up-scattering of low energy photons, it is possible to infer estimates of the electron density and dimensions of the Flare region: $\rho_{e^-} \simeq 2.5 - 25 \times 10^{10}$ cm^{-3} and $R_{\rm Flare} \sim 6 \times 10^{12}$cm $\sim 40\ r_{\rm g}$, respectively. Moreover, PHA ratios of spectra taken during and after the Flare show clear evidence that the Fe K line intensity has varied very significantly, and may have done so in response to the Flare with a ∼1500-3000 s lag. In the simplest scenario, in which the Flare is produced in the corona and the Fe K line is reflected from the disk, the observed lag allows us to estimate the disk-corona distance as $\lesssim 4 \times 10^{13}$ cm $\sim 240\ r_{\rm g}$. With such large values for the distance from the Flare region to the disc and/or its geometrical dimensions, general relativistic effects such as those that have been involved to explain the time resolved spectral variability, would be negligible. Thus, either the physical mechanism producing the flare is not Comptonization and the mirror of the Fe K line after the flare is not the accretion disc, or this flare must have been a peculiar variability event that occurred in this source.

Another possibility to explain the delay-energy relation during the Flare can be found in the geometry and in the different spectral shape of primary and reprocessed emission. One assumes that the primary source is compact and elevated above the disc. It then produces a hot spot on the disc surface that re-emits the reflected spectrum. The light travel time between the source and the disc induces an intrinsic delay between the variations of the primary and the corresponding variations of the spot re-emission. As a result, the combined (primary plus reflection) spectrum pivots during the Flare period. Goosmann et al. 2007 investigate if such a pivoting can explain the time delays shown in Fig. 4.6 (Right Panel). It follows that the delays cannot be reproduced by the model if the reprocessing medium is highly-ionised. A solution only exists if one assumes that the Flare occurs in the vicinity of a magnetically confined, cold and clumpy reprocessing medium. This assumption differs from interpretations, which explain the X-ray spectrum of MCG-6-30-15 mostly with the help of ionised reflection. Hence, again the time delays suggest that the Flare is a rather peculiar event.

Chapter 5

Key study objects: ii) NGC 4051, the prototypical Narrow Line Seyfert 1 galaxy

5.1 Introduction

NGC 4051 is a nearby (z=0.0023) low–luminosity Narrow–Line Seyfert 1 (NLS1) galaxy which exhibits extreme X–ray variability in flux and spectral shape on both long and short timescales. The source sometimes enters relatively long and unusual low flux states in which the hard spectrum becomes very flat ($\Gamma \sim 1$) while the soft band is dominated by a much steeper component ($\Gamma \sim 3$, or black body with $kT \sim 0.12$ keV). Most remarkable is the 1998 *BeppoSAX* observation reported by Guainazzi et al (1998) in which the source reached its minimum historical flux state, the spectral slope was $\Gamma \simeq 0.8$, and the overall spectrum was best explained by assuming that the nuclear emission had switched off leaving only a reflection component from distant material (clearly visible in the hard spectrum) which still responded to a previous higher flux level. A different interpretation assumes that the nuclear emission in low flux states originates so close to the central black hole that only a tiny fraction can escape the gravitational pull of the hole so that the nuclear continuum is virtually undetectable at infinity (e.g. Miniutti & Fabian 2004).

In general, the 2–10 keV spectral slope appears to be well correlated with flux. However, the correlation is not linear with the slope hardening rapidly at low fluxes and reaching an asymptotic value at high fluxes (see e.g. Lamer et al 2003, based on *RXTE* monitoring data over about three years). This behavior is relatively common in other sources as well, such as MCG–6-30-15, 1H 0419–577, NGC 3516 (among many others) and might be due to flux–correlated variations of the power law slope produced in a corona above an accretion disc as originally proposed by Haardt & Maraschi (1991; 1993) and Haardt et al. (1993) and related to changes in the input soft seed photons (e.g. Maraschi & Haardt 1997, Haardt, Maraschi & Ghisellini 1997, Poutanen & Fabian 1999, Zdziarski et al 2003). On the other hand, such slope–flux behavior can be explained in terms of a two–component model (McHardy et al 1998; Shih, Iwasawa & Fabian 2002) in which a constant slope power law varies in normalization

only, while a harder component remains approximately constant hardening the spectral slope at low flux levels only, when it becomes prominent in the hard band, as observed in MCG-6-30-15 (e.g. Fabian & Vaughan 2003; Vaughan & Fabian 2004).

It should be stressed that, in the framework of the two–component model, the 2–10 keV slope–flux correlation in NGC 4051 cannot entirely be explained by the contribution of a distant reflector in the hard band (the presence of which is required by the detection of a narrow component to the iron line). Indeed, as shown by Lamer et al (2003) the correlation is still present even if the distant reflector contribution is taken into account. Even at low flux levels, soft and hard components are significantly variable and well correlated, which excludes any dominant extended emission (torus and/or extended scattering region). Extended emission is undetected by *Chandra* on $\sim$ 100 pc scales (Collinge et al 2001; Uttley et al 2003). Therefore, the residual slope–flux correlation can be due to intrinsic pivoting or to an additional, almost constant, spectral component (i.e. ionized reflection from the disc, as for MCG–6-30-15).

Other important clues on the nature of the spectral variability in NGC 4051 (and other sources as well) come from the so–called flux–flux plot analysis, first presented by Churazov, Gilfanov & Revnivtsev (2001) to demonstrate the stability of the disc emission in the high/soft state of Cyg–X1. Taylor, Uttley & McHardy (2003) have applied the same technique to a few Seyfert galaxies by using *RXTE* data. In the case of NGC 4051, Uttley et al (2004) have performed such an analysis by using the same *XMM–Newton* data we are presenting here and showed that the distribution of high, intermediate, and low flux state data points are smoothly joined together, indicating that the same process causing the spectral variability in high and intermediate flux states continues to operate even at the very low flux levels probed by the *XMM–Newton* data (Uttley et al 2004). This evidence seems to challenge the interpretation of the spectral variability as due to variable absorption by a substantial column of photoionized gas (Pounds et al. 2004).

Analyzing the two *XMM–Newton* observations of NGC 4051 Uttley et al (2004) and Pounds et al (2004) reached different conclusions on the nature of the spectral variability in NGC 4051 and on the main spectral components that come into play. We studied the same *XMM-Newton* data but our analysis is complementary to previous studies and offers a novel point of view because it considers also the relativistic disc reflection interpretation.

5.2 Spectral variability: a quick look

The *XMM–Newton* broadband light curve of NGC 4051 exhibits large amplitude count rate variations in both observations (see Fig. 5.1), typical for this source and for NLS1 galaxies in general. Fast large amplitude variability is superimposed on longer trends which are mainly characterized by persistent low flux periods in which variability is suppressed. The *XMM–Newton* light curves shown in Fig. 5.1 are a good representation of this behavior which can be described in more general terms by the RMS–flux relation in which the absolute RMS variability is proportional to the source flux (Uttley & M^{c}Hardy 2001). Light curves such as those shown in Fig. 5.1 are just a realization of the RMS–flux relation which naturally produces large amplitude spikes at high fluxes and periods of relative quiescence at low fluxes (e.g. Uttley, M^{c}Hardy & Vaughan 2005).

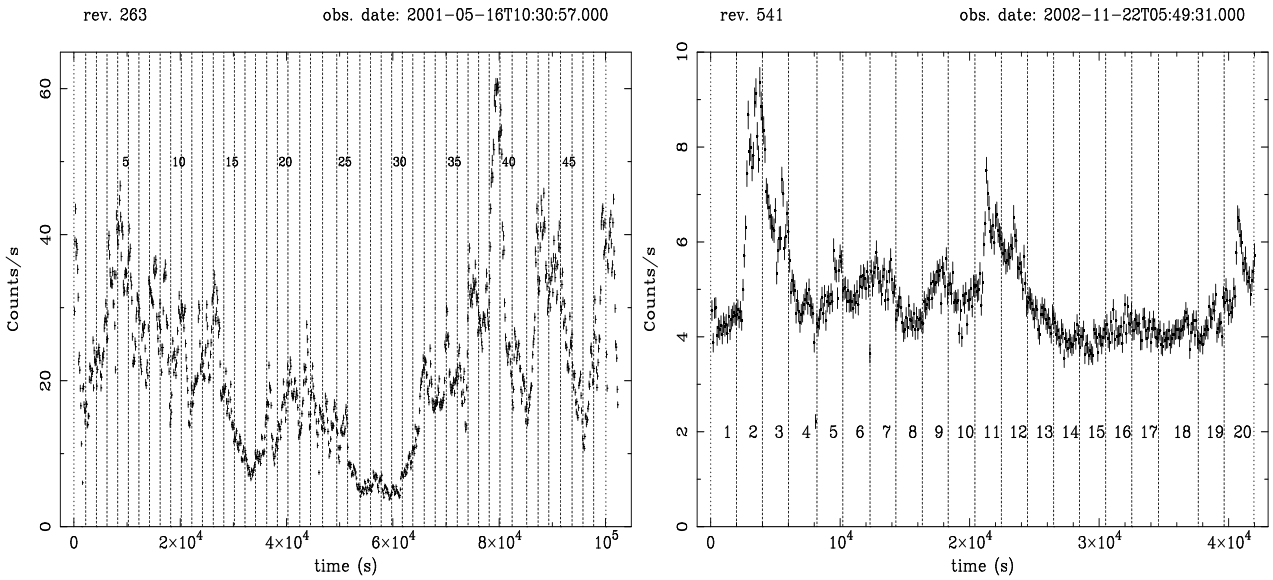

Figure 5.1: The broadband 0.2–10 keV *XMM–Newton* EPIC–pn light curves of NGC 4051 for the first (left panel, rev. 263) and the second (right panel, rev. 541) observations. The 2 ks time slices used in the time–resolved spectroscopic analysis are also shown.

The general shape of the broadband spectrum of NGC 4051 in both observations can be roughly described by the presence of a power law continuum, reflection from distant matter including a narrow 6.4 keV Fe line, and a prominent soft excess below about 1 keV. The Fe line is unresolved and fluxes are consistent with each other in the two observations. A warm absorber imprints its presence in the spectrum particularly through two edge–like features at 0.74 and 0.87 keV (O VII and O VIII). Even modeling the absorption, some structures persist between 0.8 keV and 1 keV, particularly evident in the low flux state. This further structure can be interpreted as a broad absorption structure (as suggested by Pounds et al 2004), emission around 0.9 keV (see Collinge et al 2001, Uttley et al 2004), or a combination of the two.

Spectral variability is clearly present between the two observations with the source being much harder in the second, lower flux observation. Moreover, when the source is faint and hard, the spectrum above $\sim$ 2 keV appears to be more curved than in the high state. To illustrate the differences in spectral slope and hard curvature between the two observations we show the two 3–10 keV time–averaged spectra in the left panel of Fig. 5.2. The best–fitting power law slope is indicated, the fit includes a narrow 6.4 keV Fe line as well. The spectral curvature can be interpreted as the effect of absorption by a relatively high column of ionized gas or could be the signature of a relativistically blurred reflection component from the accretion disc.

Two main mechanisms have been proposed so far to explain the spectral variability of NGC 4051. Pounds et al (2004) performed a comparative analysis of the two *XMM–Newton* observations based on the time–averaged spectra and on the simultaneous high–resolution RGS data in the soft band. Their main conclusion is that the spectral variability between the

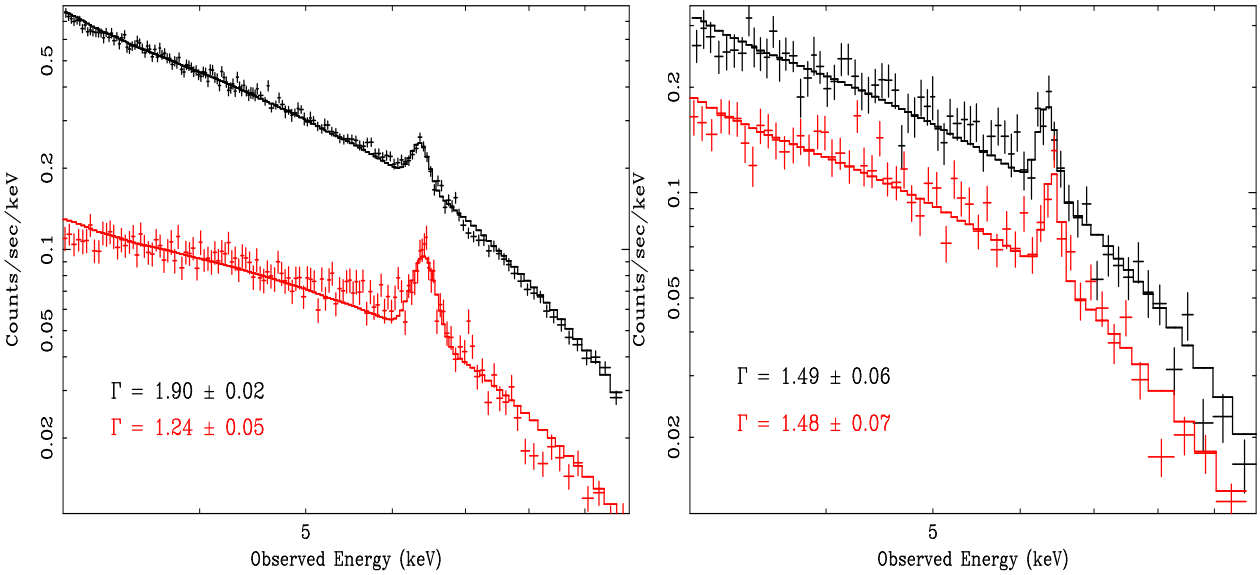

Figure 5.2: In the left panel we show the time averaged 3–10 keV for the first and second observation. The spectrum in the second low flux observation is flatter and much more curved that during the first high flux one. In the right panel we show two $\sim$ 10 ks spectra extracted from the first and second observation respectively. The one from the first observation is taken around 60 ks (see right panel of Fig. 5.1) and is representative of the low flux state during that (higher mean flux) observation. The two spectra are chosen from intervals that have approximately the same count rate. The two spectra have the same spectral slope and the same hard curvature showing that the spectral variability is clearly flux–dependent and that the same flat spectrum and curvature characteristic of the second observation can be found also in the first, if low flux levels are selected.

high flux (rev. 263) and low flux (rev. 541) observations is mainly due to variable absorption by a substantial column of photoionized gas in the line of sight. The authors suggest that in the low state (observed about 20 days after the source entered one of its characteristic low state periods) part of the gas had recombined in response to the extended period of lower X–ray flux so providing a partial coverer (with $N_H \sim 3.6 \times 10^{23}$ cm^{-2}). The variable opacity of the absorber could then explain in a natural way both the flat spectrum and the hard curvature that is observed in the second low flux observation.

This interpretation is challenged by the analysis by Uttley et al (2004) who proposed spectral pivoting as the main driver of the spectral variability in NGC 4051 and pointed out that a variation in the absorber opacity in the line of sight during the low state is not consistent with the nature of the spectral variability, as revealed by the flux–flux plot analysis, in which no sharp transition is seen between the two observations. The flux–flux relationship rather indicates that the spectral variability is flux–dependent and the low flux states of the first observation are virtually identical in spectral shape to the high flux state of the second. This would rule out that the low flux spectral shape during the second observation depends on the fact that data were obtained following an extended low flux state allowing the absorbing gas

to recombine.

It is clear that the Pounds et al interpretation implies that the spectral shape is different in the two observations. For instance, the low flux states of the first (high flux) observation should not be as flat and curved as the spectrum in the second observation. This idea can be easily checked by comparing two spectra: the first one is representative of the very low flux state during the first observation (around 60 ks, see Fig. 5.1) and the second one is extracted from the second observation. We choose the two spectra to have the same exposure and approximately the same count rate. The two spectra are shown in the right panel of Fig. 5.2 in the hard 3–10 keV band. The best fitting power law slope is also indicated. The fit also includes Fe emission at 6.4 keV. Firstly, the spectral slope is exactly the same in the two spectra. Therefore the slope is count–rate dependent and the time–averaged flat spectrum during the low flux observation has thus little to do with the extended period of low flux preceding the second observation. Secondly, the two spectra have the same spectral shape also in the broad redshifted Fe K line region. In fact when the two spectra are fitted with a partial covering model, both spectra require a large column density of ~ 0.5–2×10^{23} cm^{-2} and a covering fraction of 60–70 per cent. This demonstrates that not only the apparent spectral slope is flux–dependent, but also that the hard curvature in the Fe K region depends on flux only.

From the above analysis, it seems likely that the spectral variability in NGC 4051 is simply flux–dependent and that the second low flux observation is not peculiar but indeed identical to low flux states during the first observation. As already mentioned by Uttley et al (2004) one possible explanation for the flux–dependent spectral variability is spectral pivoting. In this paper we shall explore an alternative explanation invoking a reflection component from the accretion disc. Before considering a time–resolved spectral analysis, we perform some model–independent tests with the aim of identifying the main spectral components and their relative contribution to the spectrum and variability, in order to have a guide for our subsequent analysis.

5.3 RMS spectra

Fig. 5.3 shows the RMS spectra of NGC 4051 during rev. 263 and 541. The RMS spectra have been calculated with time bins of $\sim$2 ks (the same as the subsequent time–resolved spectral analysis) and with energy bins chosen in order to have at least 300 counts per energy–time bin. In this way the poissonian noise is negligible compared to the RMS value (see §2.4).

During the high flux observation of rev. 263 (see the left panel of Fig. 5.3) the variability rapidly increases toward softer energies, i.e. the broadband emission tends to steepen as it brightens. Some reduction in the variability is seen below about 800 eV followed by a plateau below 500 eV. The two simplest explanations for the broadband trend invoke either spectral pivoting of the variable component, or the two–component model (see Fig. 3.2.1, 3.2, 3.3 and 3.4 and §2.4.1, 2.4.2 and 2.4.3; Markowitz, Edelson & Vaughan 2003). Another important feature of the RMS spectrum is a drop of variability at 6.4 keV, the energy of the narrow Fe line which is seen in the time–averaged spectrum. Such a drop shows that the narrow Fe line (and therefore the associated reflection continuum) is much less variable than the continuum

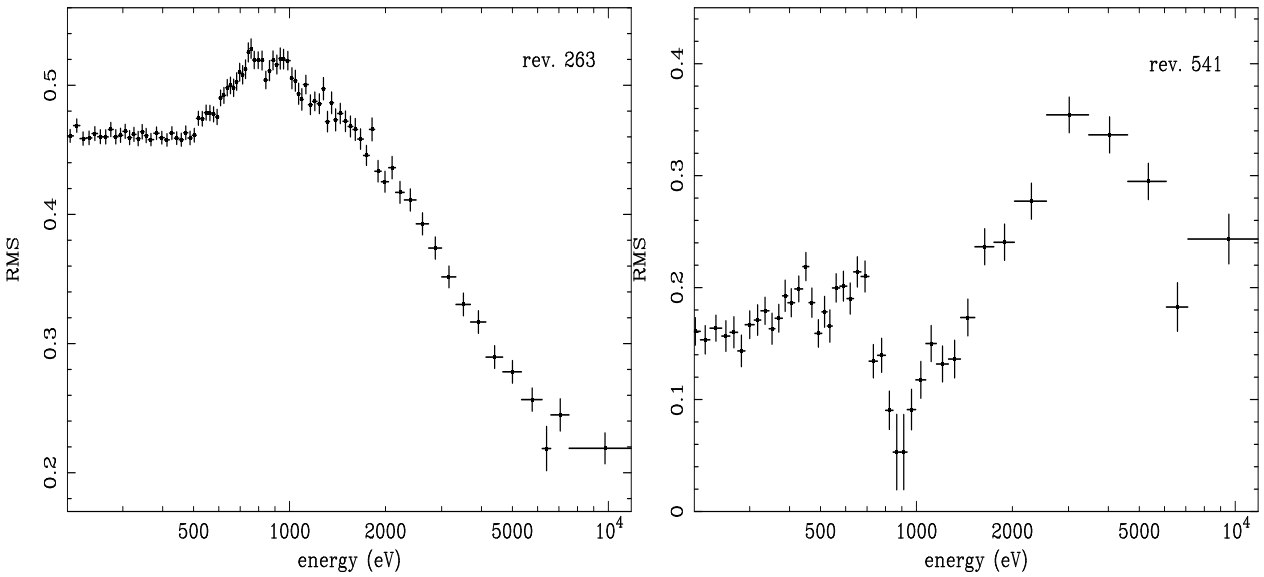

Figure 5.3: The RMS spectra of the rev. 263 (left panel) and rev. 541 (right panel). The RMS spectra are computed with time bins of 2 ks with a minimum of 300 counts per energy bin.

(if variable at all) indicating an origin in distant material. Some structure is also present around 0.9 keV, with the possible presence of either a drop at that energy or two peaks.

In the right panel of the same Figure, we show the RMS spectrum obtained for the low flux observation during rev 541. The variability below 3 keV is strongly suppressed with respect to the high flux observation. Moreover, the shape of the RMS spectrum is totally different and rather unusual. The trend of increasing variability toward softer energies breaks down completely and the most striking feature is the marked drop of variability around 0.9 keV. This feature, as well as the other drop of variability at $\sim$0.55 keV, could have the same nature as the structure seen in the high flux RMS spectrum, but is much more significant and prominent here. As a sanity check, we show in Fig. 5.4 the source light curve around 0.9 keV and in two bands below and above for comparison. The source appears to be constant around 0.9 keV (χ^2=144.2 for 140 degrees of freedom). The constant hypothesis yields unacceptable fits in the other two bands. As in the high flux observation, the variability is also suppressed around 6.4 keV. The drop at 6–7 keV is here even more dramatic due to the reduced continuum level and therefore increased visibility of the constant narrow Fe line.

5.3.1 Constant components

The RMS spectrum analysis given above clearly demonstrates the presence of two constant or weakly variable components. The first is related to X–ray reflection and Fe emission and is seen in both observations. The second is associated with the drop in variability around 0.9 keV which is clearer in the low flux data where the contribution of the continuum is lower.

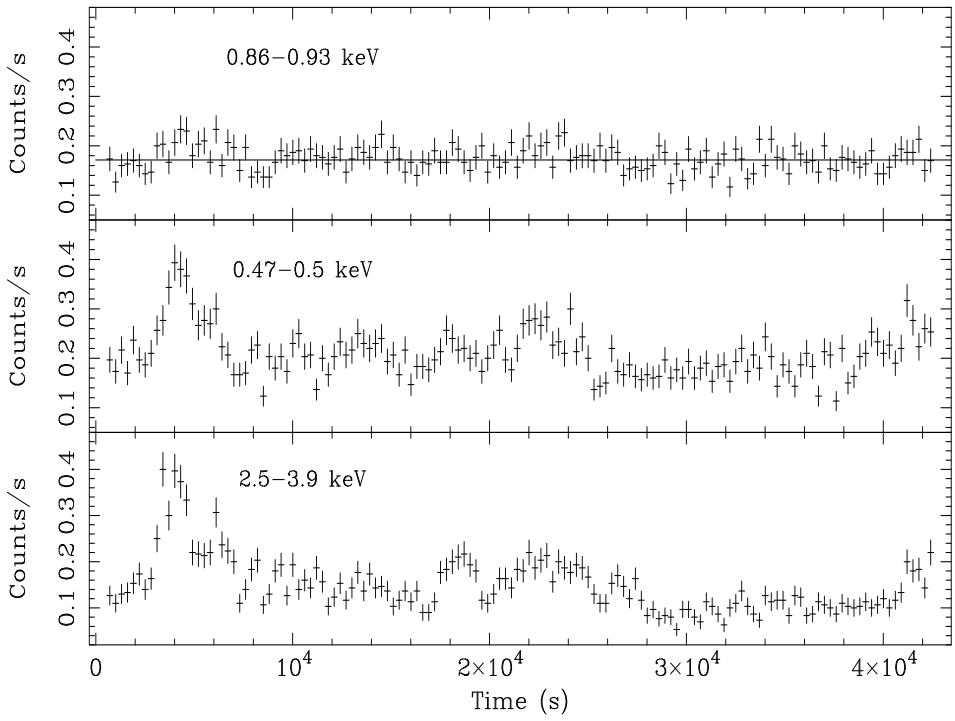

Figure 5.4: Source light curves during the rev. 541. *The top panel* shows the light curve in the big drop of variability energy band (0.86–0.93 keV, see Fig. **??**); *the middle panel* shows the same in the 0.47–0.5 keV band; *the bottom panel* shows the 2.5–3.9 keV band.

Reflection from distant material

Fig. 5.3 show a clear minimum at 6.4 keV indicating that the narrow Fe emission line is less variable than the continuum in both observations. The Fe line is clearly detected in the time–averaged spectra of both observations. In the low flux one, the line is unresolved, has an energy of 6.42 ± 0.015 keV, a flux of $(1.5 \pm 0.2) \times 10^{-5}$ ph s^{-1} cm^{-2}, and an equivalent width of about 260 eV. The line energy and flux are consistent with measurements obtained in the high flux observation and also with previous data from *Chandra* (Collinge et al 2001) and *BeppoSAX* (Guainazzi et al 1998). As mentioned, a constant and narrow Fe emission line is also required by the RMS spectra. Since the Fe line must be associated with a reflection continuum, in all subsequent fits we always include a constant and neutral reflection model from Magdziarz & Zdziarski (1995) and a narrow Fe line. The reflection continuum normalization is chosen such that the Fe line equivalent width (with respect to such continuum only) is consistent with the *BeppoSAX* observation (EW_{FeK} ∼700 eV) by Guainazzi et al (1998). This is because that observation caught NGC 4051 in a particularly low flux state in which the primary continuum had switched off leaving only reflection from distant matter in the hard band, thereby providing a most useful way to constrain that component (under the reasonable assumption that it remained constant).

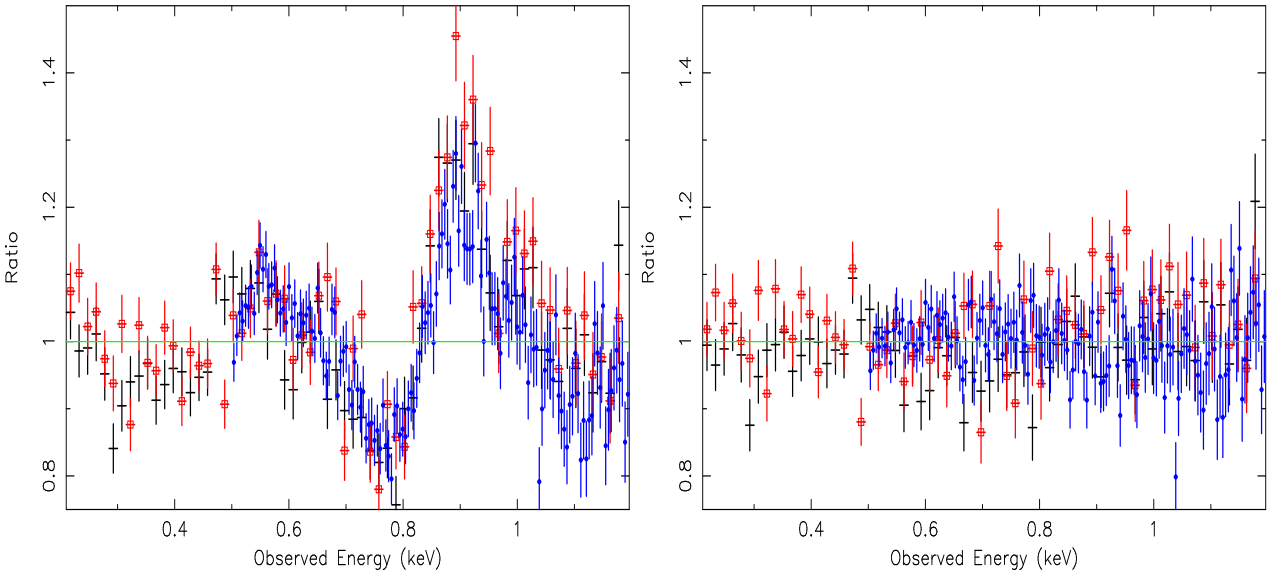

Figure 5.5: A portion of the MOS and pn data during the low flux observation. The left panel shows the ratio to a simple continuum model (power law plus thermal emission absorbed by the Galactic column). In the right panel we show the ratio to a model in which we added Oxygen lines (and edge) and emission around 0.9 keV consistently with what is seen in the high–resolution simultaneous RGS data.

Photo-ionized plasma emission

The second constant component is clearer in the low flux state RMS spectrum (right panel of Fig. 5.3) and appears as a deep minimum, that reach almost null variability, at around 0.9 keV and with a lower variability at ∼0.55 keV (see also Fig. 5.4). These prominent drops indicate the presence of constant emission around ∼0.9 and ∼0.5 keV. Moreover, an emission–like feature is seen in the pn spectrum of the low flux observation and in previous *Chandra* low flux spectra as well (Collinge et al 2001; Uttley et al 2003). The energy of the feature in the pn spectrum is ∼ 0.9 keV, consistent with Ne IX (and possibly Fe emission plus O VIII recombination continuum, or RRC). A second feature is also detected around 0.5–0.6 keV, where emission from O VII and O VIII is expected. As an illustration, in the top panel of Fig. 5.5, we show the ratio of the low flux pn and MOS data to a simple continuum model comprising Galactic absorption power law and black body in the relevant energy band. The energies of the emission features and their intensities over the continuum correspond with the two drops seen in the RMS spectrum. The larger strength of these features during rev. 541 is due to the weaker continuum. In fact, the same drop of variability at about 0.9 keV observed during the rev. 263 can be reproduced by the same constant emission lines with a higher continuum.

To understand the nature of these constant emission components, we then inspected the simultaneous high–resolution RGS data to better search for possible narrow emission lines that could explain the features seen at CCD resolution. As already shown by Pounds et al

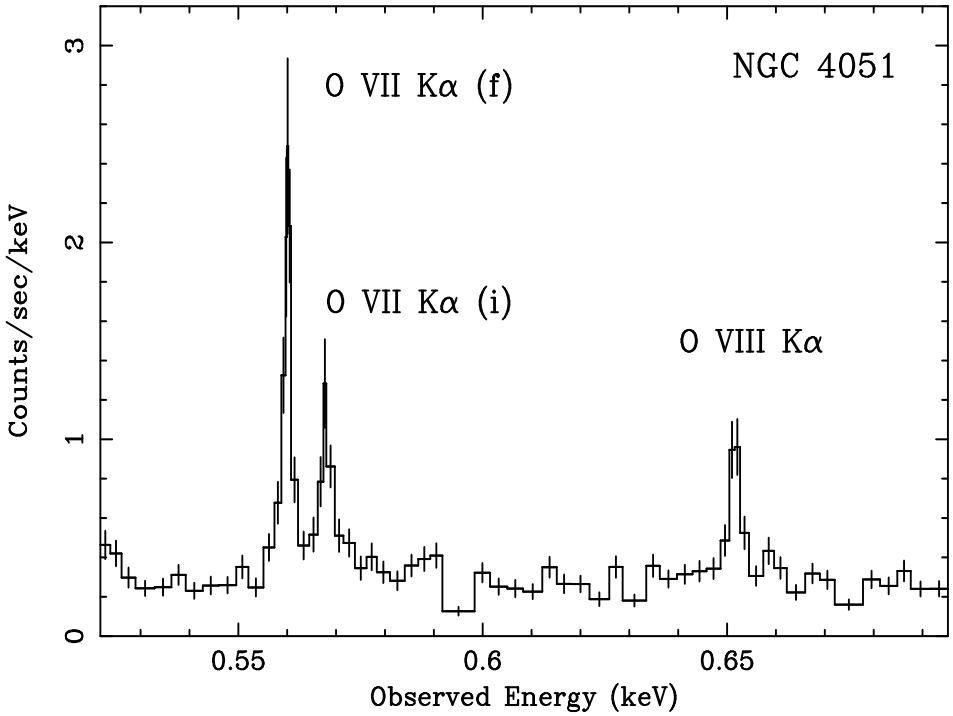

Figure 5.6: A portion of the RGS 1 spectrum of NGC 4051 in its low flux state. Emission by photo-ionized gas is clearly visible in the form of several emission lines. Here we show the O Kα lines only. Such emission line spectrum is generally seen in Seyfert 2 galaxies and is detectable here thanks to the extremely low continuum.

(2004) the high–resolution RGS data during the low flux *XMM–Newton* observation indeed show an emission line spectrum which is very similar to that of typical Seyfert 2 galaxies (e.g. Kinkhabwala et al 2002; Bianchi et al 2005). We take the same continuum as in the CCD data and add a O VII edge at 0.74 keV to account for the absorption seen there. The most prominent emission lines are due to the O VII triplet (dominated by the forbidden and intercombination lines and with no clear resonance), the O VIII Kα line and the N VII Kα line (see Fig. 5.6). The Ne IX (forbidden) line is also clearly detected at 0.905 keV with a flux of $(3.5 \pm 1.0) \times 10^{-5}$ ph s^{-1} cm^{-2}, not enough to account for the pn feature around 0.9 keV. However, the Ne line sits on top of a broad feature most likely due to O VIII RRC and possibly unresolved Fe emission lines. When fitted with a crude Gaussian model in the RGS data, such a feature has an energy of 0.88 ± 0.01 keV and a flux of $(5.0 \pm 1.5) \times 10^{-5}$ ph s^{-1} cm^{-2}. By combining the Ne line with this broad feature ($\sigma \simeq 20$ eV) we obtain a flux of (0.7-1.1)$\times 10^{-4}$ ph s^{-1} cm^{-2} around 0.9 keV.

We then included (with all parameters fixed to the RGS results) the N and O lines in the MOS/pn model, together with a O VII edge at 0.74 keV (fixed energy) and a Gaussian emission line with free energy, width, and normalization to account for the blend of Ne line plus broad feature around 0.9 keV. The resulting fit is acceptable and is shown as a ratio plot in the bottom panel of Fig. 5.5. As for the emission feature at 0.9 keV, we measure an energy

of 0.88 ± 0.02 keV and a flux of $(1.2 \pm 0.2) \times 10^{-4}$ ph s^{-1} cm^{-2}, consistent with the RGS upper limit. As mentioned in Pounds et al (2004) excess absorption might be present around 0.76 keV (possibly related to a M–shell unresolved transition array from Fe). If included in both CCD and RGS data, this has the effect of reducing the broad 0.9 keV feature intensity, making so much more difficult to reproduce the variability drop in the RMS spectra.

The above analysis demonstrates that emission from photoionized gas is present in the low flux data and detected both in the RGS and in the lower resolution CCD detectors. Such components, as shown by the RMS spectra, are constant over time, thus then are likely to come from relatively extended gas (see Pounds et al 2004). A constant emission component, indeed, does explain the unusual drop of variability around 0.9 keV in the low flux RMS spectrum. The line intensities are also consistent (though not detected) with the higher flux observation data. They are not detected because of the much higher continuum level. We then included, in addition to the constant neutral reflection from distant material, such lines with fixed energies and intensities (as obtained from the low flux RGS data) in all subsequent fits.

5.4 Flux–flux plots: is pivoting the only solution?

Another model–independent approach that provides information on the dominant driver of the spectral variations is the flux–flux technique (see Taylor, Uttley & M^{c}Hardy 2003; Uttley et al 2004). We recall here that a linear flux–flux relationship reveals that the data can be described by a simple two–component model where one component varies in flux but not in spectral shape, while the other remains constant both in flux and spectral shape. An offset on the hard or soft axis allows one to infer in which of the two bands the constant component contributes the most. On the other hand, if the flux–flux relationship has a power law functional form, then the data are consistent with spectral pivoting of the variable component.

Uttley et al (2004) plotted the 2–10 keV band count rate versus the 0.1–0.5 keV one and found a very accurate power law flux–flux relationship which was interpreted as evidence for spectral pivoting of the variable component. The choice of the soft and hard energy ranges by Uttley et al (2004) was driven by the requirement of having well separated bands to best reveal the spectral variability. However the 0.1–0.5 keV band does not seem to have the same variability properties of the broadband continuum. This is clearly seen in the top panel of Fig. 5.3 in which the soft plateau indicates the presence of a component with different variability properties than the continuum above 1 keV. Such a component is likely to be ascribed to the soft excess. Therefore we consider as a reference a soft band between 1–1.4 keV to avoid possible contamination from undesired components. In all previously reported analysis of the X–ray spectrum of NGC 4051, the intermediate 1–1.4 keV band is dominated by a power law continuum which is not strongly affected by absorption, soft excess, or reflection. As for the hard band, we consider the 4-10 keV range, simply to allow enough leverage for spectral variability to show up clearly.

In the top panel of Fig. 5.7, we show the flux–flux relationship in the chosen hard and soft bands. The two *XMM–Newton* observations are shown with different symbols. As already

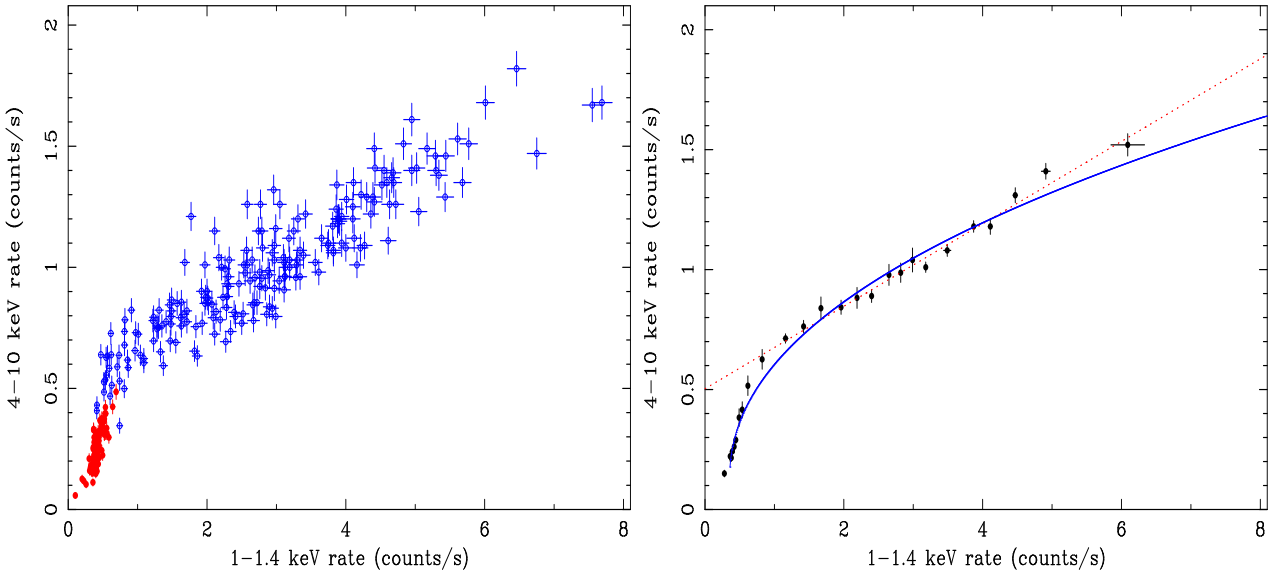

Figure 5.7: The flux–flux plot obtained by plotting the (pn) 4–10 keV count rate versus that in the 1–1.4 keV band. The bottom panel is just the binned version of the original flux–flux plot (top panel). The solid line is the best fit power–law relationship, while the dotted one is the best fit linear relationship if the lowest flux data points are excluded (see text for details).

pointed out by Uttley et al (2004) the low flux state data join gently on to the normal/high flux state ones, showing that the spectral variability is likely to be due to the same mechanism at all flux levels. There is no dramatic discontinuity between the two observations suggesting, once again, that the spectral changes are not due to a dramatic change in one of the physical parameters (such a substantial change in the absorbing column, as suggested by Pounds et al 2004). The flux–flux relation is clearly non–linear with some curvature showing up especially at low fluxes. In the right panel of 5.7, we show a binned version of the same plot (minimum of 10 points per bin). In the same figure, the solid line is the best fit for a power law model representing a situation in which the main driver of the spectral variability is spectral pivoting (see e.g. Taylor, Uttley & M$^{\rm c}$Hardy 2003 for details). The fit is performed as in Uttley et al (2004) with a power law relationship including constant components which are required in both the hard and the soft band. The power law relationship does not provide a good fit to the data ($\chi^2 = 62.4$ for 22 degrees of freedom), mainly because the model has too much curvature at high fluxes and not enough at low fluxes. This does not exclude spectral pivoting as the main driver for the spectral variability, but suggests that we need to look for an alternative explanation.

In fact, if the lowest flux data points are excluded, the flux–flux relationship is linear with high accuracy. This is shown as a dotted line in the bottom panel of Fig. 5.7 which is the best fit linear relationship obtained when the lowest flux data points are ignored. We obtain a very good fit ($\chi^2 = 14.3$ for 15 degrees of freedom) with a large hard offset of 0.50 ± 0.02. As mentioned, a linear relationship suggests that the spectral variability is due to a two–component model, i.e. to the relative contribution of a variable component whose spectral

shape is flux–independent (e.g. a constant Γ power law varying in normalization only) and a constant or weakly variable harder component. If the flux–flux relationship at normal/high fluxes is indeed linear, one can compute the contribution of the constant component in the 4–10 keV from the y–axis offset $C_{\rm h}$. Since the mean 4-10 keV rate for the normal/high flux data points is $F_{\rm h} \simeq 1.0$, this means that the putative constant component contribution in the 4–10 keV band is as large as 50 per cent in the normal/high flux states.

However, if indeed the two–component model is a fair representation of the spectral variability at normal/high fluxes, the low flux data imply that the spectral variability must smoothly change regime at low fluxes producing the gentle low–flux bending in the relationship. Such a transition could be reproduced if, below a given flux level, the constant component (or part of it) is not constant anymore but rather follows the changes of the variable one. In fact, any two–component model in which the less variable component varies together with the variable one at low fluxes and saturates to an approximately constant flux at higher fluxes would produce the same kind of relationship as observed here.

5.4.1 Is the two component model consistent with the shape of the RMS spectrum?

In order to check if the source spectral variability could be due to the two–component model we try to reproduce the RMS spectrum during rev. 263 with a simple phenomenological parametrization (the RMS spectrum during rev. 541 is not considered because its shape is mainly dictated by the constant components coming from distant material). The model is composed of a direct power law component and an ionized disc reflection component, from Ross & Fabian 2005) the spectrum of which is convolved with a `LAOR` kernel with fixed inner and outer disc radius (to 1.24 r_g and 100 r_g respectively), and fixed disc inclination (30°). In the RMS simulation the contribution from neutral distant reflection is also considered.

We assume that all the source variability is due to the variation of the normalization of the direct power law that has a spectral index fixed at Γ=2.4 (Lamer et al. 2003) and that the reflection component is completely constant not only in normalization, but also in spectral shape (i.e. ionization and relativistic blurring parameters). To simulate the RMS we vary the power law normalization from the lowest to the highest value observed. For the reflection component we have chosen the best fit values of the spectrum during the low flux state of rev. 263 ($\xi \simeq$50 and disc emissivity index of $\alpha \simeq$6). Figure 5.8 shows the simulated RMS (dotted line, green in the color version) and, for comparison, the simulated RMS with the reflection parameters of ξ=5 and α=4 (solid line, blue in the color version), that also roughly reproduce the low flux spectrum (see also §2.4.3).

The interplay between the power law and the ionized reflection can roughly reproduce the shape of the RMS (within $\Delta RMS \lesssim 0.02$; see also §2.4.3). This means that the two component model can explain the bulk of the spectral variability requiring no further variable component at low energy. The variability in the soft band can be explained by a variable power law and a constant soft excess (which is in this case due to constant disc ionized reflection).

Clearly, a completely constant reflection component is an over–approximation. In fact, although it is possible to reproduce the bulk of the variability, some variations of the normalization of the ionized reflection are required in order to match with more details the RMS

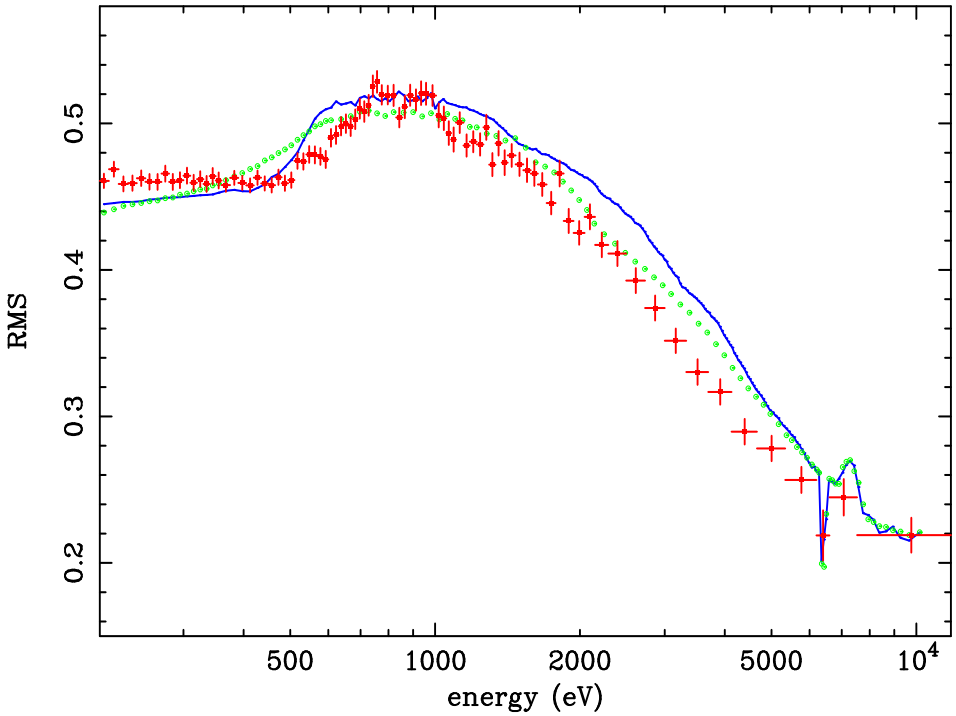

Figure 5.8: The observed RMS spectrum obtained during rev. 263 is compared with synthetic ones (see also §2.4.3). The solid line (blue in the color version) is obtained varying in normalization (from the lowest to the highest value observed) a power law with Γ=2.4 and keeping a ionized disc reflection component with ionization parameter ξ=5 and disc emissivity index α=4 completely constant. While the simulated RMS shown by the dotted line (green in color) is calculated in the same way as above, but with $\xi \simeq 50$ and $\alpha \simeq 6$. In both models the contribution from neutral distant reflection is considered.

spectra and to reproduce the constant spectral shape below 0.5 keV (see Section 6.3.2).

5.5 Time–resolved spectral analysis

In sources such as NGC 4051 where large amplitude fast variability is associated with spectral variability, time–resolved or flux–resolved spectroscopy provides much more detailed information on the nature of the source than time–averaged spectroscopy. In the particular case of NGC 4051, flux–resolved spectroscopy could be a risky procedure to adopt because of the small central black hole mass (and therefore the short dynamical timescale associated with it). As an example, if we were to consider the very high flux state of the first *XMM–Newton* observation (see left panel of Fig. 5.1) and make a selection say above 40 counts/s, we would accumulate spectra from intervals sometimes spaced by 70 ks. This timescale is about 140 times the dynamical timescale at 10 r_g (where $r_g = GM/c^2$) for a black hole mass of $\sim 5 \times 10^5$ $M_\odot$ (e.g. Shemmer et al 2003) which is, in our opinion, too large a factor to extract any truly significant information on the nature of the spectral variability of the source.

We therefore explore time–resolved spectroscopy on the shortest possible timescale (set by requiring good quality time–resolved individual spectra). In the following, we present results obtained by performing such an analysis on a 2 ks timescale (about four dynamical timescales at 10 r_g). The 2 ks slices that have been used in the analysis are shown in Fig. 5.1 and have been numbered for reference.

5.5.1 The 2–10 keV Γ–flux relationship

It is well known that the 2–10 keV spectral slope in NGC 4051 (and other sources) is correlated with the source flux. In the top panel of Fig. 5.9, we show such a correlation when all the 2 ks spectra are fitted with a simple power–law model in the 2–10 keV band. Data for the two observations are shown with different symbols. The photon index increases with flux and seems to saturate around $\Gamma \simeq 2.2$ with a $\Delta\Gamma \simeq 1.2$ between the low and high flux states. However, the power law model is clearly inadequate to fit the 2–10 keV spectra in NGC 4051. This is because of the presence of a narrow 6.4 keV Fe Kα line and the associated reflection continuum in the hard band. As shown above, such a component is constant and likely originates in some distant material (such as the torus).

We then fit again the 2 ks data by including the constant reflection component and show in the bottom panel of Fig. 5.9 the resulting Γ–flux relationship. The $\Delta\Gamma$ between the low and high flux states is now reduced to about 0.7–0.8. Again the photon index seems to saturate at high fluxes to $\Gamma \simeq 2.2$. This value is slightly different from the one ($\Gamma \simeq 2.3 - 2.4$) observed during a long RXTE observation campaign (Lamer et al. 2003). The difference could be due to long term spectral variability. Moreover, the photon index seems to saturate not only at high fluxes but also at low fluxes (to $\Gamma = 1.3$–1.4). Since the two asymptotes are not extremely well defined, such behavior could still be consistent with spectral pivoting, even though it should be stressed that the low flux photon index is still somewhat hard to be explained in terms of standard Comptonization models and would suggest some peculiar physical scenario (such as a photon–starved corona).

On the other hand, the Γ–flux relationship seen in the bottom panel of Fig. 5.9 can be explained if an additional and weakly variable component is present in the 2–10 keV band. If so, such a component dominates the low flux states and the hard photon index measured there is just a measure of its intrinsic spectral shape in the 2–10 keV band, while it is overwhelmed by the power law at high fluxes where $\Gamma \simeq 2.2$ is then the intrinsic power law photon index.

In other words, as an alternative to spectral pivoting, the Γ–flux relationship can be explained by assuming the presence of i) a constant reflection component from distant matter; ii) a variable power law with constant or weakly variable slope $\Gamma \simeq 2.2$; iii) an additional component with approximate spectral shape of $\Gamma = 1.3$–1.4 in the 2–10 keV band which must be almost constant at normal/high fluxes and is allowed to vary significantly only at low fluxes.

We point out here that our flux–flux plot analysis showed that the two–component model might indeed be appropriate in the normal/high flux states. If so, the constant component contributes by about 50 per cent in the 4–10 keV band (from the y–axis offset in the linear fit) and this is much too large a fraction to be accounted for by constant reflection from distant material (and associated narrow Fe line) which contributes in that band by only 10 per cent. The two–component model interpretation of the flux–flux relationship at normal/high fluxes

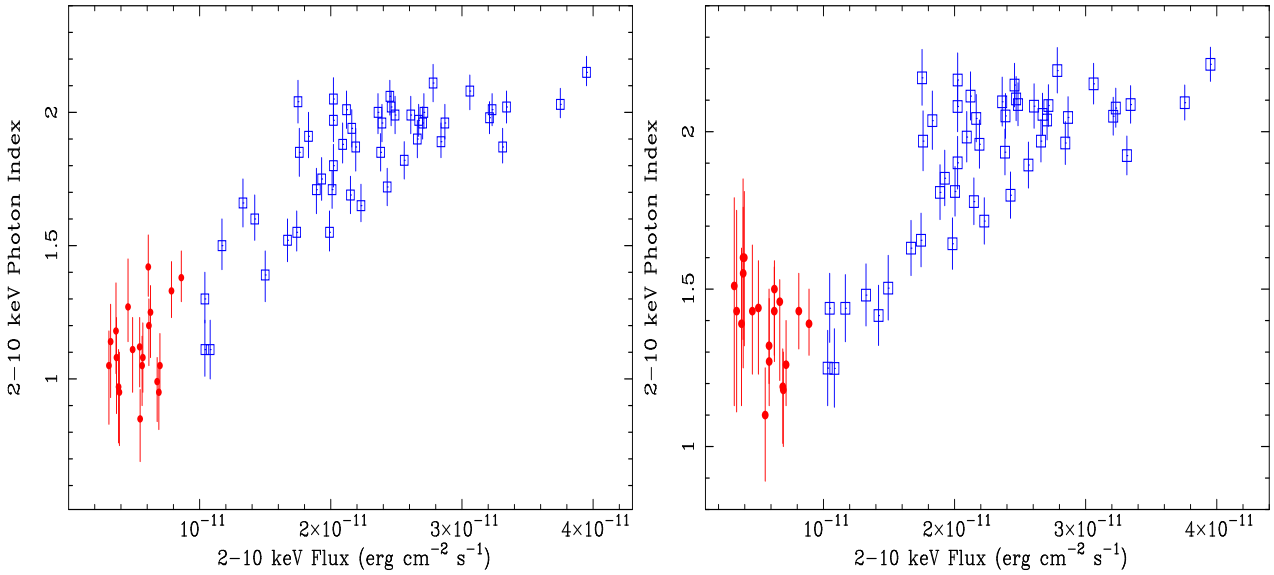

Figure 5.9: The best fit spectral index vs. flux in the 2–10 keV band. In the top panel the spectral model is a simple power law, while constant reflection (including a narrow Fe line) is added to the model for the bottom panel results.

implies that an additional constant component is present in the normal/high flux states and contributes by about 40 per cent to the 4–10 keV band. Such a component naturally produces the observed Γ–flux relationship because as the flux drops the spectrum becomes more and more dominated by it.

5.5.2 Broadband analysis I: the standard model

As a first step, we consider a simple continuum model comprising a power law plus black body emission to model the prominent soft excess. This is, in many respects, the "standard model" to fit AGN X–ray spectra and, though often crude and phenomenological, provides useful indications that can guide further analysis. The power law slope is free to vary to account for possible spectral pivoting. We add to the model neutral photoelectric absorption with column density fixed to the Galactic value. To account for the presence of absorbing ionized gas in the line of sight we include two edges (O VII and O VIII). We searched for possible variations of their energies without finding any evidence, so we fixed the absorption energies to the rest–frame ones. This is clearly a crude approximation for the effects of the warm absorber in NGC 4051, but the quality of the 2 ks spectra is not such to suggest the use of more sophisticated models. In addition, the constant components discussed above (reflection from distant matter and emission from photoionized gas) are also included in the spectral model. The overall model has six free parameters only.

The resulting fits are very good with a reduced χ^2 ranging between 0.9 and 1.2 with a mean close to unity. Therefore, from a statistical point of view, a single model is able to describe the spectral variability of the source in a very satisfactory way. Below, we discuss

the main results of the fitting procedure and their main physical consequences.

Variations of the central source

In Fig. 5.10 (top panel) we show the relation between the measured BB temperature and its intensity, which is proportional to the luminosity (in the present case $A_{BB}=10^{-4}$ correspond to $L_{BB}=9.7\times10^{40}$ ergs s^{-1}, assuming $H_0=71$ Mpc km^{-1} s^{-1}). The BB luminosity spans about one order of magnitude, while the BB temperature ranges from about 90 eV to 140 eV with an average of 110–120 eV. Such a temperature is somewhat high, but can still be consistent with that expected from a black hole with mass $\simeq 5\times10^5\ M_\odot$ (Shemmer et al 2003; M$^{\rm c}$Hardy et al 2004) accreting at high rate (for the given black hole mass, the expected disc temperature is of the order of 70 eV for an object accreting at the Eddington rate). We point out that even in the lowest flux states the temperature (about 100 eV) is larger than predicted and, in the framework of standard disc models, would already require the system to be accreting at the Eddington rate.

If the soft excess in NGC 4051 is really due to BB emission from a constant area, we should be able to detect the BB law ($L_{BB} \propto T^4$) in data spanning one order of magnitude in BB luminosity. However, such a relation is ruled out here. A fit of the L_{BB} versus temperature data (top panel of Fig. 5.10) with the BB law (leaving only the normalization as a free parameter) produces a very bad fit with $\chi^2 = 1552$ for 67 degrees of freedom. The relation appears to be much steeper (with an index of 6.3–6.4 rather than 4), but even so, a power law fit is unacceptable. The measured temperature appears to be much more constant (the fit with a constant gives a $\chi^2 = 75$ for 67 degrees of freedom) than predicted by standard disc models.

The properties of the soft excess in NGC 4051 are remarkably similar to the time averaged properties of the radio–quiet quasars studied by Gierlinski & Done (2004; see §1.1.3). The coincidence is rather surprising considering that the black hole mass in NGC 4051 is about 3 orders of magnitude smaller than the typical black hole mass in the quasar sample. These findings, thus, strengthen the indication of an atomic rather than thermal origin for the soft excess (see also §1.1.3).

The "standard model" of the source emission seems to be inadequate to describe the corona parameters as well. In the bottom panel of Fig. 5.10 we show the power law slope as a function of the 0.5–10 keV flux. In the normal/high flux observation the photon index steepens with flux, as already pointed out in the 2–10 keV analysis. This behavior is consistent with spectral pivoting. Once again, the lowest Γ are of the order of 1.4 which is a hard spectral shape to be accounted for by standard Comptonization models and might require a photon–starved corona scenario. The main problems arise at very low fluxes, where the Γ–flux relation is inverted in a manner that is not consistent with simple spectral pivoting. Such behavior could indicate the presence of an additional soft (steep) component which becomes prominent at low fluxes and is not properly accounted for by the black body component. In fact, the power law is trying to fit the soft data by steepening the index at low fluxes and leaves significant residuals in the hard band where a slope of about 1.3–1.4 would be more appropriate even at very low fluxes (see Fig. 5.9).

As a final comment, the mean optical depth of the ionized absorber (here modeled crudely

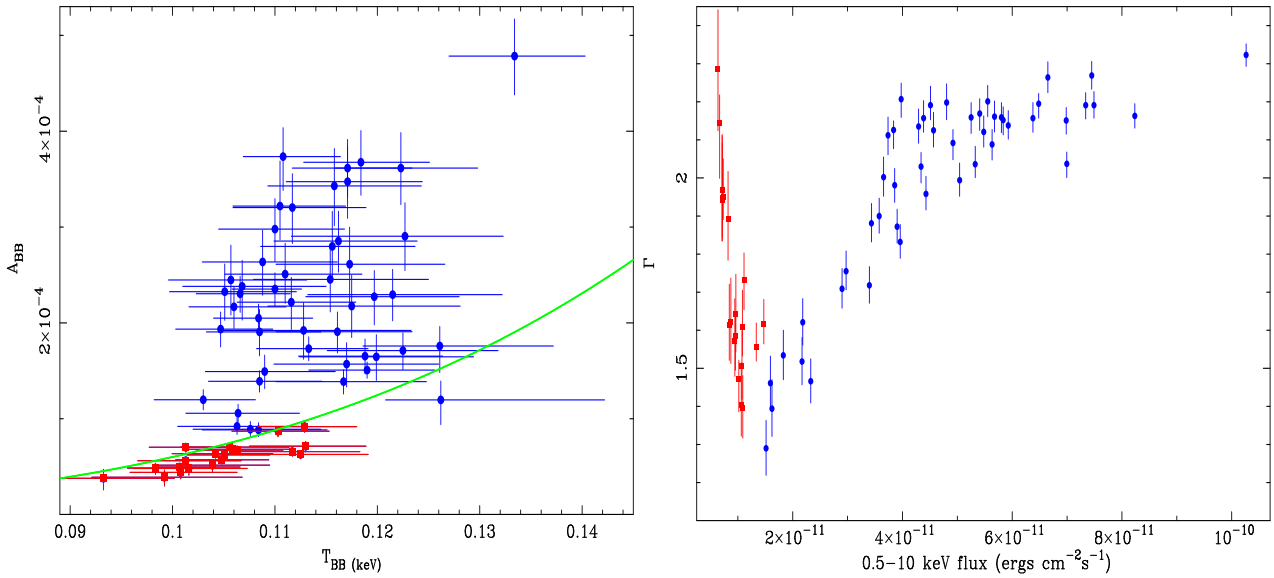

Figure 5.10: In the top panel we show the black body intensity as a function of its observed temperature. The green line shows the best fit relation between the $A_{BB} \propto T^4_{BB}$. In the bottom panel, we show the broadband Γ–flux relationship as obtained from the standard model fits (see text for details).

by the O VII and O VIII edges) is of the order of 0.1–0.3, consistent with the value obtained from the RGS analysis (Pounds et al. 2004). These values are left free to vary and they seem to suggest some variations during the two observations (see Krongold et al. 2007). Nevertheless, the uncertainty associated with these is so big that a fit to the optical depth with a constant during the first observation results in a χ^2 of 26 (O VII) and 47 (O VIII) for 47 degrees of freedom, while during the second low flux observation the χ^2 are 29 and 7 for 19 degrees of freedom.

5.5.3 Broadband analysis II: the two–component model

The results of the fits with the "standard model" presented above suggest that the soft excess is not (or not completely) truly disc black body emission. Moreover, if the spectral variability is due to spectral pivoting, the power law slope at low fluxes is somewhat too hard to be accounted for by standard Comptonization (Haardt et al. 1997). In addition, a steeper component appears in the soft band at the lowest flux levels. We then explore here an alternative model to describe the spectral variability of NGC 4051.

Spectral fitting results and discussion

The two–component model we have tested comprises then i) a power law with fixed slope at $\Gamma = 2.2$ (consistent with the high–flux asymptote of the Γ–flux relationship) and variable normalization and ii) an ionized disc reflection (from Ross & Fabian 2005) the spectrum of which is convolved with a `LAOR` kernel with fixed inner and outer disc radius (to 1.24 r_g

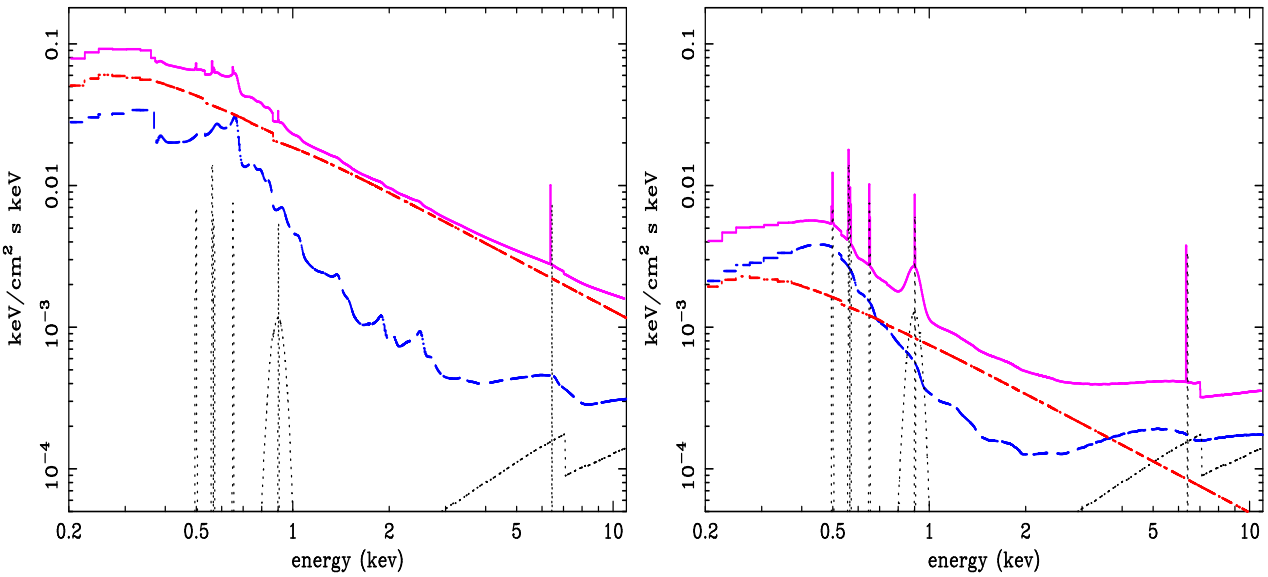

Figure 5.11: In the left panel we show the best fit model during the highest flux period. The power law is shown with a dash–dotted red line; the blurred ionized reflection component is shown with a dashed blue line; the constant reflection component and the emission from photionized gas is shown with dotted gray lines and the total emission is shown with solid magenta line. In the right panel we show the the best fit model, as before, during a low flux spectrum, showing the typical variability properties in the two–component model.

and 100 r_g respectively), and fixed disc inclination (30°). The inner disc radius corresponds to the innermost stable circular orbit around a Kerr black hole. The only free parameters of the relativistic kernel is then the index q of the disc emissivity profile ($\epsilon = r^{-q}$). The ionized reflection model is appropriate for solar abundances and has ionization parameter and normalization as free parameters, while the photon index of the illuminating power law in the ionized disc reflection model is tied to that of the power law and therefore fixed to $\Gamma = 2.2$. As for the "standard model" discussed in the previous Section, the overall spectral model also includes Galactic absorption, constant emission from photoionized gas and from a distant reflector and the O VII and O VIII edges with fixed energies. The number of free parameters in the model is just the same as in the "standard model" case (6 free parameters).

The model reproduces very well the data at all flux levels with a reduced χ^2 between 0.8 and 1.2. Given that the standard model and the two–component one have the same number of free parameters, we can directly compare the resulting averaged reduced χ^2 which are 1.08 ± 0.07 for the standard model and 1.06 ± 0.08 for the two–component one. Therefore, the two–component model is statistically indistinguishable from the standard one and has to be considered as a possible alternative to be accepted or rejected on a physical rather than statistical basis.

As mentioned, the power law used to model the data has a fixed slope of $\Gamma = 2.2$ at all flux levels. In fact, we also tested a variable Γ fit to the data and found that all 68 spectra are consistent with $\Gamma = 2.2$ with only three exceptions in which the statistics is significantly

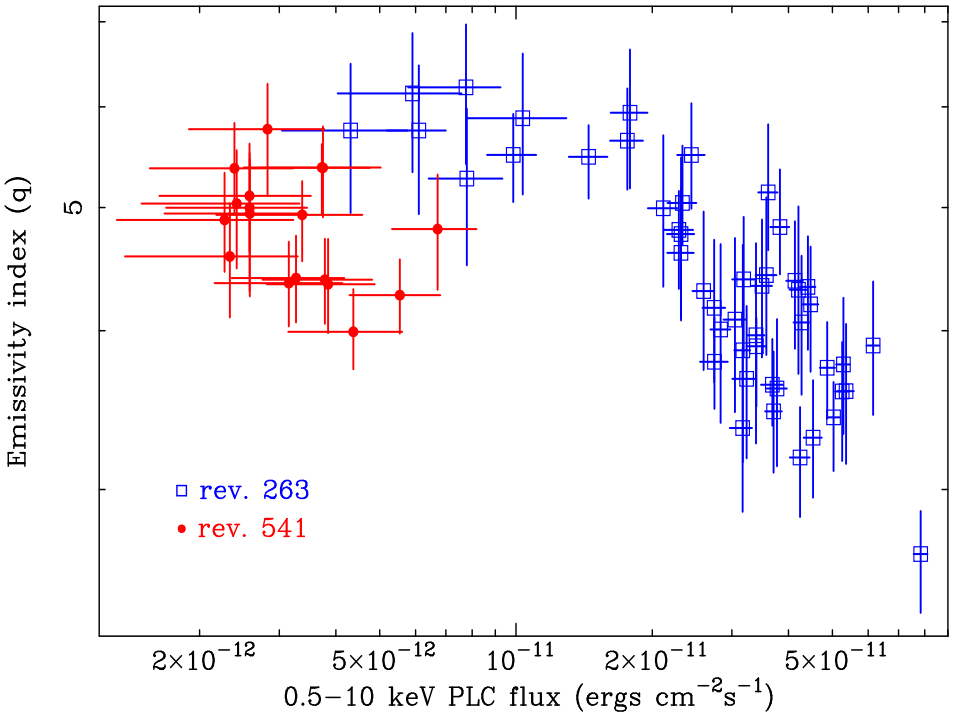

Figure 5.12: The emissivity index of the relativistic blurring model is plotted versus the power law flux in the 0.5–10 keV band.

better with a different power law slope (with small $\Delta\Gamma < 0.15$). Therefore, we demonstrate here by direct spectral fitting that the curvature in both the flux–flux plot and the Γ–flux relationship does not imply spectral pivoting but is only consistent with it.

The second characteristic of the model is that the soft excess is not due to a thermal component anymore (see Fig. 5.11). It is in fact the result of including ionized reflection from the disc, which naturally produces a soft excess. The "constant temperature" problem can then be naturally solved because of the very non–thermal nature of that component.

The ionization parameter of the reflection spectrum is not very well constrained by the data and most spectra are consistent with ξ between 50 and 300 erg cm s^{-1} with only few exceptions below and above (and no clear trend with flux). The reason for the non–accurate measurement of ξ is probably twofold. Firstly, the spectra lack sharp emission lines which would help in constraining the ionization state (if present, the emission lines are broadened and skewed because emitted from the inner disc). Secondly, we are using a reflection model with a single uniform ionization parameter over all the disc surface from the innermost to the outermost regions. This is clearly a rough approximation for a real case in which the ionization parameter has a structured radial profile. Such approximation is likely to play a role in the non–accurate measurement of ξ.

On the other hand, the disc reflection emissivity index of the relativistic blurring model is better constrained. In Fig. 5.5.3 we show the emissivity index q as a function of the power

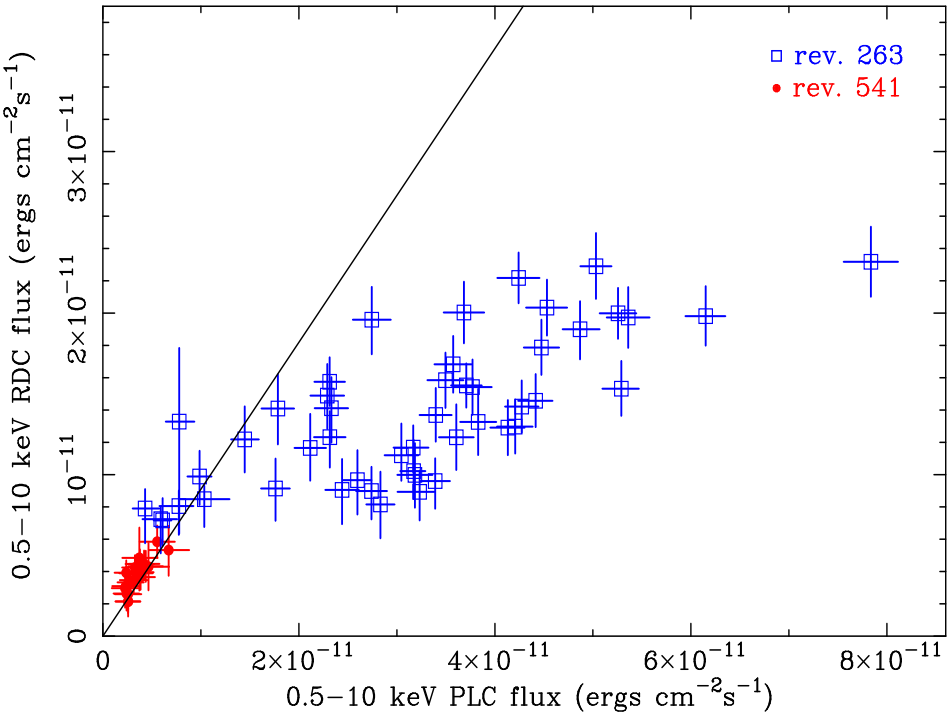

Figure 5.13: Disc ionized reflection vs. power law 0.5–10 keV fluxes. The data clearly rule out a perfect correlation between the two components (solid line). The disc reflection is well correlated with the power law at low fluxes only and varies with smaller amplitude in normal/high flux states.

law flux. Some trend can be seen in the Figure with low flux states generally corresponding to steeper emissivity profiles (with q of the order of 5) than high flux ones. As mentioned above, this result is in line with the predictions of the light bending model (Miniutti & Fabian 2004).

The other main prediction of the light bending model is the disc reflection versus power law relation. As mentioned, the model predicts a correlation at low flux levels and an almost constant disc reflection at higher flux levels, despite large variation in the power law. In Fig. 5.13 we show the 0.5–10 keV flux of the disc reflection versus the power law flux in the same band. The disc reflection is well correlated with the power law at low flux levels (the solid line represent perfect correlation between the two components). However, as the power law flux increases, the correlation clearly breaks down and the reflection is much less variable (about a factor 2.5) than the power law (about a factor 7) in very good agreement with the qualitative predictions of the model. The main difference between the predicted and observed behavior is that some residual correlation is seen at normal/high flux (while the model predicts an almost constant reflection). Such residual correlation can be easily interpreted by intrinsic luminosity variations of the power law source which are not accounted for in the model.

We finally remark that, if the light bending interpretation is correct, the disc reflection versus power law behavior requires the primary source of the power law to be centrally concentrated above the accretion disc within 15 gravitational radii at most from the central black

hole (see Miniutti & Fabian 2004). In particular, the correlation between the two component is predicted to occur only if the primary source of the power law is within ~ 5 gravitational radii from the hole. Therefore, one consequence of this interpretation is that low flux states are characterized by an extremely compact region of primary emission, well inside the relativistic region around the black hole.

5.6 Reproducing the RMS spectra

We tested both spectral models further by comparing the RMS spectra with synthetic ones, obtained from the best–fitting models discussed above. Obviously, the better the fits to the 2 ks spectra are, the more closely the RMS spectra will be matched, but the comparison is not trivial because the χ^2 obtained from the time–resolved spectroscopy is a global quantity in the energy space (in fact it depend over all the energies considered) while the RMS is a local quantity (it does not depend on what is the model at other energies). It is possible, for example, that the spectral model slightly fails always in the same energy band. If this is the case, a comparison between observed and simulated RMS spectra is useful.

In Fig. 5.14 we show the observed and synthetic RMS spectra for both observations. In back we plot the RMS spectra obtained from the two–component model best–fitting parameters and in gray that from the standard BB plus power law model. Both models reproduce well the broadband shape of the RMS spectra in the two observations with residuals of the order of few per cent only. This is possible, allowing the three parameters of the disc reflection component (ionization, emissivity index and normalization) to vary (see Sect. 6.3). We do not exclude the presence of further soft component with a possibly different physical origin, but we show that that is not required when variations of the parameters of the disc reflection are considered. In particular, the sharp features in the RMS spectra have been reproduced thanks to the inclusion of the two constant components due to distant neutral reflection and photoionized gas emission. This reinforces our previous qualitatively interpretation indicating that the emission line intensities and their constancy (not only during each observation but also between the two one year apart) are needed in order to reproduce the RMS spectra.

The variability spectrum during the rev. 263 is less affected by the two constant components and carries more information about the nuclear variability. Its shape can be explained equivalently well by the two models investigated. In the "standard scenario" the gradual drop of variability with energy is mainly due to the steepening of the power law slope with flux, while the lower variability at low energy is due to a less variable BB component. In the two–component model scenario it is expected that the source has lower variability both at high and low energy, because these are the regions where the almost constant relativistic reflection component is more important.

In order to estimate the contribution, to the overall spectral variability, due to the variations of the warm absorber, we have simulated the RMS spectra both with constant and varying optical depth edges. The inserts of Figure 5.14 show the enlargement of the RMS in the soft energy band, where the effects of the warm absorber are stronger. The gray line shows the synthetic RMS obtained starting from the best–fitting parameters with the "standard model" and with varying optical depth edges, while the black line shows the RMS

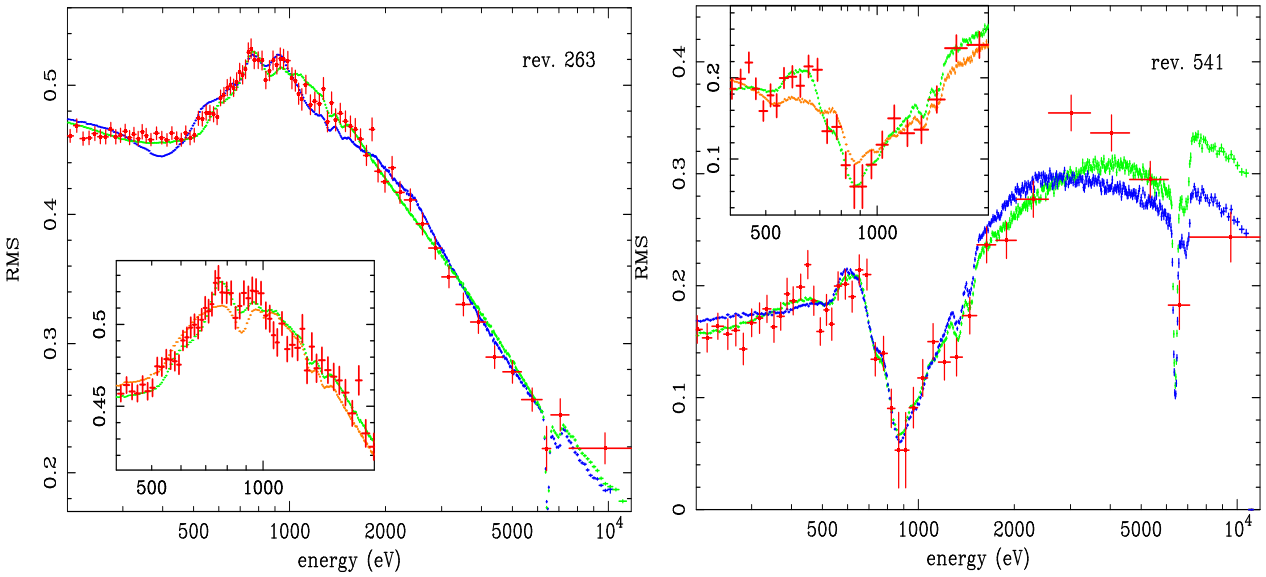

Figure 5.14: The observed RMS spectra of both observations are compared with synthetic ones obtained from the best–fitting standard (gray, green in the color version) and two–component models (black, blue in color). The inserts show the enlargement of the RMS in the soft energy band. The gray (green in the color version) line shows the synthetic RMS obtained starting from the best–fitting parameters with the standard model and with varying optical depth edges, while the black (orange in color) line shows the RMS expected from refitting the data with the imposition of a constant warm absorber.

expected from refitting the data with the imposition of a constant warm absorber. We show here only the results obtained considering the standard model, but similar results are obtained with the two component model. The inserts of Figure 5.14 show that, when the constancy of the optical depth is imposed, some deviations in the reproduction of the RMS are present. The intensity of these deviations are of the order of few percent suggesting that a variation of the warm absorber is possible and likely but the bulk of the spectral variability is due to the interplay of the back body and power law components (power law and reflection, in the two component model) if the continuum is left completely free to vary.

5.7 Summary and Discussion

The analysis presented above shows that RMS spectra, flux-flux plots and individual 2 ks spectra can be explained either in terms of a standard back body plus power law model or of a two–component model. In both cases, the presence of constant emission from photoionized gas and from a distant reflector are required.

The standard model comprises a black body component which provides the soft excess and a power law with variable slope (and normalization). The black body temperature is surprisingly constant given that its luminosity spans one order of magnitude and does not

seem to follow the black body law ($L \propto T^4$). Moreover the average temperature we measure (about 110-120 eV) is remarkably similar to the average temperature measured in a sample of 26 radio–quiet quasars with typical black hole masses three orders of magnitude larger than in NGC 4051. These surprising results suggest that a pure thermal component is not appropriate to account for all the soft excess in NGC 4051. In fact, as shown in Crummy et al. (2006) the soft excess in type 1 active galactic nuclei is consistent, like here, with being produced by ionized reflection. The power law slope in NGC 4051 correlates with flux except at very low flux levels where the relation expected from simple spectral pivoting breaks down. Moreover the hardest photon index we measure (about 1.3–1.4) seem too hard to be explained in terms of standard Comptonization models. It should be stressed also that while spectral pivoting describes well the flux–flux plot relationship between the 0.1–0.5 keV and 2–10 keV bands (see Uttley et al 2004), it fails (or at least reduces its accuracy) when the reference soft band is chosen to be between 1 keV and 1.4 keV. This is somewhat surprising because the latter band is dominated (whatever spectral model is preferred) by the power law component, while at softer energies a contribution from the prominent soft excess is unavoidable.

In the context of the two–component model, the soft excess is instead accounted for by ionized reflection from the accretion disc which simultaneously hardens the hard spectral shape as the flux drops. The apparent constant temperature of the soft excess is then explained, because the soft excess spectral shape is dictated by atomic rather than thermal mechanisms. The two–component model is consistent with the variability being dominated by a constant–slope power law which varies in normalization only. The Γ–flux relationship is then interpreted as spurious and due to the relative flux of the power law and reflection components. The disc reflection is in fact correlated with the power law at low fluxes and varies with much smaller amplitude at normal/high fluxes. Such behavior explains not only the spurious Γ–flux relationship, but is also consistent with the flux–flux plot analysis.

Chapter 6

Key study objects: iii) IRAS 13224–3809, the object with the strongest soft excess of the sample

6.1 Introduction

The Narrow Line Seyfert 1 galaxy IRAS 13224–3809 (z=0.0667) is one of the most X–ray variable radio quiet AGN known. During a *ROSAT* monitoring it showed variations up to a factor of about 60 in just 2 days (Boller et al. 1997). It has the strongest soft excess (Boller et al. 1996) of the sample (see Fig. 4.5) and one of the highest Fe II to Hβ ratio (Boller et al. 1996) of its class.

The *XMM-Newton* observation of IRAS 13224–3809 revealed a dramatic spectral drop, by a factor of 5, at 8.2 keV (Boller et al. 2003). The authors explored two different models to explain the mean spectrum and this feature, one involving a partial–covering scenario and the other involving a strong relativistic reflection component. In the former interpretation the energy of the absorption edge ($\sim$8.2 keV) implies that the absorbing material is either highly ionized or outflowing with a velocity of $\sim$0.15 c (which implies a huge mass and energy loss rate in the outflow). In the latter, the spectral drop, that appears as a sharp edge, is due to the blue horn of a strong and relativistically blurred Fe K line.

The *XMM-Newton* data show also the presence of an absorption feature at about 1.2 keV, when the soft excess is modeled with a thermal model (Boller et al. 2003). This feature has been observed in other two NLS1 galaxies, 1H0707–495 and PG 1404+226 (Leighly 1999; Vaughan et al. 1999). It appears as an absorption line in the range 1.1–1.4 keV with equivalent width being typically $\sim$100 eV, with a width of about 0.1–0.3 keV. Leighly 1999 identifies this feature as absorption due to a warm absorber that imprints its presence through O VII and/or O VIII edges. In this case very significant relativistic outflow velocities are required to match the blue-shift of the absorption edge energy. An alternative explanation has been proposed by Nicastro et al. (1999) who considered a warm absorber illuminated by a steeper soft X–ray spectrum than usually observed in Seyfert 1 galaxies. The different illuminating continuum produces a different ionization structure in the warm absorber, fully stripping oxygen and

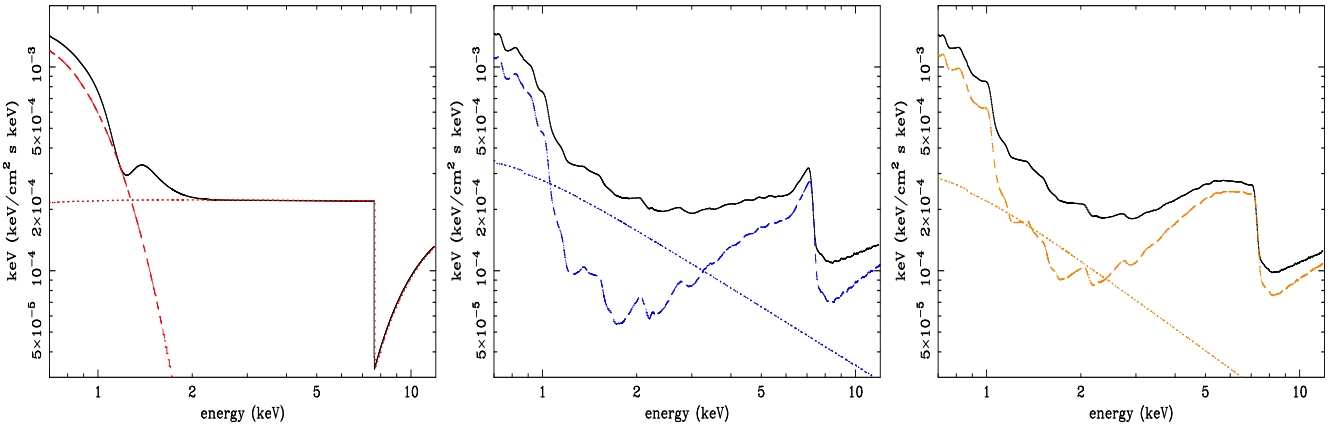

Figure 6.1: *Left panel* Phenomenological model of the mean spectrum, composed by black body emission (dashed) and power law (dotted) absorbed by two different components, an edge and a Gaussian line. *Middle panel* Two component models, composed by a steep power law (dotted line) and an ionized disc reflection model. *Right panel* Two components model with the reflection component calculated from an incident power law with low energy cut off at 22 eV.

carbon. The absorption is thus produced around 1–2 keV (with no requirement for relativistic outflow) mainly by the bunch of lines due to Fe L transitions and the total equivalent width being so high as few hundred electron volts.

Nevertheless, the energy at which this absorption feature occurs is exactly the energy where the flux of the soft excess is comparable with the one of the power law. A new possibility, that will be addressed here, is that the feature is spurious, being the result of a wrong parametrization of the soft excess continuum. In fact, both in the case of 1H0707–495 and of PG 1404+226 (the other two NLS1 showing such a low energy absorption line), the absorption feature is not required any more when the soft excess is fitted with a relativistically blurred ionized reflection component (Fabian et al. 2004; Crummy et al. 2005), that has a different spectral shape from the thermal, black body like, emission.

The source spectral variability has been studied in order to check if a power law plus ionized disc reflection model could explain not only the mean spectrum, but also the spectral variability.

6.2 The mean spectrum

As a first step, we fit the mean spectrum with a phenomenological model. We consider a simple continuum model comprising a power law plus black body emission for the soft excess. We fitted the 0.5–12 keV EPIC pn mean spectrum. Large residuals, of the order of 30% are present at 1–1.5 keV and above 8 keV. We find a good phenomenological description of these structures adding to the model two absorptions features, a Gaussian line at $\sim$1.2 keV (Leighly 1999; Vaughan et al. 1999) and an edge at about 8.2 keV (Boller et al. 2003).

Thus the best fit phenomenological model of the mean spectrum (see left panel of Figure

6.1) is composed by a black body emission with temperature of 127^{+2}_{-2} eV, a power law with Γ=$2.08^{+0.06}_{-0.05}$, an high energy edge observed at $8.22^{+0.12}_{-0.14}$ keV with an optical depth τ=$1.9^{+2.1}_{-0.78}$, and the absorption line observed at E=$1.24^{+0.02}_{-0.02}$ keV with a width of σ=$0.093^{+0.016}_{-0.014}$ keV and an EW$\simeq$-83 eV (having a normalization of -$3.32^{+0.5}_{-0.7}\times10^5$). All subsequent fits, unless otherwise specified include Galactic absorption with column density fixed at its nominal value (4.8×10^{20} cm^{-2}; Dickey & Lockman 1990). The total observed flux is 5×10^{-13} ergs s^{-1} and 2.3×10^{-12} ergs s^{-1} in the 2–10 keV and 0.5–10 keV band, respectively. This parametrization give an acceptable fit to the mean spectrum with a total chi square of 588.1 for 435 dof.

The high energy spectral drop could be due to the presence of an absorber along the line of sight. The rest frame energy of the absorption (8.2 keV) is significantly different from the one expected from neutral material at rest. Thus the absorption has to be produced either in ionized or outflowing material. Nevertheless, the sharpness (width$\simeq$0.2 keV) of the feature is not in agreement with an ionized absorber at rest. In this case, in fact, the drop would be due to many absorption lines (Fe XIX to Fe XXIII) resulting in a broader feature. For this reason an absorber outflowing with a velocity of 0.15 c seems to be favorite (Boller et al. 2003). Moreover, in order to match the intensity of the spectral feature and the high energy spectral shape, two outflowing absorbers only partially covering the nuclear source are required (Boller et al. 2003).

These two outflowing partially covering absorbers are not able to reproduce the soft absorption structure. In fact the feature at 1.2 keV may be related with a classical warm absorber. As pointed out by Nicastro et al. (1999), the distribution of relative ionic abundances in photo-ionized gas dramatically depends on the exact shape of the ionizing continuum. For this reason, we used the tables calculated with the UV-Xray continuum actually observed for this source (Leighly 2004[1]). We tried the Xstar tables with different turbulent velocity of the absorbing gas (from 100 to 3000 km/s). It is possible to find different combinations of the ionization parameter, column densities and velocity outflow that could roughly reproduce the feature. The ranges of the best fit ionization parameters (ξ=$\frac{L}{nR^2}$), column density (nH) and blue-shift velocities (v$_{blue}$) are: $\xi\gtrsim$1000 erg cm s^{-1}, nH$\sim10^{22}$–$few\times10^{23}$ cm^{-2} and v$_{blue}$ $\sim$0.22–0.3 c. Nevertheless, the determination of the true nature of the 1.2 keV feature is questionable. In fact, the low energy resolution of the pn camera does not allow to have a clear evidence of the presence of the absorbing gas. Nevertheless, the data of the high resolution RGS camera have not enough statistics to discriminate between an absorption feature that is composed by many narrow lines or a smooth continuum.

One interesting possibility is, in fact, that the low energy absorption feature could be somewhat fake, being just the result of a wrong parametrization of the soft excess emission that was here simply fitted with a black body emission. In particular a steeper high energy tail of the black body emission is required to get rid of this feature. We explored this hypothesis trying to fit the spectrum with different thermal models. First we considered models which take into account the expected temperature distribution of an accretion disk consisting of multiple black body components both with a zero and non–zero torque at the inner edge (EZDISKBB

[1]The Xstar tables grids "soft" (ftp://legacy.gsfc.nasa.gov/software/plasma_codes/xstar/xspectables/) have been used.

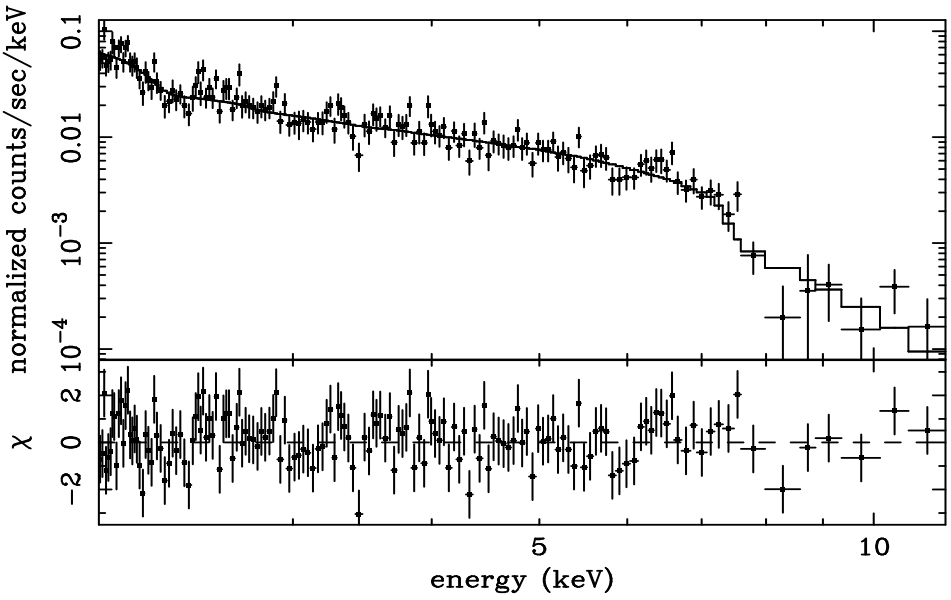

Figure 6.2: (Left panel) The 2–12 keV *XMM-Newton* EPIC–pn spectrum of IRAS 13224–3809 (observed frame). The high energy sharp feature is well reproduced by an ionized disc reflection model. The best fit Fe abundance is 10 times the Solar value.

and DISKBB respectively in Xspec). Then we tried models that take into account the presence of a Comptonizing plasma (COMPBB in Xspec). In all these cases (we also considered the relativistic effects occurring near to the black hole) it was not possible to have a so steep high energy tail of the thermal emission that allowed to fit the data without requiring the low energy absorption feature.

6.2.1 An ionized disc reflection model

Following Boller et al. (2003) we have fitted an ionized disc reflection model (Ross & Fabian 2005) to the high energy 2–12 keV observable band, in order to see if a very strong broad iron line could generate the feature at ∼8.2 keV that has been interpreted as absorption so far. The strong reflection component considered, is consistent with being produced by an accretion disc. The relativistic blurring is accomplished using a Kerr kernel (Laor 1991) with a broken power law radial profile as observed in the Seyfert 1 galaxy MCG-6-30-15 (Fabian & Vaughan 2003) and predicted by the models which take into account the light bending effect (Martocchia, Matt & Karas 2002, Miniutti et al. 2003, Suebsuwong et al. 2006).

The fit is very good with a χ^2/dof of 165/153 (Figure 6.2) and the sharp high energy feature is very well reproduced. The high energy spectral shape requires a disc inclination (α) between 60° and 62° and an extremely steep inner emissivity index of $q \sim 6-7$ with a break radius of ∼3.3 r_g. We assumed an outer disc emissivity index of 3, an inner and outer disc radii equal to the innermost stable circular orbit around a $a/M = 0.998$ Kerr black hole and to 100 r_g. The best fit model requires a strong overabundance (∼10 times solar) of Fe.

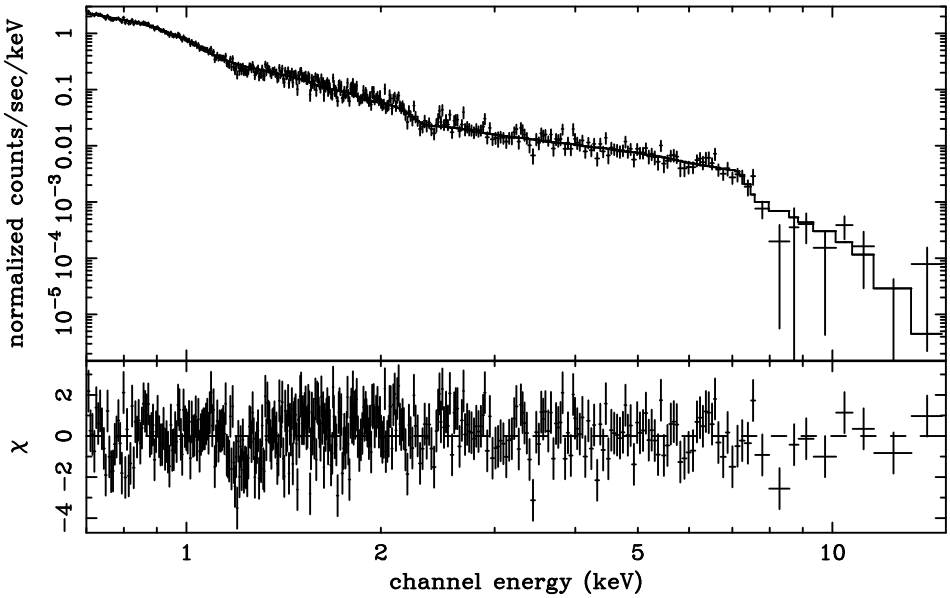

Figure 6.3: Blurred ionized reflection plus power–law model plotted on the mean spectrum of IRAS 13224–3809. The model fits the data reasonably well over the 0.7–10 keV band considered, see text for details.

We then extrapolate the best fit model to low energy, considering the whole pn energy band. The reflection component being ionized naturally reproduces also the soft excess. Nevertheless, in the reflection model we are using, all the abundances are fixed to the solar value and the only variable element is iron. It is expected that if the iron is so highly overabundant also the abundances of the other metals should be higher than the Solar value. A more extensive grid of variable abundance reflection models is thus required to fit the low energy part as well. A range of ionization parameters may also be needed to match the range of disc radii, so leading to a highly multiparameter solution which is beyond the scope of this paper. Thus, instead of using the entire band with a new multiparametric model, we decide to fit the data only above 0.7 keV, where the strongest emission lines are due to Fe only, with the reflection model appropriate for solar abundances with only the Fe overabundant (∼10 times solar).

Reasonable agreement is obtained (see Fig. 6.3 and middle panel of Fig. 6.1) with a model which is relativistically blurred and that has a photon index $\Gamma \sim 3$. The best fit parameters of the relativistic kernel do not change significantly ($\alpha \sim 61$, $q_{in} \sim 7$, $r_{in}=1.235$, $r_{br} \sim 2.2$, $r_{out}=100$ r_g, $q_{out}=2.8$). The ionization parameter of the reflection model is $\xi=1000$. Some residuals at less than 3 sigma are still present between 1–2 keV, but the gross shape of the big low energy absorption feature is now roughly reproduced. In fact adding a further absorption Gaussian line to the spectrum gives now a much lower EW of about 10–15 eV, the feature being now narrow and at ∼1.3 keV. It may be possible that this remaining feature is not real being just the result of the inaccuracies of the reflection model. The best fit model of the mean spectrum gives a $\chi^2/\mathrm{dof} = 480/395$.

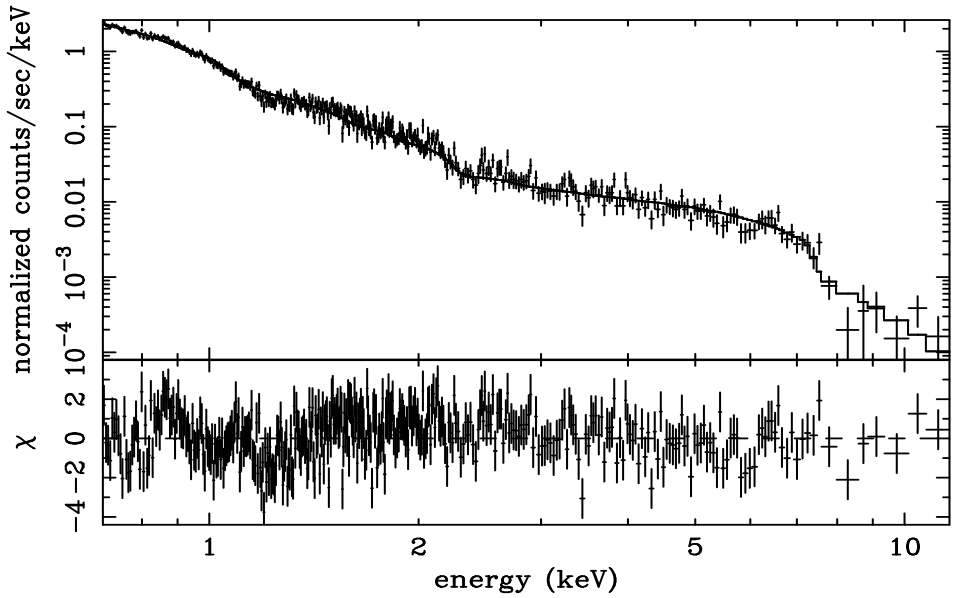

Figure 6.4: Blurred ionized reflection plus power–law model, with low energy cut off at ∼22 eV, plotted on the mean spectrum of IRAS 13224–3809, see text for details.

To calculate the reflection the assumed spectrum of the illuminating source is a power law with an high energy cut off at 300 keV and low energy at 1 eV (Ross & Fabian 2005). Nevertheless, in the cases where the primary illuminating source has a steep spectral index ($\Gamma \simeq 3$) the assumption of a low energy cut off is critical, because most of the energy is contained there. For this reason a new grid of reflection models with variable low energy cut off has been calculated.

Through a significantly worse fit (see Figure 6.1 right panel) is obtained with this new grid (χ^2/dof=558/395), however the gross shape of the spectrum is reproduced (see Fig. 6.4). The parameters of the relativistic blurring are similar to the previous case (α ∼61, q_{in}∼6.5, r_{in}=1.235, r_{br}∼3.3, r_{out}=100 r_g, q_{out}=3). While the low energy cut off is now 22 eV, the disc ionization is ∼200 erg cm s^{-1} and the power law spectral index is 3.12. Figure 6.4 shows that residuals are present between 0.9 and 1.3 keV. If these wiggles are fitted with an emission and an absorption lines the required EW are now bigger than in the previous case, being now of about 15-20 and 20-30 eV, respectively. We then refitted the data adding to the previous model an absorption line at 1.3 keV. The new parameters of the reflection model do not change within the errors demonstrating the solidity of the obtained values. Nevertheless, a significantly better fit, from a statistical point of view, is obtained with a χ^2 of 445 for 392 dof. The fits with the disc ionized reflection are not as good as that of Boller et al. (2003) obtained with a partial–covering model (χ^2/dof=509/470), but that model had five separate components, many of which operating on separate parts of the spectrum, whereas the reflection model used here has only two components (the power–law and the reflection), both of which are broad band. When emission/absorption low energy features are considered, the reduced χ^2 becomes comparable.

In fact, the main advantage of the reflection interpretation is that it is possible with this single component plus the power law to explain both the high energy (E∼8.2 keV) feature as well as the soft excess as well as at least part of the low energy structure (the absorption line at 1.2 keV). The direct comparison between these models is presented in Fig. 6.1 that shows the best fit "phenomenological" and "reflection" models. The left panel shows the black body emission (dashed) and power law (dotted) absorbed by two different components, while the middle and the right panels show the sum of reflection (dashed) and a steep power law (dotted) components. Figure 6.1 shows that in the reflection interpretation at least part of the absorption line is not required because the shape of the soft excess generated by the reflection is steeper than the one due to the black body emission. Moreover, the high energy drop is mainly generated by the strong Fe K emission line. The feature is observed at 8.2 keV because the disc inclination is high (∼61°). Moreover the main difference between the two models involving ionized reflection is the relative importance of the reflection component. In particular the right panel of Figure 6.1 shows an almost reflection dominated spectrum.

6.3 Source spectral variability

The *XMM-Newton* broadband light curve of IRAS 13224–3809 (see Figure 6.5) exhibits large amplitude count rate variations, typical for NLS1 in general. Nevertheless giant–amplitude flaring events, as observed in the *ROSAT* and *ASCA* observations, are not present during this observation. The source, during the *XMM-Newton* observation, is fainter and it appears to be in a period of relative quiescence compared with those earlier observations.

We start our analysis of the spectral variability of IRAS 13224–3809 by calculating the RMS spectrum. Figure 6.6 shows the RMS spectrum calculated with time bins of about 5 ks. The shape of the RMS is similar to the one presented in Gallo et al. (2004) that, instead, was calculated on a shorter time scale (200 s bins). The RMS spectrum of IRAS 13224–3809 shows a constant value of the variability at low energy between 0.2 and 0.5–0.6 keV. Then the variability rapidly increases showing a peak at about 1–1.5 keV. At higher energies the variability decreases with the lowest value between 4–6 keV. It is interesting to note that IRAS 13224–3809 shows the same amount of variability at low (below ∼0.6 keV) and high (above ∼5 keV) energy, exactly where the contribution to the spectrum of an ionized reflection would be more important. The RMS peaks, instead, where the power law component is expected to dominate.

6.3.1 Time resolved spectral variability

A steep power law and an ionized reflection component may roughly reproduce the mean spectrum of IRAS 13224–3809. In order to further test their model, a time–resolved spectroscopy on the shortest possible timescale (set by requiring good quality time–resolved individual spectra) has been explored. We sliced the source light curve in ten intervals (see Figure 6.5) of ∼5 ks each and accumulated a spectrum in each interval. These were then fitted with the two best fit ionized reflection models which were able to reproduce the mean spectrum. We decided to study both models, and not only the more physically plausible one, in order to better understand the robustness of the results. Thus, each of the ten spectra was fitted twice

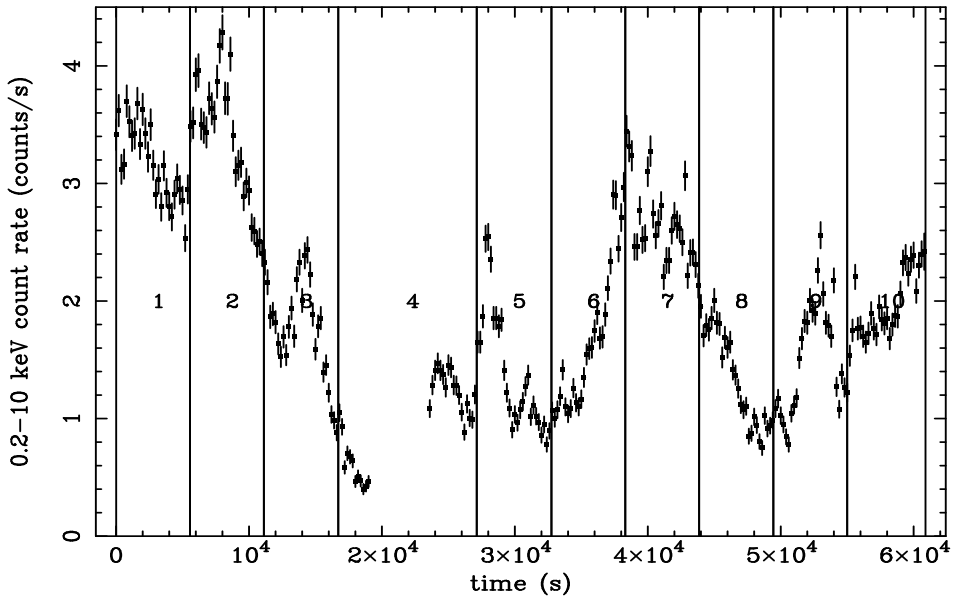

Figure 6.5: Broadband 0.2–10 keV *XMM-Newton* EPIC–pn light curve of IRAS 13224–3809. The 5 ks slices used in the time–resolved spectroscopic analysis are also shown.

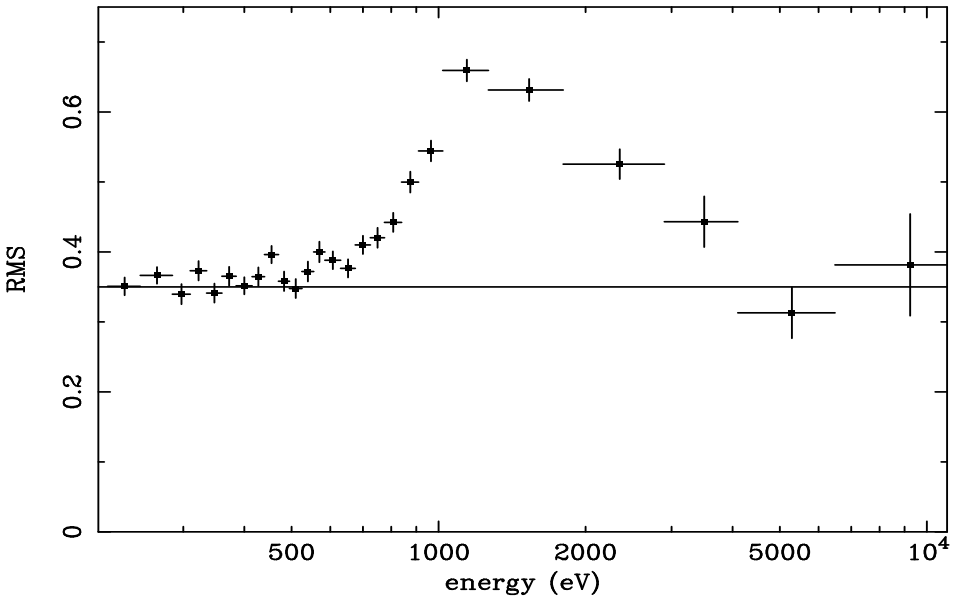

Figure 6.6: RMS spectrum computed with time bins of about 5 ks, the same as used in the as time-resolved spectroscopic analysis. The variability at high and low energy is the same.

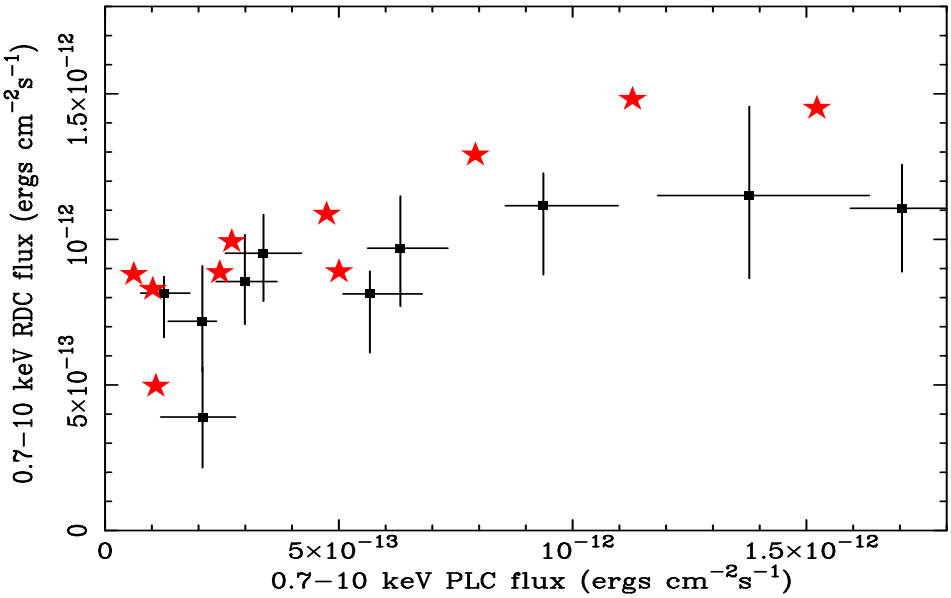

Figure 6.7: Ionized reflection flux versus power law 0.7–10 keV flux. The reflection varies with smaller amplitude with respect to the power law. The filled squares with the error bars and the red stars show the best fit with the reflection from a power law with low energy cut off at 1 eV and at 22 eV, respectively. The error bars are similar in the two cases and they are shown only once for clarity.

with a power law with fixed slope and variable normalization plus a disc ionized reflection convolved with the same LAOR kernel of the mean spectrum. Clearly the ionized reflection had in the former case a low energy cut off at 1 eV while at 22 eV (in the latter one). In the fit, the only free parameter of the relativistic kernel is the index q of the inner disc emissivity profile ($\epsilon = r^{-q}$). The ionized reflection model has the normalization as free parameter (the disc ionization is fixed to 1000 and 200 erg cm s^{-1}, respectively), while the photon index of the illuminating power law in the ionized reflection model is tied to that of the power law and therefore fixed to $\Gamma \sim 3$ and 3.12, respectively. In both cases the model reproduce very well the data at all flux levels with a reduced χ^2 between 0.9 and 1.2.

Fig. 6.7 shows the 0.7–10 keV flux of the ionized reflection versus the power law flux in the same band. The filled squares with the error bars show the best fit results with the first model, while the red stars with the second. In this latter case the amount of reflection is higher, in agreement with the fit of the mean spectrum (see Fig. 6.3). Nevertheless, in both cases, the disc ionized reflection appears to be much more constant than the power law. The first, in fact, has variations lower of a factor of 3 while the second has variations up to a factor of ten during the observation. Moreover the disc reflection seems correlated with the power law at low flux levels, while the correlation breaks down and the disc reflection becomes almost constant as the power law flux increases. This behavior is similar to the one observed in MCG-6-30-15 and NGC 4051 and it is in very good agreement with the qualitative predictions of the light

bending model (Miniutti et al. 2003; Suebsuwong et al. 2006; see §1.3.1).

Fig. 6.8 shows the disc reflection emissivity index q as a function of the power law flux. The value of the inner disc emissivity is extremely high. The more extreme values could be relaxed allowing other parameters of the model to vary (i.e. the radius of the break of the disc illumination profile, the disc ionization state). However the statistic is not sufficiently for such a multiparametric fit. Moreover, a trend is found in Fig. 6.8 where low flux states generally correspond to steeper emissivity profiles. This result is consistent with the predictions of the light bending model (Miniutti & Fabian 2004).

6.4 Reproducing the RMS spectrum

As a further test we compared the RMS spectrum with the one calculated for a constant reflection component. We assumed that all the source variability is due to the variation of the normalization of the direct power law that has a spectral index fixed at Γ=3 and that the reflection component is completely constant not only in normalization, but also in spectral shape (the reflection parameters are fixed to the best fit obtained for the mean spectrum). To simulate the RMS we vary the power law normalization from its lowest to highest values observed. The gray (light blue in the color version) line in Fig. 6.9 shows this simulated RMS. The interplay between the power law and the reflection can roughly reproduce the shape of the RMS (within $\Delta RMS \lesssim 10$ %). This means that the spectral variability could be roughly reproduced by just the variations of the intensity of a power law added to a constant component that has the shape of the best fit blurred ionized reflection of the mean spectrum. The peak of the variability is, in fact, where the power law component is more important with respect to the reflection.

We then simulated the RMS spectrum allowing the ionized reflection to vary. The variations that we consider are the one observed in the time resolved spectral variability study (similar results are obtained with both cases of ionized reflection). The black (red in the color version) line in Fig. 6.9 shows the RMS spectrum simulated from the best–fit values. It very well reproduces the data showing no significant deviations. This confirms that the modelization of the time resolved spectral analysis is correct needing no other components. In particular we want to stress that the variations of the parameters of the reflection, and in particular of the disc illumination index (q) introduces spectral variability at a $\sim$10 % level and they introduce variability where the reflection component is more important in comparison to the power law, that is below 1 keV and above 4–5 keV.

6.5 Discussion

The spectrum of the NLS1 galaxy IRAS 13224–3809 exhibits: i) the strongest soft excess of the sample; ii) an impressive drop of emission at $\sim$8.2 keV; iii) an absorption feature at 1.2 keV well modeled by a Gaussian absorption line reproduced, when the soft excess is fitted with a BB model.

A relativistic blurred reflection–dominated model plus a steep power law component is not able to reproduce all the features leaving wiggles in particular at low energy. It gives, however,

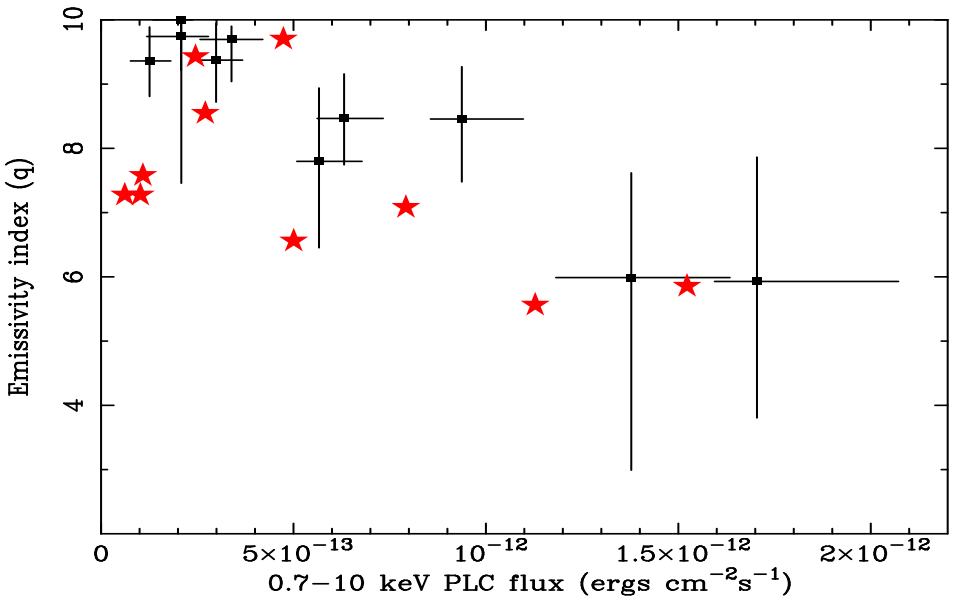

Figure 6.8: The inner emissivity index of the relativistic blurring model is plotted versus the power law flux in the 0.7–10 keV band. Symbols as before.

a reasonable fit to the mean spectrum, broadly reproducing the spectral shape and the high energy drop, and at least part of the 1.2 keV feature. Remarkably, this simple model also allows to account for the spectral variability which can be described by a strongly variable power law with constant spectral shape and an almost constant ionized reflection. In order to best match the spectral variability, some variations in the normalization and in the shape of the reflected component are required. Nevertheless the major source of variations are just due to the power law. A major consequence of this variability is that the spectrum becomes more and more reflection–dominated as the flux drops. During the lowest flux periods, the 0.7–10 keV flux of the ionized disc reflection greatly exceeds the flux of the power law, leading to an almost reflection dominated spectrum.

The reflection is affected by strong relativistic effects, suggesting that it originates in the innermost regions of the accretion disc around a rapidly rotating Kerr black hole. Indeed, the disc illumination radial profile is consistent with a broken power law with a steep (q$\sim$6-7) inner index and a flat (q$\sim$3) outer one. A similar broken power law disc illumination radial profile has been observed in the well studied Seyfert galaxy MCG-6-30-15 and it is consistent with the predictions of the models which take into account the light bending effect. Nevertheless the extreme values of the inner illumination radial profile obtained during the low flux periods (q$\simeq$8–10) do not fit within the light bending model. So extreme values would require tapping of the BH spin in order to be reconciled with the model.

The strong ionized reflection interpretation requires an extreme value not only of the disc illumination parameter, but also for the iron abundance, which is needed to be 10 times super-solar. Nevertheless it is important to stress that an even higher iron abundance is required

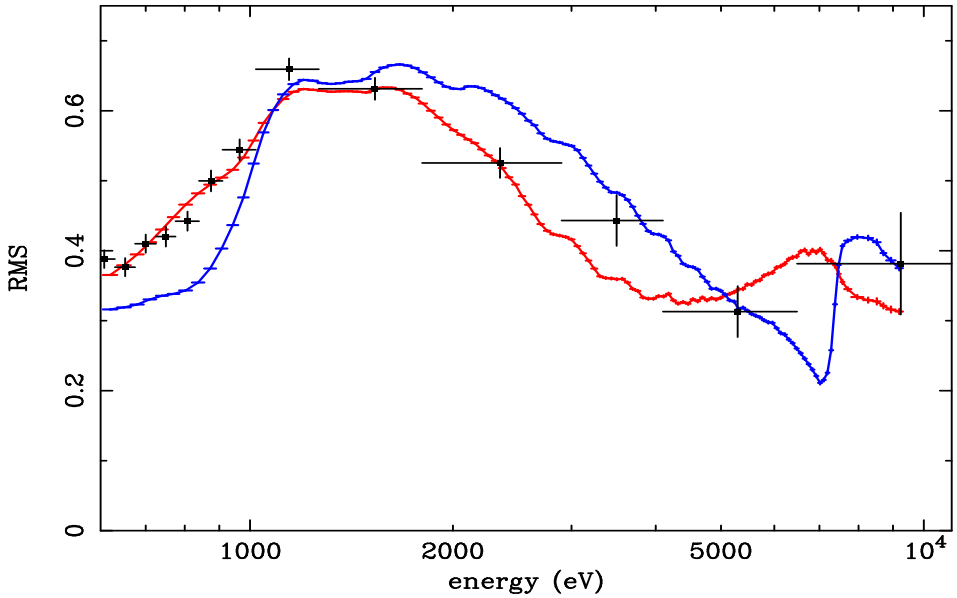

Figure 6.9: The observed RMS spectrum is compared with synthetic ones. The gray (light blue in the color version) line is obtained varying in normalization (from the lowest to the highest value observed) a power law with Γ=3 and keeping an ionized reflection component completely constant and with the same shape as observed in the mean spectrum. While the black (red in color) line is calculated starting from the best–fitting two–component model (Sect. 5.1).

in the partial covering interpretation (Boller et al. 2003). Moreover, the observation of an Fe overabundance is in line with the fact that IRAS 13224–3809 shows one of the strongest Fe II line of its class. Such an extreme overabundance of iron could be explained by an high rate of type Ia supernovae that produce much more iron (more than an order of magnitude) than type II ones (Nomoto et al. 1997a,b).

Probably the major remarkable characteristic of IRAS 13224–3809 is its strong variability. In fact after a 30–d *ROSAT* monitoring, in which it showed variations by up to a factor of about 60 (Boller et al. 1997), it was recognized as the most variable Seyfert galaxy of the sky. During the *XMM-Newton* observation the source was in a relatively quiet and low flux period. An interesting possibility is that part of the variability is due to a beaming effect as expected due to the observed high inclination of the disc (62°). In fact, the flux of the reflection is enhanced by a factor of about ∼5e with such an high inclination of the disc compared with a face on accretion disc (Crummy et al. 2005). The beaming effect, lowering the intrinsic luminosity, may alleviate the considerations about the high accretion rate that thought to be present in this object. Nevertheless the high inclination does not fit very well with the unification model of AGN (Antonucci & Miller 1985; Antonucci 1993), in which type 1 objects should be seen at low inclination because the molecular torus is not along the line of sight. However, IRAS 13224–3809 is pretty luminous and, as suggested by Lawrence (1991) and

Brandt & Hasinger (2005), more luminous objects seems to have less absorption.

At low energy the reflection model is steep enough to reproduce at least part of the feature at 1.2 keV. A broad absorption line is however still required by the data. Other NLS1s of the *ASCA* catalogue studied by Leighly et al. (1997) which showed this apparent absorption feature near 1 keV have been reproduced with just a power law plus an ionized disc reflection (Fabian et al. 2004; Crummy et al. 2005). Thus even if the reflection is not able to completely reproduce the feature here it can not be excluded that the absorption feature is spurious and the remaining low energy wiggles are due to the approximated calculations of the reflected spectrum. Longer observations with higher energy resolution are needed to clarify this issue.

The model proposed here for IRAS 13224–3809 naturally reproduces also the soft excess. The "constant temperature" problem (Gierlinski & Done 2003) can then be naturally solved because of the very non-thermal nature of the reflection component. Other interpretations like the double "partial covering" model cannot be excluded (Boller et al. 2003), however, the reflection interpretation has the great advantage of explaining the broad–band spectrum and its variability with the interplay of only two (broad–band) components, without the need to invoke separate components in the different energy bands.

Chapter 7

Key study objects: iv) MKN 841, a Seyfert 1 with puzzling Fe K line variability

7.1 Introduction

MKN 841 is a bright Seyfert 1 galaxy (z=0.0365, Falco et al. 1999), one of the rare Seyfert 1 detected by OSSE at more than 3 σ (Johnson et al. 1997). It is known for its large spectral variability (George et al. 1993; Nandra et al. 1995), its strong soft excess (this was the first object where a soft excess was observed, Arnaud et al. 1985) and its variable iron line (at least on a year time scale, George et al. 1993). The latter was observed in some cases with a relatively large equivalent width (hereafter EW) of about 400 eV (Day et al. 1990; Bianchi et al. 2001) significantly above the value predicted by standard cold reflection models (e.g. George & Fabian 1991).

Recent *XMM-Newton* observations (Petrucci et al. 2002; Longinotti et al. 2004) have revealed a puzzling behavior of the iron line in MKN 841. Indeed the presence of a highly variable, but narrow iron line feature as observed in OBS 2 and OBS 3 (see Tab. 7.1) in 2001 was completely at odds with any currently accepted interpretation of the line origin (Petrucci et al. 2002) and required further investigations. Longinotti et al. (2004) re-analyzed the *XMM-Newton* data and proposed that the line may have varied in width rather than in flux. Their interpretation then invokes local illumination by a flare inducing a hot spot in the inner disc, which then becomes progressively broadened as the disc rotates. For a better understanding of the puzzling spectral and temporal behavior of this source, it has been observed again in 2005 for a total duration of $\sim$75 ks.

7.2 Model-independent analysis

Before going into the details of the spectral variability study, we investigated the source using model independent techniques.

	OBS 1	OBS 2	OBS 3	OBS4	OBS5
Start date	2001-01-13 (05h20m55s UT)	2001-01-13 (09h33m50s UT)	2001-01-14 (00h52m28s UT)	2005-01-16 (12h38m21s UT)	2005-07-17 (06h38m03s UT)
Exposure (s)	8449	10900	13360	45982	29071
Cts.s^{-1} pn	18.0	22.2	21.8	5.6	7.2

Table 7.1: Observation epochs, exposure and mean count rates.

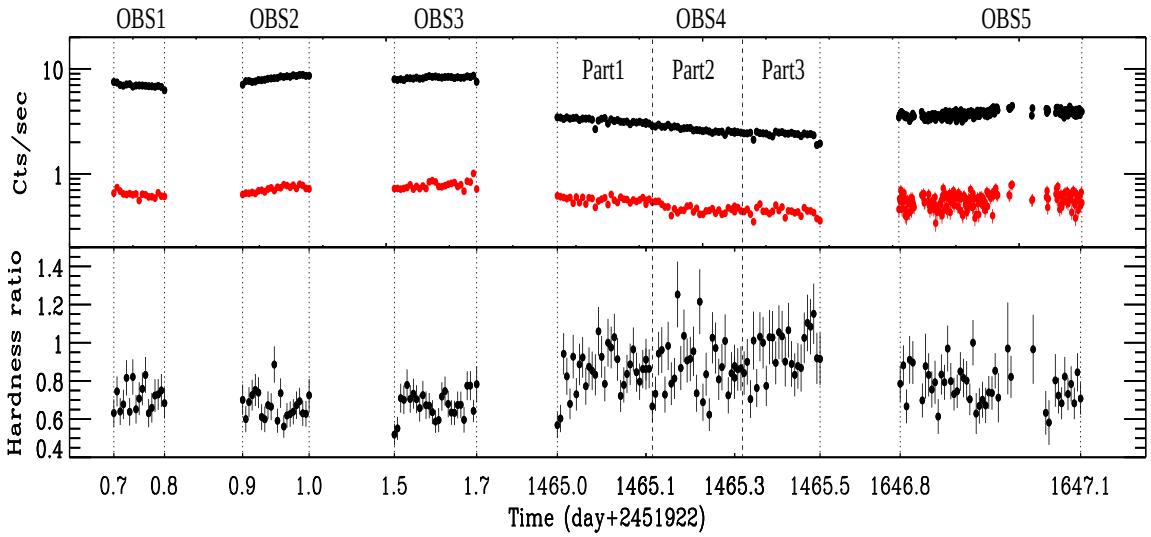

Figure 7.1: (*Upper panel*) Total (0.5-10 keV, upper curve) and hard (3-10 keV, lower curve) X-ray light curves of the different EPIC-pn observations of MKN 841. The broad band flux is clearly dominated by the soft (< 3 keV) bands. The soft X-ray count rate varies by a factor 4 in 4 years while the hard X-ray one varies by only $\sim$ 60 %. On the other hand flux variability up to $\sim$50 % is also observed on tens of ks. The hardness ratio is plotted on the lower panel.

7.2.1 Light curves and hardness ratios

The top of Fig. 7.1 shows the 0.5-10 keV EPIC-pn count rate light curve (upper data points, in black) of the different *XMM-Newton* observations of MKN 841 as well as the hardness ratio (5-10)/(3-5) at the bottom. The time binning is 500 s. The total 0.5-10 keV count rate decreases by a factor $\sim$5 in 4 years while the hardness ratio increases, reaching maximum values during OBS 4. The 3-10 keV count rate has been also plotted on top of Fig. 7.1 (lower data points, in red). Between 2001 and 2005, it shows variations of a factor two lower than the total count rate meaning that the broad band count rate variability is dominated by the soft (less than 3 keV) X-ray variability, at least on long time scale. Smooth soft and hard flux visibilities up to $\sim$50 % are also visible on tens of ks.

7.2.2 Spectral ratios

Fig. 7.2 shows the ratios of the different EPIC-pn spectra with the EPIC-pn spectrum of OBS1. The binning is such that each bin has a 5 σ confidence level significance. While no

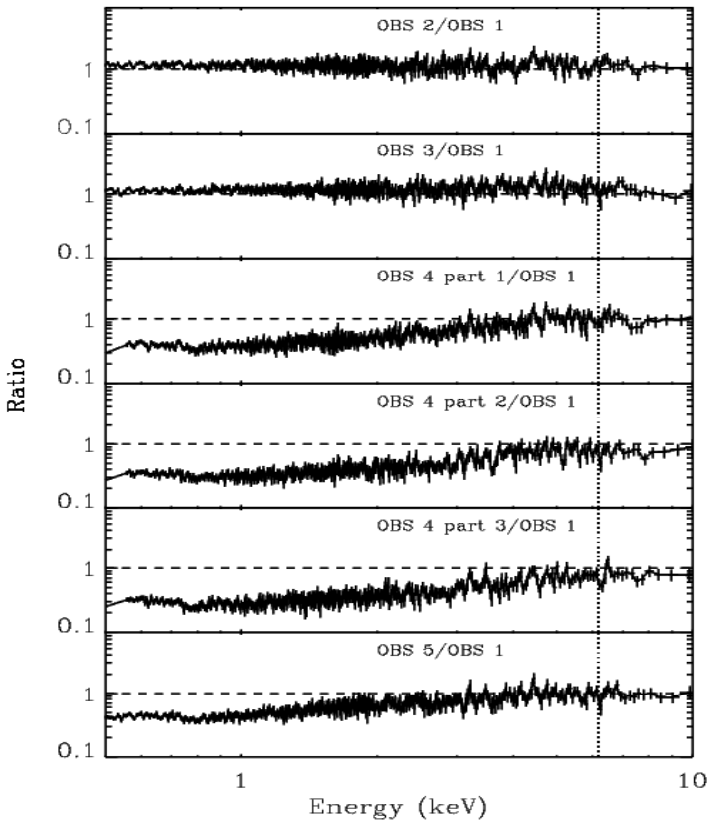

Figure 7.2: Ratios between the different EPIC-pn spectra and the EPIC-pn spectrum of OBS 1. The dashed line correspond to the position of the 6.4 keV line in the source frame.

strong spectral variations are observed on time scales as short as hours (i.e. the time between OBS1, OBS2 and OBS3), the 3-10 keV spectral shape hardens between 2001 and 2005, in agreement with the increases of the hardness ratio shown in Fig. 7.1, and more strongly below 6-8 keV. Above 8 keV the spectra keep staying roughly constant at least in shape. We can also notice some variations of the iron line complex especially on long and short time scale.

7.2.3 RMS

The three panels of Fig. 7.3 show the RMS spectra of each observation calculated in the 0.5-10 keV energy band with a time binning of about 1-2 ks. To increase the statistics we have grouped OBS 1, 2 and 3 to produce a single RMS spectrum (left panel of Fig. 7.3). Due to the low statistics we were not able to produce spectra with a large number of energy bins especially at high energy. Anyway some comments can still be done. The different RMS spectra are relatively flat and those of OBS 1/2/3 and OBS 5 are consistent with being constant with less than $\sim$4 and 5 % of variability respectively. On the contrary the OBS 4 one is not consistent with being constant (at more than 99.99 %). In this case we note a rough increase of the RMS from 0.5 to about 2-3 keV and then a clear decrease at higher energies down to a few

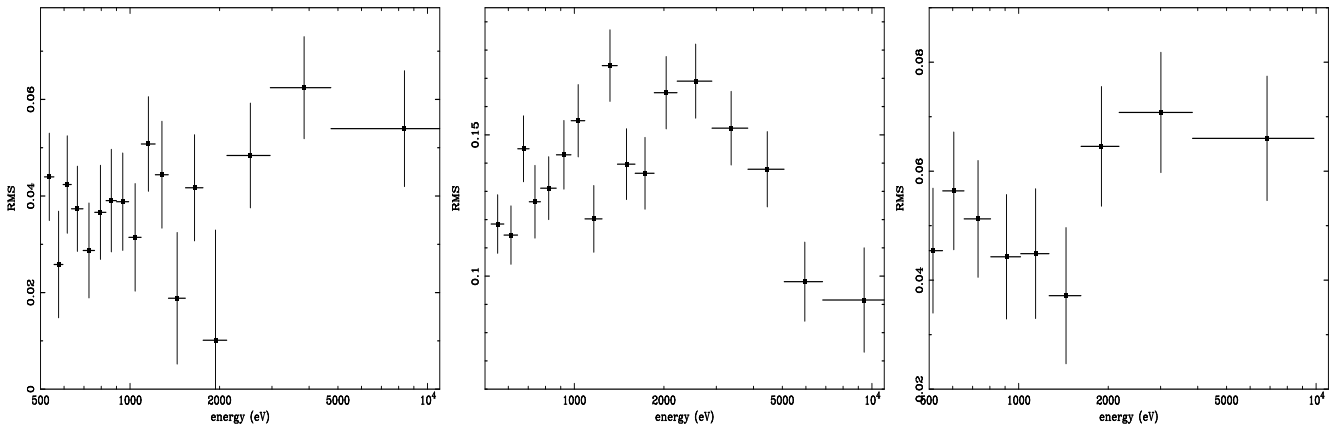

Figure 7.3: *Left, Middle* and *Right* panels show the RMS spectra during the three summed observations OBS 1/2/3, the observation OBS 4 and the OBS 5, respectively. The time binning used in the calculation is about 1-2 ks.

percent. Thus the weak variability observed at high energy (above 8 keV) on month and year time scale is also observed on the short timescales probed by the RMS spectra (see §7.2.2 and Fig. 7.2).

7.3 Spectral analysis

7.3.1 Phenomenological analysis

The first step of the spectral analysis was to fit the data with a simple power law model, excluding the data below 3 keV. Figure 7.4 shows the ratio between the *XMM-Newton* data of OBS 4 with the corresponding best fit power law. We clearly observed a strong soft excess below 2-3 keV and a fluorescent iron line complex near 6.4 keV.

The second step was to include very simple spectral components to reproduce the observed features in the 0.5-10 keV band. We use a power law for the high energy continuum and a multicolor black body component for the soft excess plus a Gaussian for the iron line.

The fits are clearly not satisfactory for all the observations and large discrepancies are present especially below 3 keV due to the poor black body approximation for the soft excess. Different considerations can already been done:

- The photon index reaches values as small as $\Gamma \simeq 1.3$ during OBS 4 where the flux is the weakest.

- The flux variation in the soft band (lower than 3 keV) between 2001 and Jan 2005 is more than a factor 2 larger than the flux variation above 3 keV. Moreover, once again the best fit black body temperature is observed to be between 0.12 and 0.18 keV, a too high value for the standard interpretation, considering the mass of the black hole in MKN 841.

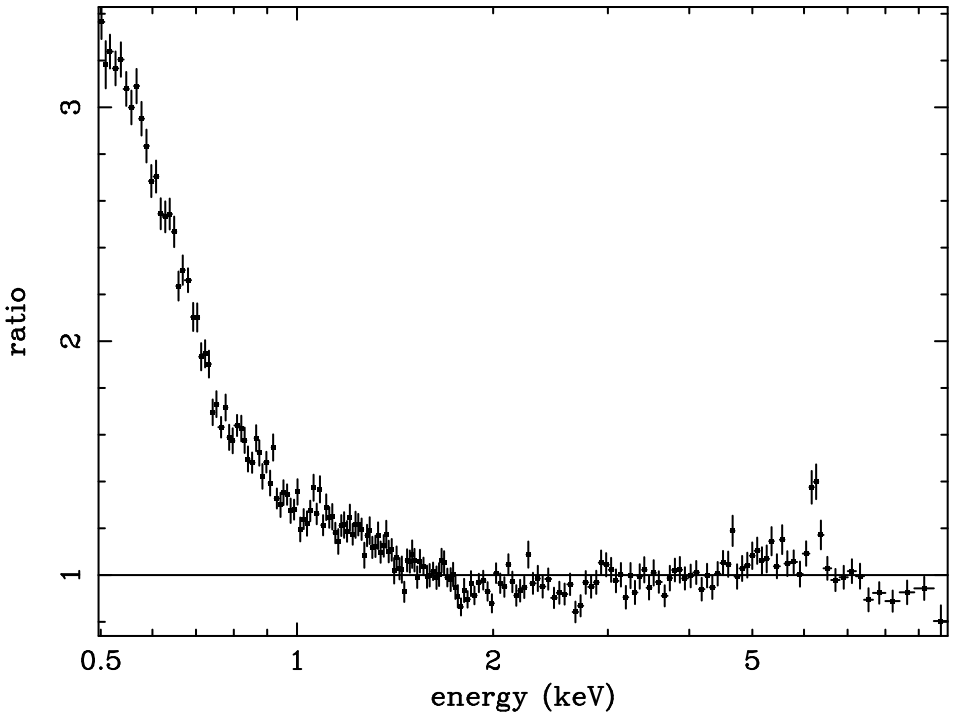

Figure 7.4: Ratio data/model for OBS 4. The model is a simple power law fitted between 3 and 10 keV and extrapolated down to low energies. A strong soft excess and a line near 6 keV are clearly apparent. Note also the presence of a narrow feature near 4.5 keV.

- The iron line profile appears variable on relatively short time scale, <15 ks, e.g. between part 1 and part 2 of OBS 4.

Concerning the iron line, the 2005 observations confirm the line variability already observed in 2001 by Petrucci et al. (2002) and Longinotti et al. (2004). The spectral variability agrees with the results shown previously with model-independent methods and suggest a spectral pivot at high energy. However the presence of a simple power law continuum is unlikely given the unusually (for a Seyfert galaxy) hard spectral index of OBS 4.

7.3.2 The iron line complex

Rapid variability

The best fit results with the phenomenological analysis indicate the presence of a narrow line in all the observations but OBS 3 and part 2 of OSB 4 where a broad component is preferred. The contour plots (at 68 and 90 % confidence level) of the line flux vs. line width for the different observations are plotted on Fig. 7.5 for 2001 (left panel) and 2005 (right panel). The rapid (on hour time scale) variability of line complex seems to be a typical characteristic of this source. For a better visualization of this variability we have plotted on Fig. 7.6 the excess map of the complete set of the *XMM-Newton* observations. This map has been obtained following

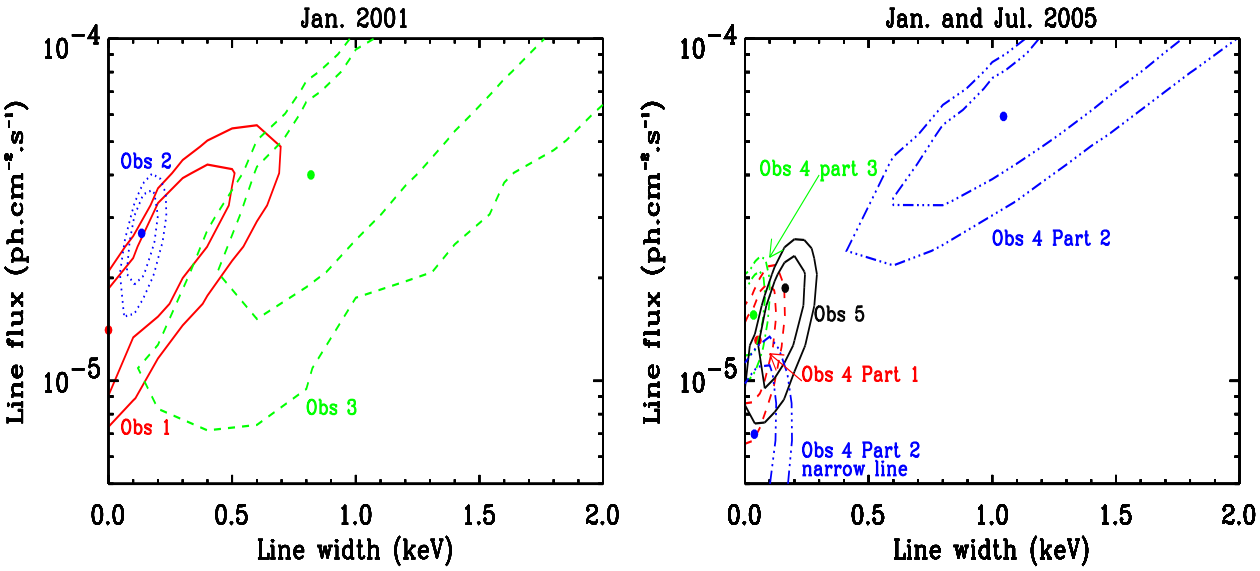

Figure 7.5: Contour plots (68 and 90 %) of the line width vs. line flux for the 3 observations of Jan 2001 (left) and the 3 parts of Jan. 2005 (right). In both cases, the model includes a simple power law and a Gaussian line. We have also over plotted on the right the contour plots of OSB 5 as well as the contours of the narrow component detected in part 2 of OBS 4.

the method of Iwasawa et al. (2004) and Tombesi et al. (2007). We use resolutions of 2 ks in time and 100 eV in energy. Each temporal slit represents the residuals obtained when fitting each 2 ks spectrum with a power law between 3.5 and 8 keV but ignoring data between 4 and 7 keV. This map is useful to reveal narrow features but broad ones can be mixed up with the underlying continuum. A narrow feature close to 6.4 keV is clearly present during most of the different pointings, but it seems to disappear from time to time on a very short time scale (of the order of a few ks) like in OBS 3 or in the middle of OBS 4 and OBS 5 .

Another way to strongly the rapid variability of the narrow line component is to plot the light curve of its flux and equivalent width. It is plotted on the left panel of Fig. 7.7 with a 4 ks binning time scale. The model includes a power law and a narrow Gaussian line with energy fixed to 6.4 keV. Different remarks can be done. From time to time the narrow line is poorly detected with only upper limit on its flux and EW. However both are also consistent with a constant (at more than 98 %).

Remote reflection

The spectra of AGNs have shown the evidence of a widespread presence of a constant and narrow component of the Fe K line. This line is produced by reflection from the outer part of the accretion disc or even farther away from for example the dusty torus expected in the unification framework of AGNs and surrounding the inner regions of the galaxy. To further test this hypothesis, we simply fit the 3-10 keV data of OBS 1/2/3, OBS 4 and OBS 5 with a power law and a narrow Gaussian line. The contour plots of the narrow line flux vs. line

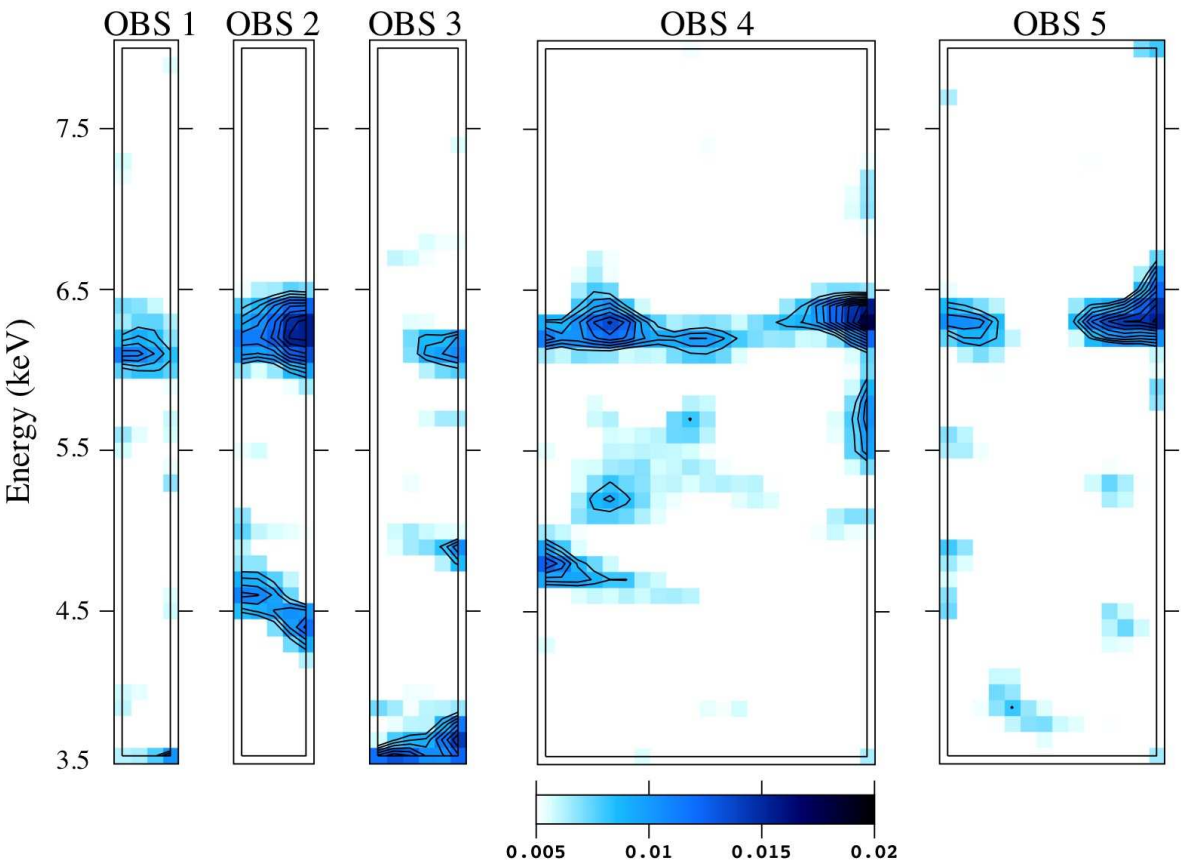

Figure 7.6: Map excess of the different *XMM-Newton* observations.

energy are plotted on the right panel of Fig. 7.7. The line fluxes obtained in the different observation periods are consistent with each other, nevertheless the contour plots suggest a variation of the energy of the line. This peculiar behavior could be understood if the line is composed by two different components: i) a constant and narrow component coming from distant material, stabilizing the line flux at 6.4 keV; ii) a broad component, variable on short timescales.

In this last case, the line observed at ∼6.2-6.3 keV, during OBS 1/2/3, may be due to a slightly redshifted narrow iron line produced in the innermost regions of the accretion disc without excluding the presence of a constant Fe K line from a distant material. In fact if we add a second narrow line component fixing the parameters of the first line to their best fit values, the best fit energy (E_{line} =$6.4^{+0.4}_{-0.3}$ keV) and flux ($F_{line} \lesssim 6.5\times10^{-6}$ ph cm^{-2} s^{-1}) of this second line is in agreement with those obtained in OBS 4 and OBS 5 and is thus consistent with the presence of a constant remote reflection between the different observations.

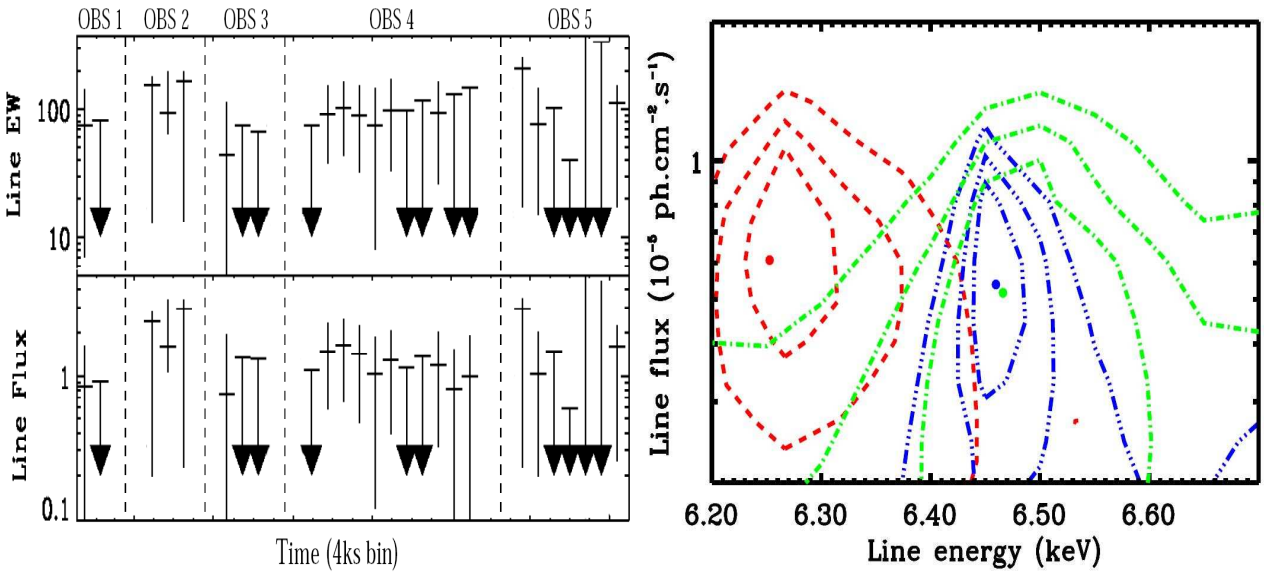

Figure 7.7: (*Left panel*) Equivalent width (top) and flux (bottom) light curves of a narrow Gaussian line whose energy is fixed to 6.4 keV. We use a 4 ks time binning. (*Right panel*) Contour plots line flux vs. line energy (in the source frame) of the narrow line component added to mimic emission from remote reflection. OBS 1/2/3, red dashed; OBS 4, blue/dot-dot-dot-dashed; OBS 5 green/dot-dashed contours, respectively.

Relativistic effects

On the other hand the rapid variations of the line (see Fig. 7.5, 7.6 and 7.7) suggest the presence of a broad and rapidly variable line component. This is also illustrated in Fig. 7.8 where we have plotted the ratio of the complete OBS 4 data spectrum and the best fit power law obtained fitting only the data above 3 keV but ignoring the 4-7 keV energy range. The presence of a complex line profile is clearly visible with a broad component down to ∼4.5 keV.

The shape of the line is well reproduced with a relativistic profile (DISKLINE model in XSPEC) fixing the accretion disc outer radius to 1000 r_g. The best fit energy is E_{FeK}=$6.35^{+0.47}_{-0.53}$ keV, the line EW is 350^{+50}_{-50} eV, the inner disc radius r_{in}=$8.9^{+14.6}_{-1.7}$ r_g, the disc emissivity power law index q >3.6 and the disc inclination i=26^{+26}_{-8} degree. The fit is very good with χ^2/dof=148/166, suggesting that relativistic effects could be a good explanation of the line profile. Following this interpretation we fit the spectra of the different observations with the same model fixing the inclination angle to 30 deg. The fits are acceptable for all observations but the physical interpretation of the line variability is not clear each parameter (e.g. q, T_{in}) being potentially responsible of a part of the line variability. The disk emissivity power law index is poorly constrained and relatively large (especially in 2005) but still in agreement with theoretical expectations from Martocchia et al. (2002).

7.3.3 A more physical analysis: blurred ionized reflection?

The clear presence of a broad component of the Fe K line during OBS 4 with the presence of a variable line profile, as well as the presence of a strong soft excess and an high reflection fraction during a period of high flux (Matt et al. 2000; Bianchi et al. 2001; Petrucci et al. 2002) suggest that ionized reflection may have an important role in this source.

To test this assumption we have used a model with the following components: 1) a neutral absorption, free to vary above the Galactic value; 2) a cut-off power law continuum (the high energy cut-off being fixed to 300 keV); 3) a blurred photo ionized reflection; 4) a constant neutral reflection (for the neutral reflection we fix the illuminating power law continuum to 1.9). For the neutral and ionized reflection, we use the constant density approximation (Ross & Fabian, 2005). The blurring is done by convolving the reflection spectrum with a profile that assumes that the black hole is spinning. The disc ionized reflection is expected to reproduce the soft excess and the broad iron line while the neutral reflection is expected to reproduce the narrow line component. The free parameters of this model are the continuum power law photon index and normalization, the inner radius of the reflecting accretion disc as well as the disc emissivity power law index and the normalization and ionization parameter of the ionized reflection component. The iron abundance is fixed to the solar one for the computation of the reflection, the disc outer radius to 1000 Schwarzschild radii and the inclination angle to 30 degrees. We apply this model to the 0.5-10 keV energy range of the pn detectors, analyzing OBS 1, 2, 3 and the three parts of OBS 4 simultaneously. In the fitting process we kept all the parameters constant between the different data sets except the continuum and ionized reflection normalizations and the ionization parameters.

While this model reproduce relatively well the global spectral shape of the data the fits are not very good. The residuals show some features especially in the soft band and suggest the presence of absorption. These features are more pronounced in 2005. Such absorbing material is indeed confirm by a quick look to the RGS data. A detailed analysis of this component is beyond the scope of this dissertation. For the present analysis, we model these absorption features by adding a standard warm absorber component (ABSORI in XSPEC) in our fits, letting the absorber hydrogen column density and ionization parameter free to vary. The improvement is highly significant with a $\Delta\chi^2$ of 30, 79 and 75 for the addition of two parameters for OBS 1/2/3, OBS4 and OBS 5, respectively. The best fits becomes now statistically acceptable. The corresponding best fit parameter values are reported in Tab. 7.2.

The continuum power law index is now noticeably steeper than in our previous fits reaching $\Gamma \sim 2.5$ in OBS 1/2/3, $\Gamma \sim 1.6$ in OBS 4 and $\Gamma \sim 2.0$ in OBS 5. If such steepening is indeed expected with the addition of a reflection component, the value obtained in 2001 is relatively unusual for a Seyfert 1 galaxy. The ionization parameter of the blurred reflection as well as the ionization parameter of the WA are significantly smaller in OBS 5 compared to OBS 1/2/3 and OBS 4. Interestingly, while the disc inner radius keeps still extreme values, the disc emissivity power law index, now also constrained by the soft excess, is close to 4 in OBS 4 and OBS 5, in better agreement with theoretical expectations (Martocchia et al. 2002; Miniutti et al. 2003; Miniutti & Fabian 2004).

On the contrary q is still very large (q>8.6) in OBS 1/2/3. The relatively extreme values of q and Γ in 2001 may then reveal the limits of the model used. Anyway, the two parameters

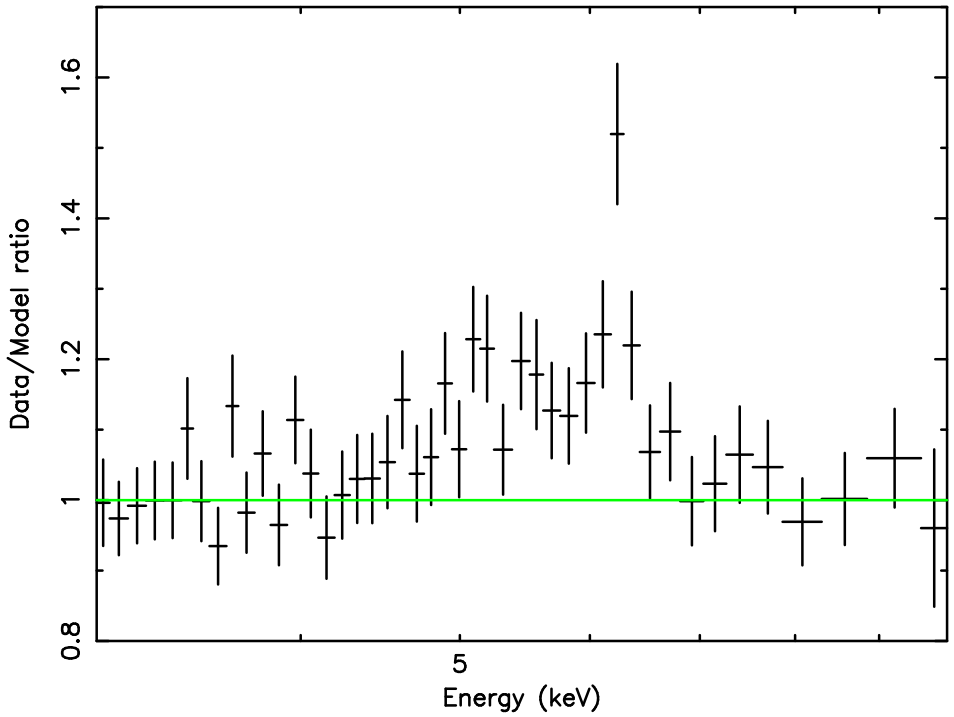

Figure 7.8: Ratio data/model for OBS 4. The model is a simple power law fitted between 3 and 10 keV, ignoring the 4-7 keV range. Broad and narrow components are clearly visible.

Table 7.2: Best fit results obtained with the blurred ionized reflection model plus warm absorber. $\Delta\chi^2$ is the fit improvement with the addition of the warm absorber.

Obs.	Γ	ξ	q	r_{in}	N_h^{WA}	ξ^{WA}	$\Delta\chi^2$	χ^2/dof
1/2/3	$2.45^{+0.05}_{-0.04}$	130^{+10}_{-10}	>8.6	<1.38	$1.1^{+0.1}_{-0.4}$	>900	30	783/787
4	$1.59^{+0.01}_{-0.02}$	310^{+10}_{-10}	$3.7^{+0.2}_{-0.2}$	<2.5	$2.7^{+0.8}_{-0.5}$	1500^{+470}_{350}	73	859/808
5	$2.01^{+0.09}_{-0.05}$	80^{+40}_{-20}	$4.3^{+0.4}_{-0.4}$	<2.7	$0.4^{+0.3}_{-0.4}$	50^{+10}_{-10}	75	303/277

are quite degenerate and a more physically plausible model can be found constraining q to be smaller than 5. In fact, in this case a more reasonable photon index with $\Gamma=2.26^{+0.07}_{-0.05}$ is obtained while the other parameters do not significantly change. The χ^2 is now however significantly larger (χ^2=804 with a $\Delta\chi^2$=20) but still acceptable.

7.4 Indication of redshifted narrow iron lines

7.4.1 A strongly redshifted line at 4.8 keV in OBS 4

We focus here on the marginal detection of a narrow line at 4.8 keV in the first part of OBS 4. This feature is visible on the excess map shown on Fig. 7.6 and it is still visible in the mean spectrum of the entire Jan. 2005 observation (see Fig. 7.4). To estimate its confidence level,

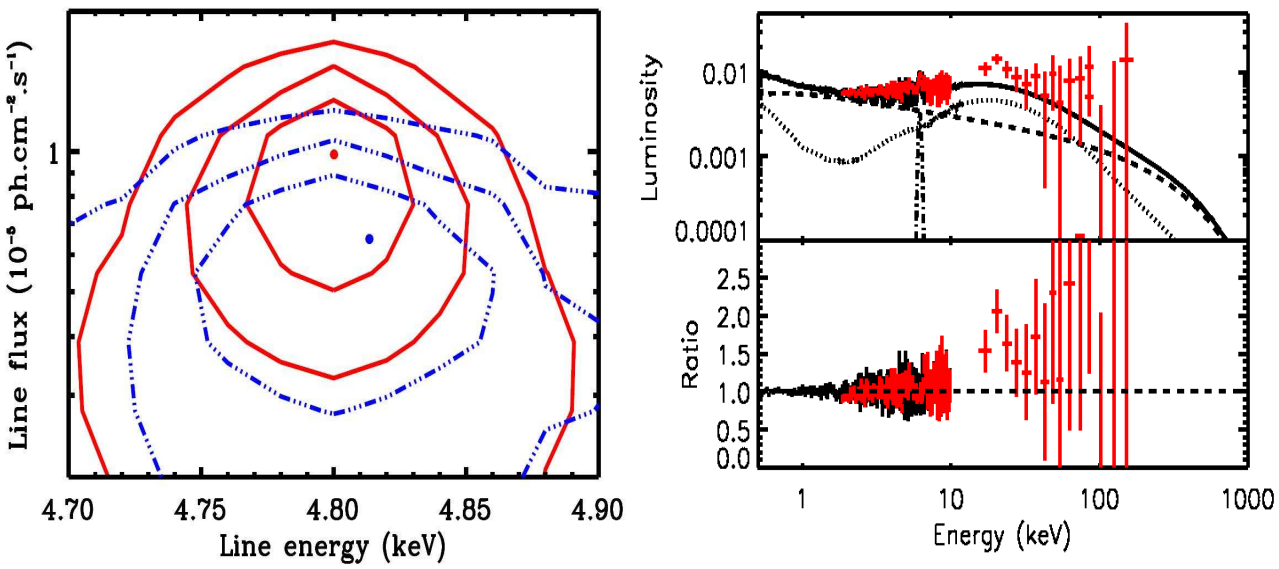

Figure 7.9: (*Left panel*) Contour plot energy vs flux of the line detected close to 4.8 keV during part 1 of OBS 4. The solid and dash-dotted contours correspond to the pn and pn+MOS data respectively. (*Right panel*) Top: The solid line is the best fit blurred ionized reflection model of OBS 1, the cut-off power law continuum and blurred ionized reflection being plotted in dashed and dotted lines respectively. The dot-dashed line is the narrow iron line. The dark (black) crosses are the OBS 1 *XMM-Newton* data and the clear (red) crosses are the MECS and PDS data of the simultaneous 100 ks BeppoSAX. The PDS/MECS cross normalization was fixed and only the pn/MECS one was let free to vary. Bottom: Data/model ratio.

we first fit the first part of OBS 4, above 3 keV, with a power law and then add a Gaussian with energy ∼4.8 keV. The Gaussian energy and flux are let free to vary but, given the apparent narrowness of the feature, we fix the Gaussian width to zero. The excess is clearly detected with an improvement of the fit of $\Delta\chi^2 = 11$ (significant at more than 99.8 % following the F-test). The best fit parameters of the line are $E_{line} = 4.80^{+0.03}_{-0.03}$ keV and an equivalent width EW = 50±20 eV. The contour plot of the line energy versus the line flux is plotted in solid line on the left panel of Fig. 7.9. The strong detection in the pn data is however attenuated by the weak detection in the MOS data. Indeed we have plotted in dashed line on the left panel of Fig. 7.9 the corresponding contour plot when fitting the pn and MOS data simultaneously. The detection is now significant at only 96.8 % following the F-test.

If we assume that this line is a redshifted neutral fluorescent iron line, its observation at 4.8 keV (source frame) implies a redshift factor of ∼0.75. Such high redshift value suggests an origin close to the central engine where relativistic effects become important. Moreover, the narrow shape of the line constrain the emitting region to be sufficiently small. There are growing evidences of such narrow emission features in the X-ray spectra of several AGNs in the literature (Petrucci et al. 2002; Iwasawa et al. 2004; Turner et al. 2004; Porquet et al. 2004). The common scheme to explain these components suppose the presence of transient magnetic

flares briefly illuminating a localized part (hot spot) of the accretion disc and producing the iron line by fluorescence.

For an inclination of 25 degree the line emission can come from a region at a distance as small as 3 r_g from the central black hole and even closer for larger inclination. Moreover, if we assume that we observed the same hot spot on the disc for more than a complete disc rotation, then the global line profile is expected to be relatively complex (e.g. Dovciak et al. 2004) with a strong blue peak. And if we interpret the observed feature with this blue peak, a Kerr solution is unavoidable (Pechacek et al. 2005).

We want to point out here that the narrow line feature near 6.2 keV (source frame) in the first observation of 2001 as already noted in §7.3.2 (see Fig. 7.7) may have a similar origin, being a less redshifted narrow Fe K line.

7.5 Summary and Discussion

MKN 841 has been observed by *XMM-Newton* three times in January 2001 (OBS 1, OBS 2 and OBS 3) and two times in 2005 in January (OBS 4) and July (OBS 5). A strong soft excess as well as a complex iron line profile, known to be present in this source since a long time, are clearly detected in all these pointings, the high sensitivity of the *XMM-Newton* unveiling a very puzzling spectral and temporal behavior. The 0.5-10 keV flux varies by a factor 3 on 4 years and is dominated by the soft band (lower than 3 keV) variability, the data above ∼5 keV remaining roughly constant on short and long time scale. Fitting the 3-10 keV data with a simple power law, the spectral index varies from ∼1.9 in 2001 down to ∼1.3 in Jan. 2005. However a simple variable power law component cannot explain by itself the broadband 0.5-10 keV spectral variability observed on a year time scale, revealing a more complex spectral variability.

The line profile is also complex, being a mixed of broad and narrow components. It is highly variable and the 2005 data confirm the rapid line variability observed in 2001 by Petrucci et al. (2002) and Longinotti et al. (2004) with a variability time scale as short as a few ks. This strong X-ray variability suggests small emitting regions close to the black hole. Fitting the line with a DISKLINE model gives a good representation of the line profile but requires in some cases steep disc emissivity power law index.

The relativistically distorted line profile, as well as a strong soft excess and an high reflection fraction (Matt et al. 2000; Bianchi et al. 2001; Petrucci et al. 2002) are all features characteristic of a strong disc ionized reflection. Thus, we apply this model to our different data sets in addition to a neutral reflection to reproduce the narrow line component. Although the model is already satisfactory in reproducing the soft excess and the broad line component with a unique component, we obtain good (in broad band shape) but statistically unacceptable fits, due to the presence of absorption features in the soft energy range. The addition of a warm absorber strongly improves the fits and allow to converge to a statistically acceptable representation of the data. Moreover the disc emissivity power law index and the other parameters of the model have now reasonable values (i.e. $q \simeq 4$) in good agreement with theoretical expectations.

Finally we also note the presence of a strong narrow feature near 4.8 keV in the first part of OBS 4. Its detection is highly significant in the pn data (>99.8 %) but the significativity decreases to 96 % when we include the MOS data. If it is real and if interpreted as the blue horn of a relativistically distorted neutral iron line, the large redshift implies the presence of a Kerr black hole.

The blurred ionized reflection is certainly not the unique representation of the different spectra of MKN 841. Moreover our best fit results depend on some assumptions. For example we fixed the inclination angle to 30 degrees and the iron abundance to the solar one. Letting these parameters free to vary would certainly provide significantly different parameter best fit values. For example the best fit obtained by Crummy et al. (2006) with the OBS 3 data gives a photon index of ∼2.1 with an inclination of ∼60 degrees, an iron abundance of ∼0.4 and a ionization parameter of ∼500 erg cm^{-2} s^{-1}. This certainly reveals some degeneracy of the model that results in part by the lack of data above 10 keV. But it has the advantage to reproduce reasonably well the broad band (0.5-10 keV) and complex spectral characteristics of MKN 841 with a small number of spectral components.

This model suggests the presence of different reflection components in MKN 841. The fraction of the observed flux coming from these components is of the order of 30-50 % in the 0.5-500 keV energy range which is relatively large. We should expect ∼10-20 % in the case of an isotropic illumination without blurring effects. We were able to check the consistency of this model with the *BeppoSAX* data obtained simultaneously with the *XMM-Newton* observation of 2001. The *BeppoSAX* instruments cover the 0.1-200 keV range and thus better constrain the reflection component. The source was pointed by *BeppoSAX* between the 11th and 14th of January 2001 for a total net time exposure of ∼90 ks for the MECS instrument, ∼40 ks for the PDS and only 20 ks for the LECS. The unfolded best fit spectrum of blurred ionized reflection obtained with OBS 1/2/3 is plotted on the right panel of Fig. 7.9 with the *XMM-Newton* pn and *BeppoSAX* MECS and PDS data. Only the MECS normalization was let free to vary, the PDS one being fixed to 0.86 the MECS one (following Fiore et al. 1999). The agreement is relatively good given the possible variability of the reflection component during the *BeppoSAX* pointing and the fixed value of 300 keV of the power law continuum high energy cut-off. Interestingly the presence of two reflection components may explain the large values of the reflection parameter R generally obtained in the literature for MKN 841 when fitting with a simple neutral reflection (Matt et al. 2000; Petrucci et al. 2002; Bianchi et al. 2001).

Interestingly, the light bending model also predicts that the reflection spectrum is less variable than the power law continuum. Looking to the RMS spectrum of OBS 4 (see Fig. 7.3), we see that most of the variability arises in the 1-5 keV energy range where the power law dominates indeed the spectrum.

Other different interpretations (involving high column densities of highly ionized and relativistic matter) may reproduce the 0.2-10 keV emission and variability of this source. Nevertheless, we expect large differences between these models above 10 keV, outside the *XMM-Newton* energy range, but well inside the *Suzaku* one. Two accepted observations of 50 ks each with this satellite will be of strong interest to test this and the above interpretation.

Chapter 8

Key study objects: v) MKN 509, the brightest Seyfert 1 galaxy not affected by strong absorption

8.1 Introduction

Markarian 509 (z=0.034, Fisher et al. 1995) is the brightest Seyfert 1 galaxy of the Piccinotti sample in the 2–100 keV band that is not strongly affected by neutral (Murphy et al. 1996) or ionized absorbing material (N_H=$2.06^{+0.39}_{-0.45}\times10^{21}$ cm^{-2}; log ξ=$1.76^{+0.13}_{-0.14}$, Yaqoob et al. 2003). In fact, the weighted mean BATSE 2–100 keV flux, calculated over nearly 4 yr of observations, is 1.25×10^{-10} ergs cm^{-2}s^{-1} (Malizia et al. 1999).

A soft excess in its X–ray spectrum was observed with ROSAT and *Ginga* simultaneous observation (Pounds et al. 1994) confirming the previous *HEAO1* (Singh et al. 1985) and *EXOSAT* findings (Morini et al. 1987). The *ASCA* observation, however, suggested a warm absorber component in MKN 509 rather than a true soft excess (Reynolds 1997; George et al. 1998), but *BeppoSAX* (Perola et al. 2000) and *XMM-Newton* (Pounds et al. 2001) confirmed the soft X-ray excess below 1 keV (see Fig. 1 right panel); this data also showed the presence of a narrow constant component of the iron line (already detected by *Ginga* and *ASCA*) and a Compton reflection bump above 10 keV (Singh et al. 1990; De Rosa et al. 2004). A *Chandra* observation with the high–energy transmission gratings shows the presence of a warm absorber with n_H=$2.06^{+0.39}_{-0.45}\times10^{21}$ cm^{-2} and logξ=$1.76^{+0.13}_{-0.14}$ (Yaqoob et al. 2003) and confirms the presence of a narrow component of the Fe K line with an EW of 50 eV (Yaqoob et al. 2004). The presence of a second ionized component of the Fe K line at 6.7–6.9 has been claimed by Pounds et al. (2001), but Page et al. (2003) showed that the same spectral feature could be also due to a relativistic accretion–disc line or Compton reflection from cold material.

8.2 Study of the continuum emission

MKN 509 was observed by *BeppoSAX* two times in 1998 (May and October) and four times in 2000 (November) with a total exposure of 88 and 150 ks for the 1998 and 2000 observations respectively. The source does not show variability onto short (few ks) time–scales, but it shows variations of more than a factor of 2 on longer time scales.

The *BeppoSAX* observations have been extensively studied by De Rosa et al. (2004). In order to have a better statistics broad band spectrum, the authors simultaneously fitted the four 2000 pointings of MKN 509. The soft excess can be fitted by including two different thermal components. Once again, the best fit temperature ($T_{BB} \simeq 70$ eV and $\simeq 250$ eV) seems to be too high for being due to emission from a standard accretion disc around a black hole of mass $M_{BH}=1.4\times10^8$ $M_\odot$ as measured in of MKN 509 (Peterson et al. 2004). The high energy emission has been fitted, firstly, with a very flat primary power law ($\Gamma\sim1.6$), plus a reflection component due to cold matter and a superimposed Fe K emission line. The authors obtained a satisfactory fit with this standard model. MKN 509 showed the evidence of an high energy cut-off between ∼80-150 keV.

De Rosa et al. (2004) tested also a ionized reflection model (Ross & Fabian 1993). Although providing a slightly worse statistical description than the above thermal model, this ionized disc reflection model is able to reproduce the broad band spectrum with the need of only 2 broad band components (in addition to the neutral reflection from distant material). The best fit parameters are fairly standard with an ionization parameter of $\log(\xi)\sim1.5$ and a disc illumination parameter of β=-3 (with the disc radial emissivity law: $\epsilon(r)\propto r^{\beta}$). The main achievement of this model is the explanation of both the flux at high energy, the presence of a strong soft excess and the flatness of the 2-10 keV spectral index, with the presence of ionized reflection. Nevertheless, the model is not very well constrained due to the fairly low *BeppoSAX* statistics at low energies.

For this reason the *XMM-Newton* data (that have the highest ever statistics at energies below 10 keV), of the 2 observation available, have been studied. Figure 8.1 shows the 0.2-10 keV *XMM-Newton* spectrum fitted with a power law in the 3-10 keV and then extrapolated at low energy. It shows a strong soft excess starting around 2 keV which shape is influenced by the presence of a warm absorber (Yaqoob et al. 2003; Smith et al. 2007). In the inset in Figure 8.1, an enlargement of the spectrum and of the ratio with the power law, in the region of the Fe K line is shown. The *XMM-Newton* data confirm the presence of a narrow component of the Fe K line without any clear evidence for a broad component, and also show the presence of further spectral complexities around 8 keV.

The *XMM-Newton* data have been fitted with either the standard (black body plus power law) and with the power law plus ionized disc reflection models, with similar results from a statistical point of view.

The spectral variability does not seem to help in disentangling the two interpretations. Figure 8.1 shows the RMS spectrum of the longest *XMM-Newton* observation. MKN 509 shows a low degree of variability and an RMS shape typical of the sources of group 1 (see §3.2.3), with a drop of variability at low and high energy and a peak at about 2 keV. Unfortunately, this spectral variability shape may be produced by both physical scenario. The discrimination between these two models could be done through the simultaneous observation

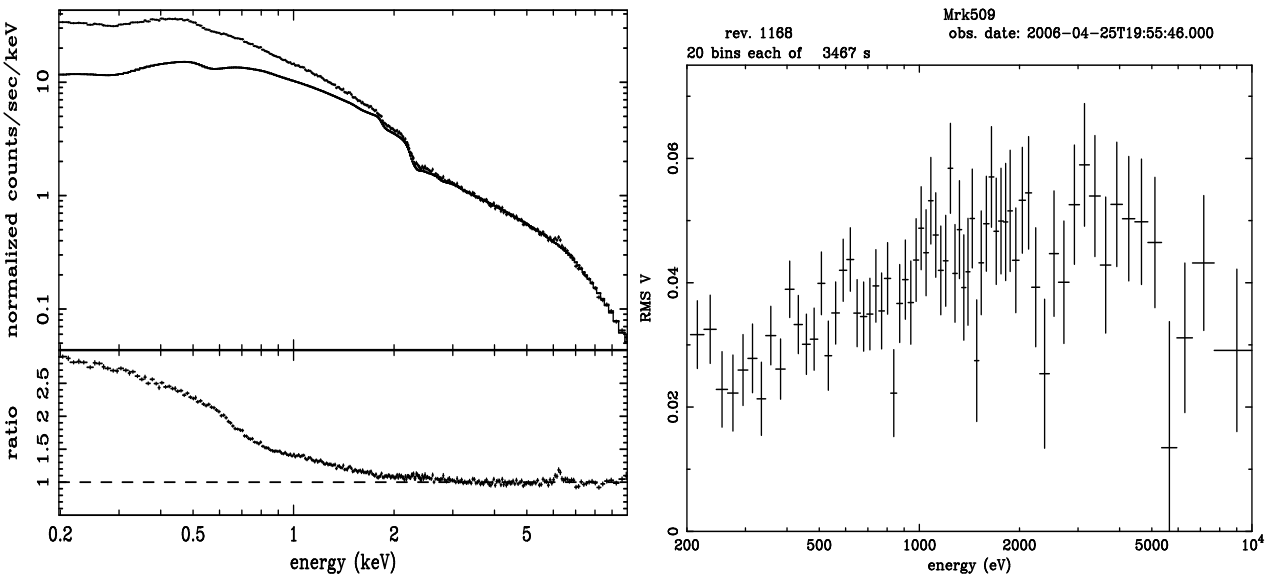

Figure 8.1: Left panel: EPIC pn spectrum of MKN 509 fitted, in the 3-10 keV band, with a power law absorbed by neutral Galactic material and data-model ratio. A clear strong soft excess is present at low energy. The sharp drop of emission around 0.6-0.9 keV suggest that the soft excess shape is modified by the presence of the warm absorber. In the inset the enlargement of the spectrum and of the ratio, in the region of the Fe K line complex, is shown. Right panel: RMS spectrum of the longest *XMM-Newton* observation. The spectral variability shape is similar to the one presented by all the sources studied in detail. For the RMS spectrum calculation a time binning of ∼3.5 ks has been used.

and the variability of both the soft excess (with high statistics) and the Compton hump. I have been awarded Suzaku time (a monitoring of 4 observations) for precisely this goal.

The main argument against an interpretation involving ionized disc reflection is related with the Fe K line. In fact, if the reflection is produced in the innermost part of the accretion disc, the broad component of the Fe K line should be present. Nevertheless, the historical data show no clear sign of the presence of a broad component of the Fe K line. Anyway, in this object the Fe K line region seems to be complex.

In fact, an interesting absorption feature in the Fe K band has been noted during the 6^{th} *BeppoSAX* pointing. Figure 8.2 (panel a) shows in greater detail the 3-10 keV data-to-model ratios for a simple power law model fit during this observation. These features have a great potential, thus a detailed study of this structure has been performed.

8.3 Detailed study of the Fe K line region

8.3.1 SAX6 observation

All the panels in Figure 8.2 show the spectral complexities at the Fe K energies. These clearly indicate an emission feature close to the energies typical of the Fe K line and the possible

presence of an absorption feature at E∼5.3 keV. To exclude that this count drop could be due to a calibration artifact of the response matrices and to adopt a model-independent representation of the data, we calculated the PHA ratios between MKN 509 and the reference spectrum of 3C 273 acquired on January 9, 2000. 3C273 was chosen since it ensures a very good statistics and has an almost featureless spectrum with a flat photon index similar to the one of MKN 509 during SAX6. We have checked that the Fe K line known to be present in the *BeppoSAX* spectrum of 3C 273 (Grandi & Palumbo 2004, and references therein) is much too weak (less than ∼5% above the continuum) to have a significant impact on our conclusions on the absorption feature measured between 5-6 keV. The PHA ratios (Fig. 8.2, panel b) are indeed very similar to what shown in panel a) of Figure 8.2, thus excluding response matrix problems and/or an erroneous modeling of the data.

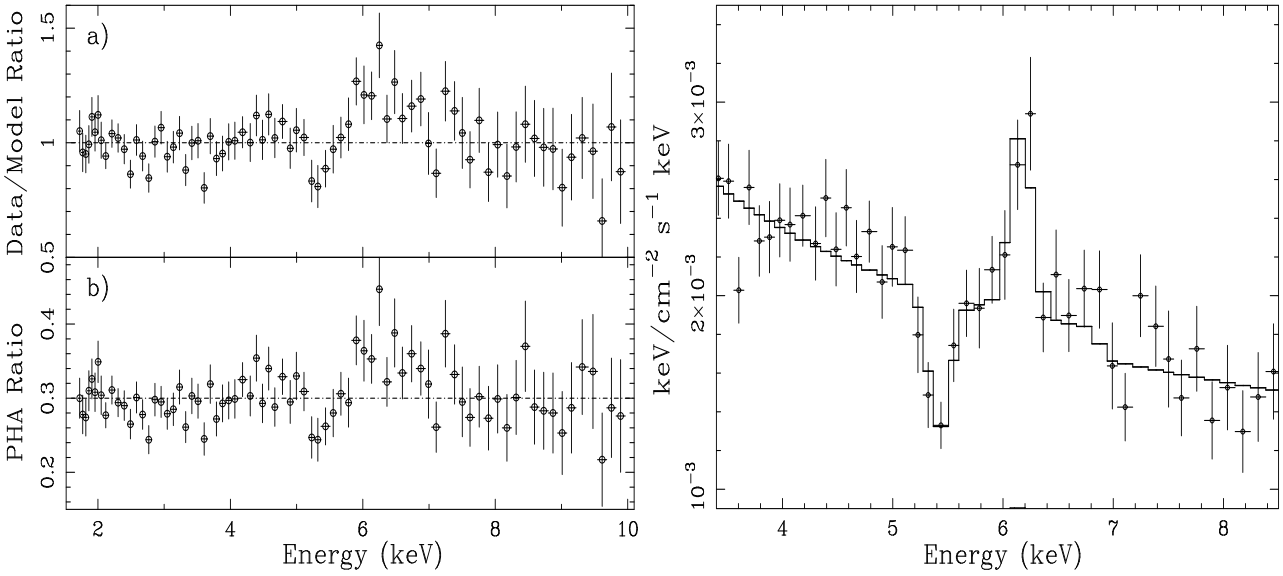

Figure 8.2: Panel a: data-to-model ratios for SAX6 when the data are fitted with a simple power law model. Panel b: PHA ratios between MKN 509 and 3C273 *BeppoSAX*. Right panel: Unfolded 3-10 keV spectrum measured in SAX6. The continuous line indicates model number 2 in Table 2. In producing the plot, the line widths were fixed to σ=0.1 keV for clarity.

The fit improves significantly when a Gaussian absorption line is added to the model ($\Delta\chi^2$=12.4 for two more parameters), yielding best fit parameters for the line: E_{ab}=5.60±0.14 keV, and EW_{ab}=93±50 eV. Best-fit unfolded spectrum and confidence contours for the absorption line parameters are shown in right panel of Figure 8.2 and left panel of Figure 8.4, respectively.

A complex photoionized plasma model (Kinkhabwala et al. 2003) has been used to fit the line. Once the ionization state was fixed to FeXXVI, we obtained that the receding velocity of the putative absorbing matter is v∼0.2c with a dispersion Δv∼3500 km s^{-1}, with an Iron absorbing column density of N_{Fe}∼1.3×10^{18} cm^{-2}. However, these parameters are only poorly constrained by the quality of the present data.

We searched for absorption lines between 5 and 6 keV also in the other *BeppoSAX* and *XMM-Newton* observations but obtained only upper-limits ranging between 10 and 50 eV (at 90% confidence).

Time-resolved analysis

The occurrence of such an absorption feature in only one out of six *BeppoSAX* observations of MKN 509 suggests a sporadic nature. This led us to dissect the SAX6 observation so as to further investigate the feature variability. We found a best trade-off between time resolution and collected photons (available statistics) in sectioning the observation in five intervals of ∼20 ks, hereinafter called T1, T2, T3, T4 and T5. To exclude systematic effects, we performed the PHA ratios with 3C273 data also in these time intervals (Figure 8.3). During periods T2, T3 and T4, three different "absorption features" are clearly visible at E ∼5.3 keV (T2 and T4) and 7.9 keV (T3) (observer frame). The count drops account for deviations as large as ∼60% and 40% in T2 and T4, respectively. A check of the relative importance and shape of the background during these short intervals confirmed that no anomalous features were present in the local background during T2, T3 and T4 periods. To model these spectral features we restricted the spectral analysis only to the ∼2-10 keV MECS data. The data were fitted with a simple power-law model. We find that the addition of absorption features increases significantly the quality of the fit in T2, T3 and T4 (see Table 8.1). The addition of a narrow or broad Fe K emission line is not required by the data but we have checked and found that the absorption line detections are also robust to the inclusion of either narrow or broad emission lines above and/or below the absorption line energy. Right panel of Figure 8.4 shows the confidence contours plots for the (rest frame) parameters of interest of these absorption lines. The line widths are consistent with the instrumental energy resolution. We also tried to fit the feature at ∼8 keV during T3 with an absorption edge but the result was a poorer fit ($\Delta\chi^2$∼14 for the same degrees of freedom) when compared with that obtained with the absorption Gaussian line.

8.3.2 *XMM-Newton* observation of Oct. 25, 2000 (XMM1)

This observation was previously analyzed by Page, Davis & Salvi (2003). These authors commented the presence of residuals at E∼8 keV to their best-fit model, but did not attempt to model them.

Fitting the 2-10 keV data with a simple power-law, the addition of a narrow absorption line at E=8.27±0.05 keV with an EW_{ab}=40±20 eV, leads to a reduction of the $\Delta\chi^2$=12.5 (Figure 8.4). As for SAX6, also in this case the modeling of this absorption feature with an edge leads to a worse fit ($\Delta\chi^2$∼10 for the same number of degrees of freedom).

In this energy range, the background of the EPIC CCDs is strongly affected by a Cu activated emission line. The net effect of an inadequate removal of this background feature could, in principle, cause the presence of an absorption and/or emission feature in the source spectrum. We tested this possibility by using different background regions. This did not change significantly the results on the absorption line parameters Moreover, at the energy of

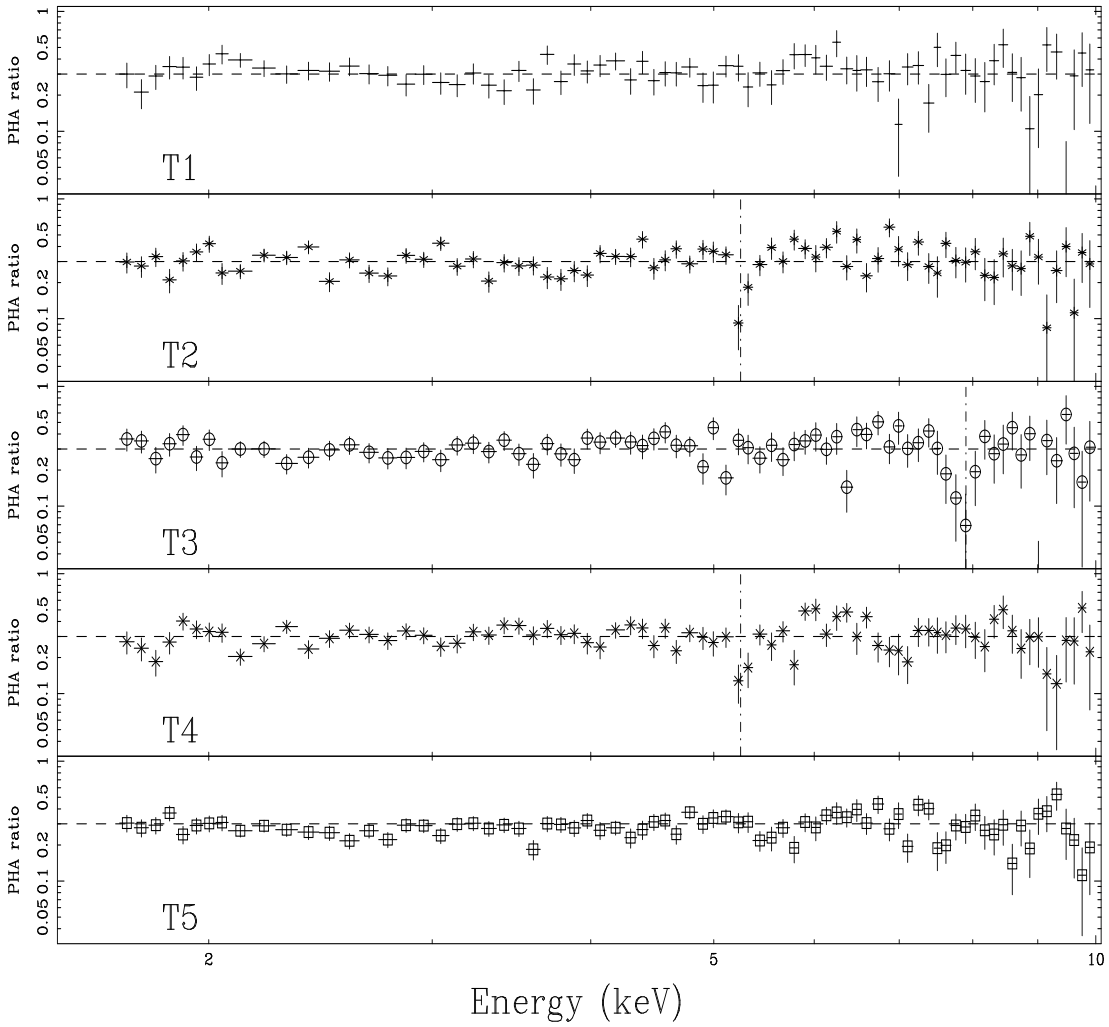

Figure 8.3: MKN 509/3C273 PHA ratios obtained dividing the SAX6 observation in 5 intervals (see text for details).

Table 8.1: Time resolved analysis of SAX6. Column I: name of the time interval. Column II: energy centroid of the absorption line. Column III: line intensity. Column IV: line EW. Column V: χ^2 variation after inclusion of an absorption Gaussian line to a simple power law model. Column VI: F-test significance of the absorption line. Errors are 90% confidence for one interesting parameter.

SAX6 Period	E	Line Intensity	EW_{ab}	$\Delta\chi^2$
	(keV)	(10^{-5}ph s^{-1}cm^{-2})	eV	
I	II	III	IV	V
T2	$5.50^{+0.12}_{-0.12}$	$-7.82^{+3.25}_{-3.49}$	195^{+81}_{-85}	16.8
T3	$8.14^{+0.15}_{-0.13}$	$-8.48^{+4.14}_{-4.49}$	383^{+96}_{-203}	16.4
T4	$5.45^{+0.15}_{-0.15}$	$-6.97^{+3.65}_{-3.66}$	173^{+90}_{-90}	9.6

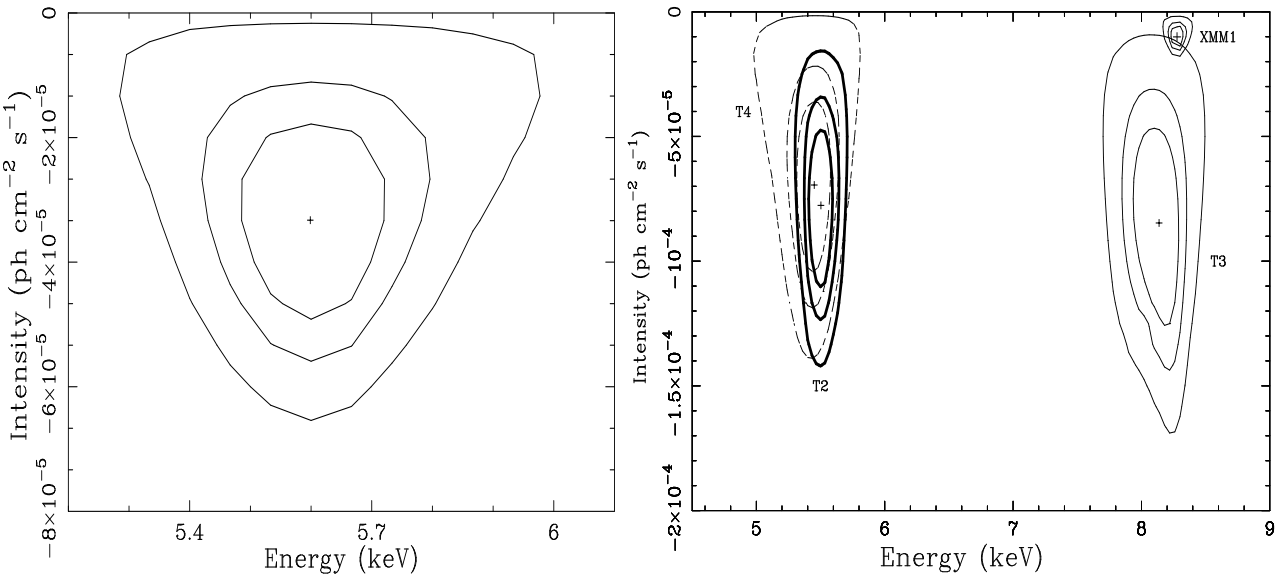

Figure 8.4: Left panel: 99, 90 and 68% confidence contours of the absorption line parameters detected in SAX6 (rest frame energy vs. intensity). The reference X-ray continuum used to calculate these contours is the number 2 in table 2. Right panel: Confidence contours for parameters of interest of the absorption features measured during periods T2 (thick solid line), T3 (solid line) and T4 (dashed line) of SAX6 and XMM1. The line width was fixed to σ=0 eV. Rest-frame line energies are reported.

the absorption feature, the background contributes for $\lesssim$5% to the source counts (Figure **??**), thus excluding that the $\sim$8 keV absorption feature is due to background subtraction problems.

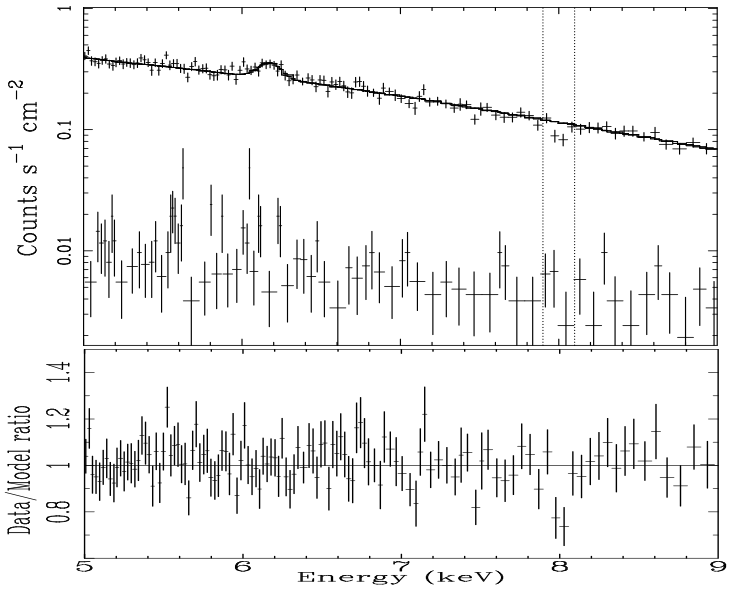

Figure 8.5: Upper panel: source and background (5-9 keV) spectra during XMM1. Dotted lines highlight the energy range of the detected absorption line. A Fe Kα narrow emission line has been added to the model. Lower panel: data-to-model ratio with respect to a spectral model composed by a power-law plus an narrow emission line.

8.3.3 Other *BeppoSAX* and *XMM-Newton* Observations of MKN 509

We performed a time resolved search for absorption features also in the other observations of MKN 509 performed by *BeppoSAX* and *XMM-Newton*, but without success. This confirms the indication that these features are of transient nature and partially explains why these features were not detected before despite the same data were already analyzed. Moreover, the occurrence of these features seems to be independent from the source state. So a bias against their detection is expected since they are expected to be washed out in spectra averaged over long exposures.

8.3.4 On the significance of the absorption lines

A word of caution should be stated for the statistical significance of the absorption lines detected in SAX6 and XMM1 at ∼5.5 and ∼8.2 keV, respectively. If the F-test is applied to these observations, the output is that these features are significant to a ∼99.9% confidence level. Nonetheless this does not account for the total number of trials performed, as well as for the total number of resolution elements used for the line detection (see, e.g., Protassov et al. 2002; Porquet et al. 2004; Yaqoob & Serlemitsos 2005). If we consider only the 5.5 keV feature and the average spectra, we find that the F-test significance decreases to ∼99.2% because of the number of trials involved (the eight *BeppoSAX* and *XMM-Newton* observations). The same arguments could be applied for the time-resolved analysis (a total of 33 time-resolved spectra) thus reducing the overall significance in detecting a single absorption line at ∼96.7%.

Moreover, Protassov et al. (2002) discussed how the F-test like indicators could fail in assessing the real significance of an absorption feature maybe overestimating it. We cannot, therefore, strongly fix the "true" significance of our results that could be, most probably, lower than what deduced by the application of the F-test.

It is encouraging, however, that the four lines detected with the time resolved analysis of the data, have been found to be consistent with only two energies. Moreover, recently, detections of both blue- and red-shifted lines have been claimed by some authors (Pounds et al. 2003a,b, Yaqoob & Serlemitsos 2005, Matt et al. 2005), thus suggesting that the features reported here are not a statistical artifact. To conclude, it is worth noting here that confirmations by means of instruments with larger collecting area and/or greater energy resolutions, are needed to definitively fix the veridicity of the spectral and time patterns measured here.

8.4 Discussion

The X-ray spectrum of MKN 509 generally shows a really flat 2-10 keV spectral index, a strong flux at high energies (10-40 keV) and a clear soft excess. All these features may be introduced by the presence of an ionized disc reflection component. When the source spectrum is interpolated with such a model, fairly standard values of the best fit parameters are obtained. Nevertheless a spectral degeneracy is present, in fact, also the standard model is able to reproduce the X-ray data. 4 *Suzaku* observations, that have the potential to solve the degeneracy, will be available soon.

Evidences for absorption features in the X-ray spectrum of MKN 509 have been detected at ∼5.5 keV (twice in BeppoSAX data) and at ∼8.2 keV (in both *BeppoSAX* and *XMM-Newton* non-simultaneous data). Both features appear to be transient on time scales as short as ∼20 ks.

As previously proposed for other Seyferts and QSOs, the most natural explanation of such narrow components is in terms of both blue-shifted and red-shifted resonant absorption lines from H-like or He-like Iron (Nandra et al 1999; Pounds et al. 2003; Reeves, O'Brien & Ward 2003; Longinotti et al. 2003; Yaqoob & Serlemitsos 2005; Matt et al. 2005). This is also consistent with the fact that the best-fit model requires an ionized reflection component with logξ∼3.5, thus implying the presence of FeXXV and FeXXVI (De Rosa et al. 2004).

If associated to FeXXVI (6.96 keV rest-frame), the inferred shifts in energy correspond to receding velocities of (0.21±0.02)c (T2 and T4) and to approaching velocities of (0.16±0.02)c (T3) and (0.19±0.02)c (XMM1). If associated mainly to FeXXV (6.7 keV rest-frame), the velocities become ∼0.18, 0.20 and 0.23c, respectively.

Nandra et al. (1999) first discussed the interesting possibility that the red-shifted line seen in NGC 3516 could be the direct signature of matter inflow/infall. Alternatively, Ruszkowski & Fabian (2000) explained how the NGC 3516 feature could be due to a warm plasma surrounding the X-ray source. In their picture, the absorbing matter is located close to the black hole and the resonant absorption line is red-shifted by the gravitational field produced by the supermassive black hole. A similar interpretation has been given by Yaqoob & Serlemitsos (2005) for the red-shifted Iron line observed with the Chandra HETG in the QSO E1821+643.

Present results cannot rule out that the line red-shifts measured in T2 and T4 are partially or even totally due to gravitational red-shift. Nonetheless, the data seem to require either a transient or an "un-steady" absorber in order to explain the sporadic presence of the absorption features.

If confirmed, the red-shifted lines, like the one observed in MKN 509, would be particularly interesting because they could be one of the best direct evidence of matter free-falling onto a supermassive black hole. Broadly speaking, these evidences are in good agreement with most theoretical models which imply important radial motions close to the supermassive black hole (such as, for example, the "aborted jet" model). Other scenarios which explain the line red-shifts in terms of gravitational red-shift cannot be ruled out but seem to require a higher degree of complexity to account for the pattern and sporadic nature of the absorption lines. A detailed analysis of the line profile is needed in order to test these hypotheses. If confirmed, these results may offer a new potential to study the kinematics and dynamics of the gas close to the supermassive black hole via detailed absorption line X-ray spectroscopy. If the inflow is due to a wind rather than blobs, one would expect the features to exhibit a typical inverted P-Cygni profile (Edwards et al. 1994). On the other hand, a blob scenario, as favored here, would provide test-particles suitable to verify predictions of General Relativity in strong gravitational fields.

Chapter 9

Overall Discussion

In this dissertation the study of the spectral variability of a group of Seyfert 1 galaxies has been presented. Light curves, average spectra and RMS spectra have been calculated and put together for the whole sample. Then for a sub-sample of 5 among the brightest, a detailed time-resolved spectral analysis has been presented. The main aim of the study has been to answer to two open questions, one regarding the nature of the soft excess and the other aimed at understanding if the reflection component is affected (and its features broadened) by relativistic effects. Through spectral studies alone, it has not been possible to answer mainly because different physical models have been fit the mean spectra equally well. In order to break this degeneracy we have performed spectral variability studies.

In fact, there are two different models, one involving broad lines and the other involving complex partial covering absorbers that can explain complexities at the energy of the Fe K line. These are hardly distinguishable from the fitting of the mean spectrum in the 2-10 keV band, even in the best available data. Nevertheless, a clear demonstration of the existence of broad lines is important because these may allow to directly measure the geometry and the flow patterns of the material falling into the black hole. In particular reverberation mapping studies of the reflection component have the potential to map the innermost regions around black holes (Iwasawa et al. 1999; Ponti et al. 2004; Iwasawa et al. 2004; Tombesi et al. 2007). Moreover, they may provide a tool to test the general relativity in its strong field domain and give the possibility to measure the spin of black holes (Brenneman & Reynolds 2006).

Another spectral degeneracy involves the soft excess that may be successfully fitted, from a statistical point of view, with either a standard model (power law and black body for the soft excess) or a power law plus an ionized disc reflection component (other possibilities involve i.e. an high column density of relativistically moving matter absorbing the primary X-ray emission, but the detailed test of these models are beyond the scope of this work). The problems that emerge fitting the mean spectra of Seyfert galaxies with the standard interpretation has been already pointed out in the literature (Gierlinski & Done 2004; Piconcelli et al. 2005; Crummy et al. 2006). In fact the study of a sample of PG quasars shows that the the black body components would be too hot to be the high energy tail of the thermal emission of the accretion disc. Moreover, the best fit temperatures are too constant compared to expected variations due to the range of luminosities of the sources and masses of their black holes (Gierlinski &

Done 2004; Piconcelli et al. 2005; Crummy et al. 2006). Here the spectral variability of the standard model has been investigated, as well as the power law plus disc ionized reflection one, in order to further test these two models and, in this way, to get a closer look to the physical properties of the soft excess.

To study these topics RMS spectra and time resolved spectral variability have been, thus, primarily used. Moreover, in order to investigate these topics in a way as general as possible, a large sample of bright Type 1 AGN has been selected. The sample is composed by all the sources with a *ROSAT* PSPC count rate higher than 0.2. counts s^{-1}, with Galactic latitude higher than 15 degree and observed by *XMM-Newton* for more than 30 ks. Finally the sample is composed of 36 objects (see Table 3.1).

9.1 General properties of the Sample

I have found that the sources of the sample show a clear anti correlation between the total source variability and the black hole mass (see §3.3). This relation has been already found by many authors with different instruments (Lu & Yu 2001; Bian & Zhao 2003; Papadakis 2004; O'Neill et al. 2005; Nikolajuk et al. 2006), but it is confirmed here in the 0.2-10 keV band with the high statistics *XMM-Newton* data. This relation suggests that the same process responsible for the variability is at work in all these sources. The timescales of the system are related to the gravitational radius (which is proportional to the black hole mass), thus a different variability amount is observed only because the excess variance is calculated within the same fixed range of frequencies for all the sources (independently from the black hole mass). In fact, this is what is expected if all the AGNs have the same PSD, only scaled in frequency accordingly to the black hole mass, and the variability is integrated over a fixed frequency range. The observed important scatter in the relationship suggests the possibly that other physical quantities may be important (McHardy et al. 2006).

9.1.1 RMS spectra

In several (14 out of 36) objects, the low degree of the variations, as well as the data with low statistics, prevented a detailed study of the spectral variability. The RMS spectra of all the other sources showed interesting spectral shapes that have been grouped in three classes (see §3.2.3).

Continuum emission and Soft Excess

The first class has a low degree of variability both at low and high energy and shows a peak between a few hundred eV and 1-2 keV. The drop of variability at low energy indicates that the soft excess, that is dominating the source emission there, is less variable than the power law continuum.

The second group of sources includes the ones with a RMS spectral shape either flat or decreasing with energy. In this case the component producing the soft excess should follow the variations of the power law in order not to imprint any variability features at low energy.

This difference in the soft excess variability between these two classes of sources does not seem to be directly related either with a particular shape of the soft excess or with the presence of a warm absorber. In fact in both groups there are sources with strong warm absorber components and complex soft excess shapes.

The RMS shapes characteristic of these two classes of sources could be due to a variable power law plus an ionized disc reflection component. In particular, in this interpretation, the different variability pattern could be explained if the location of the primary X-ray source with respect to the central black hole is different in the two categories. In fact, if the X-ray source is at a distance lower than about 10-20 r_g from the black hole, then strong gravity effects (like the light bending) are important and the variability of the reflected component is lowered with respect to the power law. This would generate a drop of variability where the disc ionized reflection has a larger contribution, i.e. at low and high energy. Otherwise, if the source is more distant than about 20 r_g the strong gravity effects are negligible and, as expected, the reflected component would follow the variations of the power law in a correlated way, generating no drops of variability. These findings, suggested by the RMS spectra, are confirmed by the detailed spectral variability studies performed on single objects (i.e. MCG-6-30-15, NGC 4051 and IRAS 13224–3809, for the first group, see §4, 5 and 6; and NGC 3783 for the second; Tombesi et al. 2007).

Thus, the RMS spectra are in agreement with the presence in the spectrum of a strong ionized disc reflection component. The standard interpretation is instead not favored here. It could explain the drop of variability at high energy with spectral index variations of the power law but would need a black body emission that is constant in the sources of the first group but variable as much as the continuum for the second group. Moreover, another component that may give a contribution to the spectral variability is the warm absorber. In fact in some sources it is observed to be variable even in short timescales (Otani et al. 1996; Krongold et al. 2007) and it may explain some of the sharp features in the RMS spectra.

The third group of objects is made by only three peculiar sources. In these sources another component such as a strong warm or complex absorber seems to play an important role.

Broad Lines

The RMS spectrum is an extremely powerful tool to separate spectral components with different variability behaviors. For this reason it may be fruitful to study the variability of the Fe K complex with this technique. For most of the RMS spectra, at the energy of the Fe K line, there is not enough statistics to perform a detailed spectral variability analysis. Nevertheless, for MCG-6-30-15 the broad component of the Fe K line is so strong that its variability clearly emerges above the underlying continuum, in the low flux *XMM-Newton* observation. This is a strong, because model independent, evidence for the presence of a spectral component (most likely a redshifted broad Fe K line) different from the continuum. Also MKN 766, MKN 335, NGC 3783, IC4329A and NGC 4593 show evidence, although less significant, for an higher degree of variability at energies redshifted with respect to the Fe K line (see §3.2.3).

In addition, most of the sources with a strong narrow component of the Fe K line show a drop of variability at 6.4 keV (emitted frame) indicating the constancy of this narrow emission line.

9.2 General properties of the key study objects

The main result of this work has been, from my point of view, to be able to probe that the two questions under investigation here may be closely connected. In fact, in all the sources that have been studied in detail (on key study objects), only one broad band component (the disc ionized reflection) is able to reproduce not only the mean spectrum, but also the spectral variability of both the broad component of the Fe K line (when present) and the soft excess. This finding is further strengthened by the study of the sample of Seyfert 1 galaxies that showed that this hypothesis may be true for all the objects analyzed (apart from the three peculiar sources that may need a more complex scenario).

Continuum emission and Soft Excess

The main results of this work show that a power law plus ionized disc reflection component may explain the emission of these AGNs. The standard interpretation has been tested as well. From a statistical point of view it works as well as the disc ionized reflection model. Nevertheless, in the cases like NGC 4051, where the source has enough statistics and variability to detail the spectral variability on short time scales and with a large range of luminosities, the black body temperature is surprisingly constant given that its luminosity spans one order of magnitude. Moreover it does not follow the black body law ($L \propto T^4$). This result strengthens the evidence against the standard picture, and suggests that only a pure thermal component is not appropriate to account for all the soft excess in NGC 4051.

Moreover in the standard interpretation the high energy drop of variability is due to the power law slope that correlates with flux. This behavior is expected by Comptonization models and it could be associated to changes in the coronal physical properties (Haardt & Maraschi 1993; 1994; Haardt, Maraschi & Ghisellini 1997; Zdziarski et al. 2003). Nevertheless, for NGC 4051 and MKN 841 the hardest photon indexes measured (about 1.3–1.4) seem too hard to be explained in terms of standard Comptonization models. Moreover, it is observed, for the first time in NGC 4051, thanks to the large spread in the observed luminosity, that at very low flux levels the relation expected from simple spectral pivoting breaks down.

On the contrary, in the context of the power law plus ionized disc reflection model, the soft excess is accounted for by ionized reflection from the accretion disc which simultaneously hardens the hard spectral shape as the flux drops. The apparent constant temperature of the soft excess is then explained, because the soft excess spectral shape is dictated by atomic rather than thermal mechanisms. Moreover, in the low black hole mass sources (like MCG-6-30-15, NGC 4051 and IRAS 13224–3809), where the variability can be studied continuously, the power law plus ionized disc reflection model is consistent with the variability being dominated by a constant-slope power law which varies in normalization only. In these sources the ionized disc reflection component is in fact correlated with the power law at low fluxes and varies with much smaller amplitude at normal/high fluxes. The observed 2-10 keV Γ-flux relationship is then interpreted as spurious and due to the relative flux changes of the power law with respect to the almost constant reflection component.

Broad Lines

Thanks to the detailed study of the spectral variability of the key study objects, we have shown strong evidence for a broad component of the Fe K line in Seyfert galaxies. In fact for 4 of the 5 objects studied in detail a broad component of the Fe K line is required by the data. Anyway, it is not possible to drive conclusions about the percentage of source with a broad component, because the sources that have been studied are most probably not representative of a greater sample. Nevertheless recent results on complete samples of AGN show that a broad Fe K line is present in about 50 % of the objects (Guainazzi et al. 2006; Nandra et al. 2006).

The results of the analysis performed for this dissertation show also the almost ubiquitous presence of a narrow component of the Fe K line in agreement with Perola et al. (2002), Bianchi et al. (2004) and Yaqoob & Padmanabhan (2004). The detailed study of NGC 4051 and the RMS spectra showed that this component is generally constant. Thus, its origin is most probably related to material distant from the primary X-ray source.

9.3 Spectral variability in the ionized disc reflection interpretation: The Light Bending

For the sources in which it has been possible to detail the spectral variations, it has been probed that the spectral variability is in agreement with the prediction of the light bending model. In the objects in which the light bending effect is important, as expected, the flux of the relativistic ionized disc reflection is observed to be almost constant, in the medium high flux states, and correlated with the power law one, during the low flux states (see §4, §5 and §6). Moreover, as expected, the disc illumination becomes more centrally concentrated when the observed flux is decreasing. Moreover a consequence of the almost constant ionized disc reflection component is that the broad component of the Fe K line is more evident in the low flux spectra, because the contribution of the power law is lower (this is thought to be the reason why the broad iron line in MKN 841 is observed only during a low flux period; see §7).

Clearly not in all sources the light bending effect is expected to be important. The sources with a flat RMS variability, or decreasing with energy, may be dominated by an X-ray source quite distant from the black hole. In this case, in fact, the reflected component is expected, and at least in the case of NGC 3783 observed (Tombesi et al. 2007), to be correlated with the direct power law.

One of the main requirements of the light bending model is that the primary source of X-ray radiation is small. This requirement is supported by the observation of strong and fast variations in the light curves of these sources. In fact it is possible to observe variations as short as a few hundred seconds during which the source doubles its flux[1]. Thus, the causality argument imposes an upper limit to the X-ray source dimensions of about 20, 40 r_g for a 5, 3×10^6 $M_\odot$ black hole, respectively. Such fast variations in the light curve are present not

[1]The observations of such variations are at the limit of actual instruments, thus faster flux variations can not be excluded, at least in the less massive objects (see Fig. 4.5).

only at low energy, but also in the middle and high energy range. Thus, the source of 10 keV photons should have a similar upper limit to its dimensions. Moreover, from this upper limit to the dimensions of the X-ray source, if the main mechanism for the production of the X-ray radiation is thermal Comptonization, it is possible to derive a lower limit to the coronal density and an estimate of the mean free path of 10 keV photons, assuming a temperature for the coronal electrons. In fact, if the coronal temperature is 150 keV, a photon on average increases its energy of ∼50 % in an Inverse Compton interaction. Thus, a photon, starting from 0.2 keV needs about 7 interactions to become a 10 keV photon. Assuming isotropy of the Inverse Compton process, random walk of the photons, a negligible size of the 0.2 keV initial emitting source and a size of the source at 10 keV of ∼30 r_g, it is possible to estimate the photon mean free path of 10 keV photons: $\lambda_{10}=\frac{R}{\sqrt{N_{int}}}=\frac{30r_g}{\sqrt{7}}=8\times10^{12}$ cm. Moreover, it is possible to have a lower limit to the coronal density. In fact for values of the optical depth (τ) ranging between $\tau \sim 0.1-1$, a typical range for Seyfert galaxies (e.g. Petrucci & Dadina 2003), this yields a coronal density of: $\rho_{e^-} = \frac{\tau}{\sigma_T R} \sim 7-70\times10^9$ cm^{-3}, where σ_T is the Thomson cross-section.

However the light bending model requires that the primary X-ray source is much smaller than 20-40 r_g. In fact if the source is so extended, then the effects due to the light bending (see Fig. 1.5 and 1.6) would be averaged over all the source volume and the correlations between the flux of the power law and the one of the disc reflection would be broken. Thus, it seems reasonable that the dimensions of the primary X-ray source are of the order, or lower 1 r_g. Assuming this extension and calculating the source luminosity, it is possible to measure an order of magnitude of the compactness parameter ($l = \frac{L}{R}\frac{\sigma_T}{m_e c^3}$, where σ_T is the Thompson scattering cross section, L is the luminosity and R is the size of the compact X-ray source). In the case of MCG-6-30-15, the compactness parameter, obtained extrapolating above 511 keV the power law as observed during the high flux states (Larsson et al. 2007), results to be higher than ten, indicating a significative contribution due to pairs. On the other hand, the *BeppoSAX* data showed the presence of a high energy cut off in MCG-6-30-15 (Guainazzi et al. 1999; Fabian et al. 2002) that seems to rule out a dominant contribution due to pairs. However, the compactness depends critically on the high energy extrapolation of the power law. In fact, with slightly different assumptions the compactness parameter results to be lower than ten.

Another difficulty with the ionized reflection interpretation may be related with the ionization parameter. In fact, in order to explain both the soft excess, the broad Fe K line and the high energy emission with a single ionized reflection component, the ionization parameter has to be confined in a small range of values. Figure 1.2 shows that the ionized reflection is significantly different from a power law only if the ionization parameter ξ is lower than about 1000-3000 erg cm s^{-1}. On the other hand, if the ionization parameter is too low, then the reflection is neutral without emission lines at low energy to reproduce the soft excess. Thus, the disc ionization parameter has to be between about 1-10 and 1000-3000 erg cm s^{-1}, in order to be able to reproduce the soft excess and the broad Fe K line simultaneously. If all the soft excesses are due to ionized reflection, then the ionization parameter should be always within this range spanning about 3 order of magnitudes. This would mean that all

the AGNs with such a feature should have a disc with an ionization parameter in this range. Although it seems somehow a fine tuning requirement, the sample analyzed shows a spread in the observed luminosities and black hole masses spanning about 3 order of magnitudes, thus the spread expected is still within this range.

9.3.1 Peculiar behaviors

The spectral shape and the variability of MCG-6-30-15 may be reproduced by a strong ionized disc reflection component if the light bending effect is at work. Nevertheless, the biggest flare, that occurred during the low flux observation (see §4.3), does not seem to be affected by the light bending effect. This implies that during the life of the source some peculiar periods occur (Goosmann et al. 2007).

During the low flux observation of NGC 4051, the *XMM-Newton* data show evidence for the presence of photoionized gas. This emission is constant over time and its presence was not detected before, during the high flux observation, only because of its low contribution as respect to the power law. This emission from photoionized gas is typical of type 2 objects. This observation is important because, it shows for the first time that such component has been in a type 1 object and it was possible due to the low continuum emission. During the high flux observation, the data show a clear evidence for the presence of a warm absorber, typical of type 1 objects. This, in agreement with the unification models, suggests that type 1 and 2 objects have the same spectral components that appear in absorption (warm absorber), when the continuum is high, or in emission (photoionized gas), when the flux is low.

In the case of MKN 509, both a narrow redshifted and a blueshifted Fe line has been observed. This source is not unique, in fact narrow absorption lines have been observed in several other objects (Nandra et al 1999; Pounds et al. 2003; Reeves, O'Brien & Ward 2003; Longinotti et al. 2003; 2007; Yaqoob & Serlemitsos 2005; Matt et al. 2005). What is peculiar of this source is that the redshifted absorption is not imprinted above a broad Fe K line that may lead to uncertainties related with the underlying emission. Moreover the observation of the redshifted absorption line does not seem to be related with the continuum changes. When observed, during the SAX6 observation, this feature seems to be related, instead, with the blueshifted absorption at 8.2 keV. In fact, the time resolved spectral analysis shows that during the *BeppoSAX* observation the redshifted and blueshifted absorption lines appear one after the other. This behaviour suggest a sort of aborted jet scenario (Ghisellini et al. 2004). Nevertheless, the very first results from the new *XMM-Newton* observation confirm the presence of a variable blueshifted Fe K line, but they show no link with the redshifted one. Thus completely different interpretations are still open (i.e. Ruszkowski & Fabian 2000). If confirmed, these red-shifted lines would be particularly interesting because they could be one of the best direct evidence of matter free-falling onto, or being located extremely near to, a supermassive black hole.

9.4 Overall Conclusions

In this dissertation the nature of the soft excess has been studied. Although the problem is still open, the results of the time resolved spectral variability analysis on the key study

objects showed that the soft excess can be explained by an ionized disc reflection model, while a standard thermal component seems unlikely. Moreover, the analysis of the sample showed that this interpretation may be true for the whole sample of source.

The other main topic of this work has been the search/study for the presence of broad Fe lines in the spectra of AGNs. All the sources studied individually (apart from MKN 509) show the evidence for the presence of this broad component of the Fe K line. Moreover, the RMS study of the sample suggest that other sources may have the same broad component of the Fe K line. Thus, this feature seems quite a common characteristic of AGN spectra. Nevertheless, in order to derive statistical information a complete sample is needed.

The evidence for the presence of an ionized disc reflection component is particularly strong in the cases where the source spectrum shows both a broad component of the Fe K line and a soft excess that can be reproduced by the same ionized disc reflection component. In this dissertation, for MCG-6-30-15, NGC 4051, IRAS 13224–3809 and MKN 841 it has been shown that this reflection component is also in agreement with the spectral variability. The spectral variations of these sources are explained by the light bending model. In this case the source should be compact and within about 10-20 r_g from the black hole. The light bending model, that predicts an almost constant disc ionized reflection component, may explain also the RMS shapes of the sources of the first group. While the sources of the second group may be explained if the X-ray source is more distant of 10-20 r_g from the black hole and thus the light bending is not important. This is not, however, the only model that can explain the spectral shape and its variability. Models involving a large column of relativistically moving ionized material may explain the source emission and variability as well. The main differences between the different spectral modelization shall occur at energies higher than 10-20 keV. The *BeppoSAX* and *Suzaku* observations of MCG-6-30-15, NGC 4051 and MKN 841 showed the evidence for an high flux in this energy band, suggesting a strong (ionized) reflection component. Nevertheless, further studies are needed to firmly confirm these results.

One of the open issues of the soft excess interpretation as ionized disc reflection is the observation of strong soft excesses in sources where a broad component of the Fe K line is not observed. If the soft excess is due to relativistic reflection, then a broad Fe K line should be present. Many different explanations may be invoked to explain this. In fact, as shown by Fabian & Miniutti (2005) the detection of a broad Fe K line in sources without iron overabundance or an high reflection fraction, is possible only with extremely long *XMM-Newton* observations, at the limit of present instrumentation. In addition, as shown by Matt et al. (1996), the reflectivity of iron is reduced for some ionization parameters. Nevertheless, until the broad line is detected simultaneously and consistently with the soft excess, the ionized reflection model can not be said fully tested.

Appendix A

Byproducts: Discovery of the most luminous ULX?

In this appendix I report the detection of a off nuclear X-ray source in the inactive galaxy MCG-03-34-63. This discovery happened by chance while studying the active galaxy IRAS13197-1627 with the *XMM-Newton* satellite. The accidental nature of the discovery is the main reason for not being primarily related with the basic topic of the thesis.

If this X-ray source will be confirmed to be at the same distance of its apparent host galaxy (we have been awarded a FORS2 observation at the VLT telescope to measure the source redshift), the bolometric luminosity of $\sim 3 \times 10^{41}$ erg s^{-1}, exceeding by a factor > 115 the Eddington luminosity for a 20 $M_{\odot}$ stellar–mass black hole, would make it the most luminous ULX ever detected, and possibly one of the best IMBH–candidate so far.

A.1 Introduction

All known black holes belong to two families: stellar–mass black holes as those seen in X–ray binaries, and super–massive black holes that are present in the centers of galaxy bulges sometimes revealing themselves as AGN. While the former have masses up to $\sim 20 M_{\odot}$ (e.g. Fryer & Kalogera 2001), the latter have masses in the range $\sim 10^6$–10^9 $M_{\odot}$, the smaller–mass super–massive black hole to date being that in NGC 4395 with a mass of a few times 10^5 $M_{\odot}$ (Peterson et al. 2005). Although it has long been thought that intermediate–mass black holes (IMBH) with masses $\sim 10^2$–10^4 $M_{\odot}$ may form in dense stellar clusters (e.g. Frank & Rees 1976; Portegies Zwart et al. 1999), there are no IMBHs known to date filling the mass–gap between the two known families. If present, active IMBHs may reveal themselves as accreting X–ray sources exceeding by a large factor the Eddington luminosity of stellar–mass black holes ($L^{Edd}_{20\ M_{\odot}} = 2.6 \times 10^{39}$ erg s^{-1} for a "maximal–mass" stellar–mass black hole of 20 $M_{\odot}$).

Ultra–Luminous X–ray sources (ULX) are off–nuclear point–like X–ray sources seen in other galaxies (than the Milky Way) with luminosities exceeding $L^{Edd}_{20\ M_{\odot}}$ (see e.g. Colbert & Mushotzky 1999; Mushotzky 2004). Since the Eddington argument implies a lower limit of 20 $M_{\odot}$ on the mass of the central object, ULXs are often regarded as IMBH–candidates (see e.g. Miller & Colbert 2003; Fabbiano 2005). However, inferring a lower limit on the mass of an

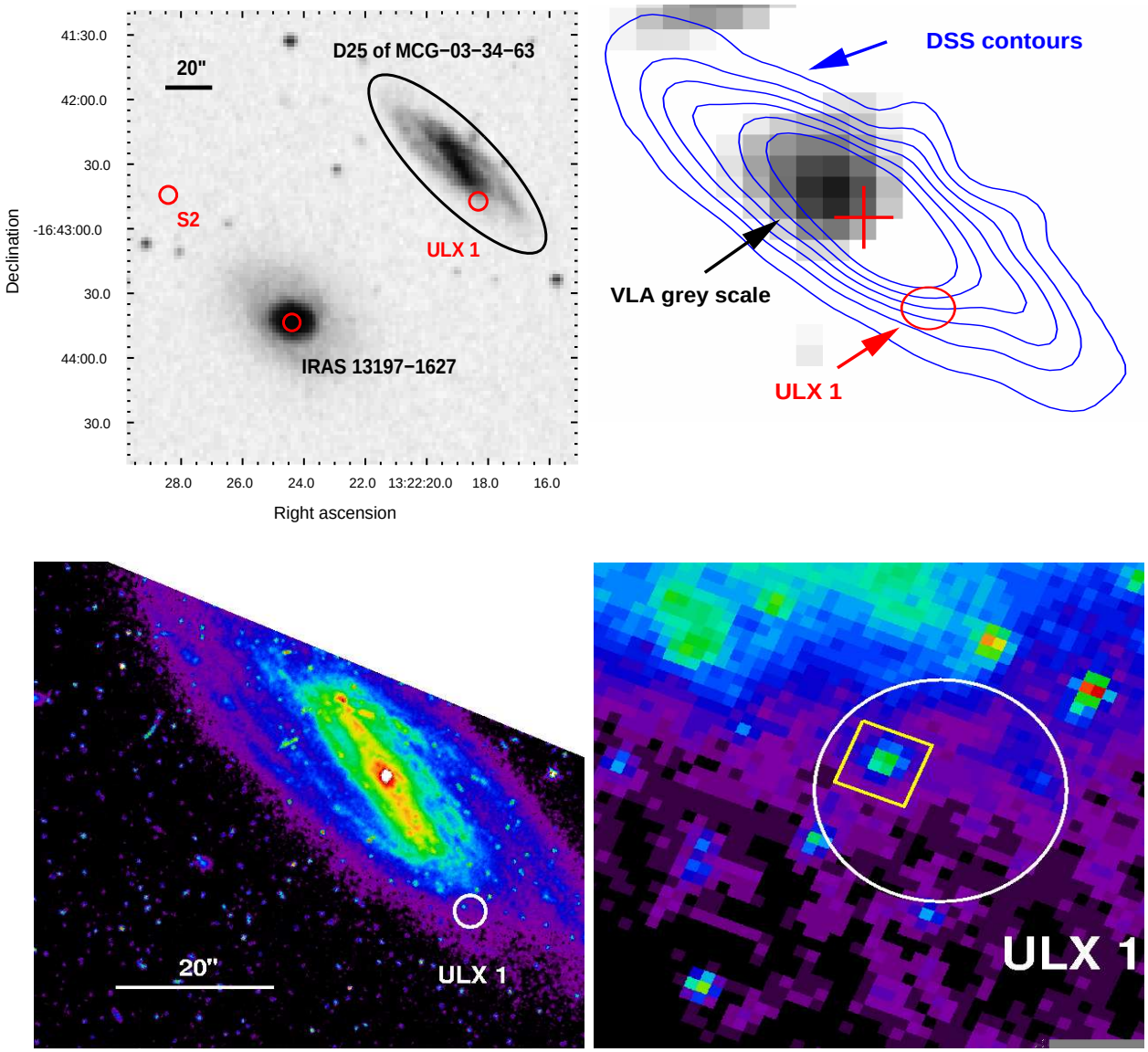

Figure A.1: For all images, North is upwards and East to the Left. **Top Left:** a 3.5'×3.5' DSS optical image in the region of IRAS 13197–1627 and MCG–03-34-63 is shown together with the detected X–ray sources (red circles). We also show the D_{25} ellipse of MCG–03-34-63 as a black ellipse. **Top Right:** the gray scale is the VLA 21 cm image in the region of of the galaxy MCG–03-34-63. Optical contours from the DSS are shown in blue. The red circle is centered on the *XMM–Newton* position of ULX 1 and the red cross is the optical center of MCG–03-34-63. **Bottom Left:** a portion of the HST WFPC2 500s exposure (F606W filter) of MCG–03-34-63 is shown together with the *XMM–Newton* error–circle (2" in radius) centered on ULX 1. **Bottom Right:** expanded view of the HST image around the X–ray error–circle. The yellow box is centered on the brightest optical source within the *XMM–Newton* error–circle and represents the position of the most likely optical counterpart of ULX 1.

accreting compact object only from its bolometric luminosity can lead to misleading results. This is because, if potential anisotropies of emission (e.g. beaming, see Reynolds et al. 1997; King et al. 2001) or accretion (e.g. radiation–driven inhomogeneous accretion, see Begelman 2002) are not taken into account, the lower limit on the mass of the object may be severely over–estimated. Both the beaming and inhomogeneous accretion scenarios can be invoked to explain luminosities up to a few times 10^{40} erg s^{-1} with accretion on standard stellar–mass black holes. However, geometric beaming (e.g. a funnel geometry) and inhomogeneous accretion can only provide an effective luminosity exceeding the Eddington limit by a factor $\sim$23 (Madau 1988) and $\sim$10 (Ruszkowski & Begelman 2003), respectively. Thus, for ULXs with luminosities exceeding 10^{41} erg s^{-1}, relativistic beaming seem the only option to avoid the presence of an IMBH. It is thus clear that the best IMBH–candidates are ULXs in the high end of the luminosity function with luminosity approaching (or possibly above) 10^{41} erg s^{-1}. The best IMBH–candidate so far is a ULX in the galaxy M 82. Its extreme luminosity (up to $\sim 9 \times 10^{40}$ erg s^{-1}), together with the detection of a 54 mHz QPO and an Fe Kα line (which both argue against a beamed source), make it difficult not to invoke an IMBH (Matsumoto et al. 2001; Kaaret et al. 2001; Strohmayer & Mushotzky 2003). We stress again here that if this off nuclear X-ray source is at the distance of its host galaxy, it would be the most luminous ULX ever detected with a bolometric luminosity of $\sim 3 \times 10^{41}$ erg s^{-1}

A.2 MCG–03-34-63 ULX–1

The new ULX candidate has been noted first while studying the *XMM–Newton* data of the active galaxy IRAS 13197–1627 (Miniutti et al. 2006). IRAS 13197–1627 is not isolated in the sky and the inactive spiral galaxy MCG–03-34-63 (z=0.0213) is only 1.8' away towards NW. MCG–03-34-63 has been often confused with IRAS 13197–1627 (a.k.a. MCG–03-34-64) until 1996, where it was detected in the radio with a total flux of 93.4 mJy at 4.9 GHz (Colbert et al. 1996). It is also a relatively luminous IR galaxy with $L_{40-122\mu m} = 2.1 \times 10^{10}\ L_{\odot}$, most likely associated with star–formation (Surace, Sanders & Mazzarella 2004).

In the top left panel of Fig. A.1, we show the optical Digitized Sky Survey (DSS) image centered between the two galaxies. We also show as circles the X–ray sources detected in the field, and the D_{25} ellipse of MCG–03-34-63 (the dimension defined to be equal to 25 mag arcsec^{-2}). Besides IRAS 13197–1627, the second strongest X–ray source is superimposed on the outer arms of the galaxy MCG–03-34-63. Its X–ray position is displaced by about 19" in the SW direction with respect to the optical center of the galaxy. We derived its position from the *XMM-Newton* observation and resulted to be RA: 13h22m18.3s and DEC -16d42m47.7s. Its official name is thus XMMU J132218.3–164247 and we shall call it ULX 1 here for brevity.

In order to detect the position of this source with greater accuracy a DDT *Chandra* observation has been successfully proposed. The *Chandra* X-ray position of the ULX is RA: 13h22m18.36s and DEC:-16d42m47.2s (J2000) No optical point–like counterpart is seen in the DSS meaning that the source is fainter than $\sim$21 in R and $\sim$22.5 in B.

We also analyzed the Optical Monitor mosaic of the field images (UVW1 filter). The UV contours trace MCG–03-34-63, peak at about 17" NE of the galaxy center, and no point–like source corresponds to ULX 1. Radio images (VLA 21 cm, 1993 May) have been analyzed

as well and, besides the AGN IRAS 13197–1627, there is an excess within the D_{25} ellipse of MCG–03-34-63 which is however not consistent with ULX 1 nor exactly centered on the galaxy optical center (see top right panel of Fig. A.1). At 4.9 GHz, the nucleus of MCG–03-34-63 is clearly detected (Colbert et al. 1996), but there is no radio excess at the position of ULX 1.

The Hubble Space Telescope (HST) also observed the region in July 1994 for 500 s with the WFPC2 and the F606W filter applied. A portion of the HST image is shown in the bottom left panel of Fig. A.1 together with a white circle of 2" radius centered on the X–ray position of ULX 1 and representing the *XMM–Newton* error–circle. It is interesting to notice that ULX 1 lies along the bar axis of MCG–03-34-63 where the interstellar medium may be stressed and where off–nuclear X–ray sources have been found in other galaxies (see e.g. in NGC 1672, Brandt et al. 1996). In the bottom right panel of Fig. A.1, we show a zoom into the HST image. The brightest optical source within the *XMM–Newton* error–circle is marked with a yellow box and represents the most likely optical counterpart (if any) of ULX 1. Another faint source is present in the error–circle and two are seen at its edges towards SE.

A.3 X–ray data analysis

ULX 1 provides 457 background–corrected counts in the EPIC–pn camera, and about 300 in each of the MOS detectors in the 0.5–7 keV band. We extracted the X–ray light curve of ULX 1 from the MOS+pn detectors to search for short–timescale variability. Given the low count rate (about 0.025 Cts/s), we chose a relatively long time bin of 2.9 ks in order to reduce the errors on the individual data points. The resulting background-subtracted light curve is shown in the left panel of Fig. A.2. A fit with a constant gives $\chi^2 = 27.3$ for 12 dof, showing the the source is variable at the 99.3 per cent confidence level. By applying the Kolmogorov–Smirnov test, the significance of the variability is increased to the 99.94 per cent level.

We also extracted the X–ray spectra from both the pn and MOS cameras in the same 0.5–7 keV band. As a first attempt to describe the X–ray spectral shape of ULX 1, we consider an absorbed power law model and we fix the absorbing column to the Galactic value, i.e. at 5.8×10^{20} cm^{-2} (Dickey & Lockman 1990). The joint fit to the pn and MOS data is unacceptable ($\chi^2 = 74$ for 51 dof) because the spectrum is more curved than the model, suggesting the presence of excess absorption. We then keep the Galactic column fixed, but add a second (neutral) absorption component. The statistical quality of the fit improves dramatically and we obtain $\chi^2 = 37$ for 50 dof. We measure an excess absorption column density of $2.3^{+0.6}_{-0.4} \times 10^{21}$ cm^{-2}, while the power law has a slope $\Gamma = 1.95^{+0.18}_{-0.16}$. The spectra, best–fit model and residuals are shown in the right panel of Fig. 10.2. We point out that the observed amount of excess absorption is typical for ULXs, suggesting that part of it originates in the ULX environment (Swartz et al. 2004; Winter, Mushotzky & Reynolds 2006). The X–ray spectral slope also compares very well with other ULXs and lies at the boundary between "low–state" and "high–state" sources (as classified by Winter et al. 2006).

The observed 0.5–7 keV flux is 8.2×10^{-14} erg cm^{-2} s^{-1}. By extrapolating the model up to 10 keV, the source has a 0.5–10 keV flux of 9.8×10^{-14} erg cm^{-2} s^{-1}. Note that the observed variability (see Fig. A.2) implies that during the observation ULX 1 reached a flux

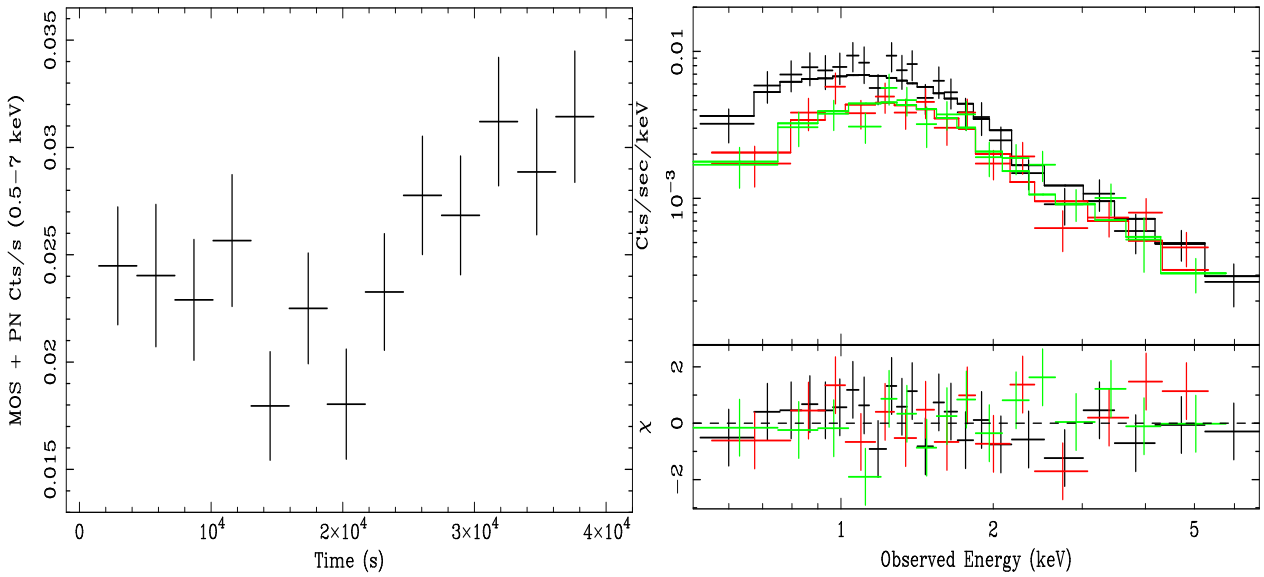

Figure A.2: Left panel shows the background subtracted light curve of ULX 1 obtained from the MOS+pn data in the 0.5–7 keV band (bin-size of 2.9 ks). The Kolmogorov–Smirnov probability that the light curve is constant in 5.7×10^{-4} only. Right panel shows the pn (black) and MOS (red and green) spectrum of ULX 1 together with the best–fitting absorbed power law model and the resulting residuals (see text for discussion).

of about $\sim 1.2 \times 10^{-13}$ erg cm^{-2} s^{-1} in the 0.5–10 keV band.

A.3.1 The extreme luminosity of ULX 1

The excess absorption we detect and the lack of a bright optical counterpart (see discussion below) makes it unlikely that the source is a foreground object, though we cannot exclude it. If so, the X–ray luminosity of the source can be computed as a lower limit under the hypothesis that it is at least at the distance of MCG–03-34-63 (z=0.0213). By using our best–fitting absorbed power–law model, it turns out that ULX 1 has an intrinsic luminosity $L_{0.5-7} = 1.1 \times 10^{41}$ erg s^{-1} in the 0.5–7 keV band and $L_{0.5-10} = 1.3 \times 10^{41}$ erg s^{-1} once extrapolated to 10 keV (with $H_0 = 70$ ks s^{-1}, $\Lambda_0 = 0.73$, and $q_0 = 0$). If the light curve variability is taken into account, the source reached a luminosity of $\sim 1.35 \times 10^{41}$ erg s^{-1} ($\sim 1.6 \times 10^{41}$ erg s^{-1}) in the 0.5–7 keV (0.5–10 keV) during the *XMM–Newton* observation.

We point out that of the ∼230 ULXs detected and cataloged up to now (e.g. Liu & Mirabel 2005; Ptak et al. 2006), only a few have luminosities exceeding 3×10^{40} erg s^{-1}. Luminosities of the order of 10^{41} erg s^{-1} or above are extremely unusual, as also shown by the luminosity cutoff in the cumulative luminosity functions (Swartz et al. 2004; Gilfanov, Grimm & Sunyaev 2004). This makes ULX 1 a rare, if not unique, source among the other known ULXs.

A.3.2 Adding a thermal component

To test the similarity of the X–ray properties of ULX 1 with stellar–mass accreting black holes, we also tried two different models: a multi–color disc (MCD) spectrum (`DISKBB`) plus power law, and a Comptonization model (`COMPTT`) that describes Compton up–scattering in a corona of optical depth τ and electron temperature $kT_{\rm el}$ from a Wien distribution of soft seed photons from the disc (with temperature kT). It is worth noting here that the detection of a thermal component could give important (though not conclusive) insights on the compact object mass since, for standard accretion disk, $T_{\rm disc} \propto M_{\rm BH}^{-1/4}$ (objects hosting black-holes of $\sim 10\ M_{\odot}$ have typical temperatures of 1 keV). A cool thermal component from the accretion disc may thus provide some indication for a particularly massive black hole (see e.g. Miller, Fabian & Miller 2004).

However, when applied to the pn and MOS data, neither model provides a statistically significant improvement with respect to the power law one. We can only measure 90 per cent upper limits for the temperature of the putative thermal component of $kT < 0.70$ keV (MCD model), and $kT < 0.35$ keV (`COMPTT`). Thus, the data are consistent with a cool disc, but the thermal component is by no means required by the data.

A.4 An extreme ULX or a background AGN?

The extreme luminosity estimated above assumes that ULX 1 lies within its apparent host galaxy MCG–03-34-63. Luminosities approaching $\sim 10^{41}$ erg s^{-1} can also be reached by extremely powerful supernovae occurring in dense environments, but given that their emission either fades or remains constant over a $\sim$1 yr timescale (e.g. Schlegel 1995), the observed X–ray short–timescale variability rules out this hypothesis. However, ULX 1 could be a background X–ray source. In this case, the inferred luminosity is only a lower limit and a background AGN could well be invoked to explain the X–ray power of the source. This hypothesis can only be tested observationally by obtaining an optical spectrum of the counterpart (if any), but we can nevertheless provide two arguments in favor of an association with MCG–03-34-63.

A.4.1 The $\log N$–$\log S$ estimator

The number of expected X–ray sources within a given area can be estimated by assuming that our field is characterized by the same $\log N$–$\log S$ as observed from deep *XMM–Newton* exposures of the Lockman Hole (Hasinger et al. 2001). Our ULX candidate has a 0.5–2 keV flux of 2.8×10^{-14} erg cm^{-2} s^{-1} and the Lockman Hole $\log N$–$\log S$ implies the presence of about 30 sources per square degree with the same or higher flux (we point out that 30 sources is a conservative estimate). Since the D_{25} ellipse of MCG–03-34-63 covers an area of 2.4×10^{-4} square degrees, the number of expected sources within D_{25} is 0.007. In the 2–10 keV band, we measure a flux of 7×10^{-14} erg cm^{-2} s^{-1} which again corresponds to about 30 sources per square degree providing the same small number of expected sources.

As mentioned, this is only the number of expected sources within a given area (the D_{25} ellipse of MCG–03-34-63) and not directly the probability that ULX 1 is a background AGN. We provide the above estimate for comparison with previous works on other ULXs, but we

must point out that an accurate estimate of the true probability that an X–ray source within a galaxy is a background AGN has yet to be produced, and is well beyond the purpose of this work.

A.4.2 The X–ray to optical flux ratio

Another possible way to constrain the nature of the source is by considering the X–ray to optical flux ratio (X/O$\equiv F_X/F_{\rm Opt}$). AGN have typical X/O below 10 and detailed studies of the optically faint sources in the *XMM–Newton* HELLAS2XMM and *Chandra* deep fields surveys reveal that less than 5 per cent of the hard X–ray selected sources have X/O higher than 90 (Mignoli et al. 2004; Civano, Comastri & Brusa 2005).

We have computed the X/O for the brightest, and most likely optical counterpart, HST source in the *XMM–Newton* error–circle (i.e. the source within the yellow box in the bottom right panel of Fig. A.1). From the HST image, we estimate a magnitude $\rm m_{F606W} = 24.5$ giving rise to R$\sim$ 23.8 (see Holtzman et al. 1995 for the conversion between HST and Johnson magnitudes). By using the definition $\log {\rm X/O} = \log {\rm F}_X + 0.4\ {\rm R} + 5.61$, we then estimate X/O$\sim$ 94 which represents a lower limit on the X/O of ULX 1 (where $\rm F_X$ is the 2–10 keV flux). As mentioned above, sources with X/O$>$ 90 represent less than 5 per cent of the hard X–ray sources population in *Chandra* and *XMM–Newton* deep fields. Moreover, the X–ray and near infrared data of high–X/O sources in the *Chandra* deep fields and the HELLAS2XMM survey identify most (if not all) sources as heavily absorbed AGN (Civano, Comastri & Brusa 2005; Mignoli et al. 2004). In the case of ULX 1, the steep photon index and moderate absorption are inconsistent with this scenario. The detection of an unobscured background AGN with X/O$>$ 94 would be a very rare event on its own, and its detection within the $\rm D_{25}$ ellipse of a spiral galaxy seems highly unlikely, supporting the idea that ULX 1 is not a background AGN but more likely a source associated to the galaxy MCG-03-34-63. It should also be pointed out that the ULXs that have been later classified as background AGN had standard rather than high X/O (Foschini et al. 2002; Masetti et al. 2003).

A.5 Discussion

If ULX 1 is indeed associated with its apparent host galaxy MCG–03-34-63, its luminosity greatly exceeds that of a neutron star, and we have to consider an accreting black hole. In this case, by considering as a template stellar–mass accreting black holes in our Galaxy, the bolometric luminosity is likely to be a few times higher than the 2–10 keV luminosity. By extending our spectral model, we estimate an intrinsic luminosity of $\sim 3 \times 10^{41}$ erg $\rm s^{-1}$ in the 0.2–150 keV band, which we take as a reasonable proxy for the bolometric luminosity of ULX 1. In the absence of beaming, the Eddington limit can be used to infer the presence of a $> 2300\ M_\odot$ black hole, i.e. ULX 1 would be powered by an accreting IMBH.

To reduce the mass of the compact object within the acceptable range of stellar–mass black holes, the intrinsic luminosity has to be boosted by a factor > 115, which could be due to beaming. The simplest candidate mechanism to produce X–ray beaming in an accreting source is to consider a thick accretion disc with a smaller optical depth over a limited range of angles around the rotation axis producing thereby a central funnel. Such a geometry has been

investigated by Madau (1998) who found that if maximal beaming is considered, the effective observed luminosity ($L_{\rm eff}$) can exceed the Eddington limit by a factor of $\sim$23 (see also Misra & Sriram 2003 who derived a much smaller factor of $\sim$5). Thus, even by considering maximal beaming with $L_{\rm eff} = 23 \times L_{\rm Edd}$, ULX 1 does still require a black hole with mass $> 100\ M_{\odot}$. The mass of the central black hole could be in principle reduced to 10–20$M_{\odot}$ by considering maximal beaming *and* a source which is super–Eddington by a large factor (5–10), which seems a rather finely–tuned choice of the parameters. However, Begelman, King & Pringle (2006) recently pointed out that such a scenario is possible though it would predict a strong soft thermalized component (not required by the X–ray spectrum of ULX 1). Beaming can also occur if the X–ray emission is associated with a relativistic jet whose axis is aligned with the line of sight, as proposed by e.g. Reynolds et al. (1997) for ULXs. Indeed, a source with the jet axis aligned within a few degrees with our line of sight and with a sufficiently high Lorentz factor ($\gamma > 4.3$) could account for the observed luminosity with a sub–Eddington jet from a stellar–mass black hole.

Appendix B

The *XMM-Newton* satellite

B.1 Basic characteristics

The *XMM-Newton* satellite (X-ray Multi Mirror, Jansen et al. 2001) is the second of ESA's four "cornerstone" missions defined in the Horizon 2000 Programme. It is dedicated to the exploration of the X-ray Universe. *XMM-Newton* (see Fig. B.1) has been designed to study sources with fluxes as low as 10^{-16} erg s^{-1} cm^{-2}, with a field of view of $30'$ in diameter. It has a pretty high energy resolution up to $E/\Delta E \sim 200 - 800$ and an angular resolution of the order of an arcsecond, but the unique characteristic of *XMM-Newton* is its effective area (4700 cm^{-2}). It has been launched on December the 10^{th} 1999 with the Ariane-5 rocket and now it is in a highly eccentric orbit between 7000-114000 km with an inclination of 40° respect to the ecliptic. The orbital period is of 47.86 hours, thus it is possible to perform uninterrupted observation as long as about 150 ks (∼40 h).

There are in total six science instruments on board XMM-Newton, which are operated simultaneously:

- **EPIC** (European Photon and Imaging Camera; Turner M. J. et al. 2001) 3 CCD cameras for X-ray imaging, moderate resolution spectroscopy, and X-ray photometry. The EPIC instrument is made by two different types of EPIC camera, MOS and pn, both working in the ∼0.1-10 keV energy band.

- **RGS** (Reflecting Grating Spectrometer; Brinkman, A. C. et al. 2001) 2 essentially identical spectrometers for high-resolution X-ray spectroscopy and spectro-photometry; the two instruments are made by dispersion gratings posed on the light path of the 2 EPIC MOS camera. On the focus plane of the 2 spectrometers there are 2 CCD MOS camera. The spectrometers are working in the ∼0.1-3 keV energy band.

- **OM** (Optical Monitor) optical-UV telescope with a aperture of ∼30 cm, for imaging and grism spectroscopy.

The strategic characteristics that make the *XMM-Newton* satellite a so powerful instrument are:

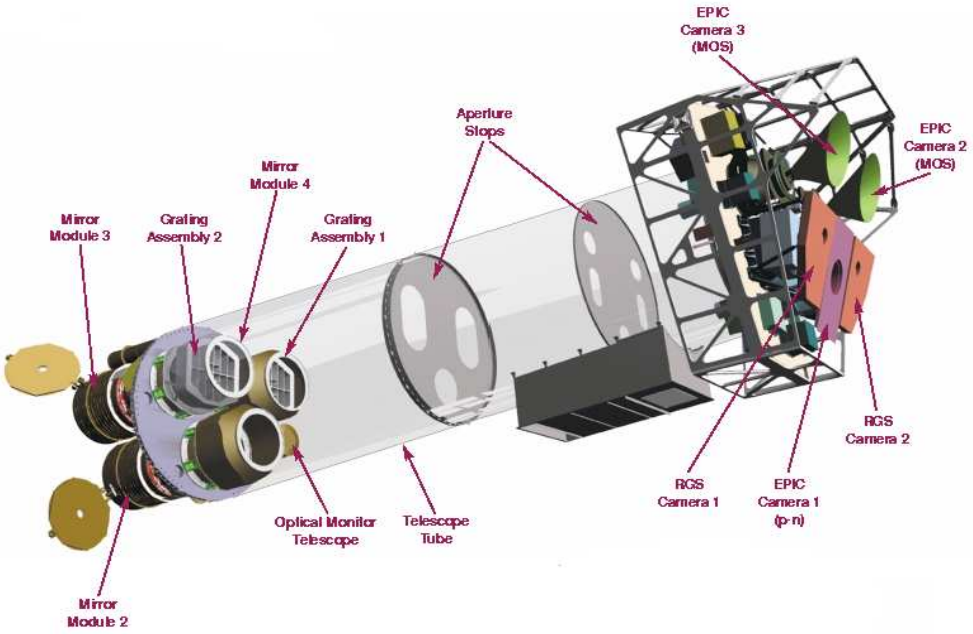

Figure B.1: *Sketch of the XMM-Newton payload. The mirror modules, two of which are equipped with Reflection Grating Arrays, are visible at the lower left. At the right end of the assembly, the focal X-ray instruments are shown: The EPIC MOS cameras with their radiators (black/green "horns"), the radiator of the EPIC pn camera (violet) and those of the (light blue) RGS detectors (in pink). The OM telescope is obscured by the lower mirror module. Figure courtesy of Dornier Satellitensysteme GmbH.*

Instrument	**EPIC MOS**	**EPIC pn**	**RGS**	**OM**
Bandpass	0.15-12 keV	0.15-15 keV	0.35-2.5 keV	180-600 nm
Orbital target†	5-135 ks	5-135 ks	5-135 ks	5-145 ks
Sensitivity‡	$\sim 10^{-14}$	$\sim 10^{-14}$	$\sim 8\times 10^{-5}$	20.7 mag
Field of view (FOV)	30'	30'	$\sim$5'	17'
PSF (FWHM/HEW)†‡	5"/14"	6"/15"	N/A	1.4"-2.0"
Pixel size	40 μm (1.1")	150 μm (4.1")	81 μm	(9×10^{-3} A)0.476513"
Timing resolution	1.5 ms	0.03 ms	0.6 s	0.5 s
Spectral resolution	$\sim$70 eV	$\sim$80 eV	0.04/0.025 A	350

Table B.1: *XMM-Newton* general characteristics

† Total time available for science per orbit.

‡ After 10 ks, in the range 0.15-15.0 keV, in units of erg s^{-1} cm^{-2} for EPIC instruments; OVII 0.57 keV line flux in photons cm^{-2} s^{-1} with a background of 10^{-4} photons cm^{-2} s^{-1} keV^{-1} for RGS; 5-σ detection of an A0 star in 1000 s for OM.

†‡ At 1 keV energy. At the energy of Fe Kα (6.4 keV), the energy resolution of both EPIC cameras is ca. 150 eV; in -1. and -2. order, respectively, at 1 keV, this corresponds to 3.2/2.0 eV (HEW); resolving power ($\lambda/\Delta\lambda$) with UV and optical grism.

High sensitivity the high effective area, the highest ever obtained for an X-ray telescope, has been realized using 58 concentric mirrors. The resulting effective area is $\sim$1550 cm^2 at 1.5 keV for each telescope;

medium and high energy resolution, the RGS instruments have an high energy resolution ($E/\Delta E \sim 200 - 800$), while the EPIC CCD camera have a lower energy resolution $E/\Delta E \sim$20-50 (that corresponds to $\Delta E \sim$60 eV at 1 keV and $\Delta E \sim$150 eV at 6 keV). The main goal of these latter camera is, in fact, the acquisition of images and high throughput spectra in the $\sim$0.1-10 keV energy band;

good angular resolution, in each telescope the Point Spread Function has a Full Width Half Maximum of the order of $6''$;

simultaneous and independent operation of all the detectors, the different instruments can work simultaneously or acquire data in different time and in different observational modes;

large uninterrupted observation windows, the eccentric and high orbit provides the possibility to observe, uninterruptedly, sources for up to $\sim$40 h. This is an extremely important characteristic for variability studies.

simultaneous observation in the X-ray and optical-UV band, the energy bands that is possible to observe simultaneously goes from 150 eV to 10 keV for the EPIC instruments, from 0.5 to 3 keV for the RGS and from 160 to 600 nm for the OM.

B.2 The X-ray telescopes

The three X-ray telescopes are made by 58 concentric mirrors and are co-aligned with a relative astrometry between the three EPIC cameras calibrated to better than 1-2" across the full FOV.

B.2.1 Effective Area

The most important characteristic of the mirror performance is their effective area which reflects the ability of the mirrors to collect radiation at different photon energies.

Figure B.2 show the mirror effective area, folded through the response of the different focal instruments. Being the product of the effective area of the X-ray telescopes and the quantum efficiency of the detectors The XMM-Newton mirrors are most efficient in the energy range from 0.1 to 10 keV, with a maximum at about 1.5 keV and a pronounced edge near 2 keV (the Au M edge). The effective areas of the two MOS cameras are lower than that of the pn, because only part of the incoming radiation falls onto these detectors, which are partially obscured by the RGS.

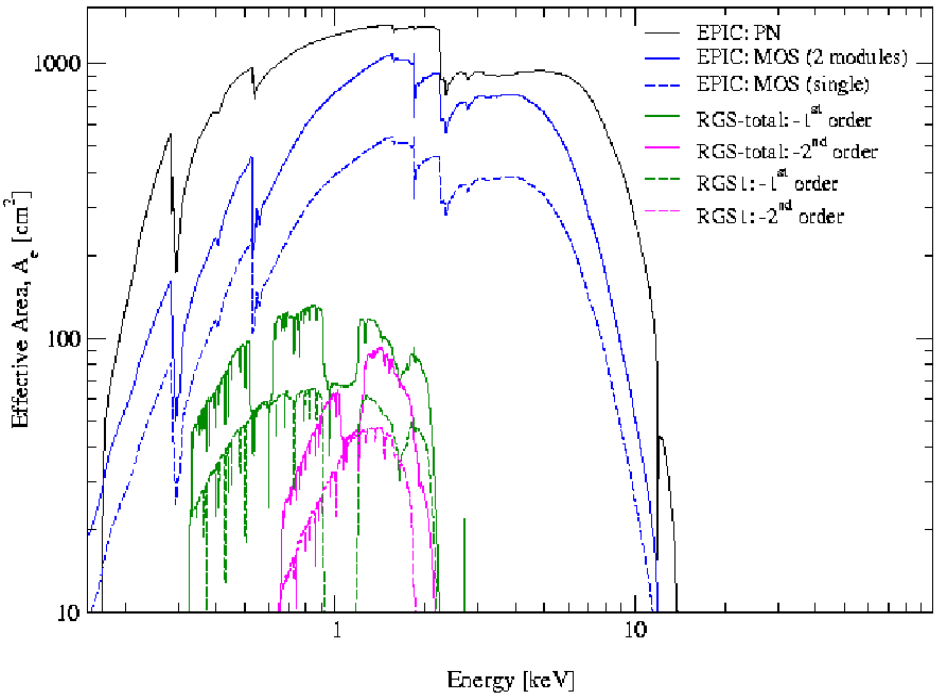

Figure B.2: *The net effective area of all XMM-Newton X-ray telescopes, EPIC and RGS (logarithmic scale). The black solid line that indicates the highest effective area characterizes the PN instrument, the blue solid line shows the one resulting from the sum of the 2 MOS camera. The green and pink solid lines show the effective area of the first order and second order summed RGS camera.*

B.3 European Photon Imaging Cameras: EPIC

EPIC is made by three CCD camera (2 MOS and 1 pn), that offer the possibility to accumulate high statistics images and spectra (it is possible to observe sources with fluxes so low as 10^{-15} erg s^{-1} cm^{-2} in observations of $\sim$50 ks). The field of view is $30'$ and the angular resolution is of about $6''$. The sensitive window of these detectors is between 0.15 e 12 keV with a spectral resolution of $E/\Delta E$ $\sim$20-50.

B.3.1 The EPIC observation modes

The EPIC cameras allow several modes of data acquisition. The main differences between the observing modes are due to the field of view and the readout time. In fact, the brightest sources generally require short readout time.

1. "full frame" e "extended full frame" (the latter is available for the pn camera only): in this observation mode all the pixels of all the CCDs are read, thus all the field of view is observed;

2. "partial window": for the pn camera, with the *large window* mode, only half of the field of view is read, while in *small window* only a piece of only one of the CCDs is used;

3. "timing": in the *timing* mode, imaging is made only in one dimension, data from a predefined area on one CCD chip are collapsed into a one-dimensional row to be read out at high speed. For the pn camera is available another observation mode the *burst* mode, which offers very high time resolution, but has a very low duty cycle of 3 %.

B.3.2 *Pile-up*

The photon pile-up happens when more than one X-ray photon arrive in one camera pixel or in adjacent pixels before it is read out. This may be a problem for the brightest sources. In fact the pile up compromises the spectral response because the charge deposited by more than one photon is added up before being read out, thus creating artificial "hard" photons where there have actually been two or more soft photons.

B.3.3 EPIC background

The EPIC background can be divided into two parts: a cosmic X-ray background and an instrumental background. The latter component may be further divided into a detector noise component, which becomes important at low energies (i.e. below 200 eV) and a second component which is due to the interaction of particles with the structure surrounding the detectors and the detectors themselves. This component is characterized by a flat spectrum and is particularly important at high energies (i.e. above a few keV).

The particle induced background can be divided into 2 components: an external flaring component, characterized by strong and rapid variability, which is often totally absent and a second more stable internal component. The flaring component is currently attributed to soft protons (E_p smaller than a few 100 keV), which are presumably funneled towards the detectors by the X-ray mirrors. The stable component is due to the interaction of high-energy particles (E larger than some 100 MeV) with the structure surrounding the detectors and possibly the detectors themselves. The intensity of this component is of the order of $\sim$2.2 10^{-3}cts cm^{-2} s^{-1} keV^{-1} for the MOS camera and of $\sim$5 10^{-3}cts cm^{-2} s^{-1} keV^{-1} for the pn. The background spectrum is quite hard and it shows clear fluorescence lines of the elements Al-K, Cu-K, Ni-K and Z-K.

Author's refereed publications related with this dissertation

A) Refereed published papers strongly related with the dissertation:

- **Chapter 4:** "Mapping the inner regions of MCG-6-30-15 with XMM-Newton"; G. Ponti, M. Cappi, M. Dadina, and G. Malaguti, 2004, A&A 417, 451
- **Chapter 4:** "Study of the spectral variability of MCG-6-30-15 during a remarkably strong flare period", G. Ponti, M. Cappi, M. Dadina, G. Malaguti, A. Malizia and G. Di Cocco. 2004. Proc. of the meeting: "The Restless High-Energy Universe" (Amsterdam, The Netherlands), E.P.J. van den Heuvel, J.J.M. in 't Zand, and R.A.M.J. Wijers Eds Nuclear Physics B Proceedings Supplements, 132, 221
- **Chapter 4:** "The structure and X-ray radiation spectra of illuminated accretion disks in AGN. III. Modelling fractional variability"; R. Goosmann, B. Czerny, M. Mouchet, G. Ponti, M. Dovciak, V. Karas, A. Rozanska and A.-M. Dumont, 2006 A&A, 454, 741
- **Chapter 4:** "Magnetic flares in Active Galactic Nuclei: Modeling the iron Kα–line" R.W., Goosmann, B., Czerny, M., Mouchet, V., Karas, M., Dovciak, Ponti G., A. Rozanska, A.–M. Dumont 2006, Astronomische Nachrichten, 327, 977
- **Chapter 4:** "Modelling time lags in the X–ray spectra of Active Galactic Nuclei"; R. Goosmann, B. Czerny, V. Karas, G. Ponti A&A in press
- **Chapter 5:** "*XMM–Newton* study of the complex and variable spectrum of NGC 4051"; G. Ponti, G. Miniutti, M. Cappi, L. Maraschi, A.C. Fabian and K. Iwasawa, 2006, MNRAS, 368, 903
- **Chapter 6:** "An ionized disc reflection component for the X-ray spectrum of NGC 4051 and IRAS13224-3809?" G. Ponti, G., Miniutti, G., Fabian, A. C., Cappi, M., & Palumbo, G. G. C. 2006, Astronomische Nachrichten, 327, 1055
- **Chapter 7:** "The origin of the strong soft excess and puzzling iron line complex in Mkn 841"; Petrucci P.O., Ponti G., Matt G., Maraschi L., Malzac J., Mouchet M., Boisson C., Longinotti A., Nandra K., Ferrando P. and Henri J., 2006, Astronomische Nachrichten, 327, 1043

- **Chapter 8:** "X-ray absorption lines reveal the presence of matter falling onto the central black-hole of Mrk 509", Dadina M., Cappi M., Malaguti G., Ponti G. and De Rosa A., 2005, A&A, 442, 461

- **Appendix A:** "Have we detected the most luminous ULX so far?"; Miniutti G., Ponti G., Dadina M., Cappi M., Malaguti G., Fabian A.C., Gandhi P. 2006, MNRAS, 373, L1

B) Refereed published papers weakly related with the dissertation:

- "IRAS 13197-1627 has them all: Compton–thin absorption, photo–ionized gas, thermal plasmas, and broad Fe line"; Miniutti G., Ponti G., Dadina M., Cappi M., Malaguti G., 2007, MNRAS, 375, 227

- "The XMM-Newton view of GRS 1915+105"; Martocchia A., Matt G., Belloni T., Feroci M., Karas V., Ponti G., A&A 2006, A&A, 448, 677

- "First XMM-Newton study of two Narrow-Line Seyfert 1 galaxies discovered in the Sloan Digital Sky Survey"; Foschini L., Braito V., Palumbo G.G.C., Ponti G., Dadina M., Della Ceca R., Di Cocco G., Grandi P. and Malaguti G., 2004, A&A, 428, 51

- "Orbital and Gravitational Modulation of the Redshifted FeKα Emission Line in NGC 3783"; F. Tombesi, B. De Marco, K. Iwasawa, M. Cappi, M. Dadina, G. Ponti, G. Miniutti, G.G.C. Palumbo A&A accepted

Bibliography

[1] Antonucci, R. R. J., & Miller, J. S. 1985, ApJ, 297, 621

[2] Antonucci, R. 1993, ARA&A, 31, 473

[3] Arévalo, P., & Uttley, P. 2006, MNRAS, 367, 801

[4] Arnaud, K., Branduardi-Raymont, G., Culhane, J., et al.: 1985, MNRAS 217, 105

[5] Balbus, S. A., & Hawley, J. F. 1991, ApJ, 376, 214

[6] Ballantyne, D. R., Vaughan, S., & Fabian, A. C. 2003, MNRAS, 342, 239

[7] Ballantyne, D. R., Turner, N. J., & Young, A. J. 2005, ApJ, 619, 1028

[8] Begelman M.C., King A.R., Pringle J.E., 2006, MNRAS in press (preprint astro-ph/0604497)

[9] Bian, W., & Zhao, Y. 2003, MNRAS, 343, 164

[10] Bianchi, S., Matt, G., Haardt, F., Maraschi, L., Nicastro, F., Perola, G. C., Petrucci, P. O., & Piro, L. 2001, A&A, 376, 77

[11] Bianchi, S., Matt, G., Balestra, I., Guainazzi, M., & Perola, G. C. 2004, A&A, 422, 65

[12] Bianchi S., Miniutti G., Fabian A.C., Iwasawa K., 2005, MNRAS, 360, 380

[13] Blandford, R. D., & Znajek, R. L. 1977, MNRAS, 179, 433

[14] Boller, T., Brandt, W. N., & Fink, H. 1996, A&A, 305, 53

[15] Boller, T., Brandt, W. N., Fabian, A. C., & Fink, H. H. 1997, MNRAS, 289, 393

[16] Boller, T., Tanaka, Y., Fabian, A., Brandt, W. N., Gallo, L., Anabuki, N., Haba, Y., & Vaughan, S. 2003, MNRAS, 343, L89

[17] Brandt W.N., Halpern J.P., Iwasawa K., 1996, MNRAS, 281, 687

[18] Brandt, W. N., & Hasinger, G. 2005, ARA&A, 43, 827

[19] Brenneman, L. W., & Reynolds, C. S. 2006, ApJ, 652, 1028

[20] Brinkman, A. C., et al. 2001, A&A, 365, L324

[21] Cappi, M. 2006, Astronomische Nachrichten, 327, 1012

[22] Collinge M.J. et al, 2001, ApJ, 557, 2

[23] Chevallier, L., Collin, S., Dumont, A.-M., Czerny, B., Mouchet, M., Gonçalves, A. C., & Goosmann, R. 2006, A&A, 449, 493

[24] Churazov, E., Gilfanov, M., & Revnivtsev, M., 2001, MNRAS, 321, 759

[25] Civano F., Comastri A., Brusa M., 2005, MNRAS, 358, 693

[26] Colbert E.J.M., Baum S.A., Gallimore J.F., O'Dea C.P., Christensen J.A., 1996, ApJ, 467, 551

[27] Colbert E., Mushotzky R.F., 1999, ApJ, 519, 89

[28] Crummy, J., Fabian, A. C., Brandt, W. N., & Boller, T. 2005, MNRAS, 361, 1197

[29] Crummy, J., Fabian, A. C., Gallo, L., & Ross, R. R. 2006, MNRAS, 365, 1067

[30] Dabrowski, Y., & Lasenby, A. N. 2001, MNRAS, 321, 605

[31] Dadina, M., Cappi, M., Malaguti, G., Ponti, G., & de Rosa, A. 2005, A&A, 442, 461

[32] Dasgupta, S., & Rao, A. R. 2006, ApJL, 651, L13

[33] Day, C. S. R., Fabian, A. C., George, I. M., & Kunieda, H. 1990, MNRAS, 247, 15P

[34] De Rosa, A., Piro, L., Matt, G., & Perola, G. C. 2004, A&A, 413, 895

[35] Dickey J.M., Lockman F.J., 1990, ARAA, 28, 215

[36] Done, C., Sobolewska, M. A., Gierliński, M., & Schurch, N. J. 2007, MNRAS, 374, L15

[37] Dovčiak, M., Bianchi, S., Guainazzi, M., Karas, V., & Matt, G. 2004, MNRAS, 350, 745

[38] Edelson, R. A. & Krolik, J. H. 1988, ApJ, 333, 646

[39] Edelson R., Nandra K., 1999, ApJ, 514, 682

[40] Edelson, R., Turner, T. J., Pounds, K., Vaughan, S., Markowitz, A., Marshall, H., Dobbie, P., & Warwick, R. 2002, ApJ, 568, 610

[41] Edwards, S., Hartigan, P., Ghandour, L., & Andrulis, C. 1994, AJ, 108, 1056

[42] Elvis, M., et al. 1994, ApJS, 95, 1

[43] Fabbiano G., 2005, Science, 307, 533

[44] Fabian, A. C., Rees, M. J., Stella, L., & White, N. E. 1989, MNRAS, 238, 729

[45] Fabian, A. C. 1999, Proceedings of the National Academy of Science, 96, 4749

[46] Fabian, A. C., Iwasawa, K., Reynolds, C. S., & Young, A. J. 2000, PASP, 112, 1145

[47] Fabian, A. C., Vaughan, S., Nandra, K. et al. 2002, MNRAS, 335, L1

[48] Fabian, A. C. & Vaughan, S. 2003, MNRAS, 340, L28

[49] Fabian, A. C., Miniutti, G., Gallo, L., Boller, T., Tanaka, Y., Vaughan, S., & Ross, R. R. 2004, MNRAS, 353, 1071

[50] Falco, E., Kurtz, M., Geller, M., et al.: 1999, PASP 111, 438

[51] Fiore, F., La Franca, F., Giommi, P., Elvis, M., Matt, G., Comastri, A., Molendi, S., & Gioia, I. 1999, MNRAS, 306, L55

[52] Fisher, K. B., Huchra, J. P., Strauss, M. A., Davis, M., Yahil, A., & Schlegel, D. 1995, ApJS, 100, 69

[53] Foschini L. et al., 2002, A&A, 396, 787

[54] Frank J, Rees M.J., 1976, MNRAS, 176, 633

[55] Fryer C.L., Kalogera V., 2001, ApJ, 554, 548

[56] Gallo, L. C., Boller, T., Tanaka, Y., Fabian, A. C., Brandt, W. N., Welsh, W. F., Anabuki, N., & Haba, Y. 2004, MNRAS, 347, 269

[57] Gebhardt K., et al., 2000, ApJ, 539, L13

[58] Genzel, R., Eckart, A., Ott, T., & Eisenhauer, F. 1997, MNRAS, 291, 219

[59] George, I. M., & Fabian, A. C. 1991, MNRAS, 249, 352

[60] George, I., Nandra, K., Fabian, A., et al. 1993: MNRAS 260, 111

[61] George, I. M., Turner, T. J., Netzer, H., Nandra, K., Mushotzky, R. F., & Yaqoob, T. 1998, ApJS, 114, 73

[62] George, I. M., Turner, T. J., Yaqoob, T., Netzer, H., Laor, A., Mushotzky, R. F., Nandra, K., & Takahashi, T. 2000, ApJ, 531, 52

[63] Gilfanov M., Grimm H.–J., Sunyaev R., 2004, MNRAS, 351, 1365

[64] Ghisellini, G., Haardt, F., & Matt, G. 2004, A&A, 413, 535

[65] Gierliński, M., & Done, C. 2004, MNRAS, 349, L7

[66] Gierliński, M., & Done, C. 2006, MNRAS, 371, L16

[67] Goosmann, R. W., Czerny, B., Karas, V., & Ponti, G. 2007, ArXiv Astrophysics e-prints, arXiv:astro-ph/0702685

[68] Goosmann, R. W., Czerny, B., Mouchet, M., Ponti, G., Dovčiak, M., Karas, V., Różańska, A., & Dumont, A.-M. 2006, A&A, 454, 741

[69] Grandi, P., & Palumbo G.G.C, 2004, Science, 306, 998

[70] Grandi, P., Malaguti, G., & Fiocchi, M. 2006, ApJ, 642, 113

[71] Grupe D., Wills B. J., Leighly K. M., Meusinger H., 2004, AJ, 127, 156

[72] Guainazzi M. et al, 1998, MNRAS, 301, L1

[73] Guainazzi, M., Matt, G., Molendi, S. et al. 1999, A&A, 341, L27

[74] Guainazzi, M., Bianchi, S., & Dovčiak, M. 2006, Astronomische Nachrichten, 327, 1032

[75] Haardt, F., & Maraschi, L., 1991, ApJL, 380, L51

[76] Haardt, F., & Maraschi, L., 1993, ApJ, 413, 507

[77] Haardt, F., Maraschi, L., & Ghisellini, G., 1994, ApJL, 432, L95

[78] Haardt, F. 1997, ASP Conf. Ser. 121: IAU Colloq. 163: Accretion Phenomena and Related Outflows, 121, 101

[79] Haardt, F., Maraschi, L., & Ghisellini, G., 1997, ApJ, 476, 620

[80] Hasinger G. et al., 2001, A&A, 365, L45

[81] Holtzman J.A., Burrows C.J., Casertano S., Hester J.J., Trauger J.T., Watson A.M., Worthey G., 1995, PASP, 107, 1065

[82] Iwasawa, K., Fabian, A. C., Young, A. J., Inoue, H., & Matsumoto, C. 1999, MNRAS, 306, L19

[83] Iwasawa, K., Miniutti, G., & Fabian, A. C. 2004, MNRAS, 521

[84] Janiuk, A., Czerny, B., & Madejski, G. M. 2001, ApJ, 557, 408

[85] Jansen, F., et al. 2001, A&A, 365, L1

[86] Johnson, N.: 1997, BAAS 190, 2005

[87] Jourdain, E., et al. 1992, A&A, 256, L38

[88] Kaaret P., Prestwich A. H., Zezas A., Murray S.S., Kim D.-W., Kilgard R.E., Schlegel E.M., Ward M.J., 2001, MNRAS, 321, L29

[89] Kataoka, J., et al. 2006, ArXiv Astrophysics e-prints, arXiv:astro-ph/0612754

[90] King A.R., Davies M.B., Ward M.J., Fabbiano G., Elvis M., 2001, ApJ, 552, L109

[91] Kinkhabwala A. et al, 2002, ApJ, 575, 732

[92] Iwasawa, K., Fabian, A. C., Young, A. J., Inoue, H., & Matsumoto, C. 1999, MNRAS, 306, L19

[93] Kinkhabwala, A., et al. 2003, in press, astro-ph/0304332

[94] Krongold, Y., Nicastro, F., Elvis, M., Brickhouse, N., Binette, L., Mathur, S., & Jimenez-Bailon, E. 2007, ArXiv Astrophysics e-prints, arXiv:astro-ph/0702399

[95] Kormendy, J., & Richstone, D. 1995, ARA&A, 33, 581

[96] Kormendy, J., & Gebhardt, K. 2001, AIP Conf. Proc. 586: 20th Texas Symposium on relativistic astrophysics, 586, 363

[97] Lamer G., M^{c}Hardy I.M., Uttley P., Jahoda K., 2003, MNRAS, 338, 323

[98] Laor, A. 1991, ApJ, 376, 90

[99] Larsson, J., Fabian, A. C., Miniutti, G., & Ross, R. R. 2007, MNRAS, 63

[100] Lawrence, A. 1991, MNRAS, 252, 586

[101] Lawrence, A., & Papadakis, I. 1993, ApJL, 414, L85

[102] Lee, J. C., Fabian, A. C., Reynolds, C. S., Brandt, W. N., & Iwasawa, K. 2000, MNRAS, 318, 857

[103] Lee, J. C., Iwasawa, K., Houck, J. C., Fabian, A. C., Marshall, H. L., & Canizares, C. R. 2002, ApJL, 570, L47

[104] Leighly, K. M. 1999, ApJS, 125, 317

[105] Leighly, K. M. 2004, ApJ, 611, 125

[106] Lewis, K. T., & Eracleous, M. 2006, ApJ, 642, 711

[107] Longinotti, A. L., Cappi, M., Nandra, K., Dadina, M., & Pellegrini, S. 2003, A&A, 410, 471

[108] Longinotti, A., Nandra, K., Petrucci, P., O'Neill, P.: 2004, MNRAS 355, 929

[109] Longinotti, A. L., Sim, S. A., Nandra, K., & Cappi, M. 2007, MNRAS, 374, 237

[110] Liu Q.Z., Mirabel I.F., 2005, A&A, 429, 1125

[111] Lu, Y., & Yu, Q. 2001, MNRAS, 324, 653

[112] Madau P., 1988, ApJ, 327, 116

[113] Maisack, M., et al. 1993, ApJL, 407, L61

[114] Malizia, A., Bassani, L., Zhang, S. N., Dean, A. J., Paciesas, W. S., & Palumbo, G. G. C. 1999, ApJ, 519, 637

[115] Maraschi, L., & Haardt, F. 1997, ASP Conf. Ser. 121: IAU Colloq. 163: Accretion Phenomena and Related Outflows, 121, 101

[116] Markoff, S., Falcke, H., & Fender, R. 2001, A&A, 372, L25

[117] Martocchia, A., Karas, V., & Matt, G. 2000, MNRAS, 312, 817

[118] Martocchia, A., Matt, G., & Karas, V. 2002, A&A, 383, L23

[119] Magdziarz P., Zdziarski A.A., 1995, MNRAS, 273, 837

[120] Magdziarz, P., Blaes, O. M., Zdziarski, A. A., Johnson, W. N., & Smith, D. A. 1998, MNRAS, 301, 179

[121] Markowitz A., Edelson R., Vaughan S., 2003, ApJ, 598, 935

[122] Masetti N., Foschini L., Ho L.C., Dadina M., di Cocco G., Malaguti G., Palazzi E., 2003, A&A, 406, L27

[123] Matsumoto H., Tsuru T.G., Koyama K., Awaki H., Canizares C.R., Kawai N., Matsushita S., Kawabe R., 2001, ApJ, 547, L25

[124] Matt, G., & Perola, G. C. 1992, MNRAS, 259, 433

[125] Matt, G. 2000, A&A, 355, L31

[126] Matt, G., Porquet, D., Bianchi, S., Falocco, S., Maiolino, R., Reeves, J. N., & Zappacosta, L. 2005, A&A, 435, 857

[127] McHardy, I. M. 1989, ESA SP-296: Two Topics in X-Ray Astronomy, Volume 1: X Ray Binaries. Volume 2: AGN and the X Ray Background, 1111

[128] McHardy, I. M., Papadakis, I. E., & Uttley, P., 1998, The Active X-ray Sky: Results from BeppoSAX and RXTE, 509

[129] M^{c}Hardy I.M., Papadakis I.E., Uttley P., Page M.J., Mason K.O., 2004, MNRAS, 348, 783

[130] McHardy, I. M., Koerding, E., Knigge, C., Uttley, P., & Fender, R. P. 2006, Nature, 444, 730

[131] Mignoli M. et al., 2004, A&A, 418, 827

[132] Miller M.C., Colbert E., 2004, IJMP D, 13, 1 (preprint astro–ph/0308402)

[133] Miller J.M., Fabian A.C., Miller M.C., 2004, ApJ, 614, L117

[134] Miniutti, G., Fabian, A. C., Goyder, R., & Lasenby, A. N., 2003, MNRAS, 344, L22

[135] Miniutti, G., & Fabian, A. C., 2004, MNRAS, 349, 1435

[136] Miniutti G., Ponti G., Dadina M., Cappi M., Malaguti G., 2006, submitted to MNRAS

[137] Miniutti, G., et al. 2007, PASJ, 59, 315

[138] Misra R., Sriram K, 2003, ApJ, 584, 981

[139] Murphy, E. M., Lockman, F. J., Laor, A., & Elvis, M. 1996, ApJS, 105, 369

[140] Mushotzky, R. F., Done, C., & Pounds, K. A. 1993, ARA&A, 31, 717

[141] Mushotzky R.F., 2004, Proceedings of "Stellar–mass, Intermediate–mass, and Supermassive Black Holes", eds. S. Mineshige and K. Makishima, 2003 Kyoto, Progr. Theor. Phys. Suppl., 155, 27

[142] Nandra K., Pounds K. A., 1994, MNRAS, 268, 405

[143] Nandra, K., Turner, T., George, I., et al.: 1995, MNRAS 273, 85

[144] Nandra, K., George, I. M., Mushotzky, R. F., Turner, T. J., & Yaqoob, T. 1997, ApJ, 477, 602

[145] Nandra, K., George, I. M., Mushotzky, R. F., Turner, T. J., & Yaqoob, T. 1999, ApJL, 523, L17

[146] Nandra, K., O'Neill, P. M., George, I. M., Reeves, J. N., & Turner, T. J. 2006, Astronomische Nachrichten, 327, 1039

[147] Negoro, H., Matsuoka, M., & Mihara, T. 1999, Astronomische Nachrichten, 320, 313

[148] Negoro, H., Matsuoka, M., Mihara, T., Otani, C., Wang, T. G., & Awaki, H. 2000, Advances in Space Research, 25, 481

[149] Nelson, C. H., & Whittle, M. 1995, ApJS, 99, 67

[150] Nicastro, F., Fiore, F., & Matt, G. 1999, ApJ, 517, 108

[151] Nikolajuk, M., Czerny, B., Ziólkowski, J., & Gierliński, M. 2006, MNRAS, 370, 1534

[152] Nomoto, K., Iwamoto, K., Nakasato, N., Thielemann, F.-K., Brachwitz, F., Tsujimoto, T., Kubo, Y., & Kishimoto, N. 1997, Nuclear Physics A, 621, 467

[153] Nomoto, K., Hashimoto, M., Tsujimoto, T., Thielemann, F.-K., Kishimoto, N., Kubo, Y., & Nakasato, N. 1997, Nuclear Physics A, 616, 79

[154] Nowak M. A., Vaughan B. A., Wilms J., Dove J. B., Begelman M. C., 1999, ApJ, 510, 874

[155] O'Neill, P. M., Nandra, K., Papadakis, I. E., & Turner, T. J. 2005, MNRAS, 358, 1405

[156] Otani, C., Kii, T., Reynolds, C. S. et al. 1996, PASJ, 48, 211

[157] Page, M. J., Davis, S. W., & Salvi, N. J. 2003, MNRAS, 343, 1241

[158] Papadakis I.E., Lawrence A., 1995, MNRAS, 272, 161

[159] Papadakis, I. E., Brinkmann, W., Negoro, H., & Gliozzi, M. 2002, A&A, 382, L1

[160] Papadakis, I. E. 2004, MNRAS, 348, 207

[161] Pecháček, T., Dovčiak, M., Karas, V., & Matt, G. 2005, A&A, 441, 855

[162] Perola, G. C., et al. 2000, A&A, 358, 117

[163] Peterson B.M. et al, 2000, ApJ, 542, 161

[164] Peterson, B. M., et al. 2004, ApJ, 613, 682

[165] Peterson B.M. et al., 2005, ApJ, 632, 799

[166] Petrucci, P., Henri, G., Maraschi, L., et al.: 2002, A&A 388, L5

[167] Petrucci, P. O., & Dadina, M. 2004, Nuclear Physics B Proceedings Supplements, 132, 217

[168] Piconcelli, E., Jimenez-Bailón, E., Guainazzi, M., Schartel, N., Rodríguez-Pascual, P. M., & Santos-Lleó, M. 2005, A&A, 432, 15

[169] Ponti, G., Cappi, M., Dadina, M., & Malaguti, G., 2004, A&A, 417, 451

[170] Ponti, G., Cappi, M., Dadina, M., Malaguti, G., Malizia, A., & di Cocco, G. 2004, Nuclear Physics B Proceedings Supplements, 132, 221

[171] Ponti, G., Cappi, M., Dadina, Maraschi, L., Palumbo, G.G.C., Foschini, L. & Malaguti, G., 2005, Proceedings of the 6th Italian Conference on Active Galactic Nuclei, http://www.arcetri.astro.it/ agn6/

[172] Ponti, G., Miniutti, G., Cappi, M., Maraschi, L., Fabian, A. C., & Iwasawa, K. 2006, MNRAS, 368, 903

[173] Ponti, G., Miniutti, G., Fabian, A. C., Cappi, M., & Palumbo, G. G. C. 2006, Astronomische Nachrichten, 327, 1055

[174] Porquet, D., Reeves, J. N., Uttley, P., & Turner, T. J. 2004, A&A, 427, 101

[175] Pounds, K. A., Nandra, K., Stewart, G. C., George, I. M., & Fabian, A. C. 1990, Nature, 344, 132

[176] Pounds, K. A., Nandra, K., Fink, H. H., & Makino, F. 1994, MNRAS, 267, 193

[177] Pounds, K., Reeves, J., O'Brien, P., Page, K., Turner, M., & Nayakshin, S. 2001, ApJ, 559, 181

[178] Pounds, K., Reeves, J., 2002, ESTEC Conf.: New Visions of the X-ray Universe in the XMM-Newton and Chandra Era, (astro-ph/0201436)

[179] Pounds, K. A., King, A. R., Page, K. L., & O'Brien, P. T. 2003, MNRAS, 346, 1025

[180] Pounds, K. A., Reeves, J. N., King, A. R., Page, K. L., O'Brien, P. T., & Turner, M. J. L. 2003, MNRAS, 345, 705

[181] Porquet, D., Reeves, J. N., Uttley, P., & Turner, T. J. 2004, A&A, 427, 101

[182] Portegies Zwart S.F., Makino J., McMillan S.L.W., Hut P., 1999, A&A, 348, L17

[183] Pounds K.A., Reeves J.N., King A.R., Page K.L., 2004, MNRAS, 350, 10

[184] Poutanen, J., & Fabian, A. C. 1999, MNRAS, 306, L31

[185] Press, W. H. 1978, Comments on Astrophysics, 7, 103

[186] Press, W. H., Teukolsky, S. A., Vetterling, W. T., & Flannery, B. P. 1992, Cambridge: University Press, Numerical Recipes in C++ 1992, 2nd ed.,

[187] Protassov, R., van Dyk, D. A., Connors, A., Kashyap, V. L., & Siemiginowska, A. 2002, ApJ, 571, 545

[188] Ptak A., Colbert E., van der Marel R., Roye E., Heckman T., Towne B., 2006, ApJS in press (preprint astro-ph/0605561)

[189] Reeves J. N., Turner M. J. L., 2000, MNRAS, 316, 234

[190] Reeves, J. N., O'Brien, P. T., & Ward, M. J. 2003, ApJL, 593, L65

[191] Reeves, J. N., et al. 2006, Astronomische Nachrichten, 327, 1079

[192] Reynolds, C. S. 1997, MNRAS, 286, 513

[193] Reynolds, C. S. 1997, ASP Conf. Ser. 128: Mass Ejection from Active Galactic Nuclei, 128, 173

[194] Reynolds C.S., Loan A.J., Fabian A.C., Makishima K., Brandt W.N., Mizuno T., 1997, MNRAS, 286, 349

[195] Reynolds, C. S., Young, A. J., Begelman, M. C., & Fabian, A. C. 1999, ApJ, 514, 164

[196] Reynolds, C. S., Brenneman, L. W., Wilms, J., & Kaiser, M. E. 2004, MNRAS, 352, 205

[197] Remillard, R. A., & McClintock, J. E. 2006, ARA&A, 44, 49

[198] Rosner, R., & Vaiana, G. S. 1978, ApJ, 222, 1104

[199] Ross, R. R. & Fabian, A. C. 1993, MNRAS, 261, 74

[200] Ross, R. R., Fabian, A. C., & Young, A. J. 1999, MNRAS, 306, 461

[201] Ross, R. R., & Fabian, A. C., 2005, MNRAS, 358, 211

[202] Ruszkowski, M. & Fabian, A. C. 2000, MNRAS, 315, 223

[203] Ruszkowski M., Begelman M.C., 2003, ApJ, 586, 384

[204] Sako, M., Kahn, S. M., Branduardi-Raymont, G. et al. 2003, ApJ, 596, 114

[205] Salpeter, E. E. 1964, ApJ, 140, 796

[206] Schlegel E.M., 1995, Rep. Prog. Phys., 58, 1375

[207] Schmidt, M. 1963, Nature, 197, 1040

[208] Schurch, N. J., & Done, C. 2006, MNRAS, 371, 81

[209] Schwope, A., et al. 2000, Astronomische Nachrichten, 321, 1

[210] Seyfert, C. K. 1943, ApJ, 97, 28

[211] Shakura, N. I., & Sunyaev, R. A. 1973, A&A, 24, 337

[212] Shakura, N. I., & Sunyaev, R. A. 1976, MNRAS, 175, 613

[213] Shemmer O., Uttley P., Netzer H., M^{c}Hardy I.M, 2003, MNRAS, 343, 1341

[214] Shields, G. A., Gebhardt, K., Salviander, S., Wills, B. J., Xie, B., Brotherton, M. S., Yuan, J., & Dietrich, M. 2003, ApJ, 583, 124

[215] Shih, D. C., Iwasawa, K., & Fabian, A. C. 2002, MNRAS, 333, 687

[216] Singh, K. P., Garmire, G. P., & Nousek, J. 1985, ApJ, 297, 633

[217] Singh, K. P., Westergaard, N. J., Schnopper, H. W., Awaki, H., & Tawara, Y. 1990, ApJ, 363, 131

[218] Smith, R. A. N., Page, M. J., & Branduardi-Raymont, G. 2007, A&A, 461, 135

[219] Sobolewska, M. A., & Done, C. 2007, MNRAS, 374, 150

[220] Stella, L. 1990, Nature, 344, 747

[221] Stern, B. E., Poutanen, J., Svensson, R., Sikora, M., & Begelman, M. C. 1995, ApJL, 449, L13

[222] Strohmayer T.E., Mushotzky R.F., 2003, ApJ, 586, L61

[223] Strüder, L. Briel, U., Dennerl, K. et al. 2001, A&A, 365, L18

[224] Suebsuwong, T., Malzac, J., Jourdain, E., & Marcowith, A. 2006, A&A, 453, 773

[225] Sunyaev, R. A. & Titarchuk, L. G. 1980, A&A, 86, 121

[226] Surace J.A., Sanders D.B., Mazzarella J.M., 2004, AJ, 127, 3235

[227] Swartz D.A., Ghosh K.K., Tennant A.F., Wu K., 2004, ApJS, 154, 519

[228] Tanaka, Y., et al. 1995, Nature, 375, 659

[229] Tanaka, Y., Boller, T., Gallo, L., Keil, R., & Ueda, Y. 2004, PASJ, 56, L9

[230] Taylor R.D., Uttley P., M^{c}Hardy I.M., 2003, MNRAS, 342, L31

[231] Turner, M. J. L., et al. 2001, A&A, 365, L27

[232] Turner, A. K., Fabian, A. C., Vaughan, S., & Lee, J. C. 2003, MNRAS, 346, 833

[233] Turner, T. J., Kraemer, S. B., George, I. M., Reeves, J. N., & Bottorff, M. C. 2005, ApJ, 618, 155

[234] Uttley P., M^{c}Hardy I.M., 2001, MNRAS, 323, L26

[235] Uttley, P., McHardy, I. M., & Papadakis, I. E. 2002, MNRAS, 332, 231

[236] Uttley P., Fruscione A., M^{c}Hardy I.M., Lamer G., 2003, ApJ, 595, 656

[237] Uttley P., Taylor R.D., M^{c}Hardy I.M., Page M.J., Mason K.O., Lamer G., Fruscione A., 2004, MNRAS, 347, 1345

[238] Uttley P., M^{c}Hardy I.M., Vaughan S., 2005, MNRAS, 359, 345

[239] Vaughan, S., Reeves, J., Warwick, R., & Edelson, R. 1999, MNRAS, 309, 113

[240] Vaughan, S., Fabian, A. C., & Nandra, K. 2003, MNRAS, 339, 1237

[241] Vaughan, S., Edelson, R., Warwick, R. S. & Uttley, P. 2003, MNRAS, 345, 1271

[242] Vaughan, S., & Fabian, A. C., 2004, MNRAS, 348, 1415

[243] Vaughan, S., Iwasawa, K., Fabian, A. C., & Hayashida, K. 2005, MNRAS, 356, 524

[244] Voges, W., et al. 1999, A&A, 349, 389

[245] Walter, R., & Courvoisier, T. J.-L. 1992, A&A, 258, 255

[246] Wandel A., Peterson B. M., Malkan M. A., 1999, ApJ, 526, 579

[247] White, R. J. & Peterson, B. M. 1994, PASP, 106, 879

[248] Wilms, J., Reynolds, C. S., Begelman, M. C., Reeves, J., Molendi, S., Staubert, R., & Kendziorra, E. 2001, MNRAS, 328, L27

[249] Winter L.M., Mushotzky R.F., Reynolds C.S., 2006, MNRAS in press (preprint astro-ph/0512480)

[250] Woo J. H., Urry C. M., 2002, ApJ, 579, 530

[251] Yaqoob, T., McKernan, B., Kraemer, S. B., Crenshaw, D. M., Gabel, J. R., George, I. M., & Turner, T. J. 2003, ApJ, 582, 105

[252] Yaqoob, T., & Padmanabhan, U. 2004, ApJ, 604, 63

[253] Yaqoob, T., & Serlemitsos, P. 2005, ApJ, 623, 112

[254] Zdziarski, A. A., Ghisellini, G., George, I. M., Fabian, A. C., Svensson, R., & Done, C. 1990, ApJL, 363, L1

[255] Zdziarski, A. A., Johnson, W. N., Done, C., Smith, D., & McNaron-Brown, K. 1995, ApJL, 438, L63

[256] Zdziarski, A. A., & Grandi, P. 2001, ApJ, 551, 186

[257] Zel'Dovich, Y. B., & Novikov, I. D. 1964, Soviet Physics Doklady, 9, 246